

# Coal and rock dynamic disasters: Advances of physical and numerical simulation in monitoring, early warning, and prevention, 2<sup>nd</sup> edition

**Edited by**

Xuelong Li, Jingjing Meng, Jia Lin, M. Younis Khan  
and Zhibo Zhang

**Published in**

Frontiers in Earth Science



## FRONTIERS EBOOK COPYRIGHT STATEMENT

The copyright in the text of individual articles in this ebook is the property of their respective authors or their respective institutions or funders. The copyright in graphics and images within each article may be subject to copyright of other parties. In both cases this is subject to a license granted to Frontiers.

The compilation of articles constituting this ebook is the property of Frontiers.

Each article within this ebook, and the ebook itself, are published under the most recent version of the Creative Commons CC-BY licence. The version current at the date of publication of this ebook is CC-BY 4.0. If the CC-BY licence is updated, the licence granted by Frontiers is automatically updated to the new version.

When exercising any right under the CC-BY licence, Frontiers must be attributed as the original publisher of the article or ebook, as applicable.

Authors have the responsibility of ensuring that any graphics or other materials which are the property of others may be included in the CC-BY licence, but this should be checked before relying on the CC-BY licence to reproduce those materials. Any copyright notices relating to those materials must be complied with.

Copyright and source acknowledgement notices may not be removed and must be displayed in any copy, derivative work or partial copy which includes the elements in question.

All copyright, and all rights therein, are protected by national and international copyright laws. The above represents a summary only. For further information please read Frontiers' Conditions for Website Use and Copyright Statement, and the applicable CC-BY licence.

ISSN 1664-8714  
ISBN 978-2-8325-4983-4  
DOI 10.3389/978-2-8325-4983-4

## About Frontiers

Frontiers is more than just an open access publisher of scholarly articles: it is a pioneering approach to the world of academia, radically improving the way scholarly research is managed. The grand vision of Frontiers is a world where all people have an equal opportunity to seek, share and generate knowledge. Frontiers provides immediate and permanent online open access to all its publications, but this alone is not enough to realize our grand goals.

## Frontiers journal series

The Frontiers journal series is a multi-tier and interdisciplinary set of open-access, online journals, promising a paradigm shift from the current review, selection and dissemination processes in academic publishing. All Frontiers journals are driven by researchers for researchers; therefore, they constitute a service to the scholarly community. At the same time, the *Frontiers journal series* operates on a revolutionary invention, the tiered publishing system, initially addressing specific communities of scholars, and gradually climbing up to broader public understanding, thus serving the interests of the lay society, too.

## Dedication to quality

Each Frontiers article is a landmark of the highest quality, thanks to genuinely collaborative interactions between authors and review editors, who include some of the world's best academicians. Research must be certified by peers before entering a stream of knowledge that may eventually reach the public - and shape society; therefore, Frontiers only applies the most rigorous and unbiased reviews. Frontiers revolutionizes research publishing by freely delivering the most outstanding research, evaluated with no bias from both the academic and social point of view. By applying the most advanced information technologies, Frontiers is catapulting scholarly publishing into a new generation.

## What are Frontiers Research Topics?

Frontiers Research Topics are very popular trademarks of the *Frontiers journals series*: they are collections of at least ten articles, all centered on a particular subject. With their unique mix of varied contributions from Original Research to Review Articles, Frontiers Research Topics unify the most influential researchers, the latest key findings and historical advances in a hot research area.

Find out more on how to host your own Frontiers Research Topic or contribute to one as an author by contacting the Frontiers editorial office: [frontiersin.org/about/contact](https://frontiersin.org/about/contact)



# Coal and rock dynamic disasters: Advances of physical and numerical simulation in monitoring, early warning, and prevention, 2<sup>nd</sup> edition

## Topic editors

Xuelong Li — Shandong University of Science and Technology, China

Jingjing Meng — Luleå University of Technology, Sweden

Jia Lin — Curtin University, Australia

M. Younis Khan — University of Peshawar, Pakistan

Zhibo Zhang — University of Science and Technology Beijing, China

## Citation

Li, X., Meng, J., Lin, J., Khan, M. Y., Zhang, Z., eds. (2024). *Coal and rock dynamic disasters: Advances of physical and numerical simulation in monitoring, early warning, and prevention, 2<sup>nd</sup> edition*. Lausanne: Frontiers Media SA. doi: 10.3389/978-2-8325-4983-4

**Publisher's note:** This is a 2<sup>nd</sup> edition due to an article retraction.

## Table of contents

05	<b>Theoretical study on longitudinal deformation of adjacent tunnel subjected to pre-dewatering based on Pasternak-Timoshenko beam model</b> Sun Yang, Rong Yao, Yu Junping, Zhu Liqing, Ding Haibin and Tong Lihong
15	<b>Effect of pre-confining pressure on unloading-induced coalburst: Insights from distinct element modelling</b> Jinrong Cao, Linming Dou, Kunyou Zhou, Jiliang Kan, Jiazhao Li and Yanjiang Chai
30	<b>Development and application of a borehole stress meter in rocks surrounding the roadway, based on optical-fiber sensing technology</b> Xiaoping Xie, Xinqiu Fang, Hongyang Liu, Xiaopeng Xing, Minfu Liang, Gang Wu and Ningning Chen
45	<b>Displacement prediction of open-pit mine slope based on SSA-ELM</b> Bo Li and Junbo Qiu
55	<b>Evaluation of bearing capacity of PHC pipe piles via the dynamic and static loading test</b> Caihua Li and Xuepeng Li
65	<b>Determination of initial velocity of gas diffusion under temperature control</b> Xianguang Shang, Jianping Wei, Zhihui Wen, Linwei Shang and Junling Yuan
73	<b>Numerical simulation study on the influence of air leakage on oxygen concentration in goafs of fully mechanized caving mining with shallow buried and large mining height</b> Xingpan Zhu and Hu Wen
83	<b>Experimental research on the water precipitation performance of polymer colloid and fly ash colloid and their applications as fire extinguishing materials in mines</b> Yuyang Shang
94	<b>Study on heat exchange of groundwater under complex geological conditions in karst area of south China</b> Kun Wang, Wanjiang Wang and Lidong Huang
105	<b>Study on shear characteristics of calcareous sand with different particle size distribution</b> Yongtao Zhang, Ruiyuan Zhang, Chengcheng Yu, Huiwu Luo and Zhiqiang Deng
119	<b>Estimation of mechanics parameters of rock in consideration of confining pressure using monitoring while drilling data</b> Yonghao Zhang, Jianbin Zhao, Zhanshan Xiao, Yanwu Gao, Shitao Cui, Daojie Cheng, Mingming He, Chaoqiang Fang, Haifang Xue and Ying Zhao

- 131 **Experimental investigation into rock burst proneness of rock materials considering strain rate and size effect**  
Xiaobin Li, Haoteng Wang, Ying Zhao, Haifang Xue and Lingyun Li
- 147 **Research on evaluation model of rock failure integrity under complex geological conditions in karst area**  
Ma Jianbo, Wang Zhongqi, Yang En and Liu Menghua



## OPEN ACCESS

## EDITED BY

Xuelong Li,  
Shandong University of Science and  
Technology, China

## REVIEWED BY

Zenian Wang,  
Jiangsu University, China  
Junlong Sun,  
Kunming University of Science and  
Technology, China

## \*CORRESPONDENCE

Ding Haibin,  
✉ hbding@ecjtu.edu.cn

## SPECIALTY SECTION

This article was submitted to  
Environmental Informatics and Remote  
Sensing, a section of the journal  
Frontiers in Earth Science

RECEIVED 03 December 2022

ACCEPTED 28 December 2022

PUBLISHED 10 January 2023

## CITATION

Yang S, Yao R, Junping Y, Liqing Z, Haibin D  
and Lihong T (2023), Theoretical study on  
longitudinal deformation of adjacent  
tunnel subjected to pre-dewatering based  
on Pasternak-Timoshenko beam model.  
*Front. Earth Sci.* 10:1114987.  
doi: 10.3389/feart.2022.1114987

## COPYRIGHT

© 2023 Yang, Yao, Junping, Liqing, Haibin  
and Lihong. This is an open-access article  
distributed under the terms of the [Creative  
Commons Attribution License \(CC BY\)](#).  
The use, distribution or reproduction in  
other forums is permitted, provided the  
original author(s) and the copyright  
owner(s) are credited and that the original  
publication in this journal is cited, in  
accordance with accepted academic  
practice. No use, distribution or  
reproduction is permitted which does not  
comply with these terms.

# Theoretical study on longitudinal deformation of adjacent tunnel subjected to pre-dewatering based on Pasternak-Timoshenko beam model

Sun Yang<sup>1</sup>, Rong Yao<sup>1</sup>, Yu Junping<sup>1</sup>, Zhu Liqing<sup>1</sup>, Ding Haibin<sup>2,3\*</sup> and  
Tong Lihong<sup>2,3</sup>

<sup>1</sup>Jiangxi Transportation Institute Co., LTD, Nanchang, Jiangxi, China, <sup>2</sup>State Key Laboratory of Performance Monitoring and Protecting of Rail Transit Infrastructure, East China Jiaotong University, Nanchang, Jiangxi, China, <sup>3</sup>Institute of Geotechnical Engineering, School of Civil Engineering and Architecture, East China Jiaotong University, Nanchang, Jiangxi, China

In this research, under the disturbance of pre-dewatering, the analytical solution of vertical displacement of the adjacent tunnel is derived using the two-stage analysis method. In the first stage, the effective stress principle was used to calculate the additional stress of the adjacent tunnel caused by dewatering. In the second stage, the Pasternak-Timoshenko beam model was used to simulate the interaction between the tunnel and soil, taking the tunnel shear deformation into account. By referring to the calculation results of existing literature, the correctness of the proposed method is verified, and the influencing factors of the longitudinal displacement of the tunnel are further analyzed. The results show that with the increase of the distance from the dewatering well and soil elastic modulus, the vertical displacement of the tunnel is reduced. The deformation of the existing tunnel increases with the permeability coefficient. The decrease of the tunnel shear modulus can lead to the rapid increase of the tunnel's vertical displacement, so the shear stiffness should be considered in the analysis of its deformation. The increase in the dropping amplitude of the water level in the well will decrease the water level in the surrounding strata. According to the different relative positions of the tunnel and the water table, there are two forms of additional load on the tunnel. Before the water level drops to the tunnel axis, the tunnel's Additional load and displacement gradually increase.

## KEYWORDS

excavation dewatering, effective stress principle, Timoshenko beam, Pasternak foundation, adjacent tunnel

## 1 Introduction

Foundation pit excavation is an effective means of underground space development. However, pre-dewatering is necessary for foundation pit engineering to improve construction conditions. In the process of dewatering, the effective stress of soil mass under the original water level will increase (Wang et al., 2013) to have a harmful effect on the existing tunnel, which is one of the main reasons for the long-term settlement of the tunnel (Zeng et al., 2019; DING et al., 2021). Therefore, investigating the longitudinal settlement of the adjacent tunnel subjected to pre-dewatering is crucial for operation safety.

At present, many scholars have studied the influence of pre-dewatering on the adjacent tunnel. For example, taking the excavation project of Shenzhen Kerry Construction Square Phase II as a research subject, (Zhang and Pan, 2013) found that the pre-dewatering of this project caused a settlement of 5.7 mm in the adjacent subway tunnel, which did not meet the requirements of metro track deformation. Liu (2013) established a numerical model to study the influence of dewatering on the adjacent subway tunnel in the excavation project of Tianjin West Railway Station. Taking an excavation project of Changsha Line 5 as an example, (Huang et al., 2018) studied the sensitivity of adjacent subway tunnels to excavation dewatering velocity by combining Biot consolidation theory and Midas GTS finite element software. Combining the finite difference method with fluid-structure coupling theory, (Jia et al., 2010) studied the stress and deformation law of the existing municipal tunnel in the process of dewatering for a new tunnel project in Chengdu. According to the geological characteristics of underground water in Shanghai, (Li, 2008) studied the influence of excavation dewatering on the longitudinal deformation of operating metro tunnels.

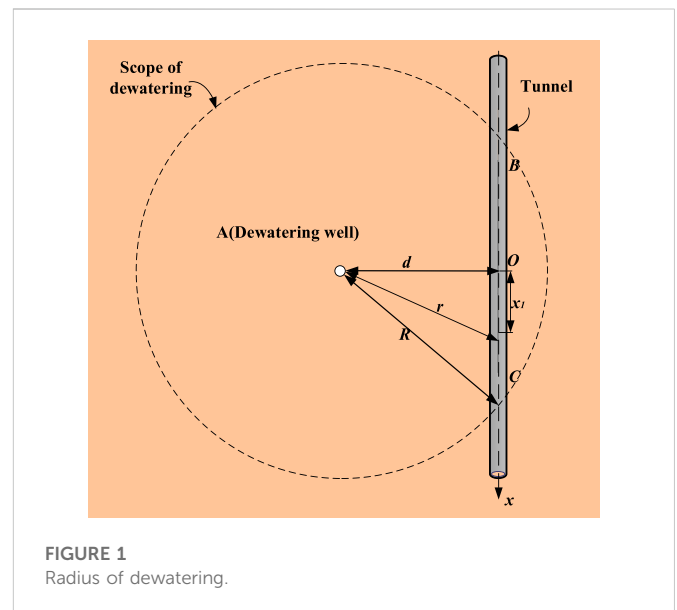
At present, there are few theoretical studies on the longitudinal deformation of adjacent tunnels caused by dewatering. Combining the effective stress principle with the Pasternak foundation model, (Xu et al., 2021) used the Euler-Bernoulli beam to simulate pipelines based on the two-stage theoretical method and deduced analytical solutions for the deformation of adjacent pipelines caused by dewatering. Under the influence of excavation and dewatering, (Zhang et al., 2017) used the two-stage theoretical method to study the deformation of the underlying tunnel and used the Euler-Bernoulli beam to simulate the tunnel, and found that the influence of excavation dewatering on the underlying tunnel should not be ignored.

In the existing studies on the deformation of shield tunnels, the shield tunnel is usually simplified as an Euler-Bernoulli beam (Zhang and Zhang, 2013; Liang et al., 2016; Liang et al., 2018). However, unlike pipelines, the shield tunnel is multi-segment ring-shaped segment splintering so that the Euler-Bernoulli beam will ignore the shear deformation generated by the tunnel. This will cause an error in the calculation. In recent years, some scholars have chosen to adopt the Timoshenko beam simulation tunnel (Li et al., 2015; Liang et al., 2017; Zhang et al., 2019; Liang et al., 2021) that can consider shear deformation.

To sum up, this paper is based on the two-stage method, the effective stress principle and Dupuit assumption are adopted in the first stage to calculate the additional stress of the adjacent tunnel caused by dewatering. In the second stage, the Timoshenko beam is used to simulate the tunnel while considering the shear deformation, and the Pasternak foundation model is used to simulate the interaction between the tunnel and soil. Then, the analytical solution of vertical displacement of adjacent tunnel caused by excavation dewatering is derived considering the shear deformation of the tunnel. Finally, the accuracy of the proposed method is verified by referring to the current literature results. The influence of the distance between the tunnel and the dewatering well, the tunnel shear modulus, the elastic modulus of soil, the permeability coefficient of soil, and the water level drawdown on the longitudinal displacement of the tunnel are studied.

## 2 Establishment of the equation

The influencing range of excavation pre-dewatering on the surrounding water level is defined as the dewatering radius, and



the existing shield tunnel within the dewatering radius will be affected by the dropping in the surrounding water level. As shown in Figure 1, A is the dewatering well, the dewatering radius is R, and the distance between the tunnel and the dewatering well is d. The X-axis is set along the tunnel direction, and the O point on the tunnel axis, that is, the nearest to the dewatering well is taken as the origin. Point B and point C are the intersection points between the dewatering radius and the tunnel.

### 2.1 Effective stress induced by pre-dewatering

Within the dewatering radius, the dewatering will cause a funnel-shaped dewatering curve in the soil; as shown in Figure 2,  $R_0$  is the radius of the dewatering well,  $H_0$  is the initial water level height of the phreatic aquifer, and  $H_t$  is the water level height in the well after dewatering. Based on Dupuit's assumption, the flow rate at different water levels is equal to the amount of water pumped from the well (Verruijt, 1982):

$$Q = 2\pi r h k_t \frac{dh}{dr} \quad (1)$$

where  $r$  is the horizontal distance from the well,  $h$  is the water level height at this position, and  $k_t$  is the permeability coefficient of soil. The dewatering curve  $h(r)$  can be obtained by substituting the water level boundary conditions of the dewatering well  $\begin{cases} h = H_0, r = R \\ h = H_t, r = R_0 \end{cases}$  and the dewatering radius into Eq. 1:

$$h(r) = \sqrt{H_0^2 - \frac{Q}{\pi k} \ln \frac{R}{r}} \\ = \sqrt{H_0^2 - (H_0^2 - H_t^2) \frac{\ln \frac{R}{r}}{\ln \frac{R}{R_0}}} \quad (2)$$

According to Sakukin's formula, the dewatering radius can be calculated by  $R = 2s_w \sqrt{kH_0}$  (Verruijt, 1982),  $s_w = H_0 - H_t$ .



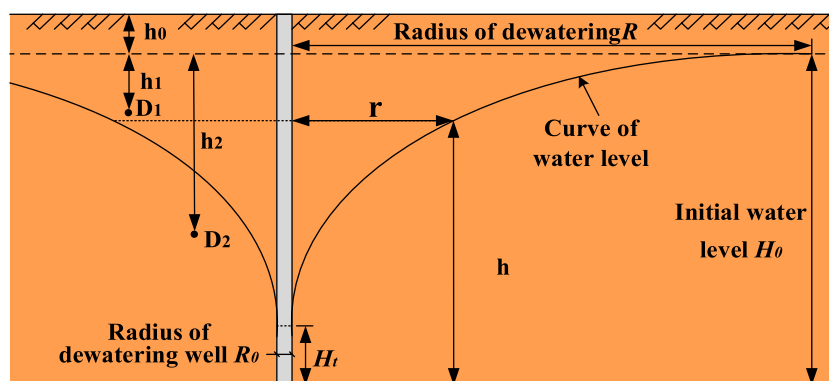


**FIGURE 2**  
Curve of water level after dewatering.

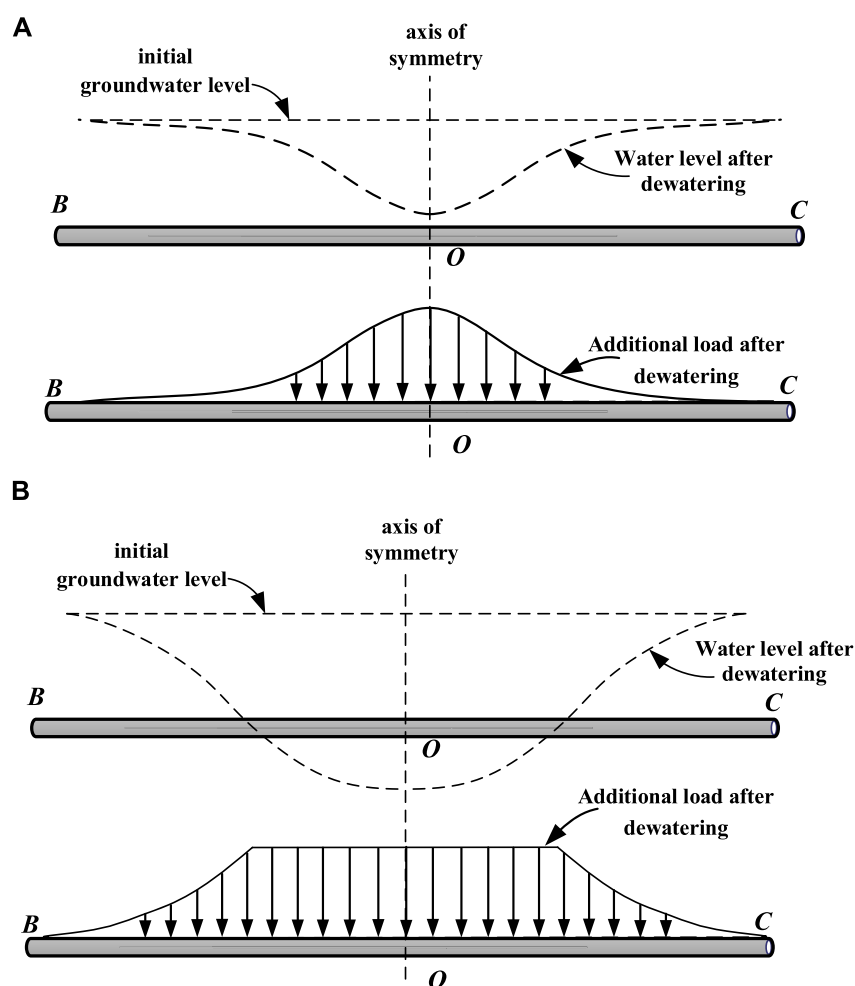


**FIGURE 3**  
Water level and additional load distribution along tunnel length after dewatering: (A) water level is above the tunnel after dewatering; (B) part of the water level is below the tunnel after dewatering.

Within the dewatering radius, the decrease in water level will reduce pore water pressure in the soil, leading to an increase in effective stress, and this increased amplitude can be calculated according to the change in water level after dewatering; It can be

divided into two cases according to the relative position of the calculated point.

As shown in Figure 2, point  $D_1$  is above the water level after dewatering, and point  $D_2$  is below the water level after dewatering.

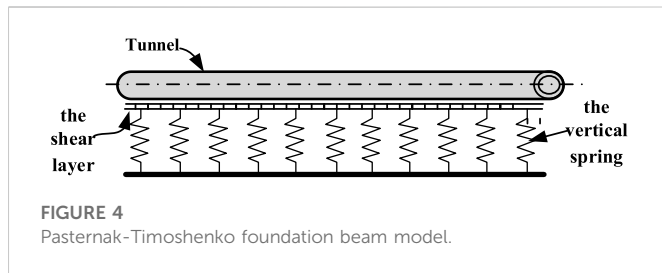


FIGURE 4  
Pasternak-Timoshenko foundation beam model.

Therefore, the effective stress increment  $\sigma_1$  and  $\sigma_2$  of the two points can be calculated as follows:

$$\sigma_1 = \sigma_{t1} - \sigma_{01} = (h_0 + h_1)\gamma - (h_0\gamma + h_1\gamma_s - h_1\gamma_w) = h_1(\gamma - \gamma_s + \gamma_w) \quad (3a)$$

$$\sigma_2 = \sigma_{t2} - \sigma_{02} = [(h_0 + H_0 - h)\gamma + (h_2 - H_0 + h)(\gamma_s - \gamma_w)] - (h_0\gamma + h_2\gamma_s - h_2\gamma_w) = (H_0 - h)(\gamma - \gamma_s + \gamma_w) \quad (3b)$$

where  $\sigma_t$  and  $\sigma_0$  are the effective stresses of  $D_1$  and  $D_2$  points before and after dewatering, respectively; and  $h_0$  is the buried depth of the initial water level from the ground surface;  $h_1$  and  $h_2$  are the elevation differences between  $D_1$  and  $D_2$  points and the initial water level, respectively;  $\gamma$ ,  $\gamma_s$  and  $\gamma_w$  are unit weight and saturated unit weight of soil, and unit weight of water, respectively.

Above and below the water level, their effective stress increments after dewatering are different. According to the relative position of the tunnel and water level, the additional stress caused by dewatering is different. Therefore, the additional stress caused by dewatering can be calculated in two cases: all parts of the tunnel are below the water level after dewatering, and part of the tunnel is above the water level, as shown in Figure 3. Based on the coordinate system established in Figure 1, the additional stress on the tunnel under the two conditions is calculated as follows:

When the tunnel is below the water level, the distance between any point on the tunnel and the dewatering well  $r = \sqrt{x^2 + d^2}$ , after substituting it into Eq. 2 and Eq. 3a can be obtained:

$$\sigma(x) = \left( H_0 - \sqrt{(H_0^2 - H_t^2) \frac{\ln \frac{R}{\sqrt{x^2 + d^2}}}{\ln \frac{R}{R_0}}} \right) \cdot (\gamma - \gamma_s + \gamma_w) \quad (4)$$

When the tunnel is partially located above the water level, the additional stress of the tunnel is divided into two parts. The additional stress of the tunnel above the water level is the same and is a fixed value.

$$\sigma = h_1(\gamma - \gamma_s + \gamma_w) \quad (5)$$

where  $h_1$  is the height difference between the buried depth of the tunnel axis and the initial water level. The calculation of additional stress of other tunnels located below the water level is similar to Eq. 4. When  $h(r) = H_0 - h_1$ , it is the intersection point between water level and tunnel, so the coordinate of this point can be obtained as

$$x = \sqrt{\left( R \frac{(H_0 - h_1)^2 - H_t^2}{H_0^2 - H_t^2} \cdot R_0 \frac{(2H_0h_1 - h_1^2)}{H_0^2 - H_t^2} \right)^2 - d^2} \quad (6)$$

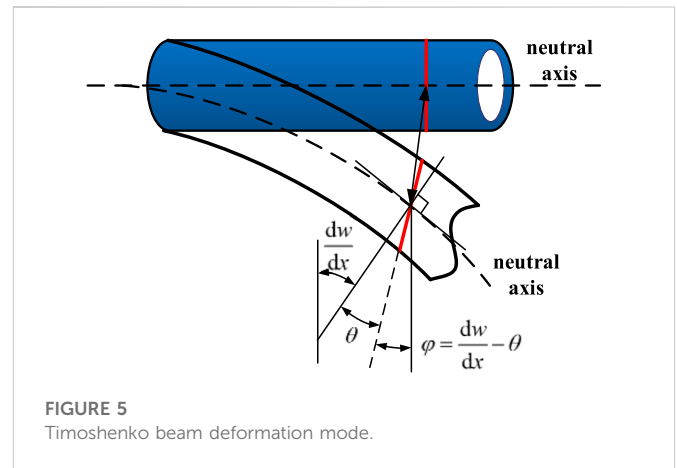


FIGURE 5  
Timoshenko beam deformation mode.

In this review, when the tunnel part is located above the water level, the formula for calculating the additional stress of the tunnel is:

$$\sigma(x) = \begin{cases} \left( H_0 - \sqrt{H_0^2 - (H_0^2 - H_t^2) \frac{\ln \frac{R}{\sqrt{x^2 + d^2}}}{\ln \frac{R}{R_0}}} \right) \cdot (\gamma - \gamma_s + \gamma_w), x^2 > \left( R \frac{(H_0 - h_1)^2 - H_t^2}{H_0^2 - H_t^2} \cdot R_0 \frac{(2H_0h_1 - h_1^2)}{H_0^2 - H_t^2} \right)^2 - d^2; \\ h_1(\gamma - \gamma_s + \gamma_w), x^2 \leq \left( R \frac{(H_0 - h_1)^2 - H_t^2}{H_0^2 - H_t^2} \cdot R_0 \frac{(2H_0h_1 - h_1^2)}{H_0^2 - H_t^2} \right)^2 - d^2 \end{cases} \quad (7)$$

## 2.2 Establishment of the governing equation of the timoshenko beam

The longitudinal deformation of the shield tunnel is composed of bending and shear deformation (Shen et al., 2014; Wu et al., 2015). When the traditional Euler-Bernoulli beam is used to simulate a shield tunnel, the tunnel is regarded as a structure with infinite shear strength, so the shear deformation of the tunnel is ignored. Since shield tunnels are composed of annular segments, unlike continuous structures such as pipelines, Euler-Bernoulli beams will underestimate the longitudinal deformation. The Timoshenko beam can take into account the shear deformation of the tunnel under additional loads (Li et al., 2015). In addition, the Pasternak foundation model can consider the continuity of foundation deformation and simulate the interaction between soil and tunnel well (Xu et al., 2021). Therefore, the tunnel is considered an infinitely long Timoshenko beam on the Pasternak foundation in this research to take into account the shear deformation generated by the tunnel, as shown in Figure 4. The section of the Timoshenko beam is no longer perpendicular to the neutral axis but crosses the normal direction of the neutral axis with an angle due to shear deformation. The stress deformation mode is more complex than the Euler-Bernoulli beam, as shown in Figure 5.

According to Timoshenko beam deformation theory, the relationship between tunnel bending moment  $M$ , shear force, and  $Q$  and displacement  $w$  is:

$$Q = (\kappa GA) \left[ \frac{dw(x)}{dx} - \theta \right] \quad (8)$$

$$M = -E_t I_t \frac{d\theta}{dx} \quad (9)$$

where  $\kappa$  is the equivalent section coefficient, the tunnel is the annular section,  $\kappa = 0.5$ ;  $G$  is the tunnel shear modulus,  $G = E_t / 2(1 + \nu_t)$ ;  $\nu_t$  is Poisson's ratio of tunnel;  $A$  is the annular section area of the tunnel;  $E_t$  is the elastic modulus of the tunnel;  $I_t$  is the moment of inertia of the tunnel. According to the equilibrium differential equation:

$$p(x)Ddx - q(x)Ddx - dQ = 0 \quad (10)$$

$$\frac{p(x)D}{2}dx^2 + Qdx - \frac{q(x)D}{2}dx^2 - dM = 0 \quad (11)$$

where  $q(x)$  is the additional load generated by dewatering,  $q(x) = \sigma(x)$ ;  $D$  is tunnel diameter.  $p(x)$  is the ground reaction force. According to the Pasternak foundation model,  $p(x)$  is obtained as

$$p(x) = kw(x) - g_s \frac{d^2 w(x)}{dx^2} \quad (12)$$

where  $k$  and  $g_s$  are the elastic coefficient and shear coefficient of the foundation, respectively, which can be calculated as follows (Attewell et al., 1986; Tanahashi, 2004):

$$k = \frac{1.3E_s}{D(1 - \nu^2)} \left( \frac{E_s D^4}{E_t I_t} \right)^{1/2} \quad (13)$$

$$g_s = \frac{E_s t}{6(1 + \nu)} \quad (14)$$

where  $E_s$  soil elastic modulus;  $\nu$  is Poisson's ratio of soil;  $t$  is the soil shear layer thickness, and  $t = 6D$  is used for calculation (Xu, 2005).

Through Eqs. 8–12, the governing equation of tunnel displacement  $w(x)$  can be obtained as:

$$E_t I_t \left( \frac{g_s D}{\kappa G A} + 1 \right) \frac{d^4 w(x)}{dx^4} - \left( \frac{k D E_t I_t}{\kappa G A} + g_s D \right) \frac{d^2 w(x)}{dx^2} + k D w(x) = \left[ q(x) - \frac{E_t I_t}{\kappa G A} \frac{d^2 q(x)}{dx^2} \right] D \quad (15)$$

### 3 Solving the governing equation

Based on the derivation process of Guan et al. (Guan et al., 2021), Eq. 15 was solved according to  $q(x) = 0$ , and the general solution was obtained:

$$w(x) = e^{\alpha x} [A_1 \cos(\beta x) + A_2 \sin(\beta x)] + e^{-\alpha x} [A_3 \cos(\beta x) + A_4 \sin(\beta x)] \quad (16)$$

where  $A_1$ ,  $A_2$ ,  $A_3$ , and  $A_4$  are undetermined coefficients;  $\alpha = \sqrt{\lambda^2/2 + \gamma/4}$ ;  $\beta = \sqrt{\lambda^2/2 - \gamma/4}$ ;  $\gamma = \frac{k D E_t I_t + g_s D \kappa G A}{(\kappa G A + g_s D) E_t I_t}$ ;  $\lambda = \sqrt[4]{\frac{k D \kappa G A}{(\kappa G A + g_s D) E_t I_t}}$ .

When the tunnel is subjected to concentrated load  $P$  at  $x=0$ , the boundary conditions of the tunnel are as follows:

$$u(\pm \infty) = 0 \quad (17a)$$

$$\left. \frac{dw(x)}{dx} \right|_{x=0} = 0 \quad (17b)$$

$$E_p I_p \left. \frac{d^3 w(x)}{dx^3} \right|_{x=0} = PD/2 \quad (17c)$$

After substituting Eqs. 17a–17c into Eq. 16, the calculation of the tunnel displacement under concentrated load  $P$  can be obtained as follows:

$$w(x) = \frac{P D e^{-\alpha x} (\beta \cos \beta x + \alpha \sin \beta x)}{4 E_t I_t \alpha \beta (\alpha^2 + \beta^2)} \quad (18)$$

It can be known from the literature (S Selvadurai, 1984) that the additional load caused by dewatering is regarded as many segments of tiny concentrated load by adopting the micro-element method and then superimposed according to Eq. 13. The additional deformation of the tunnel under the action of dewatering can be calculated by employing integration. According to Eq. 15, the right-hand side of the Equation is regarded as  $Q(x)$ , and the concentrated load  $P(\xi)$  at any point  $\xi$  on the tunnel is

$$P(\xi) = Q(\xi) d\xi = \left[ \frac{\kappa G A}{\kappa G A + g_s D} q(\xi) - \frac{E_p I_p}{\kappa G A + g_s D} \frac{d^2 q(x)}{dx^2} \right]_{x=\xi} d\xi \quad (19)$$

Substituting the distributed load  $Q(x)$  into Eq. 18, the vertical displacement  $dw(x)$  of the tunnel is:

$$dw(x) = \frac{Q(\xi) D e^{-\alpha|x-\xi|}}{4 E_p I_p \alpha \beta (\alpha^2 + \beta^2)} [\beta \cos(\beta|x-\xi|) + \alpha \sin(\beta|x-\xi|)] d\xi \quad (20)$$

In the influence range of pre-dewatering, the vertical displacement of the tunnel caused by dewatering can be obtained by integrating Eq. 20:

$$w(x) = \int_{-\sqrt{R^2-d^2}}^{\sqrt{R^2-d^2}} dw(x) \quad (21)$$

### 4 Verification

Under the impact of pre-dewatering in the excavation, the tunnel deformation of the existing subway line one of Xifeng Road of Chegongmiao Junction of Shenzhen Metro in reference (Zhang et al., 2017) is used to verify the proposed method. The initial water level of the project is  $h_0 = 1$  m, the longitudinal length of the excavation  $L = 30$  m, transverse width  $B = 20$  m, and excavation depth is 8 m. The tunnel is vertically below the excavation and parallel to the excavation longitudinally, with a buried depth  $h_2 = 14$  m, diameter  $D = 6$  m, and tunnel wall thickness is 0.3 m. The relative position of the tunnel and the excavation is shown in Figure 6. C50 concrete is generally used for the segment since its elastic modulus  $E_t = 34.5$  GPa, Poisson's ratio  $\nu_t = 0.3$ , and the tunnel is in the gravel clay soil layer, the elastic modulus of soil is  $E_s = 60$  MPa, Poisson's ratio  $\nu = 0.3$ , unit weight of soil  $\gamma = 19.9$  kN/m<sup>3</sup>, and saturated unit weight of soil  $\gamma_s = 20.4$  kN/m<sup>3</sup>. Other relevant parameters can be referred to literature (Zhang et al., 2017).

After pre-dewatering, the water level is dropped by  $s_w = 8$  m to be  $h = 9$  m, and the tunnel becomes to be under the water level. In addition, only the water falling within the scope of the excavation is considered in the literature (Zhang et al., 2017), but the dewatering radius is not considered. According to Eq. 4, the additional stress received by the tunnel in the pit range is 75.7 kPa.

Figure 7 compares the calculation results of the proposed method, the Winkler-Euler-Bernoulli model, and the results of reference (Zhang et al., 2017). The origin of the abscissa is located at the midpoint of the tunnel in the pit, so the tunnel subjected to additional load caused by dewatering is in the range  $-15 \leq x \leq 15$ .

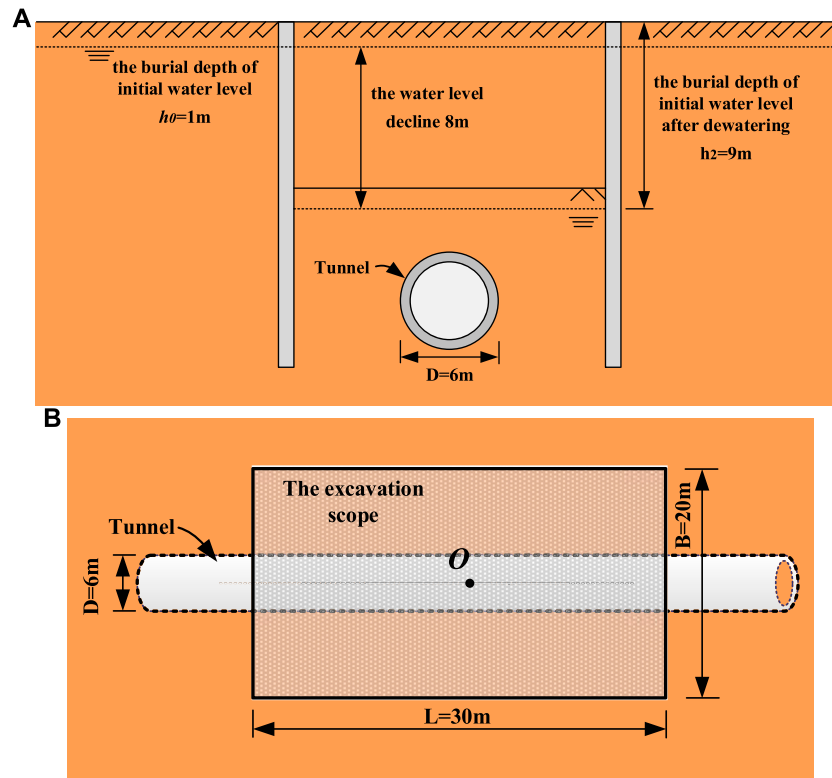


**FIGURE 6**  
Engineering schematics: (A) sectional view; (B) plan view.

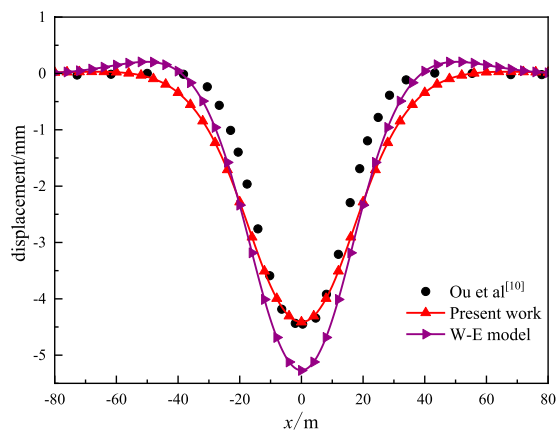


**FIGURE 7**  
Comparison with existing literature.

It can be seen from Figure 7 that the maximum longitudinal deformation of the tunnel in the results of Reference 10 is  $-4.386$  mm, and the maximum longitudinal deformation calculated by the method in this paper and the Winkler-Euler-Bernoulli model is  $-4.406$  and  $-5.262$  mm, respectively. In contrast, the calculated results in this paper are closer to those in reference 10. Because the Winkler-Euler-Bernoulli model cannot consider tunnel and foundation soil shear deformation, the Winkler calculation results

are too large. Therefore, it is proved that the calculation method of tunnel displacement considering shear deformation under the action of dewatering is correct.

## 5 Parameter analysis

The following calculation examples are designed for analyzing the influence of various factors on the displacement of the tunnel caused by dewatering, including initial water level  $H_0=40$  m, initial water depth  $h_0=1$  m, the radius of the dewatering well is  $R_0=0.2$  m, the water level in the well  $H_t=30$  m after dewatering, and dropping of water level  $s_w=10$  m after pre-dewatering. Soil permeability  $k_t=4.32$  m/d, soil elastic modulus  $E_s=30$  MPa, Poisson's ratio  $\nu=0.3$ , unit weight of soil  $\gamma=19$  kN/m<sup>3</sup>, saturated unit weight of soil  $\gamma_s=20$  kN/m<sup>3</sup>. The nearest distance between tunnel and dewatering well is  $D=10$  m, buried depth  $z=10$  m,  $h_2=9$  m, diameter  $D=6$  m, the tunnel wall thickness is  $0.3$  m, elastic modulus  $E_t=34.5$  GPa, Poisson's ratio  $\nu_t=0.3$ , shear modulus  $G_p=13.27$  GPa.

### 5.1 Distance $d$ between tunnel and dewatering well

Five groups of tests are designed to study the influence of the distance  $d$  between the tunnel and the dewatering well on the tunnel deformation while the other parameters remain unchanged, whose distances are 6, 8, 10, 12, and 14 m, respectively. It can be seen from

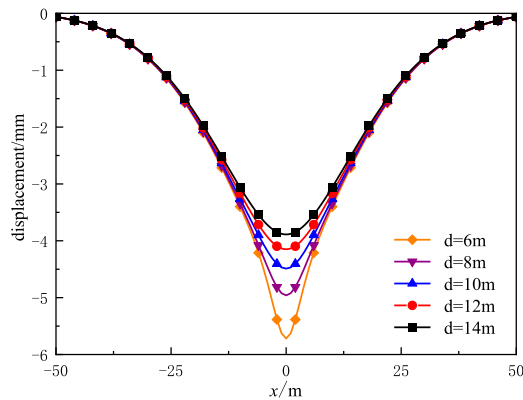


**FIGURE 8**  
Curves of tunnel displacement under different spacing  $d$ .

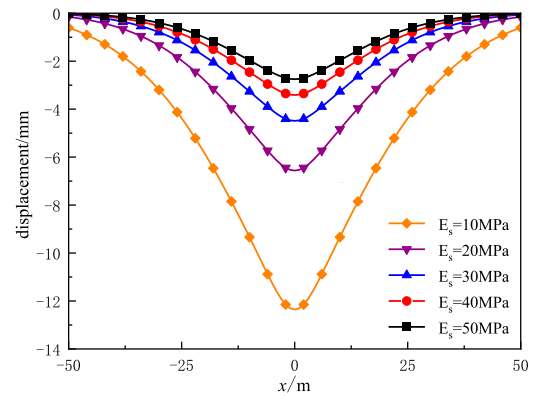


**FIGURE 10**  
Curves of tunnel displacement under different Elastic modulus of soil  $E_s$ .

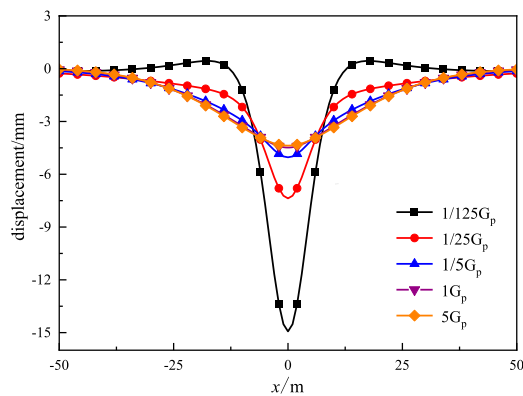


**FIGURE 9**  
Curves of tunnel displacement under different tunnel shear modulus  $G_p$ .

Figure 8 that when the spacing  $d$  increases from 6 to 14 m, the maximum vertical displacement of the tunnel decreases from 5.72 to 3.89 mm. This is because when the distance between the tunnel and the dewatering well gradually increases, the influence of dewatering on the tunnel is weakened. Therefore, the dewatering well should be as far away from the tunnel as possible to avoid excessive tunnel deformation in the project.

## 5.2 Tunnel shear modulus $G_p$

Five groups of tests with different tunnel shear modulus  $G_p$  were taken to study its influence on tunnel deformation while the other parameters remained unchanged, including  $1/125$ ,  $1/25$ ,  $1/5$ , and 5 times the original shear modulus. Figure 9 shows the tunnel displacement curves caused by pre-dewatering under different tunnel shear modulus  $G_p$ . As can be seen from Figure 9, when the tunnel shear modulus  $G_p$  decreases from  $5 G_p$  to  $1/125 G_p$ , the maximum vertical displacement of the tunnel rapidly and significantly increases from 4.38 to 14.93 mm. This is because when the shear modulus  $G_p$  decreases, the ability of the tunnel to

resist the influence of dewatering is weakened. Therefore, strengthening the soil around the tunnel can reduce tunnel deformation.

## 5.3 Elastic modulus of soil $E_s$

Five groups of tests with different soil elastic modulus  $E_s$  were designed to study its influence on tunnel deformation while other parameters remained unchanged, which were 10, 20, 30, 40, and 50 MPa. It can be seen from Figure 10 that the maximum vertical displacement of the tunnel rapidly decreases from 12.36 to 2.75 mm as the soil elastic modulus  $E_s$  increases from 10 to 50 MPa. That is, because when the elastic modulus of soil  $E_s$  increases, the foundation is less likely to deform. On the other hand, when the tunnel bends, the foundation can provide a more significant reaction force to prevent tunnel deformation. Therefore, strengthening the soil around the tunnel can reduce tunnel deformation.

### 5.3.1 Permeability coefficient $k_t$

Five groups of tests with different permeability coefficient  $k_t$  were taken to study its influence on tunnel deformation, which were  $4.32 \times 10^{-3}$ ,  $4.32 \times 10^{-2}$ , 0.432, 4.32, and 43.2 m/d. Figure 11 shows the tunnel displacement curves caused by pre-dewatering under different permeability coefficients  $k_t$ . It can be seen from Figure 11 that the maximum vertical displacement of the tunnel increases from 3.64 to 5.00 mm as the permeability  $k_t$  increases from  $4.32 \times 10^{-3}$  to 43.2 m/d. That is, because when the soil permeability  $k_t$  rises, the influence of dewatering on the surrounding stratum water level increases. Therefore, a water stop curtain can be constructed between the dewatering well and the tunnel to reduce the influence of dewatering on the tunnel.

## 5.4 Water level drawdown $s_w$

Five groups of tests with different  $H_t$  were designed to study its influence on tunnel deformation while other parameters remained unchanged, which were 30, 25, 20, 15, and 10 m, and the corresponding  $s_w$  was 10, 15, 20, 25, and 30 m respectively. Figure 12 shows the water level curve in the strata near the



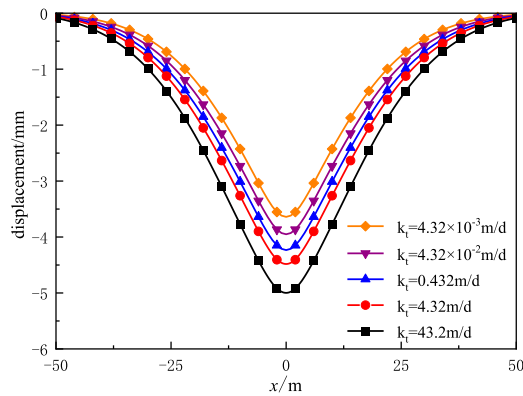


**FIGURE 11**  
Curves of tunnel displacement under different permeability coefficients of soil  $k_t$ .

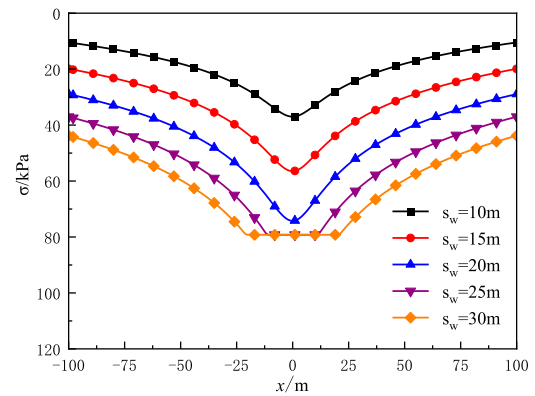


**FIGURE 13**  
Curves of effective stress under different water level drawdown  $s_w$ .

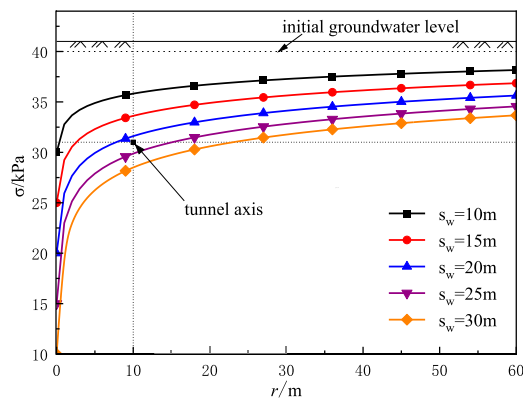


**FIGURE 12**  
Curves of water level under different water level drawdown  $s_w$ .

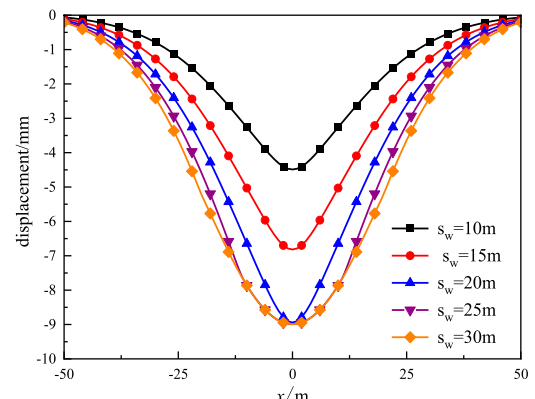


**FIGURE 14**  
Curves of tunnel displacement under different water level drawdown  $s_w$ .

dewatering well under different water level dropping depths  $s_w$ . It can be seen that with the increase of the dropping depth of water level  $s_w$  in the well, the water level in the surrounding stratum also decreases, and the decreasing range gradually decreases. When the dewatering  $s_w$  reaches 20 m, the groundwater level is still above the buried depth of the tunnel axis. The additional stress on the tunnel can be calculated by Eq. 4. However, when  $s_w$  of water level drawdown reaches 25 m, the part, that is, the closest to the dewatering well on the tunnel is already below the water level; In this case, the additional stress on this part is calculated by Eq. 5. Figure 13 shows the additional stress sustained by the tunnel under different water level drop depth  $s_w$ . It can be seen that the additional stress on the tunnel increases with the increase of  $s_w$  of the water level. This is because the more the water level drops, the less water buoyancy the soil above the tunnel receives. As shown in Figure 13, when  $s_w$  reaches 25 and 30 m, the maximum value of the additional stress on the tunnel will not increase, and the range of the whole deal of the additional stress will expand. This is because part of the tunnel is already above the water level as  $s_w=25$  m. At the same time, as the  $s_w$  continues to increase, more of the tunnel is located above the water level. However, the additional stress on the tunnel will not increase when the water level is below the tunnel.

Therefore, the curves of  $s_w=25$  and  $s_w=30$  show inconsistent change trends compared with several other curves.

Figure 14 shows the tunnel displacement curve caused by pre-dewatering under different water level drop depth  $s_w$ . It can be seen from Figure 14 that the maximum vertical displacement of the tunnel increases from 4.49 to  $-8.99$  mm when the water level drawdown  $s_w$  increases from 10 to 30 m, but the increased amplitude gradually weakens. That is, because when the water level drops depth  $s_w$  gradually increases, the influence of dewatering on the surrounding water level also increases, which leads to the increase of the effect of dewatering on the tunnel. Furthermore, the drop in water level causes the increase of additional loads on the tunnel. Therefore, with the increase of  $s_w$ , the tunnel displacement due to dewatering increases overall.

## 6 Conclusion

Based on the proposed two-stage method, a theoretical calculation method for the vertical displacement of adjacent existing tunnels under the impact of pre-dewatering of excavation is proposed in this paper. In the first

stage, the additional load induced by dewatering the tunnel was calculated. In the second stage, considering the shear effect, the Timoshenko beam model was used to simulate the deformation mode of the tunnel to derive the calculation of the tunnel displacement. After an in-depth Analysis, the following conclusions were drawn: DING et al., 2021.

- 1) With the increase in the distance between the tunnel and the dewatering well, the vertical displacement of the tunnel is reduced. The dewatering well should be as far away from the tunnel as possible to avoid excessive tunnel deformation in the project.
- 2) The decrease of the tunnel shear modulus  $G_p$  can lead to the rapid increase of the vertical displacement of the tunnel, so the influence of its shear stiffness should be considered when analyzing its deformation. Meanwhile, ensuring the shear stiffness of tunnels can effectively improve the ability of tunnels to resist external loads.
- 3) The growth of the elastic modulus of soil provides a more significant reaction force to prevent tunnel deformation. Therefore, strengthening the soil around the tunnel can reduce tunnel deformation.
- 4) When the soil permeability increases, the influence of dewatering on adjacent tunnels also increases. Therefore, a water stop curtain can be constructed between the dewatering well and the tunnel to reduce the influence of dewatering on the tunnel.
- 5) The increase of  $s_w$  will lead to the overall decrease in water level in the surrounding strata. According to the relative position of the tunnel and the water table, there are two forms of additional load on the tunnel. Before the water level drops to the tunnel axis, the additional load on the tunnel increases with the water level drop depth  $s_w$ , and the tunnel displacement also increases. When the water level drops below the tunnel axis, the additional load on the part above the water level is the same and does not increase with the increase of  $s_w$ . Therefore, excessive dewatering should be avoided to reduce the influence of dewatering on adjacent tunnels in foundation pit dewatering engineering.

## Data availability statement

The data used to support the findings of this study are available from the corresponding author upon request.

## References

- Attewell B, P., Yeates, J., and Selby, A. R. (1986). *Soil movements induced by tunnelling and their effects on pipelines and structures*. London, United Kingdom; London: Blackie and Son Ltd, 128–132.
- Ding, Z., Zhang, X., and Liang, F. Y., (2021). Research and prospects regarding the effect of foundation pit excavation on an adjacent existing tunnel in soft soil. *China Journal of Highway and Transport*. 34 (3), 21. in Chinese. doi:10.19721/j.cnki.1001-7372.2021.03.002
- Guan, L. X., Xu, C. J., Ke, W. H., Ma, X. H., Xu, L. M., and Yu, W. W. (2021). Simplified method for calculating the vertical displacement of existing pipelines caused by tunnel undercrossing. *Journal of Civil and Environmental Engineering*. 43 (05), 66–72. in Chinese. doi:10.11835/j.issn.20966717.2020.158
- Huang, K., Ma, Q., and Zhan, Y. Y. (2018). The influence of deep foundation excavation pit and dewatering on adjacent metro tunnel. *Highway engineering*. 43 (2). in Chinese.
- Jia, Y. Y., Lu, J. J., Wei, L. L., and Cui, G. Y. (2010). Research on the influence of the tunnel dewatering construction on existed municipal pipeline tunnel. *Hydrogeology Engineering Geology*. 37 (6). in Chinese. doi:10.16030/j.cnki.issn.1000-3665.2010.06.025
- Li, P., Du, S. J., Shen, S. L., Wang, Y. H., and Zhao, H. H. (2015). Timoshenko beam solution for the response of existing tunnels because of tunneling underneath. *International Journal for Numerical and Analytical Methods Geomechanics*. 40 (5), 766–784. doi:10.1002/nag.2426
- Li, W. G. (2008). *Influence of dewatering of adjacent excavation on longitudinal deformation of metro tunnel in operation*, 73. Shanghai, China: Tongji university. in Chinese.
- Liang, R., Wu, W., Yu, F., Jiang, G., and Liu, J. (2018). Simplified method for evaluating shield tunnel deformation due to adjacent excavation. *Tunnelling and Underground Space Technology*. 71 (1), 94–105. doi:10.1016/j.tust.2017.08.010
- Liang, R., Xia, T., Hong, Y., and Yu, F. (2016). Effects of above-crossing tunnelling on the existing shield tunnels. *Tunnelling and Underground Space Technology*. 58 (9), 159–176. doi:10.1016/j.tust.2016.05.002
- Liang, R., Kang, C., Xiang, L., Li, Z., Lin, C., Gao, K., et al. (2021). Responses of in-service shield tunnel to overcrossing tunnelling in soft ground. *Environmental Earth Sciences*. 80, 183. doi:10.1007/s12665-021-09374-3
- Liang, R., Xia, T., Huang, M., and Lin, C. (2017). Simplified analytical method for evaluating the effects of adjacent excavation on shield tunnel considering the shearing effect. *Computers and Geotechnics*. 81 (1), 167–187. doi:10.1016/j.compgeo.2016.08.017
- Liu, Y. S. (2013). Impact of the deep excavation dewatering on the settlement of a subway tunnel. *Soil Engineering and Foundation* 27. (1), 4. in Chinese.
- S Salvadurai, A. P. (1984). *Elastic analysis of soil-foundation interaction*. Beijing, China: China Railway Publishing House, 42–57. in Chinese.

## Author contributions

SY: Conceptualization, Data curation, Formal analysis, Funding acquisition, Investigation, Methodology, Writing—original draft, Writing—review and editing. RY: Funding acquisition, Data curation, Investigation, Methodology, Writing—review and editing. YJ: Conceptualization, Data curation, Investigation, Methodology, Validation, Writing—review and editing. ZL: Conceptualization, Investigation, Methodology, Writing—review and editing. DH: Data curation, Formal analysis, Investigation, Methodology, Validation, Writing—review and editing. TL: Conceptualization, Investigation, Methodology, Writing—review and editing.

## Funding

This work was supported by National Natural Science Fund (52168049), the Key Program of the National Natural Science Foundation of China (52238009), Natural Science Fund of Department of transportation of Jiangxi Province (2021C0006, 2021Z0002, 2022Z0001, and 2022Z0002).

## Conflict of interest

Author SY, RY, YJ, and ZL were employed by the company Jiangxi Transportation Institute Co., LTD.

The remaining authors declare that the research was conducted in the absence of any commercial or financial relationships that could be construed as a potential conflict of interest.

## Publisher's note

All claims expressed in this article are solely those of the authors and do not necessarily represent those of their affiliated organizations, or those of the publisher, the editors and the reviewers. Any product that may be evaluated in this article, or claim that may be made by its manufacturer, is not guaranteed or endorsed by the publisher.

- Shen, S. L., Wu, H. N., Cui, Y. J., and Yin, Z. Y. (2014). Long-term settlement behaviour of metro tunnels in the soft deposits of Shanghai. *Tunnelling and Underground Space Technology*. 40 (2), 309–323. doi:10.1016/j.tust.2013.10.013
- Tanahashi, H. (2004). Formulas for an infinitely long Bernoulli-Euler beam on the Pasternak model. *Japanese Geotechnical Society*. 44 (5), 109–118. doi:10.3208/sandf.44.5\_109
- Verruijt, A. (1982). *Theory of groundwater flow*, 174. London, United Kingdom; Macmillan Education UK.
- Wang, J. X., Feng, B., Yu, H. P., Guo, T. P., Yang, G. Y., and Tang, J. W. (2013). Numerical study of dewatering in a large deep foundation pit. *Environmental Earth Sciences*. 69 (3), 863–872. doi:10.1007/s12665-012-1972-9
- Wu, H. N., Shen, S. L., Liao, S. M., and Yin, Z. Y. (2015). Longitudinal structural modelling of shield tunnels considering shearing dislocation between segmental rings. *Tunnelling and Underground Space Technology*. 50 (8), 317–323. doi:10.1016/j.tust.2015.08.001
- Xu, C. J., Zeng, Y. T., Tian, W., and Chen, M. (2021). Analytical Analysis of the influence on adjacent pipelines induced by dewatering based on Pasternak model. *Journal of Shanghai Jiaotong University*. 55 (6), 11. in Chinese. doi:10.16183/j.cnki.jsjtu.2020.007
- Xu, L. (2005). *Research of the longitudinal settlement of soft soil shield tunnel*, 69. Shanghai, China: College of Civil Engineering of Tongji University. in Chinese.
- Zeng, C. F., Zheng, G., Zhou, X. F., Xue, X. L., and Zhou, H. Z. (2019). Behaviours of wall and soil during pre-excavation dewatering under different foundation pit widths. *Computers and Geotechnics*. 115, 103169. doi:10.1016/j.compgeo.2019.103169
- Zhang, D. M., Huang, Z. K., Li, Z. L., Zong, X., and Zhang, D. M. (2019). Analytical solution for the response of an existing tunnel to a new tunnel excavation underneath. *Computers and Geotechnics*. 108 (4), 197–211. doi:10.1016/j.compgeo.2018.12.026
- Zhang, H., and Zhang, Z. X. (2013). Vertical deflection of existing pipeline due to shield tunnelling. *Journal of Tongji University*. 8 (7). in Chinese.
- Zhang, M., and Pan, B. Y. (2013). Influence on subway tunnel adjacent to excavation by dewatering. *Science, Engineering and Technology*. 21 (7). in Chinese.
- Zhang, X., Ou, X., Yang, J., and Fu, J. (2017). Deformation response of an existing tunnel to upper excavation of foundation pit and associated dewatering. *International Journal of Geomechanics*. 17 (4), 04016112. doi:10.1061/(asce)gm.1943-5622.0000814



## OPEN ACCESS

EDITED BY  
Zhibo Zhang,  
University of Science and Technology  
Beijing, China

REVIEWED BY  
Kang Peng,  
Chongqing University, China  
Jing Bi,  
Guizhou University, China

\*CORRESPONDENCE  
Jinrong Cao,  
✉ jin-rongcao@cumt.edu.cn  
Linming Dou,  
✉ lmdou@126.com

SPECIALTY SECTION  
This article was submitted to  
Environmental Informatics and Remote  
Sensing, a section of the journal  
Frontiers in Earth Science

RECEIVED 30 November 2022  
ACCEPTED 28 December 2022  
PUBLISHED 10 January 2023

CITATION  
Cao J, Dou L, Zhou K, Kan J, Li J and Chai Y  
(2023), Effect of pre-confining pressure on  
unloading-induced coalburst: Insights  
from distinct element modelling.  
*Front. Earth Sci.* 10:1112249.  
doi: 10.3389/feart.2022.1112249

COPYRIGHT  
© 2023 Cao, Dou, Zhou, Kan, Li and Chai.  
This is an open-access article distributed  
under the terms of the [Creative Commons  
Attribution License \(CC BY\)](#). The use,  
distribution or reproduction in other  
forums is permitted, provided the original  
author(s) and the copyright owner(s) are  
credited and that the original publication in  
this journal is cited, in accordance with  
accepted academic practice. No use,  
distribution or reproduction is permitted  
which does not comply with these terms.

# Effect of pre-confining pressure on unloading-induced coalburst: Insights from distinct element modelling

Jinrong Cao<sup>1,2\*</sup>, Linming Dou<sup>1,3\*</sup>, Kunyou Zhou<sup>4</sup>, Jiliang Kan<sup>1</sup>,  
Jiazhao Li<sup>4</sup> and Yanjiang Chai<sup>1</sup>

<sup>1</sup>School of Mines, China University of Mining and Technology, Xuzhou, Jiangsu, China, <sup>2</sup>Geotechnical Institute, TU Bergakademie Freiberg, Freiberg, Germany, <sup>3</sup>Jiangsu Engineering Laboratory of Mine Earthquake Monitoring and Prevention, Xuzhou, Jiangsu, China, <sup>4</sup>School of Mining Engineering, Anhui University of Science and Technology, Huainan, Anhui, China

Coalburst is a violent dynamic failure of coal during underground mining. It is of significance to study failure pattern as well as energy evolution and transition during coalbursts and how they are influenced by pre-confinement. This paper presents unloading-induced coalburst simulations using the distinct element method via a combined static–dynamic loading–unloading strategy. The numerical model is calibrated and validated by comparison with the failure process observed in laboratory tests. The influence of pre-confining pressure on unloading-induced coalburst was numerically investigated from the perspective of crack propagation, fracturing process, failure pattern, and energy evolution. In addition, failure mechanism and energy conversion during coalbursts under different pre-confining pressures are discussed. The results show that the stress change caused by sudden unloading of the pre-confining results in the initiation and development of cracks. Crack density and crack propagation velocity increase with increasing pre-confining pressure. As the pre-confining pressure increases, the coalburst becomes more intense and takes less time to be completed, and the main failure pattern in coalburst transforms from a tensile type to a shear type. In addition, the conversion ratio of kinetic energy and frictional energy during coalbursts increase non-linearly with increasing pre-confining pressure.

## KEYWORDS

coalburst, pre-confining pressure, crack development, energy transition, distinct element method

## 1 Introduction

Coalburst is a dynamic failure phenomenon, characterized by an instantaneous release of a large amount of energy and ejection of coal pieces (Dou and He, 2001; Jiang et al., 2017; Zhang et al., 2017). According to its occurrence mechanism, coal burst can be classified into unloading-induced and remote mining induced seismicity triggered (Vardar et al., 2018; Mottahedi and Ataei, 2019). Unloading-induced coalbursts, which frequently occur in high stressed mining areas without remote seismic events during roadway development, also cause many casualties and severe damages (Dou and He, 2001). It is important to investigate failure mechanism as well as evolution and transition of energy during unloading-induced coalbursts.

Dynamic cracking behaviour is quite different from those under static loading conditions (Bažant et al., 1993; Zhao et al., 1999; Li et al., 2004; Zhang et al., 2021). To reproduce rock or coal bursts in the laboratory, He et al. (2010) developed a true triaxial test machine with the capacity to

rapidly unload stress at one loading face and to observe the rock burst process of limestone in the laboratory. He studied the crack fractal dimensions during rockbursts using this testing device, and results showed that the values of fractal dimension become larger after dynamic failure (He et al., 2014). Su et al. (2017) investigated the evolution of acoustic emissions (AE) using a rockburst testing machine and found that the main frequency of the AE decreased before rockburst. However, it is difficult to conduct coalburst tests using true triaxial unloading test machines. The Split Hopkinson Pressure Bar (SHPB) system was employed to study the dynamic response of coal samples, including dynamic mechanical characteristics (Kong et al., 2020; Li et al., 2022), crack propagation (Hao et al., 2020; Ju et al., 2020; Li et al., 2021), as well as the influence of bedding structure (Zhao et al., 2014; Ai et al., 2020). The above results have enriched our understanding of rock or coal bursts. However, the knowledge of the cracking mechanisms of dynamic failures at the micro-scale still needs to be further studied.

Numerical simulation can provide insights into the complicated process of rock and coal failures at the micro-scale. In past decades, many numerical methods have been applied to study crack development, including the finite element method (FEM) (Zubelewicz and Mroz, 1983; Wang and Park, 2001; Manouchehrian and Cai, 2016; Hauquin et al., 2018), discontinuous deformation analysis (DDA) method (He et al., 2016; Hatzor et al., 2017; Chen et al., 2018), and the distinct element method (DEM) (Cundall and Strack, 1979; Potyondy and Cundall, 2004; Hu et al., 2020). In particular, the DEM has become a promising method for investigating the dynamic fracturing process of rocks (Zhang and Wong, 2018). Hu et al. (2018) applied a 3D bonded block DEM model to simulate dynamic disturbance triggered rockbursts and investigated the crack evolution during rockbursts. Compared to 3D DEM simulations, 2D DEM simulations have great advantages in computational efficiency. Unstable shear and compressive failure of rock related to rockbursts were reproduced by using the 2D DEM model based on the universal Distinct Element Code (UDEC) (Gu and Ozbay, 2015). He et al. (2018) performed abruptly unloading induced strainburst simulations through the Particle Flow Code (PFC), and found that the system stiffness has a significant effect on dynamic failure. Duan et al. (2019) employed a 2D DEM model to simulate unloading-induced strainbursts, and showed that a sudden reduction in confining pressure caused non-uniform deformation in the sample. A UDEC-Trigon numerical model was employed to capture unloading-induced strainbursts including analysis of crack patterns (Gao et al., 2019a). The development of rock dynamic failure is related to the release and transition of elastic energy (Cook, 1965; Tarasov and Stacey, 2017; Gao and Yang, 2021). Therefore, particular attention should also be paid to study the energy release and transition during coalbursts.

In this study, we focus on analysis of unloading-induced coalbursts. 2D DEM simulations of unloading-induced coalbursts under different pre-confining pressures are performed. This paper is organized as follows. First, modelling method and procedure are introduced. Then, model calibration and validation are documented by comparison with typical experimental results. Subsequently, micro-cracking mechanisms and energy evolution during unloading-induced coalbursts are investigated considering different aspects, including crack propagation, failure mode and energy evolution. Finally, the influence of the pre-confining pressure on failure mechanism and energy conversion during coalbursts is discussed.

## 2 Model description and calibration

### 2.1 Modelling method

UDEC, a 2D numerical program based on the DEM, has been widely applied to investigate rock mechanical and mining engineering problems (e.g. Kazerani et al., 2011; Huang et al., 2019; Cao et al., 2020). The UDEC-Trigon model proposed by Gao and Stead (2014) has an excellent ability to capture the brittle cracking of hard rock, and has also been applied to study rockbursts or coalbursts (Gao et al., 2019a; b; Gao and Yang, 2021). Thus, for this study, a UDEC-Trigon model and a static–dynamic coupled loading strategy are adopted to simulate unloading-induced coalbursts.

#### 2.1.1 Failure criterion

In the UDEC-Trigon method, a coal sample is composed of many blocks of different size and contacts between blocks. Each block is deformable based on a finite-difference mesh. There are two possible failure patterns of a contact: shear cracking along the shear direction and tensile cracking along the normal direction (ICG, 2014). Failures of contacts are controlled by the stresses acting at the contacts and the Coulomb friction law with tension cut-off.

#### 2.1.2 Calculation of energy components

Energy analysis is an important aspect in studying dynamic failure. The UDEC-internal program language FISH was used to acquire the distribution of the three energy types: elastic energy, kinetic energy and frictional energy. The formulas (ICG, 2014) are shown below.

The total elastic energy stored in the coal sample  $W_C$  is calculated as:

$$W_C = \sum E_b \quad (1)$$

where  $\sum E_b$  is the total amount of elastic energy stored in all of the individual blocks in the numerical coal sample. The elastic energy of a block  $E_b$  is calculated as:

$$E_b = \sum E_z \quad (2)$$

where  $\sum E_z$  is the sum of elastic energy stored in all individual zones in a block. For a given zone, the elastic energy  $E_z$  is determined by:

$$E_z = \frac{A}{2E} [\sigma_1^2 + \sigma_2^2 + \sigma_3^2 - 2\nu(\sigma_1\sigma_2 + \sigma_1\sigma_3 + \sigma_2\sigma_3)] \quad (3)$$

where  $E$  is Young's modulus.  $\nu$  is Poisson's ratio.  $A$  is the area of the zone and  $\sigma_1$ ,  $\sigma_2$ , and  $\sigma_3$  are the three principal stresses.

The total amount of kinetic energy  $W_K$  is calculated as:

$$W_K = \sum E_{gk} \quad (4)$$

where  $\sum E_{gk}$  is the total amount of the kinetic energy of all individual gridpoints in the numerical coal sample at a given timestep. For a given gridpoint  $g$ , the kinetic energy can be calculated as:

$$E_{gk} = \frac{1}{2}m_g u_x^2 + \frac{1}{2}m_g u_y^2 \quad (5)$$

where  $m_g$  is the mass of the gridpoint and  $u_x$  and  $u_y$  are the corresponding velocities in the  $x$ - and  $y$ -direction at a given timestep, respectively.

The total frictional energy  $W_F$  of the coal sample is calculated as:



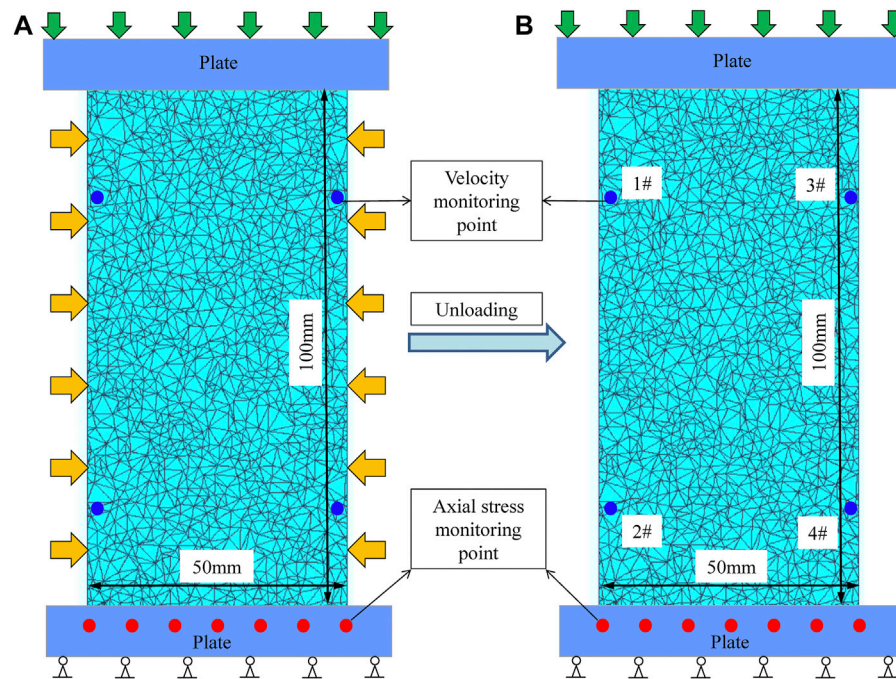


FIGURE 1

UDEC-Trigon model of coal sample incl. Location of monitoring points: (A) before unloading, (B) after unloading.

$$W_F = \sum E_{cf} \quad (6)$$

where  $\sum E_{cf}$  is the sum of frictional energy of all contacts in the numerical coal sample at a given timestep. For a given contact, the frictional energy  $E_{cf}$  at that timestep is calculated as:

$$E_{cf} = \frac{1}{2} (f_s + f'_s) \Delta u_s \quad (7)$$

where  $\Delta u_s$  is the increment in the shear displacement of the contact and  $f_s$  and  $f'_s$  are the current and previous shear forces (considering the current time step) at the contact, respectively.

## 2.2 Model configuration and modelling procedure

The numerical model considers a rectangular sample with width of 50 mm and height of 100 mm, as shown in the Figure 1. The triangular blocks have an average edge length of 2 mm. This meshing is sufficiently fine to study both the static and dynamic cracking behaviour of rocks at that scale (Gao and Stead, 2014; Gao and Yang, 2021). The block size in the model varies in a range considering the heterogeneity of the coal. However, the non-uniformity coefficients of block size are identical in all models. Several monitoring points are placed at the bottom plate and the coal sample to monitor stresses and velocities, respectively.

The modelling procedure comprises four steps. First, top and bottom plate are fixed. After that, pre-confining pressure is applied on the two lateral sides, as shown in Figure 1A. Then, the coal samples are loaded to the peak strength under the corresponding confining

pressure. The loading velocity of the top plate is set to .01 m/s, while the bottom plate is fixed. The time step of a cycle is 10–8 s in the static mode. Therefore, a loading velocity of .01 m/s implies that the model uses 10,000,000 calculation steps for 1 mm of plate movement, which is sufficient for static analysis (Gao and Yang, 2021). Finally, the dynamic calculation mode is activated. Top and bottom boundaries of the model obtain absorbing boundary conditions, and the two lateral sides of the model obtain reflecting boundary conditions. The confining pressures are unloaded abruptly (see Figure 1B). The bottom plate remains fixed. Meanwhile, the dynamic mode is adopted. Rayleigh damping of .5% is used in the dynamic analyses, similar to the method adopted by Gao et al. (2019a) and Zhu et al. (2020).

The axial stress is the average stress of all monitoring points inside the loading plate in vertical direction. Mechanical parameters of the coal are calibrated by conducting a series of numerical uniaxial compression (UCS) and Brazilian tension (BT) tests, as seen in Figure 2. This calibration method has been demonstrated to be effective for UDEC-Trigon modelling (Gao and Yang, 2021). The calibrated mechanical parameters adopted in the Trigon model are listed in Table 1. The maximum deviation between target values and numerical simulation results do not exceed 3%, which is acceptable.

## 2.3 Model validation

### 2.3.1 Stress–strain behaviour

Figure 3 displays the stress–strain curves of the numerical coal samples during static loading. The pre-confining pressures are

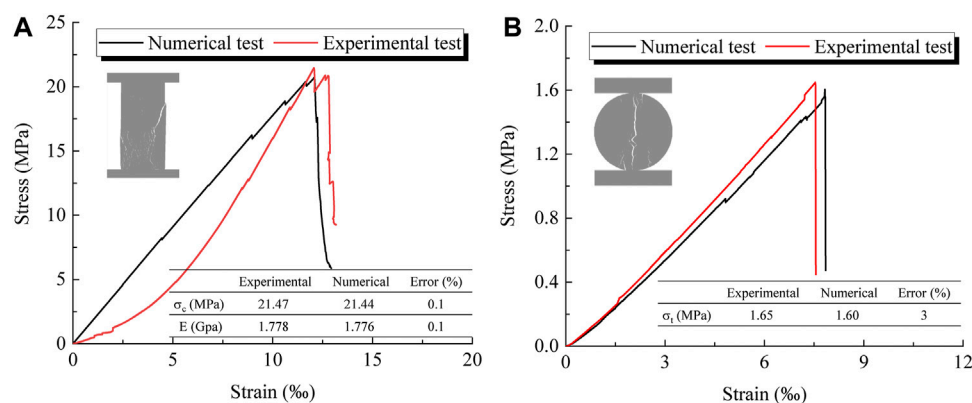


**FIGURE 2**  
Calibration of mechanical parameters in the UDEC-Trigon model: (A) uniaxial compression tests, (B) Brazilian tension tests.

**TABLE 1 Mechanical parameters for UDEC-Trigon numerical model.**

Parameters	Coal	Plate	Coal-plate contact
Density (kg/m <sup>3</sup> )	1,470	5,000	—
Young's modulus E (GPa)	1.72	17	—
Poisson's ratio $\nu$	.24	.25	—
Normal stiffness $K_n$ (GPa/m)	10,137	—	102,000
Shear stiffness $K_s$ (GPa/m)	4,055	—	40,800
Tensile strength $\sigma_t$ (MPa)	1.57/0 <sup>a</sup>	—	0
Cohesion $c$ (MPa)	10/0 <sup>a</sup>	—	0
Friction angle $\phi$ (°)	38/32 <sup>a</sup>	—	32

<sup>a</sup>Peak and residual value.

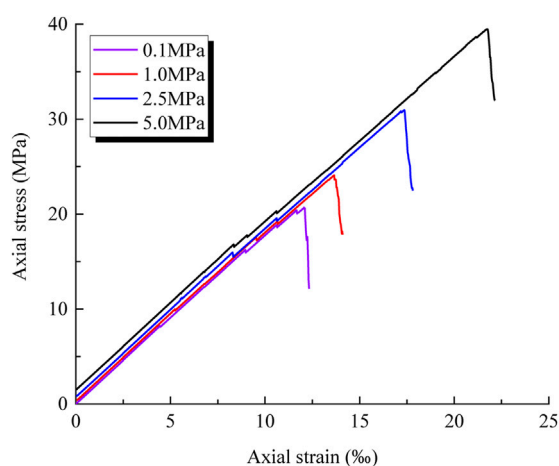


**FIGURE 3**  
Stress-strain curves of numerical samples under different pre-confining pressures.

instantly unloaded after loading to the peak strength. All the other model parameters are identical except for the pre-confining pressure. It can be seen that the starting points of the stress-strain curves are different, which is caused by the loading sequence of the simulation. First, before the confining pressures are applied, upper and lower plates are in contact with the coal sample, the force at the contact surface is 0 MPa, and then a pre-determined pre-confining pressure is applied to the sample. At this time, upper and lower pressure plates are fixed. Under the influence of Poisson's ratio, compression occurs along the vertical direction when the coal sample is compressed in the lateral direction. Therefore, vertical stresses with different magnitude appear after different pre-confining pressures are applied. When pre-confining pressures of .1 MPa, 1.0 MPa, 2.5 MPa, and 5.0 MPa are applied, the peak strength of the coal samples are 20.7 MPa, 24.1 MPa, 31.0 MPa, and 39.5 MPa, respectively, indicating that the pre-confining pressure significantly influences the peak strength. It is widely recognized that peak strength increases with confining pressure (Haimson and Chang, 2000; Liu et al., 2004; Hokka et al., 2016; Yao et al., 2016). Since the pre-confining pressure is immediately unloaded and the calculation mode becomes dynamic, the coal sample does not change from brittle to ductile.

### 2.3.2 Coalburst process

The failure characteristics observed in the simulations are compared with dynamic failure modes of coal samples as observed in experiments (Figure 4). First, after the sudden unloading of pre-confining pressure, the trigger of coalburst is marked by the ejection of localized coal fragments close to the unloading surface. Then, the area of the coal block ejection area continues to expand, and completely penetrating cracks form inside the sample with increasing tangential stress. As a result, coal plates are thrown out. Finally, coal fragments and plates are ejected in large quantities with maximum ejection velocity exceeding 10 m/s. In addition, some coalburst pits are formed on the surface of the coal sample when these ejected blocks are removed. These results show that the method adopted in this study can reproduce the unloading-induced coalbursts properly.

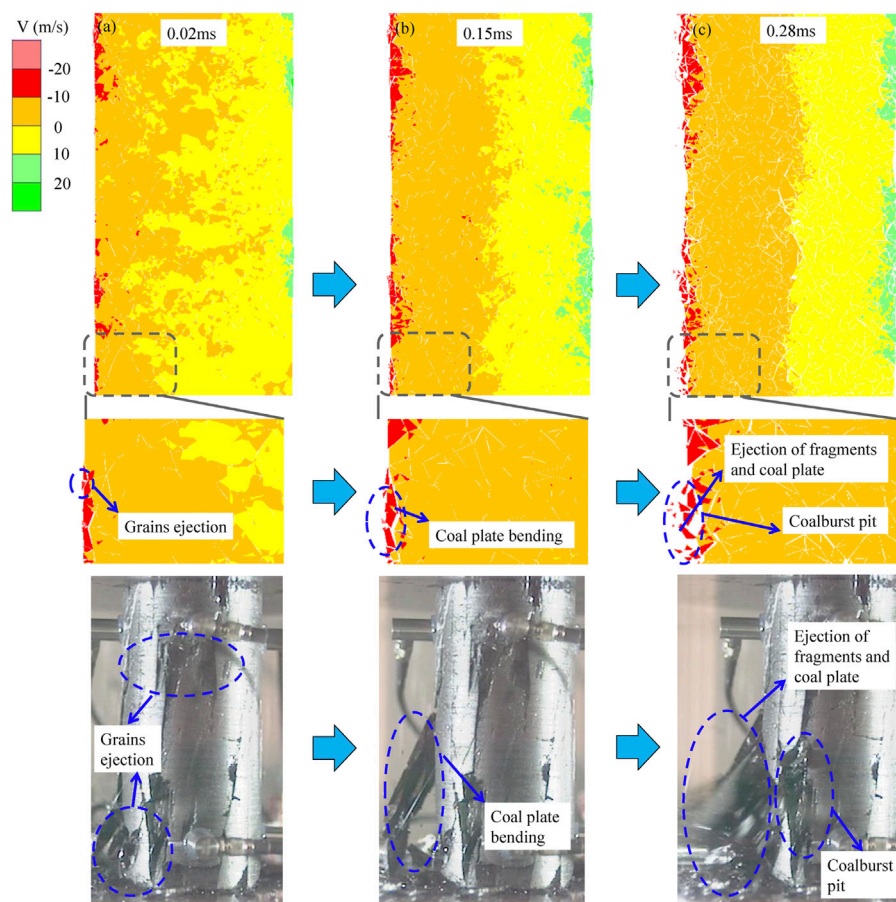


FIGURE 4

Coalburst process: numerical and experimental results: (A) grain ejection in local zones; (B) coal plate bending; (C) coal fragmentation, plate ejection and V-shaped coalburst pit formation.

### 3 Numerical results and analysis

#### 3.1 Fracturing process of coalbursts

Figure 5 shows the crack development process and the eventual velocity cloud during coalburst induced by unloading of different pre-confining pressures. The blue and red lines represent tensile and shear cracks, respectively. Tensile failure is dominant in the area close to the unloading face, while most shear cracks are distributed in the region away from the unloading face, regardless of the value of the pre-confining pressure. The abrupt unloading results in a sudden change of the stress state in the blocks near the unloading surface. The stress change formed at the moment of unloading induces a considerable horizontal deformation near to the surfaces. A great number of mainly tensile cracks form near the unloading surface and ultimately result in the ejection of fragments and coal plates. These observations are in agreement with previous study on rockbursts (Duan et al., 2019). A comparison of Figure 5A and Figure 5D shows that the pre-confining pressure has an important influence on the development of cracks during a coalburst. Cracks initiate

more intensively in coal samples under higher stress, resulting in the formation of a denser fracture network after sudden release of high pre-confining pressure. In addition, different pre-confining pressures result in significant differences in the crack propagation of coalbursts, as demonstrated in Figure 5A. When the pre-confining pressure is low, at first, few shear cracks are initiated in the interior of the coal sample after unloading. Then, the number of tensile fractures near the unloading surface increases rapidly with increasing dynamic calculation time, which results in the ejection of fragments. However, when the coal sample is under a high pre-confining pressure, a large number of cracks with different failure modes (shear and tensile cracks), appear instantaneously in almost the entire area near the unloading surface, as demonstrated in Figure 5D. Fewer shear cracks form and the distribution is more dispersed under a lower pre-confining pressure. However, the number of shear cracks in the coal sample is greater under higher pre-confining pressure. As shown in Figure 5, with increasing pre-confining pressure, the coalburst intensity increases significantly. When the pre-confining pressure is .1 MPa or 1.0 MPa, the coalburst only occurs in a local area of the unloading surface. However, under the condition that the pre-



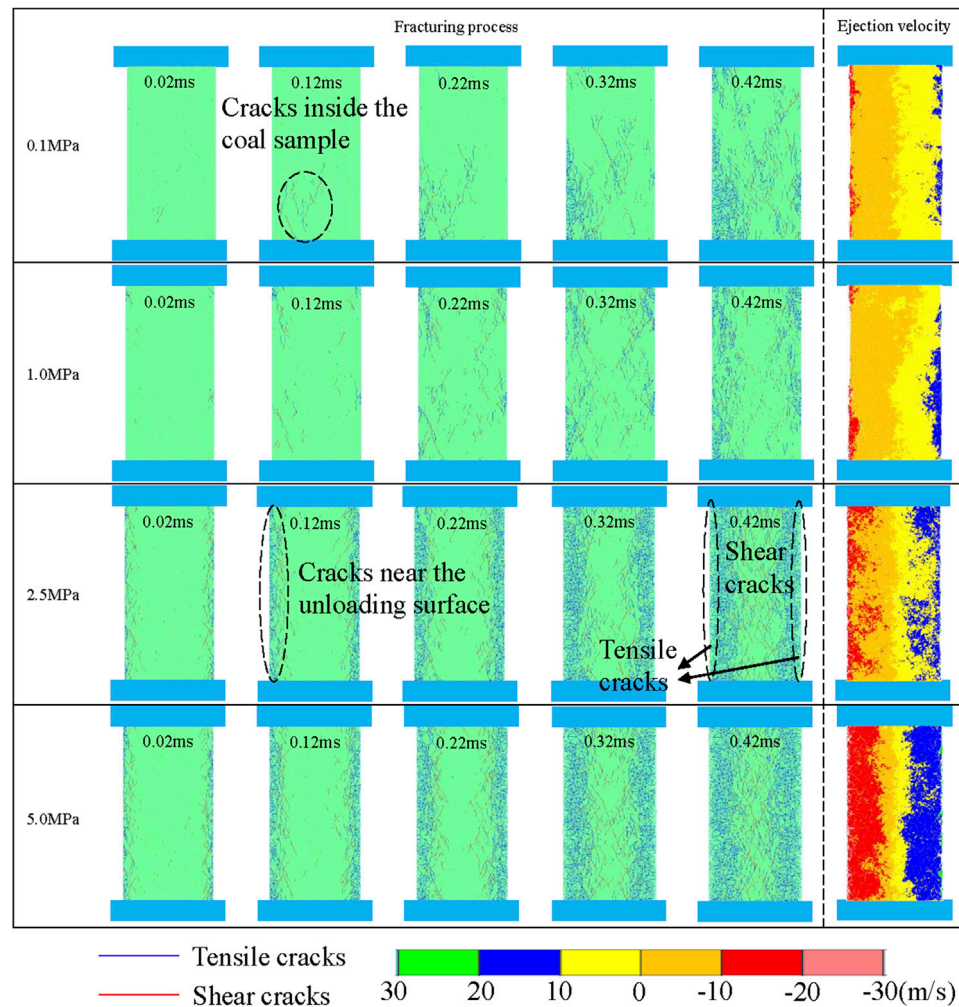


FIGURE 5

Crack development process of coalburst under different pre-confining pressures: (A) .1 MPa; (B) 1 MPa; (C) 2.5 MPa and (D) 5 MPa. Note: blue lines indicate tensile cracks, and red lines indicate shear.

confining pressure is 2.5 MPa or 5.0 MPa, the range of the coalburst covers almost the entire area on both sides of the coal sample, and many coal fragments and plates are ejected from the entire unloading surface. The ejection is more powerful when the pre-confining pressure is higher. The graph indicates that the fracturing process during the coalburst is affected by the pre-confining pressure. A coalburst under a higher pre-confining pressure has a wider fracturing range and a higher ejection velocity.

To further study the ejection of coal fragments during coalbursts, four monitoring points are set-up on both sides of the numerical model to monitor the horizontal velocities of fragments, as shown in Figure 1. The horizontal velocities of the fragments are shown in Figure 6. Positive values indicate movement towards the right and *vice versa*. Numerous studies imply that the velocities of fragments that form during coalbursts are more than 10 m/s (Frith et al., 2020; Yang et al., 2020; Gao et al., 2021). As shown in Figure 6, most of the recorded velocities exceed 10 m/s,

and the magnitude of the velocities increases with increasing pre-confining pressure. The maximum velocities of the coal fragments are 16.76 m/s, 17.76 m/s, 20.60 m/s and 30.00 m/s during coalbursts when the pre-confining pressures are .1 MPa, 1.0 MPa, 2.5 MPa and 5.0 MPa, respectively. The velocity is zero for a period of time after the pre-confining pressure of .1 MPa is released, indicating that a coalburst does not occur immediately after the low pre-confining pressure is released. However, the ejection velocity of the fragments grows rapidly with time when the pre-confining pressure becomes 5.0 MPa, indicating that a violent coalburst occurs at the moment of unloading in this situation. The rise in pre-confining pressure leads to an increase in stress and elastic energy in the coal sample, which is more prone to coalburst. The simulations suggest that a critical stress level or a critical energy level may exist for coalbursts. This result provides direct evidence of the mechanism of rock dynamic failure proposed in previous research (Dou and He, 2001; Su et al., 2017).

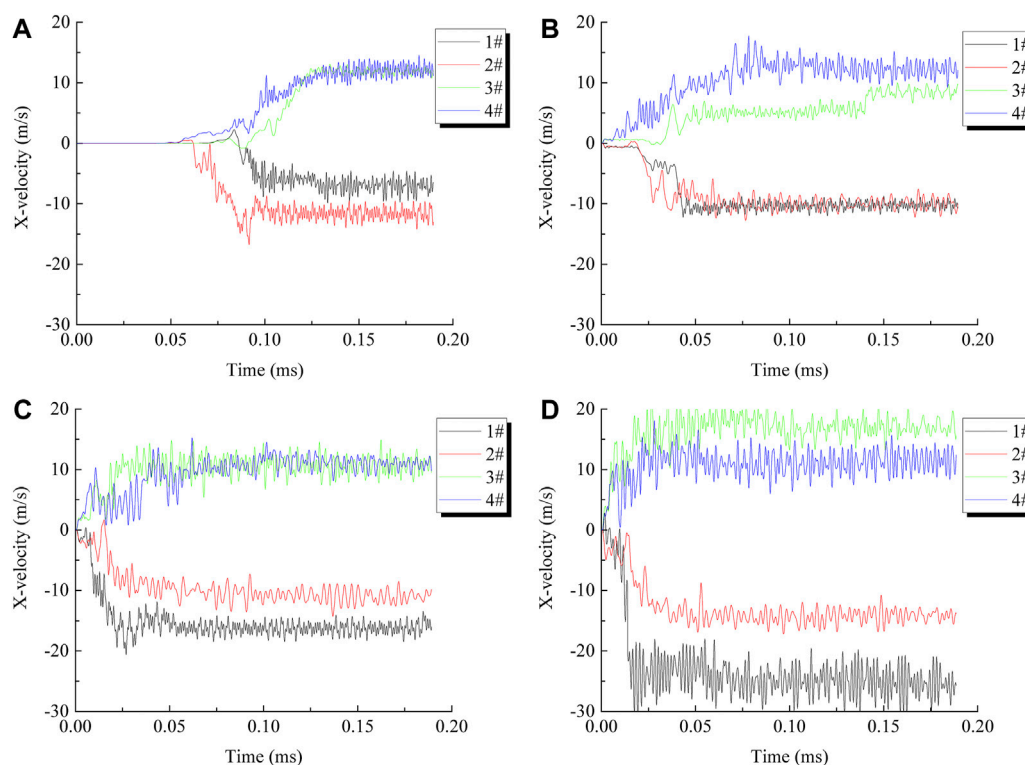


FIGURE 6

Magnitudes of horizontal velocities of fragments under different pre-confining pressures: (A) .1 MPa; (B) 1.0 MPa; (C) 2.5 MPa and (D) 5.0 MPa.

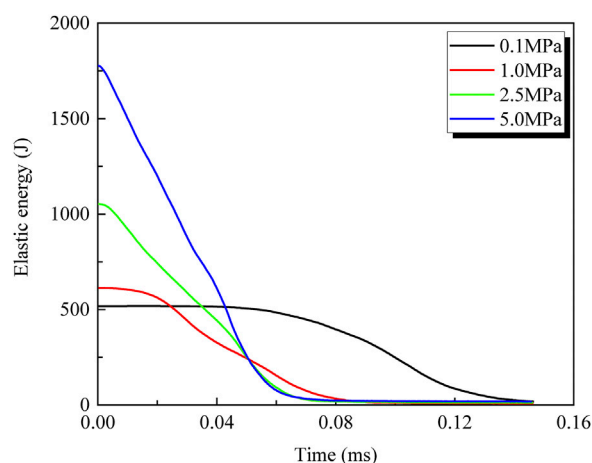


FIGURE 7

Change in elastic energy vs time for different pre-confining pressures.

## 3.2 Energy evolution of coalbursts

### 3.2.1 Elastic energy

Figure 7 illustrates how the elastic energy changes during the coalburst process. The initial elastic energy is 519 J when the pre-confining pressure is .1 MPa and increases to 1777 J when the pre-

confining pressure is 5.0 MPa. After a coal sample is completely destroyed *via* coalburst, the elastic energy is close to 0 J. No coalburst occurs under the pre-confining pressure of .1 MPa during the dynamic calculation time of .00–.05 m, and only a small number of micro-cracks are generated inside the coal sample, so the dissipation of elastic energy is not obvious at this stage. When the dynamic calculation time is greater than .05 m, the elastic energy of the sample gradually decreases with the occurrence of a small burst near the unloading surface. For coal samples with initial confining pressures of 1.0 MPa, 2.5 MPa and 5.0 MPa, various degrees of coalburst occur after the confining pressure is released, and the elastic energy decreases immediately. The initiation and coalescence of cracks as well as the ejection of fragments cause the dissipation of elastic energy. The elastic energy release rate increases with increasing pre-confining pressure. Therefore, the rate of reduction in elastic energy can be used to characterize the coalburst.

The dissipation process of elastic energy during the coalburst is fully captured by the simulations. The distribution of the elastic energy is given in Figure 8. Figure 8 reveals that the stored elastic energy increases with rising pre-confining pressure. Higher pre-confining pressures lead to a stronger inhomogeneity of elastic energy distribution in coal. High pre-confining pressure causes high local stresses inside the coal sample. Obviously, the higher the inhomogeneity of stress or energy distribution in the coal, the higher the possibility of coalburst. The dissipation process of elastic energy basically corresponds to the crack evolution process. The dissipation of elastic energy is obvious in the areas with densely distributed cracks, and the remaining elastic energy in these areas is



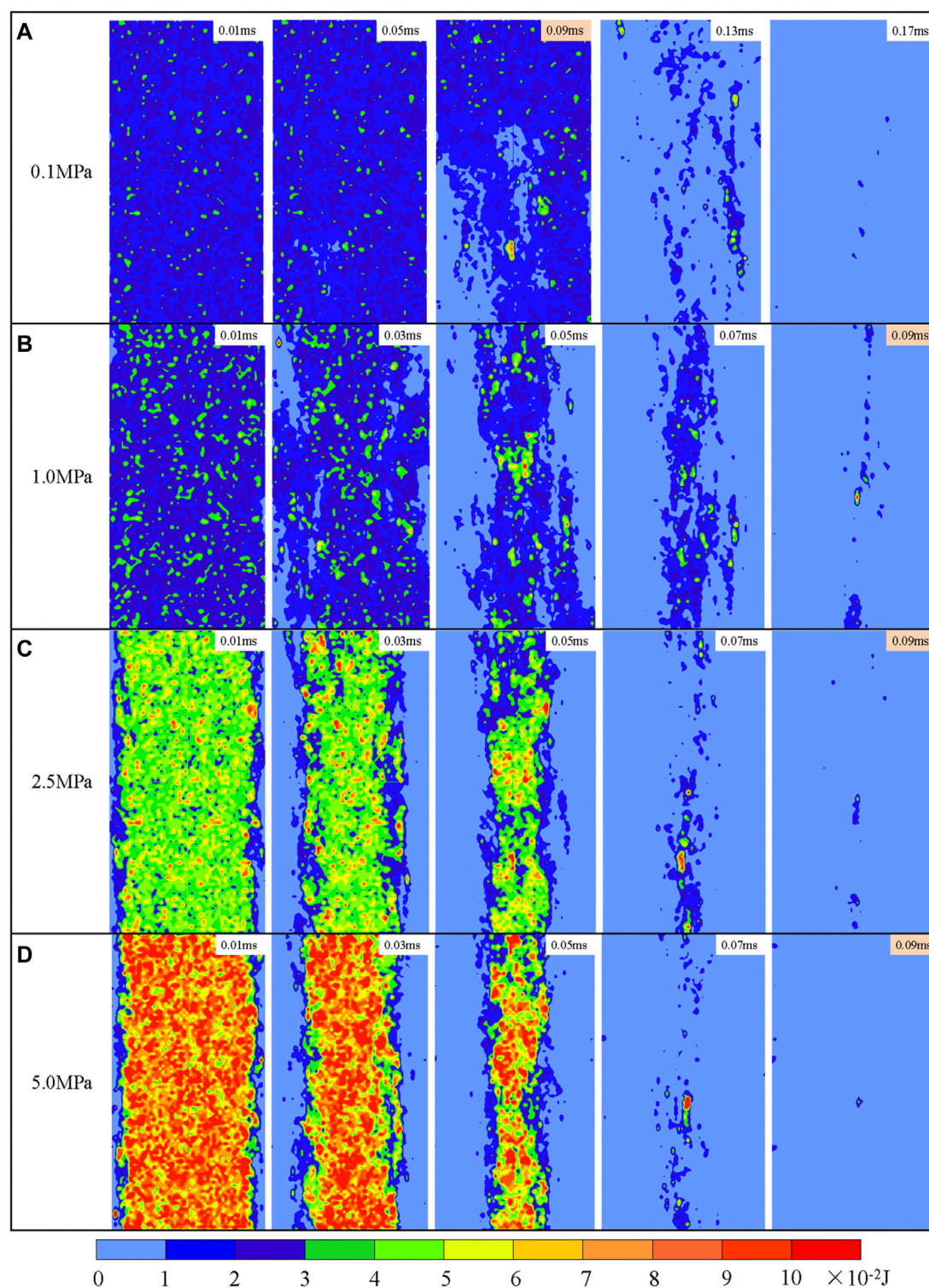
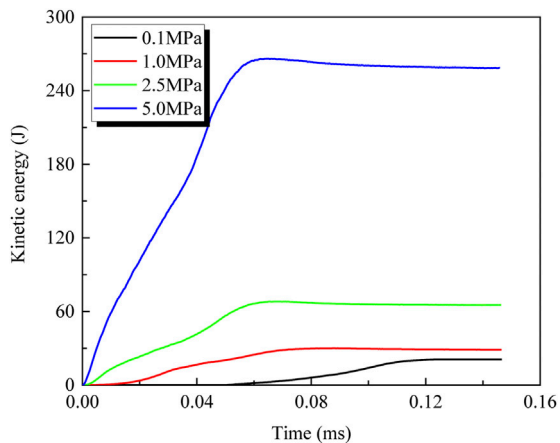


FIGURE 8

Distribution of elastic energy under different pre-confining pressures: (A) .1 MPa; (B) 1 MPa; (C) 2.5 MPa and (D) 5 MPa for different points in time.

small. In other words, development and growth of the fractures are the main reasons for the elastic energy dissipation. In the numerical simulation, the coal sample is loaded in the vertical direction and

unloaded in the horizontal direction, and the coal burst also occurs mainly in the horizontal direction, so that a large amount of elastic energy is dissipated along the horizontal direction. It can be seen



**FIGURE 9**  
Change in kinetic energy vs time for different pre-confining pressures.

that strain energy is released at different rates for different pre-confining pressures, and there is still a large amount of strain energy in the coal sample when the dynamic time is 0.09 ms for a pre-confining pressure of 0.1 MPa. As the pre-confining pressure increases, the strain energy release rate is greater when the dynamic time is the same, indicating that the coal burst more violent.

### 3.2.2 Kinetic energy

Figure 9 illustrates the kinetic energy evolution for different pre-confining pressures. The cumulative kinetic energy is zero within 0–0.05 ms when the pre-confining pressure is 0.1 MPa, indicating that a coalburst does not occur. A coalburst will end when the kinetic energy does no longer change (coal sample is completely destroyed or has reached a certain final damage state). The kinetic energy during the coalburst is larger under higher pre-confining pressure. The kinetic energy increases more rapidly and reaches the peak earlier when the pre-confining pressure increases. This indicates that a higher pre-confining pressure causes a shorter coalburst triggering time and more violent fragment ejection, resulting in a more harmful coalburst.

Figure 10 shows the distribution of the kinetic energy during the coalburst process. There is a clear difference in the kinetic energy near and far from the unloading surface, which leads to the separation of coal fragments and plates as shown in Figure 5. The evolution of kinetic energy under different pre-confining pressures shows that the cracks gradually expand from the boundaries to the centre of the coal samples, which is in good agreement with field and experimental observations (He et al., 2012; Zhang et al., 2012; Jiang et al., 2020). The evolution process of kinetic energy shows that the ejection of fragments during coalbursts starts at some areas on the unloading surface of the sample, and new areas of coalburst are continuously formed and expand, eventually leading to a violent coalburst. As shown in Figures 8, 10, the transformation between elastic energy and kinetic energy during coalbursts is captured by the numerical simulations. Notably, the distribution

of kinetic energy in the sample is not uniform. On the one hand, there are many “kinetic energy accumulation areas” near the unloading surface, which lead to the occurrence of “coalburst pits” with different depths and locations on the unloading surface of the coal samples, as can be seen in Figure 10C. There is another interesting phenomenon: some independent “kinetic energy concentration areas” form inside the coal sample under high pre-confining pressure, as shown in Figures 10C, D. These regions have a higher kinetic energy value than their surroundings, which indicates that some violent “internal burst” occur inside the coal sample, promoting the ejection of fragments and coal plates. This is because there is higher stress within the coal sample under high pre-surrounding pressure, and the internal stress and energy distribution are not uniform. When the pre-surrounding pressure was suddenly unloaded, the dynamic failure occurred inside the coal sample.

### 3.2.3 Frictional energy

Shear failure is an important element in the coalburst process. When shear failure occurs, dislocation (frictional sliding) along the blocks is triggered, so a certain amount of elastic energy is converted into work to overcome frictional resistance. This part of the energy dissipated due to the shear slip during a coalburst is called frictional energy. Figure 11 illustrates how the frictional energy changes during a coalburst. The increase in accumulated frictional energy is an indication of shear failure in the coal sample. As shown in Figure 11, the peak of the frictional energy during the coalburst increases with rising pre-confining pressure. This demonstrates that more shear cracks occur during the coalburst under high pre-confining pressure.

Figure 12 shows the distribution of the frictional energy at different stages during the coalburst. Figure 12 documents, those regions where the frictional energy is concentrated develop from areas near the unloading surface towards the centre of the sample. This is consistent with the gradual expansion of shear cracks. The pre-confining pressure has an important influence on the distribution of frictional energy. Compared with a low pre-confining pressure, the frictional energy is higher and more concentrated in the centre of the sample under higher pre-confining pressure. This shows that more shear cracks are formed in the core of the sample during the coalburst induced by release of a higher pre-confining pressure, resulting in predominant shear failure of the sample.

## 4 Discussion

### 4.1 Influence of pre-confining pressure on failure mechanism during coalburst

Strainbursts of rock are divided into tensile strainbursts (Diederichs, 2007; Hu et al., 2018) and shear strainbursts (Ortlepp, 2001; Zhang et al., 2012; Feng et al., 2016). In this study, under different pre-confining pressures different failure modes occur like analysed in Section 3.1 and illustrated in Figure 13. The coalburst induced by release of a low pre-confining pressure is dominated by tensile failure, which is

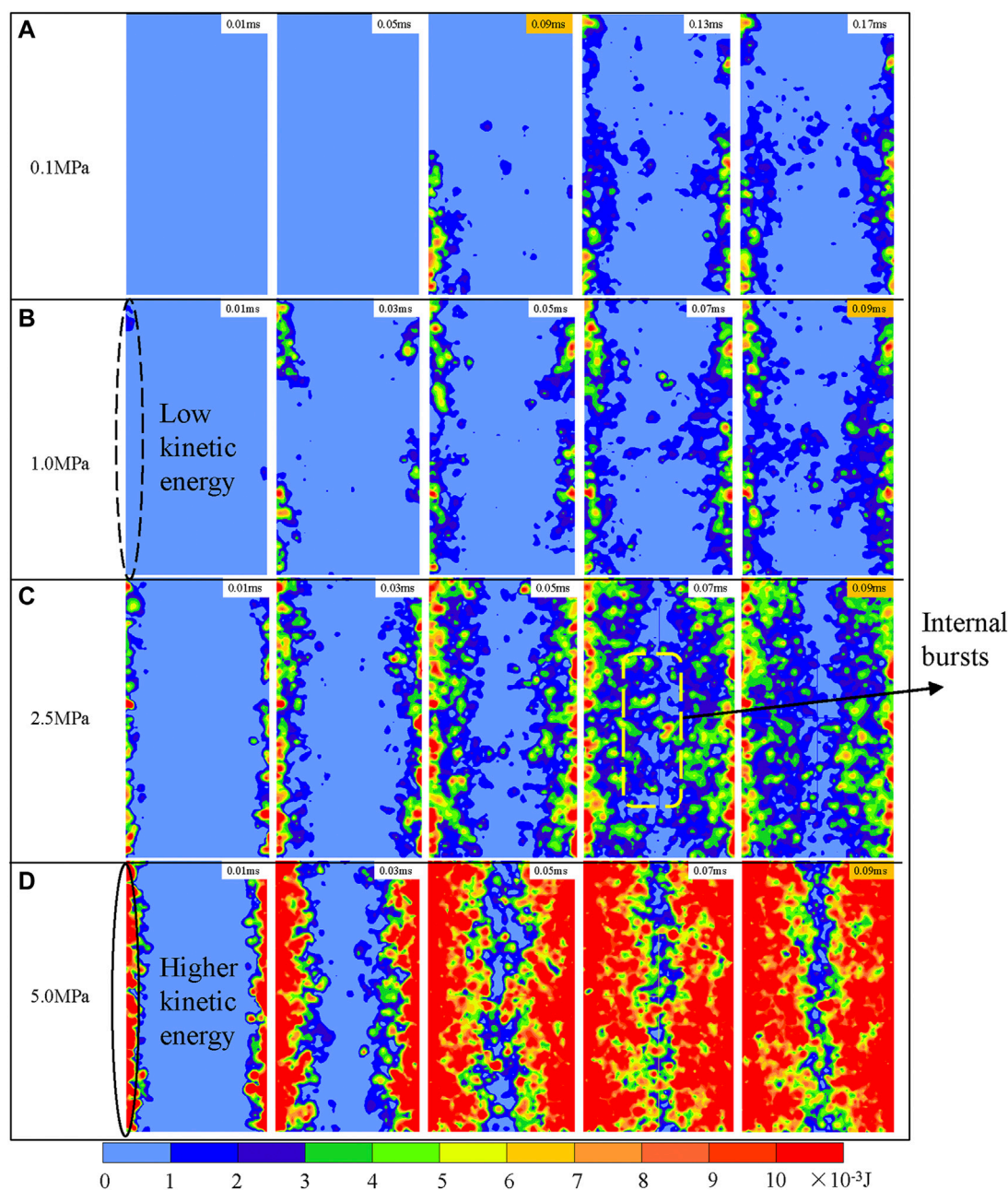


FIGURE 10

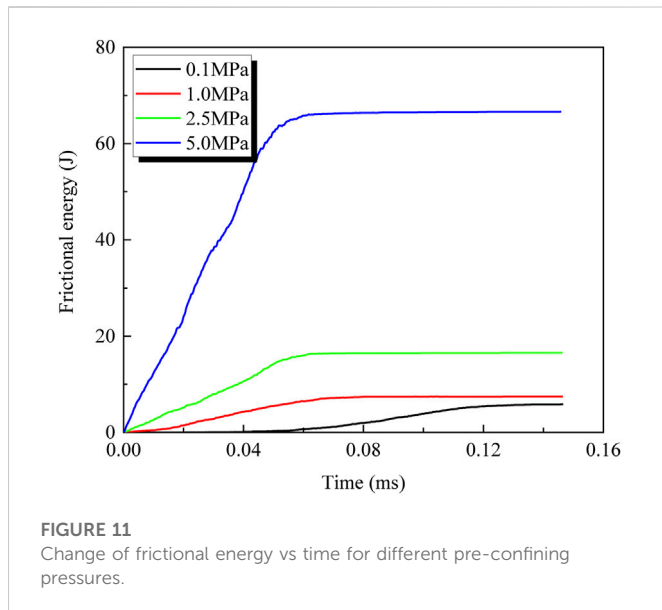
Distribution of kinetic energy under different pre-confining pressures of (A) .1 MPa; (B) 1 MPa; (C) 2.5 MPa and (D) 5 MPa for different points in time.

referred to as tensile coalburst. During a tensile coalburst, the failure is characterized by coal fragment ejection caused by tensile failure in certain areas near the unloading surface, small failure areas, and limited ejection intensity. Apart from tensile failure on both sides, there is no complete penetrating shear fracturing in the centre of the specimen. However, shear failure is the dominant during coalbursts under high pre-confining pressure, which is referred to as shear coalburst. There are two types of micro-cracks in shear coalbursts. On the one hand: splitting and throwing out of a large number of coal fragments and plates are caused by the coalescence of tensile cracks near the unloading

surface. Fragments are ejected at a fairly high velocity, such as 10–30 m/s. On the other hand, many shear cracks form in the central region of the coal sample, which is the major cause of coal failure during coalburst. Notice, that the pre-confining pressure applied to the two lateral sides are both released in the numerical simulation. Therefore, significant lateral deformation and failure occur on both sides of the coal samples in the numerical simulation.

As discussed above, the failure modes of coal during a unloading-induced coalburst are complex. As shown in Figure 13, the failure during coalbursts as presented by numerical simulations, are different from single failure under





static or quasi-static loads as presented for instance by (Haimson and Chang, 2000; Chang and Lee, 2004; Yang et al., 2012). The numerical results in this study show that tensile failures mainly occur near the unloading surface, while shear cracks are mainly distributed in the core region of the coal samples. This is in good agreement with earlier studies (Feng et al., 2018; Su et al., 2018). The density of tensile cracks rises and they expand deeper below the unloaded surface with increasing pre-confining pressure. Moreover, the number of shear cracks that appears far from the unloaded surface also increase significantly, and these cracks interpenetrate. It is possible to explain this failure phenomenon in the following way. On the one hand, the stress change caused by the sudden unloading of the pre-confining pressure causes the deformation (extension) of the coal sample near the unloading surface, and this lateral deformation is causing the tensile cracks. On the other hand, the instantaneous unloading of the pre-confining pressure causes an increase in the vertical stress in the remaining more or less intact part of the coal sample. The higher the pre-confining pressure, the greater the vertical stress of the sample after unloading. It promotes the initiation and development of shear failure in the centre of the coal sample. The failure mechanism of unloading-induced coalburst gradually transforms from tensile mode to shear mode as the pre-confining pressure increases.

## 4.2 Influence of pre-confining pressure on energy conversion of coalbursts

Figure 14 presents peak elastic energy, peak kinetic energy and peak frictional energy of the coal samples under different pre-confining pressures during unloading-induced coalbursts. The graph shows that when the pre-confining pressure rises, the three energies rise as well. The higher the pre-confining stress, the higher the peak strength of the rock. Therefore, the ultimate energy-storage capacity of the coal increases with the peak strength. Compared with low pre-confining pressures, at high

pre-confining pressures a higher stress change occur at the moment of unloading, resulting in more tensile cracks appearing near the unloading surface. Tensile failure is the main source of kinetic energy increase. The frictional energy is mainly caused by the shear slip between blocks. Severe shear failure occurs during coalburst due to the increase in vertical stress induced by unloading of the high pre-confining pressure, which causes an increase in frictional energy. The relationship between the above mentioned three energy types and the pre-confining pressure is not linear.

The elastic energy displayed in Figure 7 is only the elastic energy stored in the coal sample. It is well known that the elastic energy released during coalbursts includes the elastic energy stored in the sample and the elastic energy stored in the loading system (Manouchehrian and Cai, 2016; Tarasov and Stacey, 2017; Gao and Yang, 2021). The elastic energy in the loading plate  $W_L$  should be calculated as:

$$W_L = \frac{\sigma_{\max}^2 A_L l}{2E_L} \quad (8)$$

where  $\sigma_{\max}$  is the maximum vertical stress monitored at the loading plate, and the properties of the loading plate are  $l = .1$  m,  $E_L = 17$  GPa, and  $A_L = \pi \times .1$  m<sup>2</sup>.

Consequently, the conversion ratio of kinetic energy  $\alpha$  and the conversion ratio of frictional energy  $\beta$  are calculated by:

$$\alpha = \frac{W_K}{W_C + W_L} \quad (9)$$

$$\beta = \frac{W_F}{W_C + W_L} \quad (10)$$

where  $W_K$  and  $W_F$  are the kinetic energy and the frictional energy during the coalburst, respectively.  $W_C$  and  $W_L$  are the elastic energy stored in the coal and the plate, respectively.

Figure 15 shows the conversion ratios of elastic energy into kinetic and frictional energy during unloading-induced coalbursts under different pre-confining pressures. As illustrated in Figure 15, the pre-confining pressure has an important influence on the energy transformation during a coalburst. In this study, the conversion ratio of kinetic energy is between 2% and 4% when the pre-confining pressure is less than 5 MPa, which means only a small percentage of elastic energy is transformed into kinetic energy, which is consistent with previous findings (Gu and Ozbay, 2015; Hu et al., 2020). However, the conversion ratio of kinetic energy increases significantly as the pre-confining pressure continues to rise, suggesting that more coal fragments and plates are thrown out at a higher velocity during a severe coalburst. In addition, as the pre-confining pressure rises, the conversion ratio of frictional energy increases as well, indicating that the shear failure in coal samples intensifies and that a shear coalburst occurs under a higher pre-confining pressure.

## 4.3 Recommendations to prevent coalbursts

Violent coalbursts can occur in roadway developments as a result of the unloading of high pre-confining pressure according to simulation findings. Based on the above research results, three measures presented below are recommended to prevent the occurrence of coalbursts. First, a sudden unloading of a coal

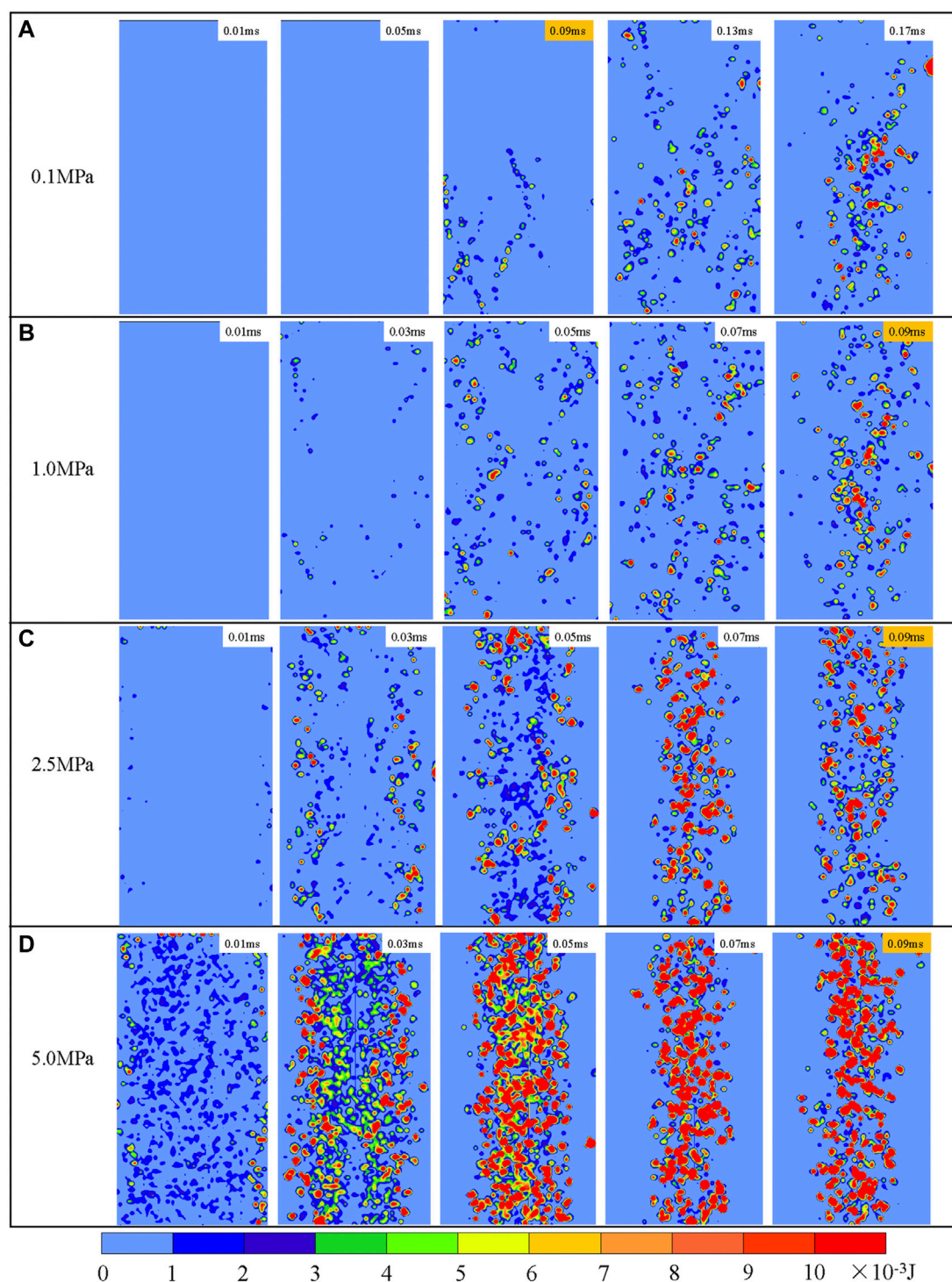


FIGURE 12

Distribution of frictional energy under different pre-confining pressures of (A) .1 MPa; (B) 1 MPa; (C) 2.5 MPa and (D) 5 MPa for different points in time.

pillar with high pre-confining pressure should be avoided, and a slower excavation speed should be adopted to reduce the unloading rate in the coal pillar. Second, some measures should be taken to reduce the elastic energy stored in the coal pillar, such as cutting the rock layer above the coal pillar to reduce the vertical load or

performing large-diameter drilling in the coal to reduce the energy storage capacity. Third, it is necessary to provide timely support to the free surface formed by the excavation, which will inhibit the formation of tensile failures and the expansion of cracks away from the unloading surface.

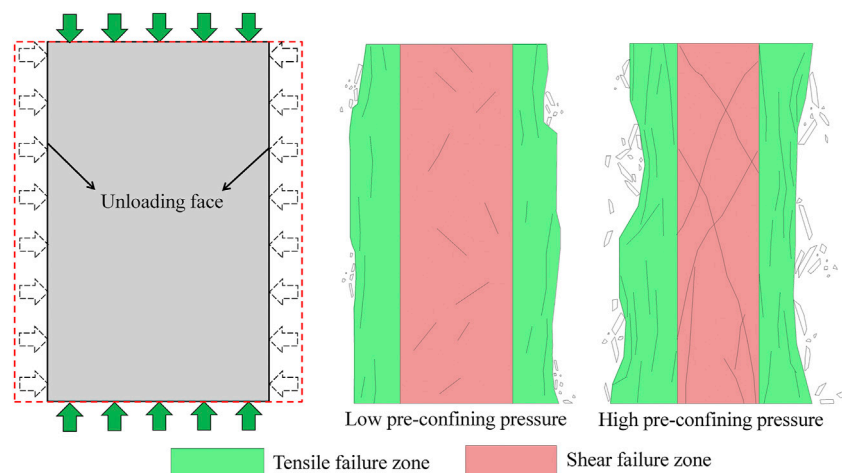


FIGURE 13

Two failure modes of coalburst under different pre-confining pressures.

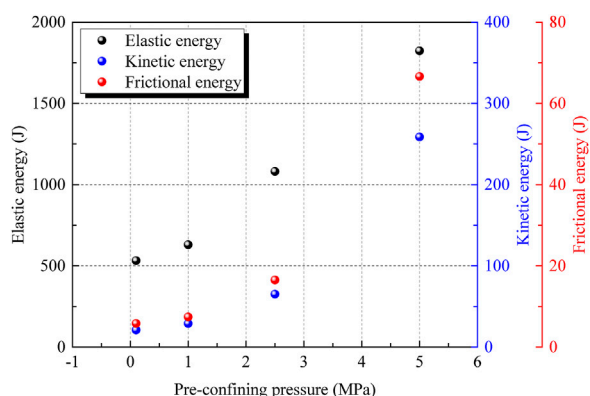


FIGURE 14

Peak elastic energy, peak kinetic energy and peak frictional energy of the coal samples under different pre-confining pressures.

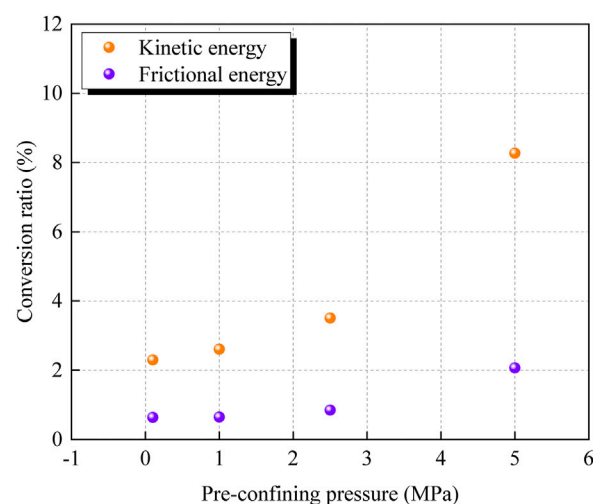


FIGURE 15

Energy conversion ratio during coalbursts under different pre-confining pressures.

## 5 Conclusion

This paper presents a numerical study of unloading-induced coalbursts failure analysis using DEM and a static–dynamic loading strategy. This method, well calibrated and validated, is effective in capturing the typical phenomena of coalbursts. The main conclusions in respect to the influence of pre-confining pressure on crack propagation, failure mechanism, energy evolution and energy conversion during unloading-induced coalbursts are as follows.

- 1) The pre-confining pressure has a significant effect on crack development and failure mode of unloading-induced coalbursts. Localized failure patterns are observed in coalbursts. Regions near the unloading surface are more prone to tensile failure, while shear cracks are the main failure type in the centre of the body. With increasing pre-confining pressure, the failure mechanism of coal transforms from a tensile coalburst towards a shear coalburst.
- 2) The numerical simulations provide direct evidence for the conversion of stored elastic energy into kinetic energy and frictional energy during

unloading-induced coalbursts. The evolution of energy is consistent with the development of cracks. During coalbursts, the higher the pre-confining pressure, the greater the rate at which the elastic energy decreases and the greater the rate at which kinetic and frictional energy increase. Some independent “kinetic energy concentration areas” are observed during unloading-induced coalbursts, indicating that violent “internal bursts” occur inside the coal, providing new insights into the mechanism of coalbursts.

- 3) The pre-confining pressure obviously affects the energy transition during unloading-induced coalbursts. The conversion ratio of kinetic energy increases non-linearly with increasing pre-confining pressure, indicating that coalbursts under high pre-confining pressure are more dangerous. The conversion ratio of frictional energy is approximately one-quarter of the conversion ratio of kinetic energy. With increasing pre-confining pressure, the



conversion ratio of frictional energy also increases non-linearly, indicating that the coalburst becomes dominated by shear failure under high pre-confining pressure.

## Data availability statement

The original contributions presented in the study are included in the article/supplementary material, further inquiries can be directed to the corresponding authors.

## Author contributions

All authors listed have made a substantial, direct, and intellectual contribution to the work and approved it for publication. Conceptualization: JC, LD, and KZ; Methodology: JC and KZ; Software: LD; Validation: JC and YC; Formal Analysis: JC, JL, and JK; Investigation: JC, KZ, and JK; Data curation: JC, LD and YC; Writing-Original Draft Preparation: JC; Writing-Review & Editing: JC and YC; Supervision: JC, LD, and JL; Project Administration: LD and JL; Funding Acquisition: LD and JL. All authors have read and agreed to the published version of the manuscript.

## Funding

This work was conducted with support from the National Natural Science Foundation of China (Grant No. 51874292, 51934007 and 52004004) and the Major Project of Natural Science Research in

Higher Education Institutions in Anhui Province (Grant No. KJ2021ZD0051).

## Acknowledgments

The authors thank for financial support from the National Natural Science Foundation of China (Grant Nos. 51874292, 51934007 and 52004004) and the Major Project of Natural Science Research in Higher Education Institutions in Anhui Province (Grant Nos. KJ2021ZD0051). The first author JC would like to express his sincere thanks to the China Scholarship Council (CSC) for the financial support for his study at TU Bergakademie Freiberg, Germany.

## Conflict of interest

The authors declare that the research was conducted in the absence of any commercial or financial relationships that could be construed as a potential conflict of interest.

## Publisher's note

All claims expressed in this article are solely those of the authors and do not necessarily represent those of their affiliated organizations, or those of the publisher, the editors and the reviewers. Any product that may be evaluated in this article, or claim that may be made by its manufacturer, is not guaranteed or endorsed by the publisher.

## References

- Ai, D., Zhao, Y., Wang, Q., and Li, C. (2020). Crack propagation and dynamic properties of coal under SHPB impact loading: Experimental investigation and numerical simulation. *Theor. Appl. Fract. Mech.* 105, 102393. doi:10.1016/j.tafmec.2019.102393
- Bazant, Z. P., Shang-Ping, B., and Ravindra, G. (1993). Fracture of rock: Effect of loading rate. *Eng. Fract. Mech.* 45 (3), 393–398. doi:10.1016/0013-7944(93)90024-m
- Cao, J., Dou, L., Zhu, G., He, J., Wang, S., and Zhou, K. (2020). Mechanisms of rock burst in horizontal section mining of a steeply inclined extra-thick coal seam and prevention Technology. *Energies* 13 (22), 6043. doi:10.3390/en13226043
- Chang, S.-H., and Lee, C.-I. (2004). Estimation of cracking and damage mechanisms in rock under triaxial compression by moment tensor analysis of acoustic emission. *Int. J. Rock Mech. Min. Sci.* 41 (7), 1069–1086. doi:10.1016/j.ijrmms.2004.04.006
- Chen, G., He, M., and Fan, F. (2018). Rock burst analysis using DDA numerical simulation. *Int. J. Geomechanics* 18 (3). doi:10.1061/(asce)gm.1943-5622.0001055
- Cook, N. G. W. (1965). A note on rockbursts considered as a problem of stability. *J. South. Afr. Inst. Min. Metallurgy* 65 (8), 437–446. doi:10.10520/AJA0038223X\_4914
- Cundall, P. A., and Strack, O. D. L. (1979). A discrete numerical model for granular assemblies. *Géotechnique* 29 (1), 47–65. doi:10.1680/geot.1979.29.1.47
- Diederichs, M. S. (2007). The 2003 Canadian Geotechnical Colloquium: Mechanistic interpretation and practical application of damage and spalling prediction criteria for deep tunnelling. *Can. Geotechnical J.* 44 (9), 1082–1116. doi:10.1139/t07-033
- Dou, L., and He, X. (2001). *Theory and technology of rock burst prevention*. Xuzhou: China University of Mining and Technology Press.
- Duan, K., Ji, Y., Wu, W., and Kwok, C. Y. (2019). Unloading-induced failure of brittle rock and implications for excavation-induced strain burst. *Tunn. Undergr. Space Technol.* 84, 495–506. doi:10.1016/j.tust.2018.11.012
- Feng, X.-T., Xu, H., Qiu, S.-L., Li, S.-J., Yang, C.-X., Guo, H.-S., et al. (2018). *Situ Observation of Rock Spalling in the Deep Tunnels of the*, 51, 1193–1213. doi:10.1007/s00603-017-1387-8China Jinping underground laboratory (2400 m depth) *Rock Mech. Rock Eng.*
- Feng, X.-T., Yu, Y., Feng, G.-L., Xiao, Y.-X., Chen, B., and Jiang, Q. (2016). Fractal behaviour of the microseismic energy associated with immediate rockbursts in deep, hard rock tunnels. *Tunn. Undergr. Space Technol.* 51, 98–107. doi:10.1016/j.tust.2015.10.002
- Frith, R., Reed, G., and Jones, A. (2020). A causation mechanism for coal bursts during roadway development based on the major horizontal stress in coal: Very specific structural geology causing a localised loss of effective coal confinement and Newton's second law. *Int. J. Min. Sci. Technol.* 30 (1), 39–47. doi:10.1016/j.ijmst.2019.12.018
- Gao, F., Kaiser, P. K., Stead, D., Eberhardt, E., and Elmo, D. (2019b). Numerical simulation of strainbursts using a novel initiation method. *Comput. Geotechnics* 106, 117–127. doi:10.1016/j.compgeo.2018.10.018
- Gao, F., Kaiser, P. K., Stead, D., Eberhardt, E., and Elmo, D. (2019a). Strainburst phenomena and numerical simulation of self-initiated brittle rock failure. *Int. J. Rock Mech. Min. Sci.* 116, 52–63. doi:10.1016/j.ijrmms.2019.03.021
- Gao, F., Kang, H., and Li, J. (2021). Numerical simulation of fault-slip rockbursts using the distinct element method. *Tunn. Undergr. Space Technol.* 110, 103805. doi:10.1016/j.tust.2020.103805
- Gao, F., and Yang, L. (2021). Experimental and numerical investigation on the role of energy transition in strainbursts. *Rock Mech. Rock Eng.* 54 (9), 5057–5070. doi:10.1007/s00603-021-02550-8
- Gao, F. Q., and Stead, D. (2014). The application of a modified Voronoi logic to brittle fracture modelling at the laboratory and field scale. *Int. J. Rock Mech. Min. Sci.* 68, 1–14. doi:10.1016/j.ijrmms.2014.02.003
- Gu, R., and Ozbay, U. (2015). Numerical investigation of unstable rock failure in underground mining condition. *Comput. Geotechnics* 63, 171–182. doi:10.1016/j.compgeo.2014.08.013
- Haimson, B., and Chang, C. (2000). A new true triaxial cell for testing mechanical properties of rock, and its use to determine rock strength and deformability of Westerly granite. *Int. J. Rock Mech. Min. Sci.* 37 (1–2), 285–296. doi:10.1016/s1365-1609(99)00106-9
- Hao, X., Du, W., Zhao, Y., Sun, Z., Zhang, Q., Wang, S., et al. (2020). Dynamic tensile behaviour and crack propagation of coal under coupled static-dynamic loading. *Int. J. Min. Sci. Technol.* 30 (5), 659–668. doi:10.1016/j.ijmst.2020.06.007
- Hatzor, Y. H., He, B.-G., and Feng, X.-T. (2017). Scaling rockburst hazard using the DDA and GSI methods. *Tunn. Undergr. Space Technol.* 70, 343–362. doi:10.1016/j.tust.2017.09.010

- Hauquin, T., Gunzburger, Y., and Deck, O. (2018). Predicting pillar burst by an explicit modelling of kinetic energy. *Int. J. Rock Mech. Min. Sci.* 107, 159–171. doi:10.1016/j.ijrmms.2018.05.004
- He, B.-G., Zelig, R., Hatzor, Y. H., and Feng, X.-T. (2016). Rockburst generation in discontinuous rock masses. *Rock Mech. Rock Eng.* 49 (10), 4103–4124. doi:10.1007/s00603-015-0906-8
- He, M., Ren, F., and Cheng, C. (2018). Mechanism of strain burst by laboratory and numerical analysis. *Shock Vib.* 2018, 1–15. doi:10.1155/2018/8940798
- He, M. C., Miao, J. L., and Feng, J. L. (2010). Rock burst process of limestone and its acoustic emission characteristics under true-triaxial unloading conditions. *Int. J. Rock Mech. Min. Sci.* 47 (2), 286–298. doi:10.1016/j.ijrmms.2009.09.003
- He, M. C., Nie, W., Zhao, Z. Y., and Guo, W. (2012). Experimental investigation of bedding plane orientation on the rockburst behavior of sandstone. *Rock Mech. Rock Eng.* 45 (3), 311–326. doi:10.1007/s00603-011-0213-y
- He, M. C., Zhao, F., Cai, M., and Du, S. (2014). A novel experimental technique to simulate pillar burst in laboratory. *Rock Mech. Rock Eng.* 48 (5), 1833–1848. doi:10.1007/s00603-014-0687-5
- Hokka, M., Black, J., Tklich, D., Fourmeau, M., Kane, A., Hoang, N.-H., et al. (2016). Effects of strain rate and confining pressure on the compressive behavior of Kuru granite. *Int. J. Impact Eng.* 91, 183–193. doi:10.1016/j.ijimpeng.2016.01.010
- Hu, L., Ma, K., Liang, X., Tang, C., Wang, Z., and Yan, L. (2018). Experimental and numerical study on rockburst triggered by tangential weak cyclic dynamic disturbance under true triaxial conditions. *Tunn. Undergr. Space Technol.* 81, 602–618. doi:10.1016/j.tust.2018.08.014
- Hu, L., Su, G., Liang, X., Li, Y., and Yan, L. (2020). A distinct element based two-stage-structural model for investigation of the development process and failure mechanism of strainburst. *Comput. Geotechnics* 118, 103333. doi:10.1016/j.compgeo.2019.103333
- Huang, F., Shen, J., Cai, M., and Xu, C. (2019). An empirical UCS model for anisotropic blocky rock masses. *Rock Mech. Rock Eng.* 52 (9), 3119–3131. doi:10.1007/s00603-019-01771-2
- Itasca Consulting Group Inc (2014). *UDEC manual*. Minneapolis. Version 6.0.
- Jiang, J., Su, G., Zhang, X., and Feng, X.-T. (2020). Effect of initial damage on remotely triggered rockburst in granite: An experimental study. *Bull. Eng. Geol. Environ.* 79 (6), 3175–3194. doi:10.1007/s10064-020-01760-8
- Jiang, Y., Zhao, Y., Wang, H., and Zhu, J. (2017). A review of mechanism and prevention technologies of coal bumps in China. *J. Rock Mech. Geotechnical Eng.* 9 (1), 180–194. doi:10.1016/j.jrmge.2016.05.008
- Ju, M., Li, J., Li, J., and Zhao, J. (2020). Loading rate effects on anisotropy and crack propagation of weak bedding plane-rich rocks. *Eng. Fract. Mech.* 230, 106983. doi:10.1016/j.engfractmech.2020.106983
- Kazerani, T., Yang, Z. Y., and Zhao, J. (2011). A discrete element model for predicting shear strength and degradation of rock joint by using compressive and tensile test Data. *Rock Mech. Rock Eng.* 45 (5), 695–709. doi:10.1007/s00603-011-0153-6
- Kong, X., Wang, E., Li, S., Lin, H., Zhang, Z., and Ju, Y. (2020). Dynamic mechanical characteristics and fracture mechanism of gas-bearing coal based on SHPB experiments. *Theor. Appl. Fract. Mech.* 105, 102395. doi:10.1016/j.tafmec.2019.102395
- Li, X., Gu, H., Tao, M., Peng, K., Cao, W., and Li, Q. (2021). Failure characteristics and meso-deterioration mechanism of pre-stressed coal subjected to different dynamic loads. *Theor. Appl. Fract. Mech.* 115, 103061. doi:10.1016/j.tafmec.2021.103061
- Li, X. B., Lok, T. S., and Zhao, J. (2004). Dynamic characteristics of granite subjected to intermediate loading rate. *Rock Mech. Rock Eng.* 38 (1), 21–39. doi:10.1007/s00603-004-0030-7
- Li, Y., Yang, S.-Q., Liu, Z.-L., Sun, B.-W., Yang, J., and Xu, J. (2022). Study on mechanical properties and deformation of coal specimens under different confining pressure and strain rate. *Theor. Appl. Fract. Mech.* 118, 103287. doi:10.1016/j.tafmec.2022.103287
- Liu, H. Y., Kou, S. Q., Lindqvist, P.-A., and Tang, C. A. (2004). Numerical studies on the failure process and associated microseismicity in rock under triaxial compression. *Tectonophysics* 384 (1–4), 149–174. doi:10.1016/j.tecto.2004.03.012
- Manouchehrian, A., and Cai, M. (2016). Simulation of unstable rock failure under unloading conditions. *Can. Geotechnical J.* 53 (1), 22–34. doi:10.1139/cgj-2015-0126
- Mottahedi, A., and Ataei, M. (2019). Fuzzy fault tree analysis for coal burst occurrence probability in underground coal mining. *Tunn. Undergr. Space Technol.* 83, 165–174. doi:10.1016/j.tust.2018.09.029
- Ortlepp, W. D. (2001). The behaviour of tunnels at great depth under large static and dynamic pressures. *Tunn. Undergr. Space Technol.* 16 (1), 41–48. doi:10.1016/s0886-7798(01)00029-3
- Potyondy, D. O., and Cundall, P. A. (2004). A bonded-particle model for rock. *Int. J. Rock Mech. Min. Sci.* 41 (8), 1329–1364. doi:10.1016/j.ijrmms.2004.09.011
- Su, G., Hu, L., Feng, X., Yan, L., Zhang, G., Yan, S., et al. (2018). True triaxial experimental study of rockbursts induced by ramp and cyclic dynamic disturbances. *Rock Mech. Rock Eng.* 51 (4), 1027–1045. doi:10.1007/s00603-017-1384-y
- Su, G., Shi, Y., Feng, X., Jiang, J., Zhang, J., and Jiang, Q. (2017). True-triaxial experimental study of the evolutionary features of the acoustic emissions and sounds of rockburst processes. *Rock Mech. Rock Eng.* 51 (2), 375–389. doi:10.1007/s00603-017-1344-6
- Tarasov, B. G., and Stacey, T. R. (2017). Features of the energy balance and fragmentation mechanisms at spontaneous failure of class I and class II rocks. *Rock Mech. Rock Eng.* 50 (10), 2563–2584. doi:10.1007/s00603-017-1251-x
- Vardar, O., Zhang, C., Canbulat, I., and Hebblewhite, B. (2018). A semi-quantitative coal burst risk classification system. *Int. J. Min. Sci. Technol.* 28 (5), 721–727. doi:10.1016/j.ijmst.2018.08.001
- Wang, J.-A., and Park, H. D. (2001). Comprehensive prediction of rockburst based on analysis of strain energy in rocks. *Tunn. Undergr. Space Technol.* 16 (1), 49–57. doi:10.1016/s0886-7798(01)00030-x
- Yang, S.-Q., Jing, H.-W., and Wang, S.-Y. (2012). Experimental investigation on the strength, deformability, failure behavior and acoustic emission locations of red sandstone under triaxial compression. *Rock Mech. Rock Eng.* 45 (4), 583–606. doi:10.1007/s00603-011-0208-8
- Yang, X., Ren, T., and Tan, L. (2020). Estimation of average ejection velocity generated by rib burst under compression load. *Int. J. Rock Mech. Min. Sci.* 128, 104277. doi:10.1016/j.ijrmms.2020.104277
- Yao, M., Rong, G., Zhou, C., and Peng, J. (2016). Effects of thermal damage and confining pressure on the mechanical properties of coarse marble. *Rock Mech. Rock Eng.* 49 (6), 2043–2054. doi:10.1007/s00603-016-0916-1
- Zhang, C., Canbulat, I., Hebblewhite, B., and Ward, C. R. (2017). Assessing coal burst phenomena in mining and insights into directions for future research. *Int. J. Coal Geol.* 179, 28–44. doi:10.1016/j.coal.2017.05.011
- Zhang, C., Feng, X.-T., Zhou, H., Qiu, S., and Wu, W. (2012). Case histories of four extremely intense rockbursts in deep tunnels. *Rock Mech. Rock Eng.* 45 (3), 275–288. doi:10.1007/s00603-011-0218-6
- Zhang, Z., Liu, X., Zhang, Y., Qin, X., and Khan, M. (2021). Comparative study on fracture characteristics of coal and rock samples based on acoustic emission technology. *Theor. Appl. Fract. Mech.* 111, 102851. doi:10.1016/j.tafmec.2020.102851
- Zhang, Y., and Wong, L. N. Y. (2018). A review of numerical techniques approaching microstructures of crystalline rocks. *Comput. Geosciences* 115, 167–187. doi:10.1016/j.cageo.2018.03.012
- Zhao, J., Zhou, Y. X., Hefny, A. M., Cai, J. G., Chen, S. G., Li, H. B., et al. (1999). Rock dynamics research related to cavern development for Ammunition storage. *Tunn. Undergr. Space Technol.* 14 (4), 513–526. doi:10.1016/s0886-7798(00)00013-4
- Zhao, Y., Zhao, G.-F., Jiang, Y., Elsworth, D., and Huang, Y. (2014). Effects of bedding on the dynamic indirect tensile strength of coal: Laboratory experiments and numerical simulation. *Int. J. Coal Geol.* 132, 81–93. doi:10.1016/j.coal.2014.08.007
- Zhu, J., Li, Y., Peng, Q., Deng, X., Gao, M., and Zhang, J. (2020). Stress wave propagation across jointed rock mass under dynamic extension and its effect on dynamic response and supporting of underground opening. *Tunn. Undergr. Space Technol.* 108, 103648. doi:10.1016/j.tust.2020.103648
- Zubelewicz, A., and Mroz, Z. (1983). Numerical simulation of rock burst processes treated as problems of dynamic instability. *Rock Mech. Rock Eng.* 16 (4), 253–274. doi:10.1007/bf01042360



## OPEN ACCESS

EDITED BY  
Xuelong Li,  
Shandong University of Science and  
Technology, China

REVIEWED BY  
Dengfeng Su,  
Southwest University of Science and  
Technology, China  
Wang Ping,  
Hunan University of Science and  
Technology, China

\*CORRESPONDENCE  
Hongyang Liu,  
✉ sdustliuwork@sdust.edu.cn

## SPECIALTY SECTION

This article was submitted to  
Environmental Informatics and Remote  
Sensing, a section of the journal  
Frontiers in Earth Science

RECEIVED 13 December 2022

ACCEPTED 28 December 2022

PUBLISHED 18 January 2023

## CITATION

Xie X, Fang X, Liu H, Xing X, Liang M, Wu G  
and Chen N (2023), Development and  
application of a borehole stress meter in  
rocks surrounding the roadway, based on  
optical-fiber sensing technology.  
*Front. Earth Sci.* 10:1122579.  
doi: 10.3389/feart.2022.1122579

## COPYRIGHT

© 2023 Xie, Fang, Liu, Xing, Liang, Wu and  
Chen. This is an open-access article  
distributed under the terms of the [Creative  
Commons Attribution License \(CC BY\)](#).  
The use, distribution or reproduction in  
other forums is permitted, provided the  
original author(s) and the copyright  
owner(s) are credited and that the original  
publication in this journal is cited, in  
accordance with accepted academic  
practice. No use, distribution or  
reproduction is permitted which does not  
comply with these terms.

# Development and application of a borehole stress meter in rocks surrounding the roadway, based on optical-fiber sensing technology

Xiaoping Xie<sup>1,2</sup>, Xinqiu Fang<sup>2</sup>, Hongyang Liu<sup>1\*</sup>, Xiaopeng Xing<sup>2</sup>,  
Minfu Liang<sup>2</sup>, Gang Wu<sup>2</sup> and Ningning Chen<sup>2</sup>

<sup>1</sup>School of Mining and Mechanical Engineering, Liupanshui Normal University, Liupanshui, China, <sup>2</sup>School of Mining, China University of Mining and Technology, Xuzhou, China

Stress in rock masses is an important parameter in the design and construction of underground engineering, such as the design and maintenance of mine roadways and the design of mining working faces. It is also a fundamental force causing the deformation and failure of geotechnical engineering excavation. At present, the abutment-pressure monitoring technology of the surrounding rocks of the coal mine roadway in China is not intelligent and systematic and lacks some high-precision sensing instruments and multi-functional monitoring systems. The mechanical model of the rocks surrounding the borehole was constructed by theoretical analysis of problems in the stress monitoring technology for underground rock masses in coal mines. Additionally, the interaction between the surrounding rocks and the borehole stress meter was analyzed. The borehole stress meters for tubular-structure fiber Bragg grating (TS-FBG) and cystic-structure fiber Bragg grating (CS-FBG) were designed by combining the sensing principle and sensing characteristics of fiber Bragg grating, and the performance of the two kinds of fiber Bragg grating borehole stress meters was compared by laboratory test. The track roadway of the 14,301 tested working faces in the Shaqu Coal Mine was taken as an example, and the stress of the rocks surrounding the 14,301-track roadway was monitored in real time by CS-FBG borehole stress meter during the mining of the working face. The following conclusions are drawn from the field application. The rig-site utilization results revealed obvious stress growth and stress peak zones in the mining-stress change curves of each measuring point on the two sides of the 14,301-track roadway in the process of mining the tested working face. Additionally, there were four stages: rapid rise, uniform growth, rapid rise to the peak, and rapid decline. Maximum stress monitored by the second station was 18.5 MPa, and the influence range of stress was over 140 m. Maximum stress monitored by the first measuring station was 19 MPa, the influence range of stress was about 80 m, and the peak stress position was about 20 m in front of the coal wall. Rig-site utilization proved the design of the CS-FBG borehole stress meter to be reasonable. Performance was stable and reliable, and the successful operation of field monitoring achieved the expected effect.

## KEYWORDS

coal mine roadway, surrounding-rock stress, fiber grating, cystic structure, borehole stress meter

## Introduction

The stress state of rock masses is an important issue in engineering rock mechanics. Stress in rock masses is an important parameter for the design and construction of underground engineering, such as in mine roadway design and maintenance and the design of mining working faces (Hao, 2022; Liu et al., 2022; Yang et al., 2022a; Yang et al., 2022b). It is also a fundamental force causing excavation deformation and damage in geotechnical engineering, such as in mining (Wang et al., 2020; Liu and Li, 2022; Liu et al., 2022; Wang et al., 2022; Zhou et al., 2022). Therefore, the stress states and stress field characteristics of rocks after being disturbed, and the real-time monitoring technology of mining-induced stress, are studied. This research has great significance for the prevention and control of dynamic coal and rock disasters (e.g., control of rock burst, coal-gas outburst, coal wall spalling, and roadway roof collapse) and for mine safety production (e.g., the risk assessment of the working face area, roof control, and roadway support) (Ma et al., 2016; Sun et al., 2022; Yang et al., 2022a).

Researchers have studied monitoring technology for mining stress in rocks surrounding mine roadways (Torres et al., 2011; Ray et al., 2018; Wang et al., 2020). At present, abutment-pressure monitoring technology for the rocks surrounding coal mine roadways in China is not intelligent or systematic, and it lacks high-precision sensing instruments and multi-functional monitoring systems. There are mature theories and field applications for commonly used electromagnetic radiation monitoring technology, microseismic testing technology, and borehole stress meter testing methods in the stress monitoring of rock surrounding roadways (Tao et al., 2019; Wang et al., 2020; Chai et al., 2021). However, electromagnetic radiation monitoring technology and microseismic testing technology are easily affected by external electrical equipment, and their cost is high. The signal conversion of the borehole stress meter test is limited to the electric type. Monitoring accuracy is not high because the electric sensor is vulnerable to electromagnetic interference. Additionally, test system matching is lacking, and the degree of intelligence and integration is low. Therefore, research on improving the signal conversion mode and the monitoring accuracy of borehole stress meters is insufficient, and further research is needed to improve its intelligence and systematization.

Fiber sensors based on fiber Bragg grating are a new type of all-fiber functional passive sensor (Zhou et al., 2012; Sonnenfeld et al., 2015; Liang et al., 2019), with the advantages of being intrinsically safe, small in size, lightweight, corrosion resistant, electromagnetic-interference resistant, and safe and reliable to use. Meanwhile, transmission and perception are integrated to form a distributed sensor network. It is a promising new sensor technology for coal mines, which can realize the sensor monitoring of temperature, strain, pressure, torque, and other physical quantities. Liang et al. (2022) proposed a three-dimensional stress monitoring method for surrounding rocks based on fiber Bragg grating sensing technology. A cube-shaped three-dimensional stress fiber grating sensor was developed based on the principle of the monitoring method. Wan et al. (2021) developed a fiber Bragg grating stress sensor to measure stress variation between the lower-excavation damaged zone and the upper undisturbed rock. Li (2015) proposed a stress monitoring system for surrounding rocks based on optical fiber sensing technology. Wei et al. (2015) used fiber Bragg grating sensing to monitor the three-dimensional stress state of surrounding rocks and its change law with mining. Additionally, a correlative simulation

experiment was carried out. Zhang et al. (2020) developed a stress-displacement monitoring system with a multi-point of one hole and tested its measuring function.

However, most of these studies contain theoretical analysis, laboratory research, or geotechnical engineering applications; the research results are rarely generalized and applied in underground coal mines. Moreover, there are few studies on fiber Bragg grating borehole stress meters in coal mines (Xu et al., 2017; Liang et al., 2018; Liang and Fang, 2018). Therefore, it is necessary to develop a fiber Bragg grating borehole stress meter suitable for the stress monitoring of the rocks surrounding coal mine roadways.

Based on existing research on borehole stress meters, interactions between rocks surrounding mines and borehole stress meters were analyzed theoretically by constructing a mechanical model of the surrounding rock of the borehole. The structure of the fiber-grating borehole stress meter was optimized, and its performance was tested by fiber sensing technology. Combined with the geological conditions of the coal mine, the abutment pressure of the rock surrounding the roadway was measured onsite using the optimized design of the CS-FBG borehole stress meter. The research results can improve the intelligent mining-stress monitoring of mine roadways and reveal the distribution characteristics and evolution law of the surrounding-rock stress field of roadways, and they can be used to study coal and rock dynamic disasters and roadway-support design.

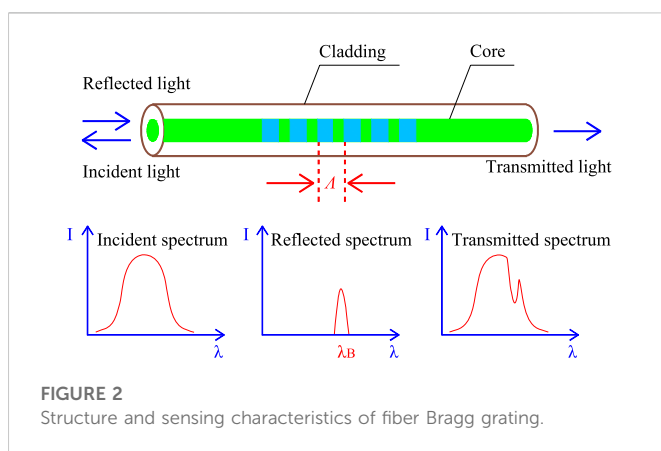
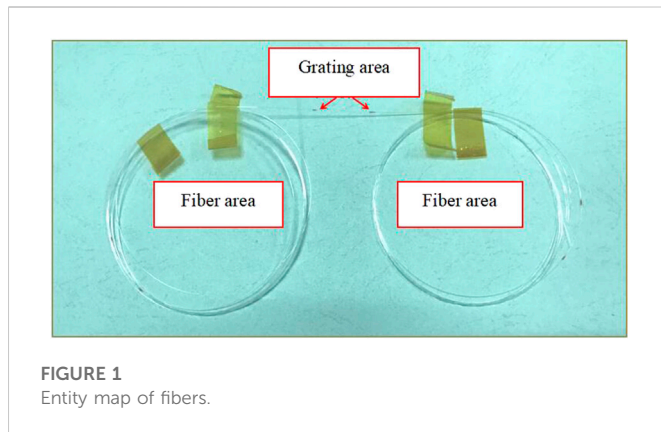
## Basic theory and characteristics of fiber Bragg grating sensing

Fiber (Daichi et al., 2018; Guo et al., 2022; Liang et al., 2022) is primarily composed of a core, cladding, coating (protective layer), reinforced fiber, and protective sheath. Core and cladding are the main parts of the fiber, with a diameter of about 125  $\mu\text{m}$ , and play decisive roles in transmitting light waves. The coating layer, reinforced fiber, and protective sleeve are mainly used to isolate stray light, improve fiber strength, and protect. The basic working principle of optical fibers (Daichi et al., 2018; Guo et al., 2022; Liang et al., 2022) is based on total light reflection. Light propagates in the core. Since the refractive index of the core is greater than that of the cladding, when the numerical aperture meets the total reflection condition, the incident light is not refracted and propagates through core reflection. Therefore, optical fibers can confine electromagnetic wave energy in the form of light in their core by total reflection and guide the light wave along the direction of the fiber axis. Figure 1 shows optical fiber (the part between the small black dots in the figure is the grating region, and the rest is the optical fiber region).

Fiber Bragg grating uses ultraviolet light to change the structure of the fiber core so that the refractive index of the core changes periodically under optical waveguides. A mirror-like device built into the core transmits light waves with a grating effect. Light that meets the grating wavelength condition is reflected, and the rest of the light is transmitted. The basic principle of fiber Bragg grating sensing (Chan et al., 2006; Ho et al., 2013; Yang et al., 2015) is that the change of external parameters shifts the reflected light wavelength, and changing external parameters can be obtained by detecting the shift of the wavelength. Figure 2 shows the structure and sensing characteristics of fiber Bragg grating.

When a light beam is injected into fiber Bragg grating, effective reflection is generated if the Bragg condition is met. The peak





wavelength of reflected light is called the Bragg wavelength, which is as follows in single-mode fibers (Chan et al., 2006; Ho et al., 2013; Yang et al., 2015):

$$\lambda_B = 2n_{eff}\Lambda \quad (1)$$

where  $\lambda_B$  is the reflected central wavelength of the Bragg grating,  $n_{eff}$  is the effective refractive index of the fiber core during fiber propagation, and  $\Lambda$  is the period of the grating.

The reflected central wavelength of the Bragg grating ( $\lambda_B$ ) changes with changed  $n_{eff}$  and  $\Lambda$ . Both parameters, sensitive to changed external stress and temperatures, change the grid distance of the Bragg grating. The central wavelength reflected after entering the grating changes accordingly.

When the fiber Bragg grating is influenced by the external environment (stress, temperature, etc.),  $\Lambda$  and  $n_{eff}$  change. Wavelength variation  $\Delta\lambda_B$  reflected from the grating can be expressed as (Chan et al., 2006; Ho et al., 2013; Yang et al., 2015)

$$\Delta\lambda_B = 2\Delta n_{eff}\Lambda + 2n_{eff}\Delta\Lambda \quad (2)$$

where  $\Delta\lambda_B$  is the wavelength variation reflected from the grating,  $\Delta n_{eff}$  is the refractive index variation of an optical fiber, and  $\Delta\Lambda$  is the grating period variation.

The wavelength of  $\lambda_B$  changes correspondingly with changed  $n_{eff}$  and  $\Lambda$ .  $\Lambda$  and the effective refractive index of the reverse coupled mode are the main factors affecting the reflection and transmission spectra

of the fiber Bragg grating, and any change in the two values changes the wavelength of the Bragg grating.

When fiber Bragg grating is used to monitor stress and strain, stress acting on it changes the grating spacing and the central wavelength ( $\lambda_B$ ) of light it reflects. Meanwhile,  $n_{eff}$  is affected by strain and temperature because of the elastic-optical and thermo-optical effects. The fiber length changes, and thermal expansion affects  $\Lambda$ , under the two effects. Changes in both cause  $\lambda_B$  drift in the Bragg grating.

## Analysis of interaction between the surrounding rocks of the roadway and borehole stress meter

### Establishment of the mechanical model

At present, the borehole stress meter (Kang et al., 2010; Waclawik et al., 2016; Waclawik et al., 2017; Yun et al., 2017) is the most common and mature monitoring instrument for the coal mine roadway. Firstly, a borehole is constructed in the rocks surrounding the roadway. Some rocks surrounding the hole shrink into the hole with unloading. The borehole stress meter, filled with hydraulic oil, is buried in the borehole. Since the stress meter has a certain initial pressure, it can support the surrounding rocks. When surrounding rocks are disturbed, they squeeze into the borehole. The stress meter in the borehole compresses and interacts with the borehole wall. The surrounding rocks squeeze the stress meter inwards, and the stress meter supports the surrounding rocks outwards. Mining stress can be accurately monitored by converting this interaction into signal output. Therefore, the key to the method is to ensure that the borehole stress meter can fully function with the borehole wall of the surrounding rocks.

The surrounding rocks of the roadway are in the original equilibrium state before drilling; the original state is broken after drilling. The borehole wall falls off and deforms, and borehole stress is released and transferred. Surrounding rock stress is redistributed after some time, forming a plastic region in the rocks surrounding the borehole. Radial stress gradually increases with the distance from the borehole center. The surrounding rocks transition from the plastic state to the elastic state in a bidirectional stress state, with improved strength. Figure 3 shows the mechanical model of drilling in surrounding rocks.  $R_0$  is the radius of the drilling hole;  $R_1$  and  $R_2$  are the radii of the plastic and elastic regions, respectively;  $\sigma_0$  is the original stress of the surrounding rocks; and  $p_i$  is the force exerted by the stress meter on the hole wall.

### Analysis of relationships

#### 1) Borehole stress meter taken as the research object

The borehole stress meter is approximated as a thin-walled cylinder, and the mechanical analysis model is established (Figure 4).  $p_i'$  is the force exerted by the borehole wall on the stress meter,  $f$  is the force exerted by the hydraulic oil on the inner wall of stress meter, and  $\sigma_t$  is the stress on the transverse section of the stress meter.

If the influence of the supporting capacity and stress transfer efficiency ( $\zeta$ ) of the stress meter material cannot be ignored (Kang

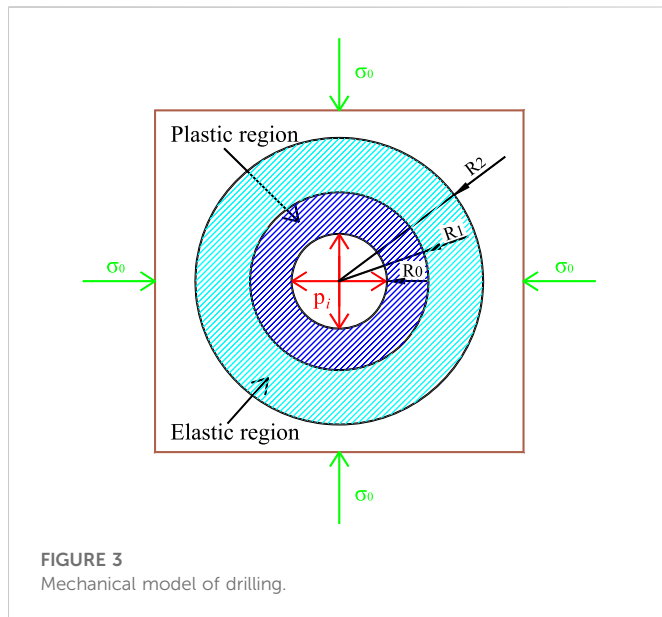


FIGURE 3  
Mechanical model of drilling.

et al., 2010; Waclawik et al., 2016; Waclawik et al., 2017; Yun et al., 2017), then the supporting force  $p_i$  of the stress meter material can be defined as

$$p_i = \zeta f \quad (3)$$

where  $\Delta\lambda_B$  is the force exerted by the stress meter on the hole wall,  $\zeta$  is the stress transfer efficiency, and  $f$  is the force exerted by the hydraulic oil on the inner wall of the stress meter.

The force balance analysis of the radial direction of the stress meter is used to obtain

$$p_i' = p_i + f = (1 + \zeta)f \quad (4)$$

where  $p_i'$  is the force exerted by the borehole wall on the stress meter.

The axial direction of the stress meter is analyzed according to knowledge of material mechanics:

$$\sigma_1 = \frac{2R_0 \times f}{4t} = \frac{R_0 f}{2t} \quad (5)$$

where  $\sigma_1$  is the stress on the transverse section of stress meter,  $R_0$  is the radius of the drilling hole, and  $t$  is the wall thickness of the stress meter.

Assuming that  $t$  is the wall thickness of the stress meter, first strength theory and cylinder-wall-thickness limit theory (Kang et al., 2010; Waclawik et al., 2016; Waclawik et al., 2017; Yun et al., 2017) are used to obtain

$$f = \frac{2t[\sigma]}{t + 2R_0} \quad (6)$$

where  $[\sigma]$  is the ultimate strength in unidirectional stretching.

According to Eq. 4 and Eq. 6, the limit value of force exerted by the hole wall on the stress meter can be denoted as

$$p_i' = \frac{2t[\sigma](1 + \zeta)}{t + 2R_0} \quad (7)$$

## 2) Surrounding rocks taken as research objects

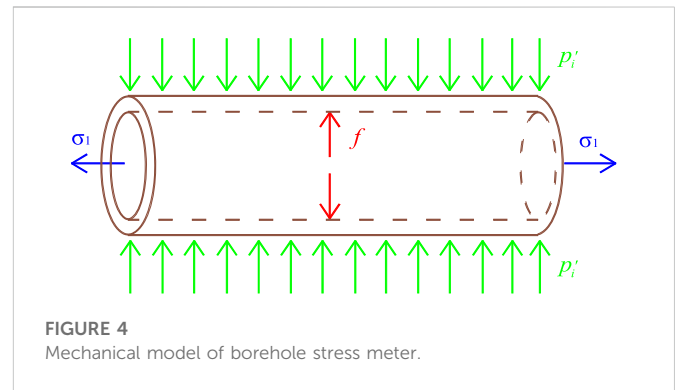


FIGURE 4  
Mechanical model of borehole stress meter.

Surrounding rocks are taken as the objects, and only radial stress is studied. A borehole built into the surrounding rocks forms plastic and elastic regions in turn. According to the principle of calculus (Kang et al., 2010; Waclawik et al., 2016; Waclawik et al., 2017; Yun et al., 2017), the tiny units in each stress zone are taken for force analysis.  $p_i$  is the stress of the meter on the hole wall,  $C_m$  is the cohesion of the coal mass, and  $\phi_m$  is the angle of internal friction.

### ① When the tiny element is located in the plastic region

The mechanical model is established (Figure 5). The force balance analysis of the element is carried out in the radial direction (Kang et al., 2010; Waclawik et al., 2016; Waclawik et al., 2017; Yun et al., 2017) to obtain

$$\sigma_r r d\theta + 2\sigma_\theta \sin\left(\frac{d\theta}{2}\right) dr = (\sigma_r + d\sigma_r)(r + dr)d\theta \quad (8)$$

where  $\sigma_r$  is the stress on the element in the radial direction;  $\sigma_\theta$  is the stress on the element in the circumferential direction, and  $r$  is the tiny unit radius.

Since  $d\theta$  is small and the plastic region meets the strength condition of Mohr's straight line (Kang et al., 2010; Waclawik et al., 2016; Waclawik et al., 2017; Yun et al., 2017),

$$\begin{cases} (\sigma_\theta - \sigma_r)dr = r dr \\ \frac{\sigma_\theta + C_m \cot \phi_m}{\sigma_r + C_m \cot \phi_m} = \frac{1 + \sin \phi_m}{1 - \sin \phi_m} \end{cases} \quad (9)$$

Based on the boundary conditions of the contact surface between the surrounding rocks and the stress meter, it is simplified and deduced that element stress (Kang et al., 2010; Waclawik et al., 2016; Waclawik et al., 2017; Yun et al., 2017) is

$$\sigma_r = (p_i + C_m \cot \phi_m) \left( \frac{r}{R_0} \right)^{\frac{2 \sin \phi_m}{1 - \sin \phi_m}} - C_m \cot \phi_m \quad (10)$$

### ② When the tiny element is located in the elastic region

The mechanical model is established (Figure 6). Surrounding rocks can be approximated as a thick-walled cylinder, and  $\sigma_{R1}$  is the stress at the outer boundary of the plastic region. According to the Lamé formula (Kang et al., 2010; Waclawik et al., 2016; Waclawik et al., 2017; Yun et al., 2017), stress in this region can be expressed as



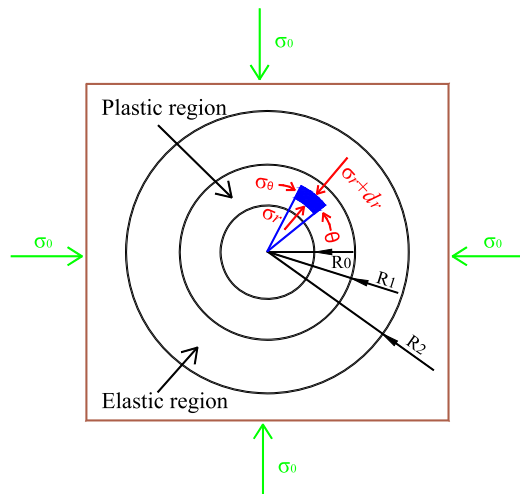


FIGURE 5  
Mechanical model of plastic region.

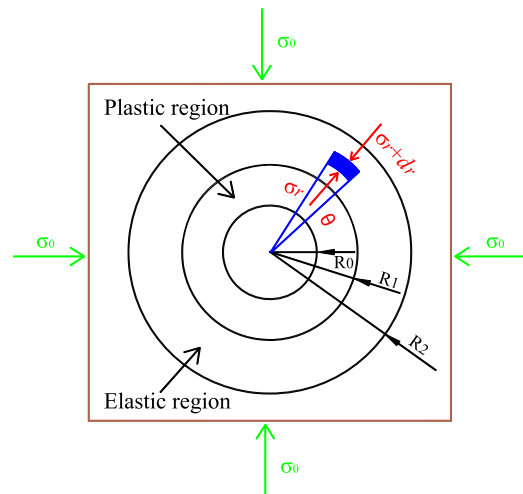


FIGURE 6  
Mechanical model of elastic region.

$$\sigma_r = \frac{\sigma_{R1} R_1^2 - \sigma_0 R_2^2}{R_2^2 - R_1^2} - \frac{(\sigma_{R1} - \sigma_0) R_1^2 R_2^2}{R_2^2 - R_1^2} \cdot \frac{1}{r^2} \quad (11)$$

where  $\sigma_{R1}$  is the stress at the outer boundary of the plastic region, and  $\sigma_0$  is the original stress of surrounding rocks.

## Interaction analysis

Surrounding rocks are in their original stress state before the borehole is constructed. Surrounding rocks in the stress-relief area shrink inward after the borehole is constructed with a certain diameter at a certain point. The borehole stress meter with certain initial stress is placed in the borehole. Surrounding rocks shrink inward and gradually interact with the stress meter with the influence of external excavation–engineering disturbance. It is assumed that the disturbance influence does not produce a collapsing hole, large crack, or large-scale fracture zone. The initial stress of the borehole stress meter is assumed to be equal to the force exerted by the stress meter on the hole wall. Figure 7 shows the interaction between the surrounding rocks of the roadway and the borehole stress meter. The interaction is analyzed as follows:

- ① Figure 7A shows the diagram when initial stress  $p_i$  of the borehole stress meter is less than  $\sigma_0$ . Since the stress on the hole wall is less than the stress before release, the stress meter cannot support the surrounding rocks. Surrounding rocks continue to shrink inward, and stress gradually increases until it is equal to the stress of the surrounding rocks at inner point A. The stress meter starts to work properly. Therefore, increasing the initial stress of the borehole stress meter is a prerequisite for the normal use of the stress meter.
- ② Figure 7B shows the interaction when the initial stress  $p_i$  of the borehole stress meter is equal to  $\sigma_0$ . Since the stress meter exerts the same force on the hole wall before stress release, the surrounding rocks return to their original position B under the support of the stress meter. The stress meter can make the

surrounding rocks no longer shrink, and it starts to work normally. The initial stress value is the optimal value for the normal operation of the stress meter in this case.

- ③ Figure 7C shows the interaction when the initial stress  $p_i$  of the borehole stress meter is greater than  $\sigma_0$ . Surrounding rocks are supported and extended outward due to large initial stress. Stress on the surrounding rocks decreases with the gradual expansion of the stress meter. The stress of the surrounding rocks gradually increases until the stress meter stress is equal to the stress of the surrounding rocks at the external point C due to mining influence. At this time, the stress meter starts to work normally.

The initial stress of the borehole stress meter and the original stress of the surrounding rocks significantly affect the working state of the stress meter. Only when the initial stress of the borehole stress meter is as large as possible and the elasticity of borehole stress meter is good enough can the borehole stress meter work well. Therefore, the monitoring accuracy of the borehole stress meter is improved by increasing the initial stress value and improving the scalability of the borehole stress meter.

## Design of fiber-grating borehole stress meter

### Design principle

The vibrating-string stress meter (Tang et al., 2016; Wang et al., 2019; Yu et al., 2021) is mainly composed of a hollow steel cylinder, steel string, and embedded electromagnetic coil. It is necessary to preload the steel string, put the cylinder into the borehole, and make the cylinder and the surrounding rocks of the borehole fit tightly together. When the cylinder is stressed, the steel strings are extruded and vibrated. According to the vibration frequency, cylinder stress can be measured to obtain borehole stress.

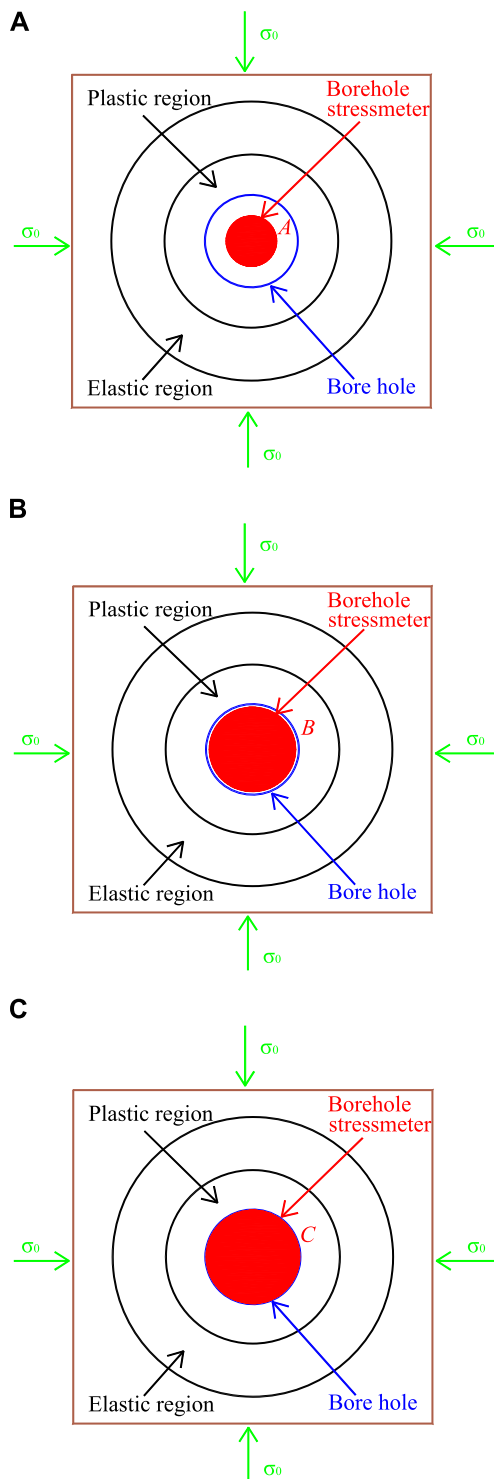


**FIGURE 7**  
Analysis of the interaction between surrounding rocks and borehole stress meter. (A)  $p_i < \sigma_0$ . (B)  $p_i = \sigma_0$ . (C)  $p_i > \sigma_0$ .

The KSE hydraulic borehole stress meter (Hei et al., 2020; Wang et al., 2020) is mainly used to connect the inclusion, guide tubing, pressure-frequency converter, and other parts into a closed oil-circuit system. When the surrounding rocks of the borehole pressure the inclusions, the pressure-frequency converter converts the liquid pressure inside the inclusions into the corresponding electrical

frequency signal, and the corresponding borehole stress variation can be obtained according to frequency variation.

Referring to the design principles of the above two kinds of stress meter, the fiber Bragg grating borehole stress meter designed in this study was mainly composed of a pressure cushion and fiber Bragg grating piezometer. When this kind of stress meter was used, fiber Bragg grating borehole stress was placed in the borehole and certain initial stress was applied. When the surrounding rocks were disturbed, the pressure cushion was squeezed. It sensed the pressure and sent it to the fiber Bragg grating piezometer through hydraulic oil in the pressure cushion. The fiber Bragg grating piezometer converted the pressure change into the wavelength drift.

## Borehole stress meter design and performance test

### 1) Design of the TS-FBG borehole stress meter

The TS-FBG borehole stress meter and the pressure cushion are designed in a thin-wall stainless-steel cylindrical tubular structure. It is made by connecting an external fiber-grating pressure meter and encapsulating it in the outer end. The tubular structure is used as the pressure sensing area and the grating area as the sensing area. Finally, optical fibers are extracted and connected with a fiber Bragg grating demodulator to realize the communication of monitoring signals. Figure 8 shows the designed TS-FBG borehole stress meter.

The TS-FBG borehole stress meter has a standard measuring range of up to 60 MPa, which can work for a long time under the mine without being affected by the electromagnetic signals of the surrounding environment. Table 1 shows the main technical parameters.

A hydraulic servo loading testing machine was used to test the performance of the designed TS-FBG borehole stress meter. The TS-FBG borehole stress meter should be sorted according to wavelength classification, and the circuit should be checked before the experimental test. The TS-FBG borehole stress meter was first placed on the fixture of two semi-arc bearing structures at the beginning of the experimental test, and the whole structure was placed under the pressure valve of the testing machine. Additionally, the bearing structure and TS-FBG borehole stress meter were checked for uniform force. The TS-FBG borehole stress meter was connected to the fiber Bragg grating demodulation system, and we checked whether the instrument works properly. The initial pressure was applied to the TS-FBG borehole stress meter, and relevant data were recorded. The pressure was continued for the performance test after data and equipment were stabilized. Figure 9 shows photos before and after the performance test of the TS-FBG borehole stress meter.

The performance test of the TS-FBG borehole stress meter shows that when the metal tube is filled with hydraulic oil, the pressure induction zone is easily deformed beyond the elastic limit of the thin-walled tube when a certain pressure is applied. Meanwhile, the metal tube is only a thin-walled tube with poor expansion and scalability, which can easily cause oil leakage and result in inaccurate tests or even failure. Furthermore, this design is time-consuming and laborious in oil injection and does not have the function of pressure regulation, which greatly affects the test results and makes the test fail to collect effective experimental data.

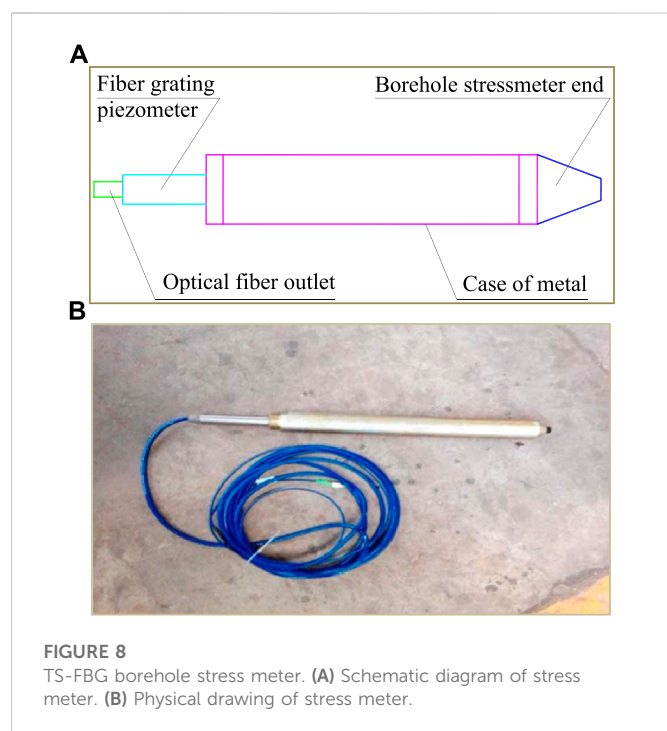


**FIGURE 8**  
TS-FBG borehole stress meter. (A) Schematic diagram of stress meter. (B) Physical drawing of stress meter.

**TABLE 1** Main technical parameters of the TS-FBG borehole stress meter.

Technical specification	Parameter
Standard measuring range	60 MPa
Wavelength range	1,510–1,590 nm
Measuring time	<1 s
Measurement accuracy	<1% F-S
Operating temperature	–10–80 °C
Overall dimensions	Φ35 × 350 mm
Encapsulation modes	Metallic stainless-steel package
Forms of efferent fibers	Single-ended single-core outgoing fiber
Joint types	FC/APC
Level of protection	IP67
Level of safety	Primary safety level

## 2) Design of the CS-FBG borehole stress meter

The second type was further optimized in view of the problems with the first type of TS-FBG borehole stress meter. Its structure is mainly composed of a quadrangular cone end, pressure cushion, sensitization pad, check valve, fiber grating piezometer, and protective sleeve. A pressure cushion was designed into a cystic structure, and four sensitizing pads were installed on its outer surface. The one-way valve was connected to a pressure cushion and fiber Bragg grating piezometer. The fiber Bragg grating piezometer and signal transmission cables were protected by protective sleeves. When used, the capsular pressure cushion and sensitizing pad were used as the pressure sensing area, and the grating area was used as the sensing area. The signal transmission cable is

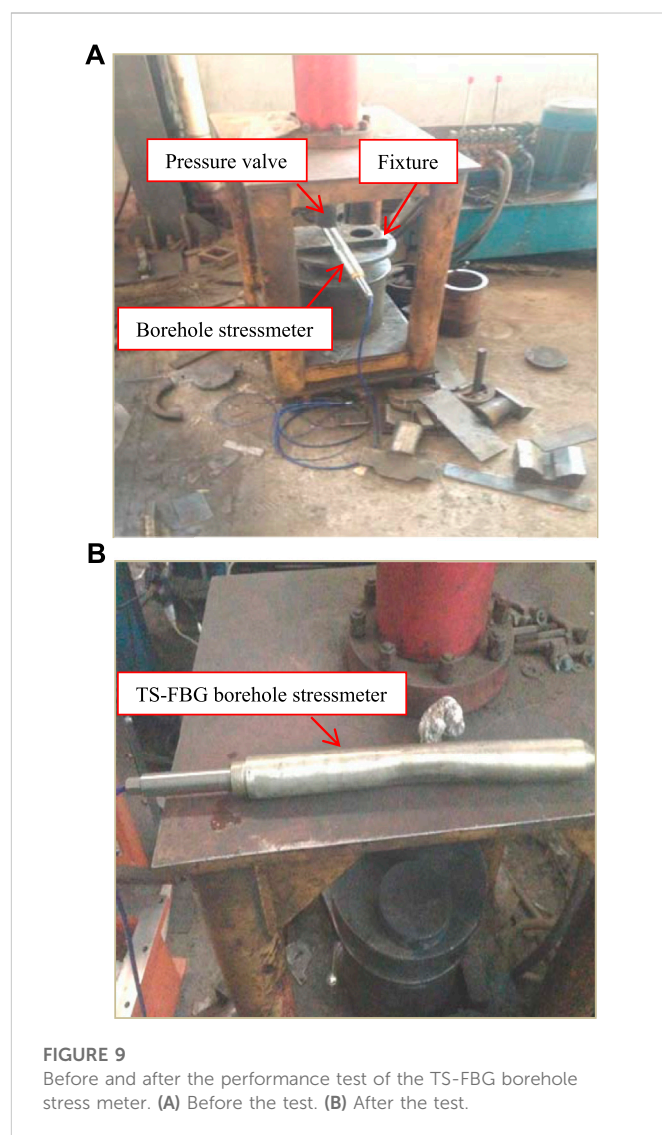


**FIGURE 9**  
Before and after the performance test of the TS-FBG borehole stress meter. (A) Before the test. (B) After the test.

connected to the fiber Bragg grating demodulation instrument to realize the communication of monitoring signals. Figure 10 shows the designed CS-FBG borehole stress meter.

The design of the CS-FBG borehole stress meter has a standard measuring range of up to 60 MPa, which can work for a long time under the mine without being affected by the electromagnetic signals of the surrounding environment. Table 2 shows the main technical parameters.

The original metal tubular pressure cushion was changed into a cystic structure to improve the compression resistance and force sensitivity of the pressure cushion, and four cuboid sensitizing pads were fixed on the outer surface of the pressure cushion. The sensitizing pad has a length of 130 mm, a width of 20 mm, and a thickness of 4 mm. There is a small gap between the sensitizing pad and the pressure cushion. The front and rear ends of the sensitizing pad were designed with a similar quadrangular cone structure, which formed four branches. Four branches met at one point and were fixed to each other.

This design increased the stability of the stress meter and the pressure sensitivity and flexibility of the pressure cushion. The design has the following advantages: it changes the contact mode of the whole

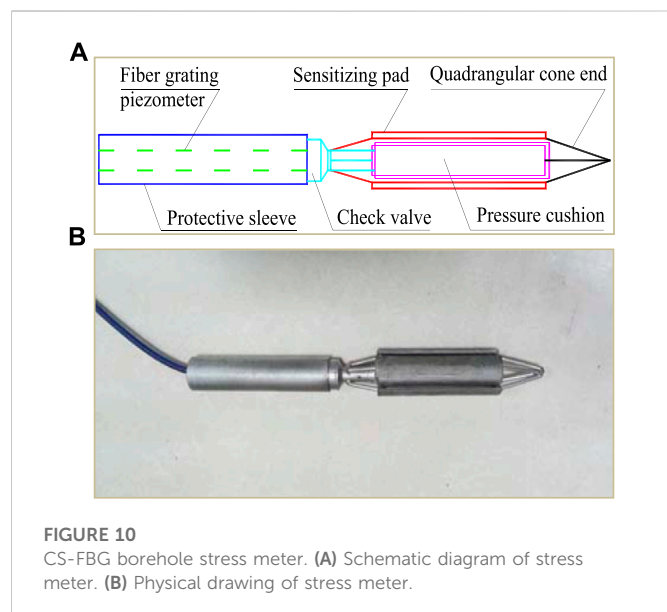


**FIGURE 10**  
CS-FBG borehole stress meter. (A) Schematic diagram of stress meter. (B) Physical drawing of stress meter.

**TABLE 2** Main technical parameters of the CS-FBG borehole stress meter.

Technical specifications	Parameter
Resolution	6 KPa
Standard measuring range	60 MPa
Wavelength range	1,520–1,580 nm
Measurement accuracy	0.01 MPa
Level of protection	IP 67
Level of safety	Primary safety level
Lead wire of the sensor head	FC/APC Armored cable
Installation mode	Drilling installation
Canning material	Stainless steel
Reflectance	>90%
Operating temperature	–20–80°C

plane between the tubular structure and surrounding rocks into a local contact mode, improves the bearing capacity of the pressure cushion under the same pressure, and prolongs the service time of the stress meter. Figure 11 shows the design of the pressure cushion quadrangle end and sensitizing pad.

A hollow check valve was installed between the pressure cushion and fiber grating piezometer to keep the oil pressure in the pressure cushion stable and make the oil injection convenient. The check valve has a thread design to facilitate the assembly and connection of the fiber grating piezometer and protective sleeves. Its outer diameter is 28 mm, with an inner diameter of 18 mm, and a wall thickness of 5 mm; an oil hole with a diameter of 6 mm exists at its bottom. Figure 12 shows the check valve.

The performance of the CS-FBG borehole stress meter was tested by an MTS automatic servo-pressure testing machine. The testing machine can realize automatic data storage and recording and has a multifunctional display function. An experimental test

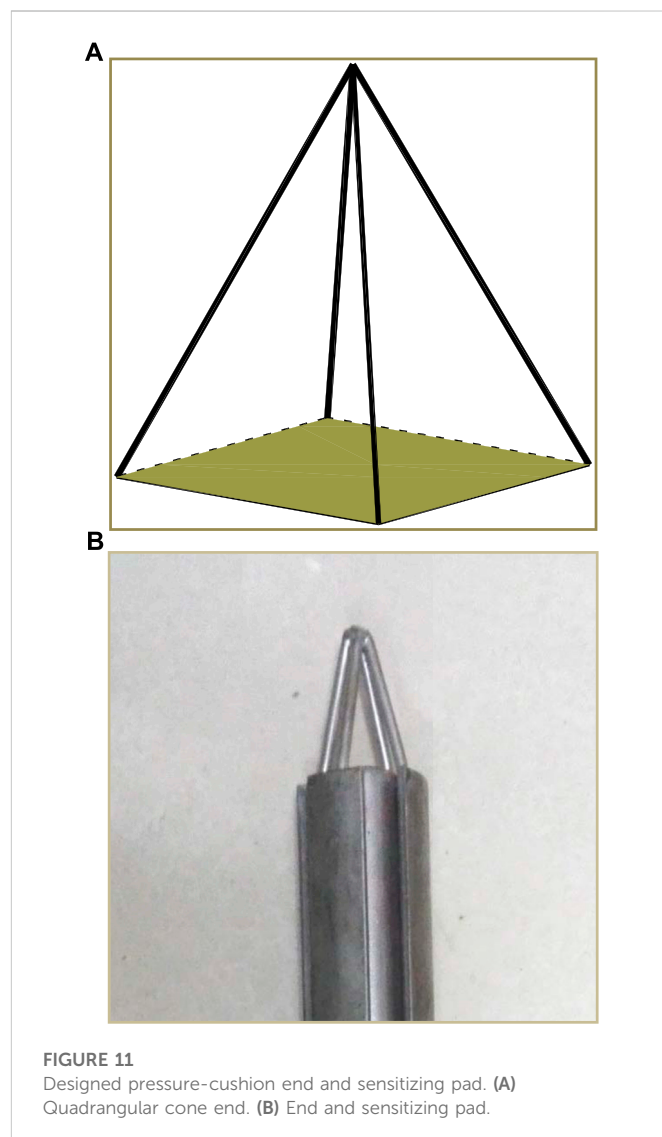


**FIGURE 11**  
Designed pressure-cushion end and sensitizing pad. (A) Quadrangular cone end. (B) End and sensitizing pad.

mold of the confining pressure was designed to keep the pressure cushion under uniform force and to restore the surrounding rock stress environment when the borehole stress meter was used in the field (Figure 13). The mold was divided into fixed and pressing molds. The fixed mold was a rectangular container with a U-shaped groove inside, and the pressing mold was a semi-cylindrical pressing plate. The cuboid of the fixed mold part was 800 mm long, 200 mm wide, and 100 mm high. The radius of the U-shaped groove was 70 mm and that of the pressing mold was 25 mm.

Micron Optic Company's classic Sm125 Fiber Bragg grating static demodulation instrument was used for the stress meter performance experiment (Sun et al., 2019; Tian et al., 2019; Wu et al., 2019). It has a wavelength resolution of 1 p.m. and a wavelength scanning range of 1,510–1,590 nm. The software system is integrated with MOI-ENLIGHT, and the client program interacts with the Windows system. Figure 14 shows a fiber Bragg grating static demodulator.

The experimental methods and operating procedures of the stress meter performance test are as follows:





**FIGURE 12**  
Check valve.

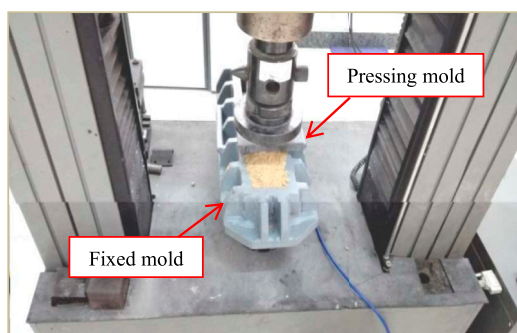


**FIGURE 13**  
Performance-test equipment of borehole stress meter.

- ① The fiber Bragg grating borehole stress meter was connected to the demodulator before the experiment. The initial stress meter pressure was small in order to test the tightness of stress meter and check for oil leakage.
- ② Sand, crushed coal, and rock blocks were laid in turn in the cuboid fixed mold and mixed with water in a certain proportion. The borehole stress meter was buried in it and placed for 24 h after compacting and filling.
- ③ The prepared model was put on the pressure plate of the pressure test machine. The pigtail of the borehole stress meter was drawn out of the model, and the semi-cylindrical pressure plate on the model of borehole stress meter was put right above the model. We ensured that the stress of the stress meter was uniform and that it played a certain protective role during the pressure.
- ④ The pressure test machine was debugged and checked for normal functioning, and users became familiar with the use of the test machine and related settings.
- ⑤ A cotton sheet glued with alcohol was used to wipe the pigtail joint of the borehole stress meter and the optical jack of the demodulator. The tail fiber of the borehole stress meter was connected to one of the channels of the demodulator after drying, and the network interface of the computer was connected to the network interface of the demodulator through the network cable. The demodulation device was started and parameters such as IP communication protocol and collection frequency were set. Then data collection was performed.



**FIGURE 14**  
Fiber Bragg grating static demodulator.

- ⑥ The height of the pressing plate was lowered to contact the mold at the beginning of the experiment, then changed to a small range pressure mode to reduce the falling speed of the pressing plate. When the pressure data of the servo system fluctuated significantly, the equal gradient pressure mode was used to increase the load by 20 KN each time until the load reached 300 KN. Demodulator software automatically recorded the monitoring data of the whole loading process.
- ⑦ Unloading was done with the same gradient until the pressure exerted by the experimental machine on the mold was zero after loading. The large-range pressure mode was used to rapidly raise the pressing plate. The remaining model was replaced and the same loading and unloading test carried out.
- ⑧ The monitoring data were sorted, and the borehole stress meter and experimental machine were checked. The site was cleaned up and the experimental test completed.

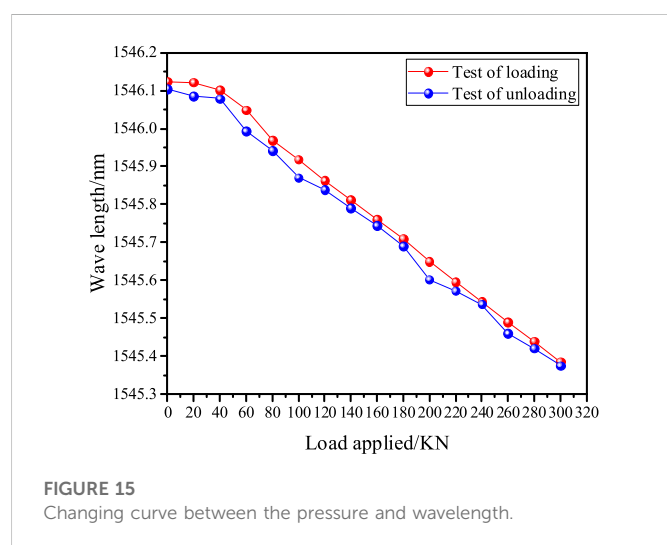
Three groups of loading and unloading experiments were carried out, and one group of experimental test data was selected for analysis (Table 3). Figure 15 shows the pressure- and wavelength-changing curve applied by the experimental machine.

The surrounding rock pressure subjected to the fiber grating borehole stress meter increases simultaneously with increasing pressure exerted by the experimental machine in the test (Figure 15). Also, the grating wavelength changes constantly. The wavelength decreases continuously during the loading process and increases continuously during the unloading process.

The changing curve of the pressure and wavelength applied by the experimental machine can be divided into two stages. 1) In the pressure-boost stage, the borehole stress meter is gradually compacted and fitted closely with sand in the mold, with a small slope of the curve and the slow change. The pressure on the mold is small at the early stage of pressurization. The initial stress of the borehole stress meter is not enough and the expansion is insufficient, failing to interact with the sands and stones in the mold. 2) The borehole stress meter and sand in the mold are compacted and fitted closely at the pressure-stabilizing stage. The borehole stress meter bears the pressure, and the slope of the curve is large. Then, the grating wavelength and the applied pressure present a linear change. The borehole stress meter interacts with the sand in the mold, and the test is reliable.

**TABLE 3** Experimental data for the performance test of the CS-FBG borehole stress meter.

Number of test	Loading pressure/KN	Wave length/nm	wavelength variation	Unloading pressure/KN	Wave length/nm	Wavelength variation
1	0	1546.1242	-	300	1545.375	-
2	20	1546.1215	0.00272	280	1545.4202	0.0452
3	40	1546.1022	0.01923	260	1545.4591	0.0389
4	60	1546.049	0.05323	240	1545.5368	0.0777
5	80	1545.9693	0.07974	220	1545.5718	0.035
6	100	1545.9183	0.051	200	1545.6018	0.03
7	120	1545.8625	0.05576	180	1545.6893	0.0875
8	140	1545.8125	0.05002	160	1545.7439	0.0546
9	160	1545.7606	0.05185	140	1545.7908	0.0469
10	180	1545.7098	0.05082	120	1545.8389	0.0481
11	200	1545.6498	0.05998	100	1545.8705	0.0316
12	220	1545.5955	0.05436	80	1545.942	0.0715
13	240	1545.5437	0.05179	60	1545.9924	0.0504
14	260	1545.4903	0.05341	40	1546.0787	0.0863
15	280	1545.439	0.05132	20	1546.0859	0.0072
16	300	1545.3852	0.05377	0	1546.105	0.0191

**FIGURE 15**  
Changing curve between the pressure and wavelength.

In summary, the second kind of CS-FBG borehole stress meter can meet the requirements of field use. A good linear relationship exists between the grating wavelength and applied pressure during the loading and unloading test. The wavelength varies with the pressure applied, and the value of the wavelength at unloading is slightly smaller than at loading. The wavelength changes unevenly during the loading and unloading process of each stage, and the change value is about .05 nm, indicating the high sensitivity of the CS-FBG borehole stress meter. However, the pressure cushion of the borehole stress meter is seriously deformed after the test (Figure 16), and it is difficult to reuse. Structural scalability must still be optimized and improved. When the borehole stress

meter is optimized, its scalability and initial pressure should be studied in the next step.

## Rig-site utilization and effect analysis

### Mine overview

The Shaqu Coal Mine of Huajin Coking Coal Co., Ltd. is located in Liulin County, Luliang City, Shanxi Province, China. The mine strike length is 22 km, the inclined direction is 4.5–8 km wide, and the area is 138.35 km<sup>2</sup>. The whole minefield is a gently inclined monoclinic structure with small local folds and faults. The structure of the minefield belongs to a simple type. The mining area is rich in high-quality coking coal, and the dip angle is gentle, generally 3°–7°. It is identified as a high gas mine with an absolute gas emission rate of 422.28 m<sup>3</sup>/min and a relative gas emission rate of 81.84 m<sup>3</sup>/t. Shaqu Mine is the second-highest gas mine in China.

The traditional electromagnetic sensor has certain dangers in the underground arrangement. Observation data have large errors and serious lag when manually observing and recording the stress variation of the surrounding rocks of the roadway. A real-time monitoring system of roadway-surrounding rock stress based on fiber Bragg grating sensor technology was installed in the 14,301-track roadway to promote the new technology and the timeliness of monitoring.

The 14,301 working face was the first mining face in the South mining area 3#, inclined to a longwall mining layout. The south was the unexcavated 14,302 working face; north and east were the village-protection coal pillars; west to the south was the main entry





**FIGURE 16**  
Deformation of borehole stress meter after the test.

of mining area 3#. The average thickness of coal seam 4# was 2.45 m, with an average dip angle of  $6^\circ$  and an average burial depth of 400 m. The inclined length of the 14,301 working face was 220 m, and the strike mining length was 1,145 m. The 14,301 working face adopted a Y-shaped ventilation mode. The length of the track roadway is 1,260 m, and the length of the belt roadway is 1,300 m. The two layers of coal were mined together due to the small spacing between coal seams 3 and 4# in the front part of the working face. However, the spacing between the coal seams 3 and 4# is larger in the back part of the working face, so the two coal layers must be mined separately. A second setup entry was dug at 805 m of the belt roadway and 769 m of the track roadway, and the track roadway was retained by gob entry technology as the roadway of the next working face. Figure 17 shows the layout of the 14,301 working face.

## Layout design of borehole stress meter

Two monitoring stations were arranged in the 14,301-track roadway, combined with the requirements of the mining stress monitoring of surrounding rocks of the roadway to test the rig-site utilization of the CS-FBG borehole stress meter. Stations 1 and 2# were arranged about 910 m and 660 m away from the open cut of the 14,301 working face respectively (Figure 17). Six measuring points were arranged in each monitoring station, and three measuring points were arranged on the upper side of the roadway and the lower side of the coal pillar (Figure 18A). A

drilling rig was used to cut holes at a height of 1.5 m from the roadway floor to simultaneously monitor the distribution and change of mining stress at different depths of surrounding rocks on two sides of the track roadway (Figure 18B). Additionally, drill holes with depths of 1, 3, and 5 m were constructed, and the spacing between adjacent holes was 2 m. The CS-FBG borehole stress meter was installed in each borehole (Figures 18C, D), and 12 were installed in two measuring stations.

The field installation process and steps of the CS-FBG borehole stress meter are as follows:

- ① Holes were drilled with depths of 1, 3, and 5 m along the floor at a height of 1.5 m in the two measuring stations of the track roadway, according to the requirements of the measuring point layout. The spacing between adjacent holes is 2 m.
- ② The borehole diameter should be about 10 mm larger than the borehole stress meter to prevent the borehole stress meter from becoming stuck in the borehole during installation and make it quickly contact with surrounding rocks.
- ③ The drilling hole should be cleaned after drilling. First, the hole bottom was cleared and then the surrounding rocks of the drilling hole were cleaned. A wooden pole was used to wrap a towel layer. Desiccants were applied to dry the drill holes, and a clean towel was replaced each time.
- ④ An anchorage agent was placed in the borehole after the borehole was cleaned to make full contact between the borehole stress meter and the surrounding rocks. Then the CS-FBG borehole stress meter was slowly pushed into the borehole with a push rod. The push rod should not be rotated during pushing into the borehole stress meter to prevent the optical fiber pigtail at the tail of borehole stress meter from being torn off during rotation.
- ⑤ Cement mortars were pushed into borehole, and grouting was stopped when mortars were filled and flowed out of the orifice. The borehole stress meter was cemented into surrounding rocks by mortars.
- ⑥ The CS-FBG borehole stress meter was drawn out to the drilling hole, and the splitter and adapter were connected in order. Then the main optical cable was connected to the base station by the flange. Figure 18 shows the field installation of the borehole stress meter.

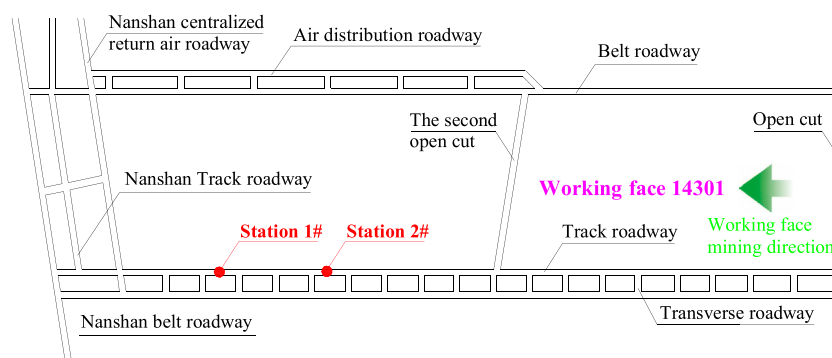


**FIGURE 17**  
Layout of the 14,301 working face.

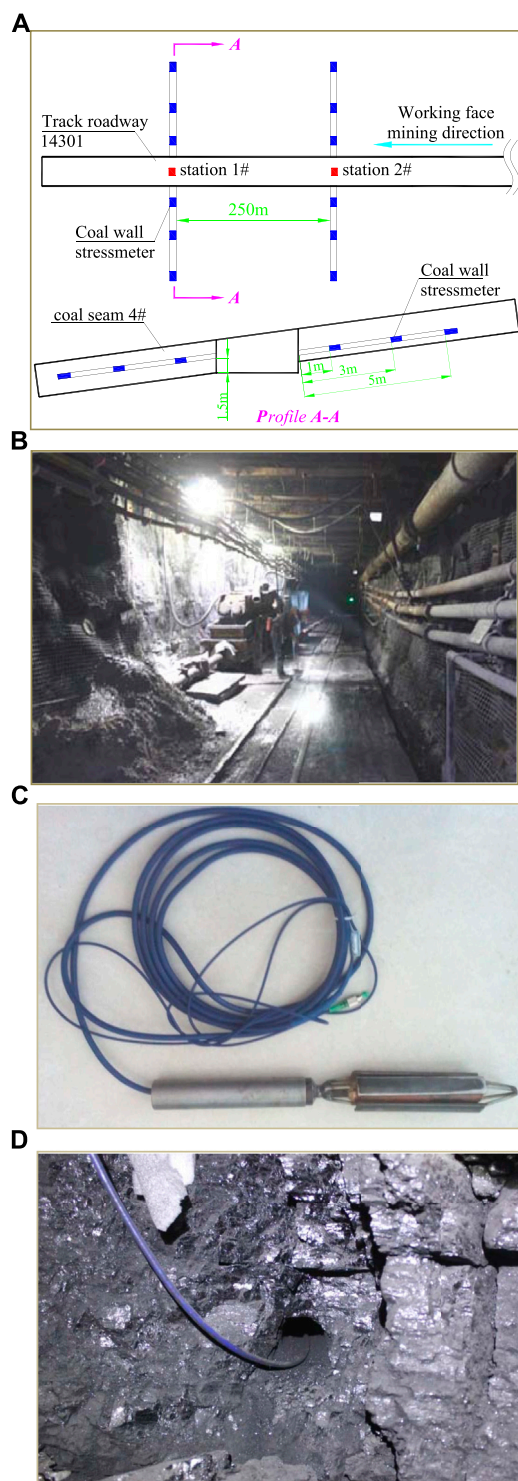


**FIGURE 18**  
Field installation and layout of the CS-FBG borehole stress meter. (A) Layout design of borehole stress meter. (B) Site construction drawing of borehole. (C) CS-FBG borehole stress meter. (D) Field installation of roadway sides.

## Rig-site utilization effect analysis

The mining-stress monitoring system of the surrounding rocks of the fiber Bragg grating roadway can monitor the abutment pressure at different depths in real time after the installation and debugging of the

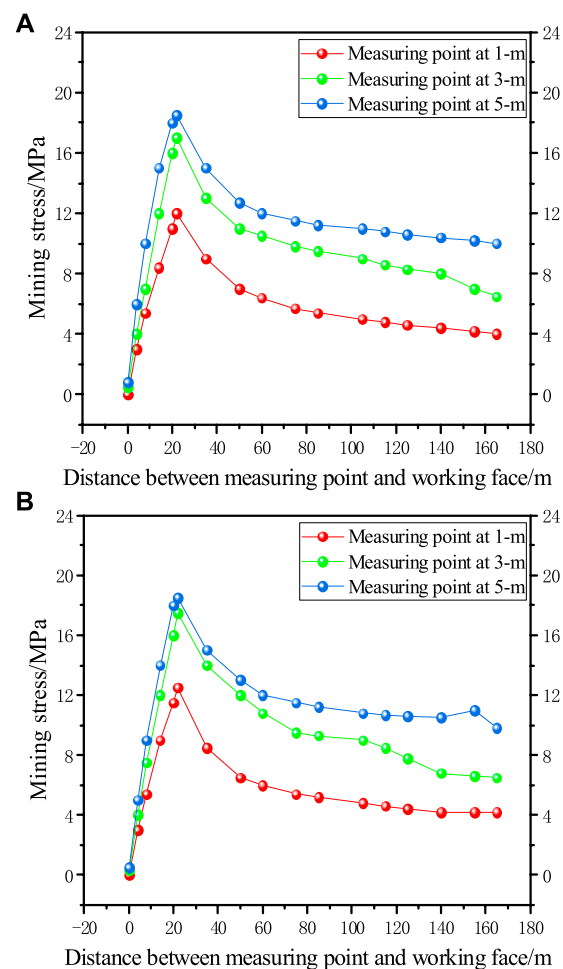
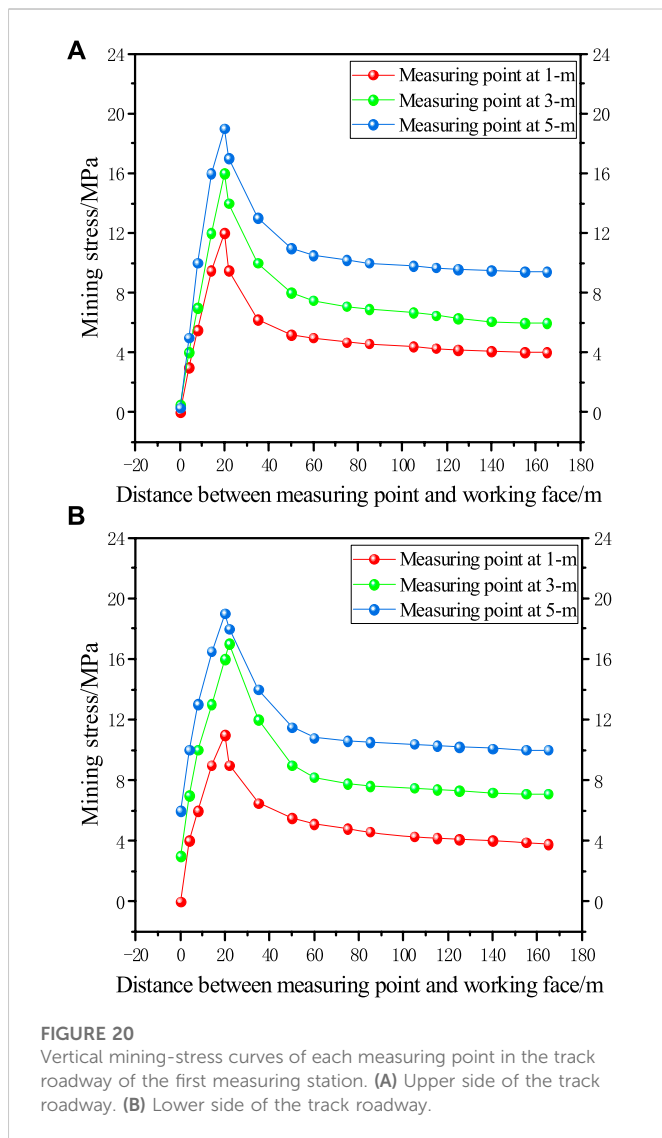


**FIGURE 19**  
Vertical mining stress curves of each measuring point in the track roadway of the second measuring station. (A) Upper side of the track roadway. (B) Lower side of the track roadway.

14,301-track roadway. The mining-stress variation curves of the surrounding rocks of the 14,301-track roadway at different depths are obtained through the collection and analysis of the monitoring data of the two stations (Figures 19A,B).

The mining-stress distribution curves of the two sides of the 14,301-track roadway have the same change law during mining of the 14,301 working face (Figure 19). It shows four stages: rapid rise, uniform growth, rapid rise to the peak, and rapid decline. When the measuring point is 50 m away from the working face, the increase in stress is small. When the distance from the working face is within 50 m, stress starts to increase rapidly. When the distance from the working face is about 20 m, stress reaches its peak. As the distance from the working face decreases further, stress drops sharply until the measuring point fails. Stress increases overall with the increased depth of the measurement point, but the increased amplitude is not uniform.

Figure 19A shows obvious stress growth areas and stress concentration areas in the stopping process. When the measuring point enters the range of 140 m, the stress of the measuring point with 3-m depth jumps up first, indicating that the surrounding rock enters the zone affected by mining stress. Subsequently, stress increases uniformly at different depth-measurement points. When the measuring point enters the working face within 40 m, the stress of



the measuring point with 1-m depth rises rapidly, indicating that surrounding rocks enter the advanced stress concentration area of the working face. When the measuring point is at about 20 m, the stress reaches a peak of 18.5 MPa and then drops rapidly until the working face advances past the measuring point, which fails the measuring point. The stress of measuring points at different depth is compared. Vertical stress increases with the increased depth of surrounding rocks, and peak stress at the measuring point at 5 m is the largest because surrounding rocks at different depths are disturbed by mining to different degrees.

The stress growth and stress concentration zones are also obvious in the process of mining the working face (Figure 19B). When measuring points are within 145 m of the working face, measuring points at 3 and 5 m first enter the mining-stress-affected zone. When the measuring point enters the working face within 50 m, the stress of each measuring point increases rapidly and enters the rapid growth area. When the measuring point enters the working face within 18 m, the stress of each measuring point reaches a peak. The disturbance influence of the measuring point with 1-m depth is not significant when comparing the stress of each measuring point without planting depth, and the increased amplitude is relatively gentle in the process of mining the working face.

The measuring points of the first measuring station are similar to those of the second measuring station during the mining of the 14,301 working face (Figure 20). The mining stress curves of the measuring points at different depths also show the stages of rapid rise, uniform growth, rapid rise to peak, and rapid decline. Additionally, the stress of each measuring point presents increases with the increased depth of the measuring point, but the increasing amplitude is not uniform.

Obvious stress growth and stress peak zones exist during the stopping of the 14,301 working face (Figure 20A). When the measuring point is 100 m away from the working face, the stress of different depth measuring points does not change. When the measuring point enters the working face within 90 m, the stress of each measuring point grows slowly, and surrounding rocks enter the stress-affected zone. When the measuring point is within 50 m of the working face, the stress of the measuring points at 3 and 5 m shows a leaping rise, while that at 1 m rises rapidly when it is 35 m away from the working face. When the measuring point is within 20 m from the working face, peak stress reaches 19 MPa. The stress value of the measuring point with 5-m depth is always greater than that with 1- and 3-m depth in the mining process.

The stress growth and stress peak zones are still obvious during the mining of the 14,301 working face, and the stress distribution pattern is similar to that of the upper coal body (Figure 20B). The stress influence range is about 80 m in front of the working face, the stress rapid growth area is about 50 m in front of the working face, and the stress peak is at about 18 m in front of the working face.

## Conclusion

- 1) The mechanical model of the rocks surrounding the borehole was built through theoretical analysis, and the interaction between surrounding rocks and the borehole stress meter was analyzed. The results showed that increasing the initial stress and elasticity of the borehole stress meter improved its monitoring accuracy.
- 2) Two kinds of fiber Bragg grating borehole stress meters, with tubular structure and cystic structure, were designed by combining the sensing principle and sensing characteristics of fiber Bragg grating, and their performance was tested by experiments. The precision of stress monitoring is affected by insufficient initial stress and scalability of the borehole stress meter. The CS-FBG borehole stress meter was more suitable for the stress monitoring requirements of the surrounding rocks of the coal mine roadway, compared with the TS-FBG borehole stress meter.
- 3) The rig-site utilization results showed that the mining stress variation curves of each measuring point on the two sides of the track roadway have obvious stress growth zones and stress peak zones in the process of mining the test working face. There were four stages: rapid rise, uniform growth, rapid rise to peak, and rapid decline. Maximum stress monitored by the second station was 18.5 MPa, and the influence range of stress was over 140 m. Maximum stress monitored by the first measuring station was 19 MPa, the influence range of stress was about 80 m, and the peak stress position was about 20 m in front of the coal wall. Field application proved the design of the CS-FBG borehole stress meter to be reasonable: the performance is stable and reliable, and the

successful operation of field monitoring has achieved the expected effect of field monitoring.

## Data availability statement

The original contributions presented in the study are included in the article/Supplementary Material, further inquiries can be directed to the corresponding author.

## Author contributions

XXe wrote the original draft of the manuscript. XF and HL contributed to the conception and design of the study. XXn and ML organized the database. GW and NC performed the statistical analysis. All authors contributed to manuscript revision and read and approved the submitted version.

## Funding

This work was supported by the Liupanshui Normal University fund (LPSSYYBZK202202, LPSSYjg-2021-34), the Science and

Technology Department of Guizhou Province Fund (Qiankehe Platform Talent-YSZ [2021] 001), the Education Department of Guizhou Province Fund (Qianjiaohe KY Zi [2020] 050, Qianjiaohe [2020] 122, Qianjiao XKTJ [2020] 23, Qianjiaohexietongchuangxinzi [2016] 02), and the Liupanshui Science and Technology Bureau Fund (52020-2022-PT-15).

## Conflict of interest

The authors declare that the research was conducted in the absence of any commercial or financial relationships that could be construed as a potential conflict of interest.

## Publisher's note

All claims expressed in this article are solely those of the authors and do not necessarily represent those of their affiliated organizations, or those of the publisher, the editors and the reviewers. Any product that may be evaluated in this article, or claim that may be made by its manufacturer, is not guaranteed or endorsed by the publisher.

## References

- Chai, J., Ouyang, Y., Liu, J., Zhang, D., Du, W., and Lei, W. (2021). Experimental study on a new method to forecasting goaf pressure based key strata deformation detected using optic fiber sensors. *Opt. Fiber Technol.* 67, 102706. doi:10.1016/j.yofte.2021.102706
- Chan, T. H. T., Yu, L., Tam, H. Y., Ni, Y. Q., Liu, S. Y., Chung, W. H., et al. (2006). Fiber Bragg grating sensors for structural health monitoring of Tsing Ma bridge: Background and experimental observation. *Eng. Struct.* 28 (5), 648–659. doi:10.1016/j.engstruct.2005.09.018
- Daichi, W., Hirotsuka, I., Masato, T., Kasai, T., Arizono, H., Murayama, H., et al. (2018). Flight demonstration of aircraft fuselage and bulkhead monitoring using optical fiber distributed sensing system. *Smart Mat. Struct.* 27 (2), 025014. doi:10.1088/1361-665X/aa588
- Guo, G. H., Zhang, D. D., Duan, Y. Y., Zhang, G. H., and Chai, J. (2022). Strain-sensing mechanism and axial stress response characterization of bolt based on fiber Bragg grating sensing. *Energies* 17 (15), 15176384. doi:10.3390/en15176384
- Hao, Z., Sun, G., Zhang, G., Sun, G. Z., and Zhang, G. H. (2022). Mechanism and inducing factors of rockburst events of roadways under ultrathick strata. *Front. Earth Sci.* 10, 860929. doi:10.3389/feart.2022.860929
- Hei, C., Luo, M. Z., Gong, P. P., and Song, G. B. (2020). Quantitative evaluation of bolt connection using a single piezoceramic transducer and ultrasonic coda wave energy with the consideration of the piezoceramic aging effect. *Smart Mat. Struct.* 29 (2), 027001. doi:10.1088/1361-665X/ab6076
- Ho, M. P., Lau, K. T., Au, H. Y., Dong, Y., and Tam, H. Y. (2013). Structural health monitoring of an asymmetrical SMA reinforced composite using embedded FBG sensors. *Smart Mat. Struct.* 22 (12), 125015. doi:10.1088/0964-1726/22/12/125015
- Kang, H., Zhang, X., Si, L., Wu, Y., and Gao, F. (2010). In-situ stress measurements and stress distribution characteristics in underground coal mines in China. *Eng. Geol.* 116 (3–4), 333–345. doi:10.1016/j.enggeo.2010.09.015
- Li, H. W., Fang, X. Q., Liang, M. F., and Xue, G. Z. (2015). Research on monitoring technology of surrounding rock stress based on fiber grating. *Ind. Min. Auto.* 41 (11), 17–20. doi:10.13272/j.issn.1671-251x.2015.11.005
- Liang, M., and Fang, X. (2018). Application of fiber Bragg grating sensing technology for bolt force status monitoring in roadways. *Appl. Sci.* 8 (1), 8010107. doi:10.3390/app8010107
- Liang, M., Fang, X., Li, S., Wu, G., Ma, M., and Zhang, Y. (2019). A fiber Bragg grating tilt sensor for posture monitoring of hydraulic supports in coal mine working face. *Measurement* 138, 305–313. doi:10.1016/j.measurement.2019.02.060
- Liang, M., Fang, X., and Ning, Y. (2018). Temperature compensation fiber Bragg grating pressure sensor based on plane diaphragm. *Photonic Sens.* 8 (2), 157–167. doi:10.1007/s13320-018-0417-9
- Liang, M., Fang, X., Song, Y., Li, S., Chen, N., and Zhang, F. (2022). Research on three-dimensional stress monitoring method of surrounding rock based on FBG sensing technology. *Sensors* 22 (7), 22072624. doi:10.3390/s22072624
- Liang, M. F., Song, Y., Fang, X. Q., Jiang, Y. Y., Zhang, F., Li, S., et al. (2022). Structural design and application of desensitized FBG force-measuring bolt. *Sensors* 22 (10), 3930. doi:10.3390/s22103930
- Liu, S. M., and Li, X. L. (2022). Experimental study on the effect of cold soaking with liquid nitrogen on the coal chemical and microstructural characteristics. *Environ. Sci. Pollut. Res.* 2022 (12), 1–18. doi:10.1007/s11356-022-24821-9
- Liu, X. W., Chen, J. X., Liu, B., Luo, Y., Zhu, Y. G., and Huang, X. (2022). Large deformation disaster mechanism and control technique for deep roadway in faulted zone. *Front. Earth Sci.* 10, 826661. doi:10.3389/feart.2022.826661
- Ma, G., Mao, N., Li, Y., Jiang, J., Zhou, H., and Li, C. (2016). The reusable load cell with protection applied for online monitoring of overhead transmission lines based on fiber Bragg grating. *Sensors* 16 (6), 16060922. doi:10.3390/s16060922
- Ray, P., Srinivasan, B., Balasubramaniam, K., and Rajagopal, P. (2018). Monitoring pipe wall integrity using fiber Bragg grating-based sensing of low-frequency guided ultrasonic waves. *Ultrasonics* 90, 120–124. doi:10.1016/j.ultras.2018.06.009
- Sonnenfeld, C., Luyckx, G., Sulejmani, S., Geernaert, T., Eve, S., Gomina, M., et al. (2015). Microstructured optical fiber Bragg grating as an internal three-dimensional strain sensor for composite laminates. *Smart Mat. Struct.* 24 (5), 055003. doi:10.1088/0964-1726/24/5/055003
- Sun, X., Guo, C., Yuan, L., Kong, Q., and Ni, Y. (2022). Diffuse ultrasonic wave-based damage detection of railway tracks using PZT/FBG hybrid sensing system. *Sensors* 22 (7), 22072504. doi:10.3390/s22072504
- Sun, X. T., Li, D., He, W. Y., Wang, Z. C., and Ren, W. X. (2019). Grouting quality evaluation in post-tensioning tendon ducts using wavelet packet transform and bayes classifier. *Sensors* 19 (24), 19245372. doi:10.3390/s19245372
- Tang, J., Jiang, C., Chen, Y., Li, X., Wang, G., and Yang, D. (2016). Line prediction technology for forecasting coal and gas outbursts during coal roadway tunneling. *J. Nat. Gas. Sci. Eng.* 34, 412–418. doi:10.1016/j.jngse.2016.07.010
- Tao, Z., Zheng, X., Zhu, C., Zhang, H., and Zhang, X. (2019). Framework and application of a big data monitoring system for mining with a pillar-free self-forming roadway. *Appl. Sci.* 9 (10), 9102111. doi:10.3390/app9102111
- Tian, Z. H., Yu, L. Y., Sun, X. Y., and Lin, B. (2019). Damage localization with fiber Bragg grating lamb wave sensing through adaptive phased array imaging. *Struct. Health Monit.* 18 (1), 334–344. doi:10.1177/1475921718755572
- Torres, B., Payá-Zaforteza, I., Calderón, P. A., and Adam, J. M. (2011). Analysis of the strain transfer in a new FBG sensor for structural health monitoring. *Eng. Struct.* 33 (2), 539–548. doi:10.1016/j.engstruct.2010.11.012
- Waclawik, P., Kukutsch, R., Konicek, P., Ptacek, J., Kajzar, V., Nemcik, J., et al. (2017). Stress state monitoring in the surroundings of the roadway ahead of longwall mining. *Procedia Eng.* 191, 560–567. doi:10.1016/j.proeng.2017.05.218



- Waclawik, P., Ptacek, J., Konicek, P., Kukutsch, R., and Nemcik, J. (2016). Stress-State monitoring of coal pillars during room and pillar extraction. *J. Sustain. Min.* 15, 49–56. doi:10.46873/2300-3960.1207
- Wan, X., Li, C., Zhao, Z., Zhang, D., Li, Y., and Zhang, J. (2021). Measurements of excavation damaged zone by using fiber Bragg grating stress sensors. *Sensors* 21 (15), 21155008. doi:10.3390/s21155008
- Wang, K., Cao, W., Su, Z., Wang, P., Zhang, X., Chen, L., et al. (2020). Structural health monitoring of high-speed railway tracks using diffuse ultrasonic wave-based condition contrast: Theory and validation. *Smart Struct. Syst.* 26 (2), 227–239. doi:10.12989/sss.2020.26.2.227
- Wang, P., Zhang, N., Kan, J., Xie, Z., Wei, Q., and Yao, W. (2020). Fiber Bragg grating monitoring of full-bolt axial force of the bolt in the deep strong mining roadway. *Sensors* 20 (15), 20154242. doi:10.3390/s20154242
- Wang, R., Wu, Q., Xiong, K., Ji, J. Y., Zhang, H. Q., and Zhai, H. Z. (2019). Phase-shifted fiber Bragg grating sensing network and its ultrasonic sensing application. *IEEE Sens. J.* 19 (21), 9790–9797. doi:10.1109/JSEN.2019.2927381
- Wang, S., Li, X. L., and Qin, Q. Z. (2022). Study on surrounding rock control and support stability of Ultra-large height mining face. *Energies* 15 (18), 15186811. doi:10.3390/en15186811
- Wang, T., Chang, J. C., Gong, P., Shi, W. B., Li, N., and Cheng, S. X. (2020). The experimental instrumented bolt with fibre Bragg grating force sensors. *Arch. Min. Sci.* 65 (1), 179–194. doi:10.24425/ams.2020.132714
- Wei, S. M., Ma, Z. Y., Li, B. F., and Chai, J. (2015). Study on the monitoring method of three-dimensional stress with FBG in surrounding rock and the simulation experiment. *J. Min. Saf. Eng.* 32 (1), 138–143. doi:10.13545/j.cnki.jmse.2015.01.022
- Wu, Q., Wang, R., Yu, F. M., and Okabe, Y. (2019). Application of an optical fiber sensor for nonlinear ultrasonic evaluation of fatigue crack. *IEEE Sens. J.* 19 (13), 4992–4999. doi:10.1109/JSEN.2019.2903323
- Xu, H.-C., Wang, S., and Miao, X.-G. (2017). Research of three-dimensional force sensor based on multiplexed fiber Bragg grating strain sensors. *Opt. Eng.* 56 (4), 047103. doi:10.1117/1.OE.56.4.047103
- Yang, C., Tan, Y., Liu, Y., Xia, P., Cui, Y., and Zheng, B. (2022a). Modeling and optimization of laser cladding fixation process for optical fiber sensors in harsh environments. *Sensors* 22 (7), 22072569. doi:10.3390/s22072569
- Yang, M., Liu, N. F., Li, N., Xu, C. B., Li, G. F., and Cao, M. M. (2022b). Failure characteristics and treatment measures of tunnels in expansive rock stratum. *Front. Earth Sci.* 10, 805378. doi:10.3389/feart.2021.805378
- Yang, X., Pang, J., Lou, H., and Fan, L. (2015). Characteristics of *in situ* stress field at Qingshui coal mine. *Int. J. Min. Sci. Technol.* 25 (3), 497–501. doi:10.1016/j.ijmst.2015.03.026
- Yu, F. M., Saito, O., and Okabe, Y. (2021). An ultrasonic visualization system using a fiber-optic Bragg grating sensor and its application to damage detection at a temperature of 1000 °C. *Mech. Syst. Signal Process.* 147, 107140. doi:10.1016/j.ymssp.2020.107140
- Yun, D., Liu, Z., Cheng, W., Fan, Z., Wang, D., and Zhang, Y. (2017). Monitoring strata behavior due to multi-slicing top coal caving longwall mining in steeply dipping extra thick coal seam. *Int. J. Min. Sci. Technol.* 27 (1), 179–184. doi:10.1016/j.ijmst.2016.11.002
- Zhang, N. B., Wang, J. D., Qin, K., Zhao, S. K., Yang, S. H., Deng, Z. G., et al. (2020). Evaluation of coal bump risk in excavation roadway based on multi-point stress and displacement monitoring system. *J. Chin. Coal Soc.* 32 (1), 140–149. doi:10.13225/j.cnki.jccs.2019.0952
- Zhou, X. M., Wang, S., Li, X. L., Meng, J., Li, Z., Zhang, L., et al. (2022). Research on theory and technology of floor heave control in semicool rock roadway: Taking longhu coal mine in Qitaihe mining area as an Example. *Lithosphere* 2022 (11), 3810988. doi:10.2113/2022/3810988
- Zhou, Z., Liu, W., Huang, Y., Wang, H., Jianping, H., Huang, M., et al. (2012). Optical fiber Bragg grating sensor assembly for 3D strain monitoring and its case study in highway pavement. *Mech. Syst. Signal Process.* 28, 36–49. doi:10.1016/j.ymssp.2011.10.003





## OPEN ACCESS

EDITED BY  
Xuelong Li,  
Shandong University of Science and  
Technology, China

REVIEWED BY  
Yu Xuguang,  
Tangshan Vocational and Technical  
College, China  
Lei Shi,  
China University of Mining and  
Technology, Beijing, China

\*CORRESPONDENCE  
Junbo Qiu,  
✉ lkdqiu junbo@126.com

SPECIALTY SECTION  
This article was submitted to  
Environmental Informatics and Remote  
Sensing,  
a section of the journal  
Frontiers in Earth Science

RECEIVED 17 December 2022  
ACCEPTED 18 January 2023  
PUBLISHED 03 February 2023

CITATION  
Li B and Qiu J (2023), Displacement  
prediction of open-pit mine slope based  
on SSA-ELM.  
*Front. Earth Sci.* 11:1126394.  
doi: 10.3389/feart.2023.1126394

COPYRIGHT  
© 2023 Li and Qiu. This is an open-access  
article distributed under the terms of the  
[Creative Commons Attribution License](#)  
(CC BY). The use, distribution or  
reproduction in other forums is permitted,  
provided the original author(s) and the  
copyright owner(s) are credited and that  
the original publication in this journal is  
cited, in accordance with accepted  
academic practice. No use, distribution or  
reproduction is permitted which does not  
comply with these terms.

# Displacement prediction of open-pit mine slope based on SSA-ELM

Bo Li<sup>1</sup> and Junbo Qiu<sup>2\*</sup>

<sup>1</sup>CCCC First Highway Consultants Co., Ltd, Xi'an, China, <sup>2</sup>Beijing Aidi Geological Engineering Technology Co., Ltd, Beijing, China

Mine geological disaster is a complex non-linear system. The traditional prediction model has the disadvantages of low prediction accuracy and poor reliability. In order to solve this problem, the open-pit mine slope displacement is taken as the research object. Based on a new algorithm extreme learning machine (ELM), the new intelligent algorithm sparrow search algorithm (SSA) are introduced to determine the weights and thresholds of the input layer and hidden layer of ELM. The open-pit mine slope displacement prediction model of improved ELM is constructed and applied to an engineering example. The results show that the root mean square error of SSA-ELM model is only a quarter of that of BP model, which is 50% higher than that of GM (1,1) and ELM models. The correlation coefficient of the prediction results of the SSA-ELM model is 0.983, and the accuracy is better than that of the traditional model. The single ELM model and the PSO-ELM model show that the SSA algorithm has better improvement effect. The SSA model has good comprehensive performance and high prediction accuracy. It is feasible to apply it to the prediction of slope displacement in open-pit mines.

## KEYWORDS

extreme learning machine, particle swarm algorithm, open-pit slope, deformation prediction, PSO-ELM, sparrow search algorithm, SSA-ELM

## Introduction

As the open-pit mine enters the deep mining stage, the mining environment becomes worse, and the frequency of geological disasters in the mine increases year by year. The mine landslide not only affects the normal mining operation, but also poses a threat to the ecological environment and the safety of the surrounding people's lives and property. According to the statistical data in 2017, the total number of accidents and deaths of non-coal mine slope landslides in China accounted for 13.5% and 9.3% of mine safety accidents respectively, ranking third (Yang, et al., 2020; Zhang, et al., 2010). At the same time, research shows that every increase of 1° in the mining slope angle of a large open-pit mine will save tens of millions or even hundreds of millions of yuan in stripping costs, but it will also bring about corresponding disaster risks (Yang, et al., 2011). Macro creep deformation is the result of gradual damage and deterioration of materials inside the slope during the evolution of slope instability (Liu et al., 2020; Li et al., 2021a). Therefore, it is of great significance to grasp the slope failure law and predict and warn the landslide according to the mining slope displacement to ensure the safety production of open-pit mines and improve economic benefits.

The prediction of open-pit slope displacement is a vital method to landslide hazard prevention. The empirical model, statistical model and artificial intelligence model are three approaches to predict displacement of slope and describe the behaviors of slope by analyzing the on-site measured data of slope. The empirical model based on site monitor data is most widely used, however, it is not suitable the prediction the periodic and stepped landslides. To avoid

above problems, other researchers have applied statistical analysis models to predict displacement considering the time and the slope surface characteristics, which included that there are grey system model (Liu, et al., 2016; Tasci, et al., 2018), Pearl Growth model (Xu, et al., 1998). However, these models only performs well when the data meets the modeling requirements or applicable to only one type slope, and its universality is not high.

In recent years, conventional models have been enhanced with some various artificial intelligence techniques such as BPNN prediction model (Feng, et al., 2018; Jiang, et al., 2018; Yang, et al., 2013), improved genetic neural network model (Guan, et al., 2015; Han, et al., 2022), support vector machine model (Yusof, et al., 2017; Zhou, et al., 2017), etc. Although the BPNN prediction model can predict under any data, it calculates the weights and thresholds of the output layer and the hidden layer through the gradient descent method. The accuracy is not high, and it needs repeated trials. The SVM model has advantages in small sample and poor data, however, its parameter selection has always restricted the application of the model. The above models are also beneficial exploration for slope displacement prediction of open pit mine (Mahmoodzaden, et al., 2022), but they also have problems in generalization ability, robustness and prediction accuracy. Therefore, it is necessary to establish a displacement prediction model with high prediction accuracy and strong generalization ability to ensure the safety production of the open pit slope (Liu et al., 2022; Li et al., 2023). The extreme learning machine (ELM) is a new method of single-layer feed forward neural network that has emerged in recent years. ELM has been verified in many engineering practices, such as concrete dam deformation prediction (Zhou, et al., 2017), landslide displacement prediction (Guan, et al., 2018), short-term power load prediction (Cheng, et al., 2018), etc., but it is rarely used in the field of safety monitoring in open pit mines. Some previous studies revealed that ELM is better than ANN and SVM in overcoming low learning rates and local minimum problems of regression analysis (Kang, et al., 2017). Therefore, the ELM is used to predict displacement of open-pit slope. However, the ELM also need to be optimized enhance the predict ability of displacement of open-pit slope (Li et al., 2021b; Zhou et al., 2022). The metaheuristic algorithms inspired by the natural behavior of animals have good performance to optimize the single neural network.

Therefore, in order to improve the shortcomings of poor prediction accuracy performance, poor robustness and weak generalization ability of traditional models, this paper establishes the SSA-ELM model for open-pit mine displacement prediction, determines the hidden layer node and activation function according to the gradual trial method, and introduces the sparrow search algorithm to optimize the connection weight and threshold value of ELM, which is applied to an example of open-pit mine slope displacement prediction.

## Extreme learning machine

ELM was first proposed by Huang (Ding, et al., 2015) as a single hidden layer feed forward neural network. Different from the gradient descent method used by BP, it randomly generates the weights and thresholds of the input layer and the output layer, which will not be adjusted during the training process. As long as the number of hidden layers is determined, the unique solution can be obtained. Therefore,

for  $N$  arbitrarily different samples  $(x_i; y_i)$ , among them  $x_i = x_{i1}, x_{i2}, x_{i3} \dots x_{i4}]^T \in \mathbb{R}^n$ ,  $y_i = y_{i1}, y_{i2}, y_{i3} \dots y_{i4}]^T \in \mathbb{R}^m$ , Then the mathematical module of ELM network can be expressed as equation (1)

$$o_i = y_i = \sum_{i=1}^l \beta_i g(x_i) = \sum_{i=1}^l \beta_i g(m_i x_i + n_i) \quad (1)$$

Where  $g(x)$  is the activation function, The number of hidden layer nodes is  $N$ ,  $m_i$ ,  $n_i$  represents the connection weight value and threshold value between the  $i$ th hidden layer and the input layer node respectively,  $\beta_i$  is the weight vector between the  $i$ th hidden layer and the output layer.

According to the theorem proposed by Huang, when the activation function is infinitely differentiable, the  $w_i$ ,  $b_i$  of the network are set randomly, and there is no need to update iterations during the training process, and the threshold between the output layer and the hidden layer is no longer needed, just calculate the output just the value. Setting the hidden layer to  $N$  nodes and the ELM with the activation function  $g(x)$  can quickly fit the input  $N$  samples with zero error, namely:

$$\sum_{j=1}^l \|o_i - t_i\| = 0 \quad (2)$$

According to equation (2), there are  $m_i$ ,  $\beta_i$ ,  $n_i$  so that equation (3)

$$y_i = \sum_{i=1}^l \beta_i g(x_i) = \sum_{i=1}^l \beta_i g(m_i x_i + n_i) = t_i \quad (3)$$

Equation (3) can be expressed in matrix form  $H\beta = T$ , Finally, it can be transformed into a problem of solving the least square norm solution of the weight matrix  $\beta$ . According to equation (3), and in most cases the number of samples is much larger than the number of hidden layer nodes, we need to find the pseudo-inverse of  $H$ , namely

$$\hat{\beta} = H^+ T = (H^T H)^{-1} H^T T \quad (4)$$

Where  $H^+$  is the Moore – Penrose generalized inverse of the hidden layer output matrix  $H$ .

## Introduction to optimization algorithm

### Particle swarm optimization algorithm

Particle swarm optimization algorithm (Yumin, et al., 2014) is a swarm intelligence global search algorithm, which performs well in the optimization and improvement of neural networks. The basic feature of this algorithm is that in the  $N$ -dimensional search space, there are  $d$  particles. Assume that a certain particle searches for the optimal value alone, which is the local extreme  $pbest$ , and at the same time shares information with the particles in the group to obtain the global extremum  $gbest$ . All particles of the particle swarm adjust their speed and position according to the local optimal value and the global optimal value, and finally obtain the optimal solution. The update formula of particle swarm optimization algorithm is shown in equations (5) and (6):

$$V_{in}^{t+1} = w V_{in}^t + c_1 r_1 (pbest_{in}^t - X_{in}^t) + c_2 r_2 (gbest_{gn}^t - X_{in}^t) \quad (5)$$

$$X_{in}^{t+1} = X_{in}^t + V_{in}^{t+1} \quad (6)$$

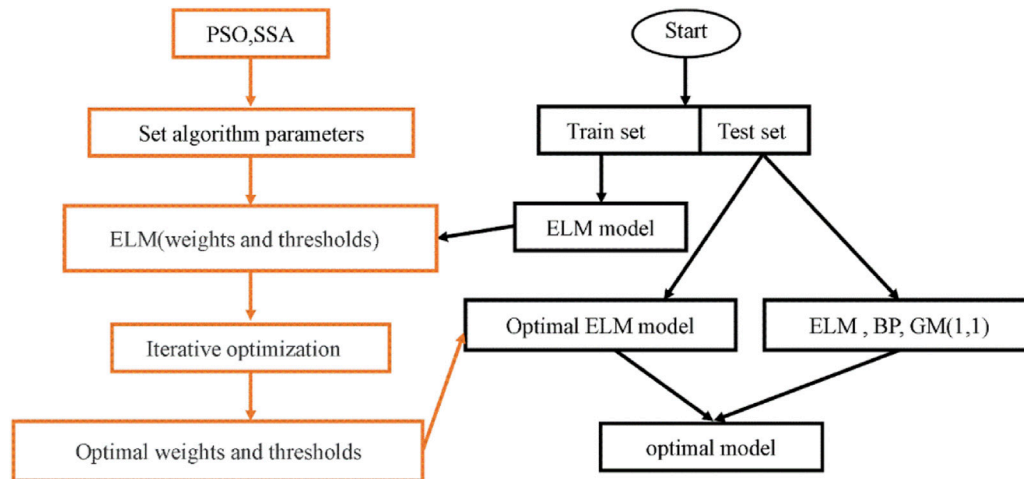


FIGURE 1  
Flow chart of SSA-ELM and PSO-ELM models

In the equations,  $w$  is the inertia weight, which decreases linearly from 0.9 to 0.4;  $t$  is the number of iterations,  $n=1,2,3,\dots,N$ ;  $i=1,2,3,\dots,d$ ;  $V_{in}$  is the velocity of the particle,  $c_1$  and  $c_2$  are non-negative numbers, called acceleration factors;  $X_{in}$  is the position of the particle,  $r_1$  and  $r_2$  are random numbers distributed between  $[0,1]$ .

In the equation (5), it can be seen that the speed of a particle is affected by its own speed  $V_{in}$ , the optimal value of the particle itself and the distance between the particle ( $pbest_{in}^t - X_{in}^t$ ) and the distance between the global optimal value and the particle ( $gbest_{gn}^t - X_{in}^t$ ) decision, and see that the inertia weight, learning factors  $c_1$  and  $c_2$  control these three parts respectively.  $c_1$  controls the contribution of the distance between the particle and its own optimal value to the particle velocity, which is called “cognitive coefficient”.  $c_2$  is called the “social learning coefficient”, which expresses the influence of the global optimal value on the particle velocity. The inertia weight is large in the early stage, focusing on the global search, and gradually becomes smaller as the number of iterations increases in the later stage, focusing on the local search and improving the ability of the particles to jump out of the local minimum.

## Sparrow search algorithm

The sparrow search algorithm (Yan, et al., 2022) is a new intelligent algorithm that imitates sparrow foraging and predation. In the SSA algorithm, the discoverer, joiner and scout cooperate to carry out local search and global search. Usually the finder has a higher fitness value and can provide the foraging area and direction for the joiner. The mathematical equation is expressed as:

$$X_{ij}^{t+1} = \begin{cases} X_{ij}^t \cdot \exp\left(\frac{-i}{\alpha \cdot iter_{max}}\right) & \text{if } R_2 < ST \\ X_{ij}^t \cdot Q \cdot L & \text{if } R_2 \geq ST \end{cases} \quad (7)$$

Where  $t$  is the current number of iterations,  $iter_{max}$  is the maximum number of iterations,  $X_{ij}^t$  and  $X_{ij}^{t+1}$  represent the position information of the  $i$ th and  $i+1$ st sparrows in dimension  $j$ ,  $R_2$  ( $R_2 \in [0, 1]$ ) is the warning value,  $Q$  is a random value with normal distribution, and  $L$  is a matrix with all 1 elements.

Joiners will always follow the discoverer to harvest better food, and at the same time monitor the discoverer and compete for food, so as to ensure their predation rate; its mathematical formula is expressed as:

$$X_{ij}^{t+1} = \begin{cases} Q \cdot \exp\left(\frac{X_{worst}^t - X_{ij}^t}{t^2}\right) & \text{if } i > n/2 \\ X_p^{t+1} + |X_{ij}^t - X_p^{t+1}| \cdot A^+ \cdot L & \text{otherwise} \end{cases} \quad (8)$$

Where  $X_p^{t+1}$  is the optimal position of the producer,  $X_{worst}^t$  is the global worst position,  $A^+ = A^T(AA^T)^{-1}$ ,  $A$  is a matrix whose internal elements are 1 or -1, when  $i > n/2$ , it means that the hungry person with the worst fitness goes after the prey.

When the scout finds a predator, it immediately sends out an alarm signal, and all the sparrows make anti-predation behaviors. The mathematical formula is expressed as:

$$X_{ij}^{t+1} = \begin{cases} X_{best}^t + \beta \cdot |X_{ij}^t - X_{best}^t| & \text{if } f_i > f_g \\ X_{ij}^t + \lambda \cdot \left(\frac{|X_{ij}^t - X_{worst}^{t+1}|}{(f_i - f_w + \delta)}\right) & \text{if } f_i = f_g \end{cases} \quad (9)$$

Where  $X_{best}$  is the global best position,  $\lambda$  is a random number between 0 and 1,  $\beta$  is a step size control parameter with a mean of 0 and an expectation of 1,  $f_i$ ,  $f_g$  and  $f_w$  represent the current individual, the current best and the current worst fitness value respectively. When  $f_i > f_g$ , it means that the sparrow is in a vulnerable state, when  $f_i = f_g$ , it means that the sparrow active in the middle is close.

## Prediction model and evaluation index based on SSA-ELM and PSO-ELM

### Improved ELM model for deformation prediction of open-pit mine slope

In order to be able to precisely forecast open-pit mine slope displacement, the extreme learning machine is used for modeling.

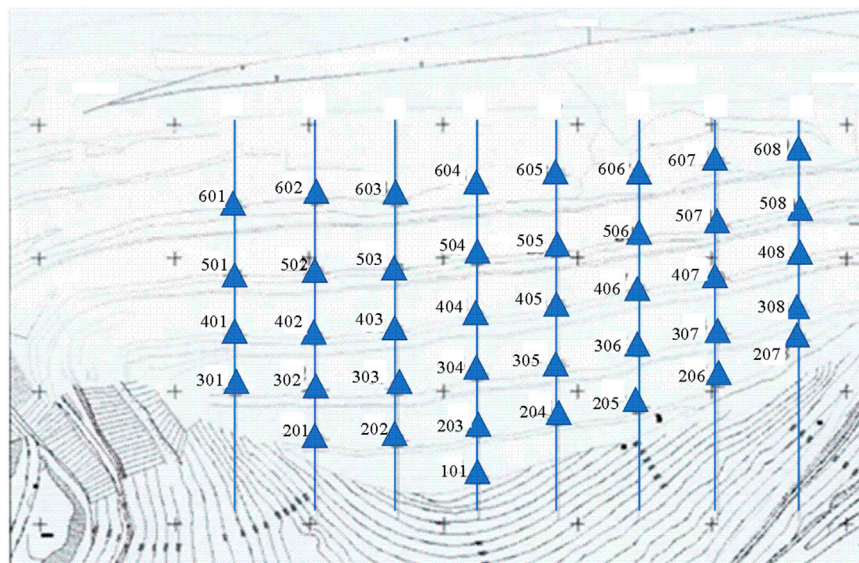


**FIGURE 2**  
Monitoring points of Jianshan mine slope.

Although the single extreme learning machine model has a simple structure and fast solution speed, it also needs to determine the number of hidden layers. The number of hidden layers can be determined according to the trial algorithm and the two-dimensional search method are determined, and the trial algorithm is used in this paper. The weights and thresholds of the ELM input and output layers are randomly generated and have nothing to do with the training data. The randomly generated values will make the algorithm good and bad, and it cannot guarantee that the solution sought must meet the requirements. Therefore, the new intelligent algorithm SSA are used to improve the ELM (Anupam, et al., 2020), and a combined open-pit mine slope displacement prediction combined model is established. The threshold of the hidden layer and the output layer, so as to obtain the expected vector that meets the requirements. Figure 1 depicts a process for optimizing ELM using the SSA and the PSO. The specific steps of the model are as follows.

**Step 1.** Divide the collected open-pit mine slope displacement data into two parts, the training set and the test set. At the same time, preprocess the data, eliminate the influence of dimensions and compress the data into the solution space of the activation function.

**Step 2.** , initialization, setting the particle swarm and sparrow dimensions, that is, the weights and thresholds of the input and output layers of the ELM, the parameters of the particle swarm algorithm and the sparrow search algorithm.

**Step 3.** Calculate the fitness function value. In this paper, the mean square error mse of the slope displacement prediction value of the open-pit mine is used as the objective function to calculate each fitness value.

**Step 4.** , iterative optimization, to obtain the optimal fitness value, at the same time, the optimization results are the optimal solutions obtained by the two algorithms, and the connection weights and thresholds of the ELM hidden layer and input layer are obtained.

**Step 5.** Based on the optimization results, establish an optimized extreme learning machine slope deformation prediction model for open pit mines, input the test set into the established model, and obtain the optimal model after evaluation.

## Evaluation index

It is very necessary to evaluate the accuracy of the prediction results of the slope displacement prediction model in open-pit mines. The corresponding evaluation of the results of the deformation monitoring model can judge the accuracy and applicability of the proposed monitoring model, which can be compared with different models, and Can be used to define warning values. Indicators include root mean square error (RMSE) and correlation coefficient (R), the optimal model has smaller RMSE and largest R.

$$RMSE = \sqrt{\left(\frac{1}{n}\right) \sum_{k=1}^n (y_i - y'_i)^2} \quad (10)$$

$$R = \frac{\sum_{k=1}^n (y_i - \bar{y})(y'_i - \bar{y}')}{\sqrt{\sum_{k=1}^n (y_i - \bar{y})^2 (y'_i - \bar{y}')^2}} \quad (11)$$

Where  $y_i$  is predictive value,  $y'_i$  is the true value,  $\bar{y}$  is the mean of predicted values,  $\bar{y}'$  is the mean of true values,  $n$  is the number of samples.

## Engineering example

### Engineering background

Jianshan mine is located in the middle of Jianshan mining area. The northern slope of Jianshan is the exposure part of rock stratum of



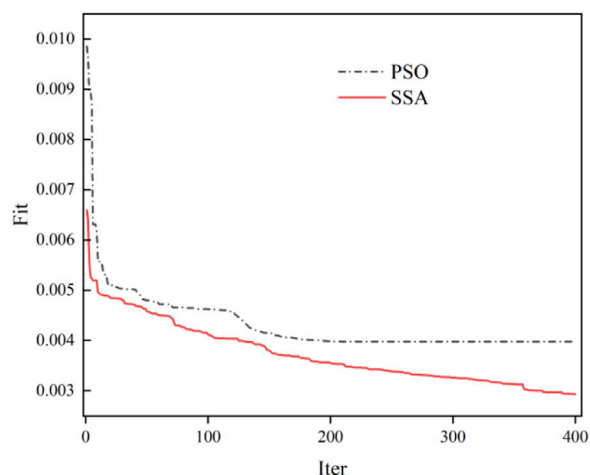


**FIGURE 3**  
Fitness optimization graph.

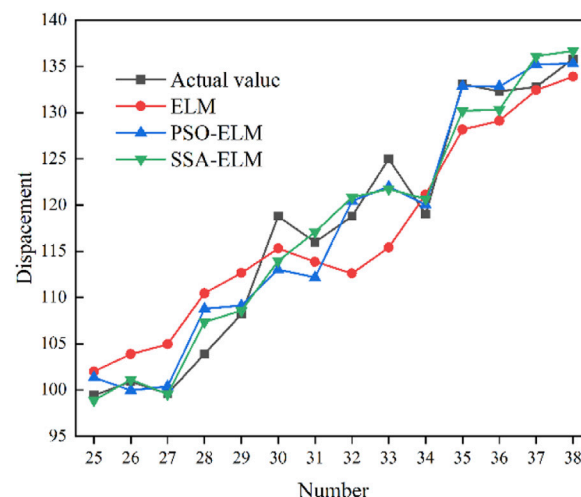


**FIGURE 5**  
Comparison of prediction results of four models.

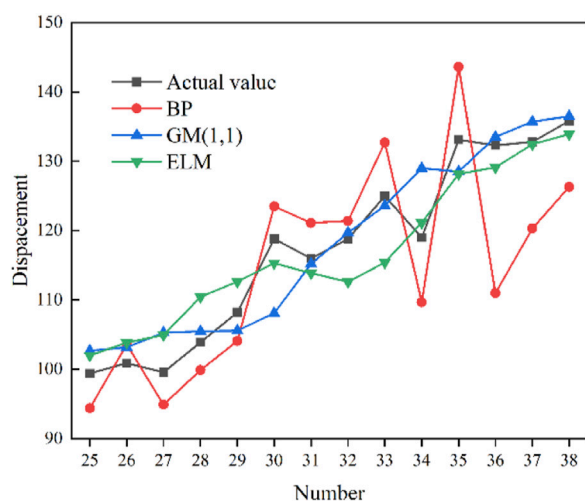


**FIGURE 4**  
Comparison of single model prediction results.

meter field floor. The slope of Jianshanle mine is a continental dip bedding rock slope, and the mining area is located in Xiangtiaocun anticline of east-west tectonic belt. The stable state of the slope makes the slope deformed, and even leads to the overall instability or local instability of the slope. During the mining period, there were continuous sheet collapses and collapses under the slope platform. If the landslide disaster occurs on the slope, it will seriously affect the personal and equipment safety of the normal mining and stripping operation of the mine, and also affect the safety of the villages, farmland, railways, highways and so on around the slope. The stability state and hazard of the slope together determine the safety monitoring of the slope. From the monitoring technology and monitoring cost analysis, considering the economic benefit and monitoring effect and other factors combined with the actual situation of the slope, the automatic monitoring system is finally adopted to carry out real-time safety

monitoring of the slope. The detailed layout of monitoring points is shown in Figure 2. There are 8 profile monitoring lines and 40 deformation monitoring points.

## Deformation prediction and result analysis

Taking the slope displacement data of an open-pit mine as an example, a total of 46 periods of monitoring data at No.601 monitoring point were selected (Sun, 2014), and only a single factor of displacement was considered. The Table 1 display the monitor data. The data of the first 8 days were used to predict the displacement of the next day, and a total of 38 sets of data were formed. The first 24 periods were used as The training set and the last 14 periods were used as the test set, ELM model, GM (1,1) and BP model were used to compare and analyze the prediction results.

The number of hidden layers of the ELM model is 6 and the transfer function is sig type through the trial algorithm, and the prediction result of ELM is obtained, and compared with the BP(Sun, 2014; Xie, et al., 2014) and GM (1,1)(Sun, 2014; Sun et al., 2016; Wu, et al., 2015) models, as shown in Figure 2. Analysis of Figure 2 shows that the prediction results of the BP model can predict the trend of displacement, but almost every predicted value deviates from the real value, and the prediction result is the worst; the prediction effect of the GM (1,1) model is better than that of the BP model, but the model predicts Unstable, the predictive effect is also poor. The prediction results of the single ELM model are significantly better than the BP model, and the prediction effect is better than that of the GM (1,1) model in the early and late stages, while the prediction value of the GM (1,1) model in the middle part is closer to the real value, indicating that the ELM model is better than the BP model. The prediction accuracy of the model is high, but because of the randomly generated weights and thresholds, the prediction results will also be unstable.

To overcome the instability of the ELM prediction results, the new intelligent algorithm SSA is used to improve the ELM model, and the



TABLE 1 Sample dataset.

Serial number	Input vector								Output vector
1	3.7	6.2	11.8	16.2	17.7	21.5	25.5	28.1	30.8
2	6.2	11.8	16.2	17.7	21.5	25.5	28.1	30.8	33.3
3	11.8	16.2	17.7	21.5	25.5	28.1	30.8	33.3	38
4	16.2	17.7	21.5	25.5	28.1	30.8	33.3	38	35.3
5	17.7	21.5	25.5	28.1	30.8	33.3	38	35.3	43.1
6	21.5	25.5	28.1	30.8	33.3	38	35.3	43.1	43.6
7	25.5	28.1	30.8	33.3	38	35.3	43.1	43.6	46.2
8	28.1	30.8	33.3	38	35.3	43.1	43.6	46.2	60.5
9	30.8	33.3	38	35.3	43.1	43.6	46.2	60.5	49.5
10	33.3	38	35.3	43.1	43.6	46.2	60.5	49.5	64.1
11	38	35.3	43.1	43.6	46.2	60.5	49.5	64.1	57.9
12	35.3	43.1	43.6	46.2	60.5	49.5	64.1	57.9	65
13	43.1	43.6	46.2	60.5	49.5	64.1	57.9	65	73
14	43.6	46.2	60.5	49.5	64.1	57.9	65	73	70.9
15	46.2	60.5	49.5	64.1	57.9	65	73	70.9	76.2
16	60.5	49.5	64.1	57.9	65	73	70.9	76.2	70.3
17	49.5	64.1	57.9	65	73	70.9	76.2	70.3	75.4
18	64.1	57.9	65	73	70.9	76.2	70.3	75.4	84.9
19	57.9	65	73	70.9	76.2	70.3	75.4	84.9	86.4
20	65	73	70.9	76.2	70.3	75.4	84.9	86.4	83.7
21	73	70.9	76.2	70.3	75.4	84.9	86.4	83.7	90.1
22	70.9	76.2	70.3	75.4	84.9	86.4	83.7	90.1	92.3
23	76.2	70.3	75.4	84.9	86.4	83.7	90.1	92.3	98.1
24	70.3	75.4	84.9	86.4	83.7	90.1	92.3	98.1	98.1
25	75.4	84.9	86.4	83.7	90.1	92.3	98.1	98.1	99.4
26	84.9	86.4	83.7	90.1	92.3	98.1	98.1	99.4	100.9
27	86.4	83.7	90.1	92.3	98.1	98.1	99.4	100.9	99.6
28	83.7	90.1	92.3	98.1	98.1	99.4	100.9	99.6	103.9
29	90.1	92.3	98.1	98.1	99.4	100.9	99.6	103.9	108.2
30	92.3	98.1	98.1	99.4	100.9	99.6	103.9	108.2	118.8
31	98.1	98.1	99.4	100.9	99.6	103.9	108.2	118.8	116
32	98.1	99.4	100.9	99.6	103.9	108.2	118.8	116	118.8
33	99.4	100.9	99.6	103.9	108.2	118.8	116	118.8	125
34	100.9	99.6	103.9	108.2	118.8	116	118.8	125	119
35	99.6	103.9	108.2	118.8	116	118.8	125	119	133.1
36	103.9	108.2	118.8	116	118.8	125	119	133.1	132.3
37	108.2	118.8	116	118.8	125	119	133.1	132.3	132.8
38	118.8	116	118.8	125	119	133.1	132.3	132.8	135.8

TABLE 2 Prediction errors of five models.

Serial number	True value	BP		GM(1,1)		ELM		PSO-ELM		SSA-ELM	
		Predictive value	Relative error (%)	Predictive value	Relative error (%)	Predictive value	Relative error (%)	Predictive value	Relative error (%)	Predictive value	Relative error (%)
25	99.4	94.4	5.03	102.7	3.32	102.0	2.62	101.4	1.97	98.9	0.53
26	100.9	103.6	2.68	103.2	2.28	103.9	2.94	99.9	0.94	101.1	0.23
27	99.6	94.9	4.72	105.3	5.72	104.9	5.37	100.4	0.79	99.5	0.06
28	103.9	99.9	3.85	105.5	1.54	110.5	6.32	108.8	4.71	107.3	3.32
29	108.2	104.1	3.79	105.6	2.40	112.7	4.13	109.1	0.86	108.6	0.36
30	118.8	123.5	3.96	108.1	9.01	115.3	2.94	113.0	4.86	113.9	4.08
31	116	121.1	4.40	115.2	0.69	113.9	1.84	112.2	3.30	117.1	0.94
32	118.8	121.4	2.19	119.7	0.76	112.6	5.21	120.5	1.39	120.9	1.74
33	125	132.7	6.16	123.6	1.12	115.4	7.68	122.0	2.40	121.7	2.62
34	119	109.7	7.82	129	8.40	121.2	1.82	120.0	0.87	120.7	1.42
35	133.1	143.6	7.89	128.5	3.46	128.2	3.70	132.9	0.17	130.2	2.18
36	132.3	111	16.10	133.5	0.91	129.1	2.40	132.8	0.39	130.3	1.50
37	132.8	120.3	9.41	135.7	2.18	132.4	0.27	135.2	1.82	136.1	2.49
38	135.8	126.3	7.00	136.5	0.52	133.9	1.40	135.3	0.36	136.7	0.64
Average value		6.07%		3.02%		3.47%		1.77%		1.58%	

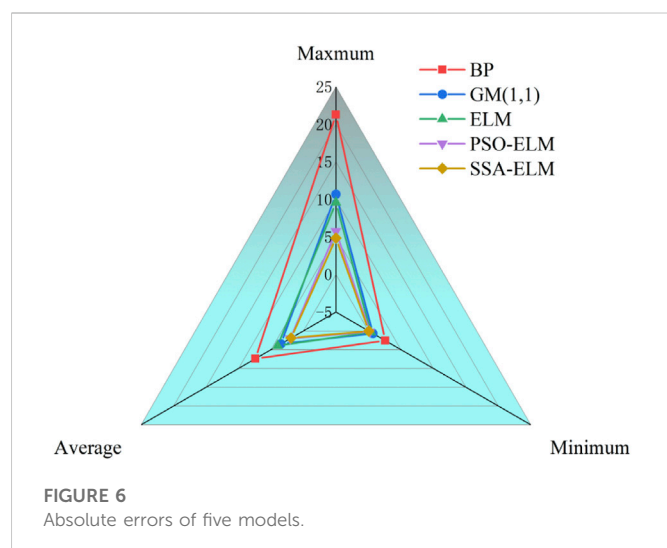


TABLE 3 Performance comparison of five models.

Algorithm	BP	GM(1,1)	ELM	PSO-ELM	SSA-ELM
RMSE	8.85	4.61	4.68	2.45	2.38
R	0.806	0.933	0.946	0.979	0.983

weight and threshold between the ELM input layer and the hidden layer are optimized through the optimization algorithm to improve the prediction ability of the ELM model.

The parameters of the PSO-ELM model are set as follows. The population size of the particle swarm optimization algorithm is 30, the maximum number of iterations is 400, and the sums are 2.4 and 1.5 respectively, and the inertia weight is linearly decreased from 0.9 to 0.4. The population size of the SSA algorithm is 30, and the maximum number of iterations is also 400, the warning value is 0.6, the proportion of discoverers is 0.7, and the proportion of sparrows aware of danger is 0.2.

Figure 3 is the fitness graph of ELM optimized by PSO and SSA algorithms. As shown in Figure 4, although the particle swarm optimization algorithm converges at iteration 150, it falls into a local optimum, while SSA has been better than the PSO algorithm after 10 iterations, and has been looking for the optimal value, although it is close to convergence at about 380, but did not fall into the local optimum, and achieved better results, indicating that the optimization effect of the SSA algorithm is better than that of the PSO algorithm.

The prediction results of ELM optimized by SSA and PSO algorithms are shown in Figure 5. Compared with the ELM model, the prediction values of SSA-ELM and PSO-ELM are closer to the real value, and the prediction value of the optimized ELM model can better reflect the development trend of slope deformation. Each stage can approach the actual value very well, and the prediction stability is high. There is no situation where the prediction effect of GM (1,1) and a single ELM model is unstable, and the robustness is high, and the prediction effect is the best. It shows that SSA and PSO can improve the prediction performance of a single ELM model and find the optimal weight and

threshold. The predicted value of SSA-ELM is closer to the on-site monitor values than the predicted value of PSO-ELM, indicating that the improvement effect of the SSA algorithm is better.

## Model accuracy evaluation

In order to further evaluate and obtain the optimal model, the prediction errors of the five models are shown in Table 2. The average relative errors of the BP model, the GM (1,1) model, the single ELM model, the PSO-ELM model and the SSA-ELM (Hu et al., 2022) model are respectively 6.02%, 3.02%, 3.47%, 1.77% and 1.58%. The relative errors of ELM model and GM(1,1) model are close to each other, obviously better than BP model, but their relative errors fluctuate greatly, and the prediction stability is slightly insufficient. Except for the 28th, 31st, 32nd and 33rd groups of PSO-ELM model, the prediction values of the 31st, 32nd and 33rd groups are slightly worse than the GM(1,1) model, the other 11 groups of prediction results are better than the GM(1,1) model, and the model is the largest. The relative error and the minimum relative error are 4.86% and 0.17%, respectively, which are better than the single ELM model and the GM (1,1) model. The maximum, minimum and average relative errors of the SSA-ELM model are 4.08%, 0.06% and 1.58%, which is the smallest among the five models, indicating that the PSO and SSA algorithms have improved the prediction ability of the ELM model, and the SSA has a stronger optimization ability than the PSO. The improved ELM model is feasible for open-pit slope displacement prediction, and the SSA -ELM model and higher prediction accuracy.

Figure 6 is the absolute error radar chart of five open-pit mine slope deformation prediction models. As shown in Figure 5, the maximum, minimum and average values of the absolute error of the BP model are the largest among the five models, and the absolute error of the single ELM model is The maximum and minimum values of the error are smaller than the GM(1,1) model, but the average absolute error of the GM(1,1) model is smaller, indicating that the ELM model needs to be further improved, and the absolute error of the PSO-ELM and SSA-ELM models The maximum, minimum and average values are smaller than those of the other three models, indicating that the SSA and PSO algorithms can improve the predictive ability of the ELM model. The ELM model does not show that the improvement effect of SSA is better.

The root mean square error RMSE and correlation coefficient R are introduced as the five evaluation indexes of model accuracy. It can be seen from Table 3 that the root mean square errors of the PSO-ELM model and the SSA-ELM model are 2.45 and 2.38mm, respectively, which are only a quarter of the BP model, and the relative prediction accuracy of the GM(1,1) and ELM models The correlation coefficient of ELM among the five models is 0.946, which is higher than that of BP and GM (1,1) models, indicating that ELM is superior to traditional models in slope displacement prediction of open-pit mines, and has a certain degree of advancement. The correlation coefficients of the PSO-ELM model and the SSA-ELM model are 0.979 and 0.983, respectively, indicating that the improved ELM model overcomes the shortcomings of the single ELM algorithm that randomly generates weights and thresholds, and improves the model prediction accuracy. Because the PSO algorithm is stronger, it further proves that SSA-ELM is feasible and effective for slope displacement prediction in open-pit mines.

## Conclusion

The slope displacement change of the open-pit mine is affected by many non-linear factors, and the traditional model performs poorly. Therefore, the new algorithm ELM is used to predict the displacement of this type of slope, which overcomes the shortcomings of the poor prediction accuracy performance of the traditional model, but the stability is slightly insufficient.

Introduce SSA and PSO algorithms to determine the weights and thresholds of the ELM input layer and hidden layer, and improve the single ELM model. Compared with the two traditional models BP and GM (1,1) and the single ELM model, the prediction results of the improved ELM model, The correlation coefficient is higher, and the correlation coefficient of the SSA-ELM model is the highest among the four models. The root mean square error of SSA-ELM is 2.38mm, which is smaller than the other four models. This model has superior performance and high reliability, and is used in open air The prediction of mine slope deformation is feasible. The main limitation of this paper is that only one dataset was utilized to evaluate the results of developed models. Meanwhile, this study did not consider that the proposed algorithms have some limitations, such as local minima trapping issues and the inability to exploit local space. The developed model in this study will be applied to other datasets to demonstrate its generalization ability and robustness. Present strategies to avoid the problem of local minima trapping issues and the inability of metaheuristic algorithms to exploit local space and illustrate their impact on the current model.

## References

- Anupam, S., and Pani, P. (2020). Flood forecasting using a hybrid extreme learning machine-particle swarm optimization algorithm (ELM-PSO) model. *Model. Earth Syst. Environ.* 6 (1), 341–347. doi:10.1007/s40808-019-00682-z
- Cheng, Y. F., Jin, L. J., and Hou, K., (2018) Ieee, "Short-Term power load forecasting based on improved online ELM-K," Proceedings of the 7th International Conference on Control Automation and Information Systems (ICCAIS), pp. 128–132, Hangzhou Dianzi Univ, Hangzhou, PEOPLES R CHINA,
- Ding, S. F., Zhao, H., Zhang, Y. N., Xu, X. Z., and Nie, R. (2015). Extreme learning machine: Algorithm, theory and applications. *Artif. Intell. Rev.* 44 (1), 103–115. doi:10.1007/s10462-013-9405-z
- Feng, X. W., Guo, Y., and Li, J. Y. (2018). "A research on the methods for prediction of the slope stability of open-pit mine," in Proceedings of the 9th China-Russia Symposium on Coal in the 21st Century - Mining, Intelligent Equipment and Environment Protection, Qingdao, PEOPLES R CHINA, October 2018, 73–77.
- Guan, S. W., Zhu, Y., Zhou, L., Deng, H. G., and Luo, X. N. (2018). "Prediction of landslide displacement using EMD-PSO-ELM with multiple factors," in Proceedings of the 7th International Conference on Digital Home (ICDH), Guilin, PEOPLES R CHINA (Guilin Univ Elect Technol), 230–235.
- Guan, S., Wang, Z., and Zhang, L. (2015). Application of improved genetic neural network on anticipation of displacements of slope in open pit. *J. Liaoning Tech. University: Natural Sci.* 34 (05), 618–622.
- Han, G., Li, W. L., Sun, X. Y., Jin, S. Y., Zheng, H. Q., and Wang, X. X. (2022). Intelligent optimization of a bolt support scheme for a single-stage slope. *Eng. Optim.* 10, 1–17. doi:10.1080/0305215x.2022.2086238
- Hu, Y. F., Li, K. Q., Zhang, B., and Han, B., "2022, Strength investigation of the cemented paste backfill in alpine regions using lab experiments and machine learning," *Constr. Build. Mater.*, vol.323, Article ID126583, 126583, doi:10.1016/j.conbuildmat.2022.126583
- Jiang, T., Shen, Z. Z., Yang, M., Xu, L. Q., Gan, L., and Cui, X. B. (2018). A new model approach to predict the unloading rock slope displacement behavior based on monitoring data. *Struct. Eng. Mech.* 67 (2), 105–113.
- Kang, F., Liu, J., Li, J., and Li, S. (2017). Concrete dam deformation prediction model for health monitoring based on extreme learning machine. *Struct. Control. Health Monit.* 24–e1997. doi:10.1002/stc.1997
- Li, X. L., Chen, S. J., Liu, S. M., and Li, Z. H. (2021a). AE waveform characteristics of rock mass under uniaxial loading based on Hilbert-Huang transform. *J. Cent. South Univ.* 28 (6), 1843–1856. doi:10.1007/s11771-021-4734-6
- Li, X. L., Chen, S. J., and Wang, S. (2021b). Study on *in situ* stress distribution law of the deep mine taking Linyi Mining area as an example. *Adv. Mater. Sci. Eng.* 9 (4), 5594181. doi:10.1155/2021/5594181
- Li, X. L., Zhang, X. Y., and Shen, W. L. (2023). Research on the mechanism and control technology of coal wall sloughing in the ultra-large mining height working face. *Int. J. Environ. Res. Public Health* 20 (2), 868. doi:10.3390/ijerph20010227
- Liu, H. Y., Zhang, B. Y., and Li, X. L. (2022). Research on roof damage mechanism and control technology of gob-side entry retaining under close distance gob. *Eng. Fail. Anal.* 138 (5), 106331. doi:10.1016/j.engfailanal.2022.106331
- Liu, S. F., Tao, L. Y., Xie, N. M., and Yang, Y. J. (2016). On the new model system and framework of grey system theory. *J. Grey Syst.* 28 (1), 1–15.
- Liu, S. M., Li, X. L., Wang, D. K., and Zhang, D. (2020). Investigations on the mechanism of the microstructural evolution of different coal ranks under liquid nitrogen cold soaking. *Energy Sources A: Recovery Util. Environ. Eff.*, 1–17. doi:10.1080/15567036.2020.1841856
- Mahmoodzaden, A., Nejati, H. R., Mohammadi, M., Ibrahim, H. H., Rashidi, S., and Mohammed, A. H. (2022). Meta-heuristic optimization algorithms for prediction of fly-rock in the blasting operation of open-pit mines. *Geomechanics Eng.* 30 (6), 489–502.
- Sun, H. F. (2014). *Study on slope monitoring and prediction of jianshan phosphate mine [D]*. China: Kunming University of Science and Technology.
- Sun, S. G., Wang, C., Zhao, J., and Destech Publicat, I., "The application of improved GM (1,1) model in deformation prediction of slope," Proceedings of the 2nd International Conference on Sustainable Energy and Environmental Engineering (SEEE), pp. Xiamen, PEOPLES R CHINA, 2016
- Tasci, L., and Tuncel, M. (2018). Monitoring of deformations in open-pit mines and prediction of deformations with the grey prediction model. *J. Grey Syst.* 30 (4), 152–163.
- Wu, H., Dong, Y. F., Shi, W. Z., Clarke, K. C., Miao, Z. L., Zhang, J. H., et al. (2015). An improved fractal prediction model for forecasting mine slope deformation using GM (1,1). *Struct. Health Monitoring-an Int. J.* 14 (5), 502–512. doi:10.1177/1475921715599050

## Data availability statement

The original contributions presented in the study are included in the article, further inquiries can be directed to the corresponding author.

## Author contributions

Conceptualization, data curation, formal analysis, Software, methodology, validation, writing—review & editing: JQ; writing—review & editing, supervision, BL. All authors have read and agreed to the published version of the manuscript.

## Conflict of interest

BL was employed by CCCC First Highway Consultants Co., Ltd. JQ was employed by Beijing Aidi Geological Engineering Technology Co., Ltd.

## Publisher's note

All claims expressed in this article are solely those of the authors and do not necessarily represent those of their affiliated organizations, or those of the publisher, the editors and the reviewers. Any product that may be evaluated in this article, or claim that may be made by its manufacturer, is not guaranteed or endorsed by the publisher.

- Xie, Z. H., Liang, S. S., and Luan, T. T. (2014). "Instability warning model of open-pit mine slope based on BP neural network," in Proceedings of the 3rd International Conference on Civil Engineering and Urban Planning (CEUP), Wuhan, PEOPLES R CHINA, 225–228.
- Xu, J. L., and Ma, H. (1998). Discussion on prediction methods of landslide imminent sliding. *Chin. J. Geol. Hazard Control* 9, 364–369.
- Yan, S. Q., Liu, W. D., Li, X. Q., Yang, P., Wu, F. X., and Yan, Z. (2022). Comparative study and improvement analysis of sparrow search algorithm. *Wirel. Commun. Mob. Comput.* 2022, 1–488252115. doi:10.1155/2022/4882521
- Yang, F.-Y., Xu, M.-L., and Guo, Z.-P. (2013). Wavelet denoising and BPANN forecast for monitoring slope deformation in open pit. *Min. METALLURGICAL Eng.* 33 (6), 1–5.
- Yang, T., Wang, H., Dong, X., Liu, F., Zhang, P., and Deng, W. (2020). Current situation, problems and countermeasures of intelligent evaluation of slope stability in open pit. *J. China Coal Soc.* 45 (6), 19.
- Yang, T.-H., Zhang, F.-C., Yu, Q.-L., Cai, M., and Li, H. (2011). Research situation of open-pit mining high and steep slope stability and its developing trend. *Rock Soil Mech.* 32 (5), 1437–1451.
- Yumin, D., and Li, Z., "Quantum behaved particle swarm optimization algorithm based on artificial fish swarm," *Math. Problems Eng.*, vol. 2014, 1, 10, doi:10.1155/2014/5926822014, Article ID 592682, 2014
- Yusof, K. W., Babangida, N. M., Mustafa, M. R., and Isa, M. H. (2017). Linear kernel support vector machines for modeling pore-water pressure responses. *J. Eng. Sci. Technol.* 12 (8), 2202–2212.
- Zhang, D. M., Yin, G. Z., Chen, J. A., and Dai, G. F. (2010). Stability analysis of multi-step anti-tilt slope at open-pit mine. *Disaster Adv.* 3 (4), 30–34.
- Zhou, X. M., Wang, S., and Li, X. L. (2022). Research on theory and technology of floor heave control in semicoal rock roadway: Taking longhu coal mine in Qitaihe mining area as an Example. *Lithosphere* 2022 (11), 3810988. doi:10.2113/2022/3810988
- Zhou, Y., Su, W. J., Ding, L. Y., Luo, H. B., and Love, P. E. D. (2017). Predicting safety risks in deep foundation pits in subway infrastructure projects: Support vector machine approach. *J. Comput. Civ. Eng.* 31 (5)–04017052. doi:10.1061/(asce)cp.1943-5487.0000700





## OPEN ACCESS

## EDITED BY

Xuelong Li,  
Shandong University of Science and  
Technology, China

## REVIEWED BY

Lin Zhang,  
Chang'an University, China  
Zayne Yu,  
China University of Geosciences Wuhan,  
China

## \*CORRESPONDENCE

Xuepeng Li,  
✉ lixuepeng1984@126.com

## SPECIALTY SECTION

This article was submitted to  
Environmental Informatics and  
Remote Sensing,  
a section of the journal  
Frontiers in Earth Science

RECEIVED 23 December 2022

ACCEPTED 24 January 2023

PUBLISHED 09 February 2023

## CITATION

Li C and Li X (2023), Evaluation of bearing  
capacity of PHC pipe piles via the dynamic  
and static loading test.  
*Front. Earth Sci.* 11:1130294.  
doi: 10.3389/feart.2023.1130294

## COPYRIGHT

© 2023 Li and Li. This is an open-access  
article distributed under the terms of the  
[Creative Commons Attribution License](#)  
(CC BY). The use, distribution or  
reproduction in other forums is permitted,  
provided the original author(s) and the  
copyright owner(s) are credited and that  
the original publication in this journal is  
cited, in accordance with accepted  
academic practice. No use, distribution or  
reproduction is permitted which does not  
comply with these terms.

# Evaluation of bearing capacity of PHC pipe piles via the dynamic and static loading test

Caihua Li and Xuepeng Li\*

Chancheng District Construction Engineering Quality and Safety Inspection Station of Foshan, Foshan, Guangdong, China

Due to its faster implementation and potential cost savings for estimating the bearing capacity of PHC pipe piles, the High Strain Dynamic Test (HSDT) offers an alternative approach to Static Load Test (SLT). The report presents a bearing capacity study via those methods with a sliding micrometer. And a Pile Driving Analyzer (PDA) imported from the United States is employed, to determine the design parameters of pile foundation engineering and provide the error sources of bearing capacity. Sliding micrometers with cone-shaped rings are embedded in the inner side of the pile piles every 1 m for measuring the strain. The law of stress and strain at various depths during loading is presented in this paper. As a new concept, the "inflection point" is proposed by the relationship between shaft resistance and relative displacement of pile-soil. By comparing the SLT and HSDT, the relationship between toe resistance and settlement of pile is demonstrated. This paper analyses the reliability and precision, and explore the error source so as to provide theoretical evidence for trail-pile testing in future. And the error of bearing capacity between SLT and HSDT with CAPWAP studies shows that the HSDT could provide adequate results for assessing the bearing capacity of PHC pipe piles.

## KEYWORDS

bearing capacity, resistance, HSDT, SLT, sliding micrometer

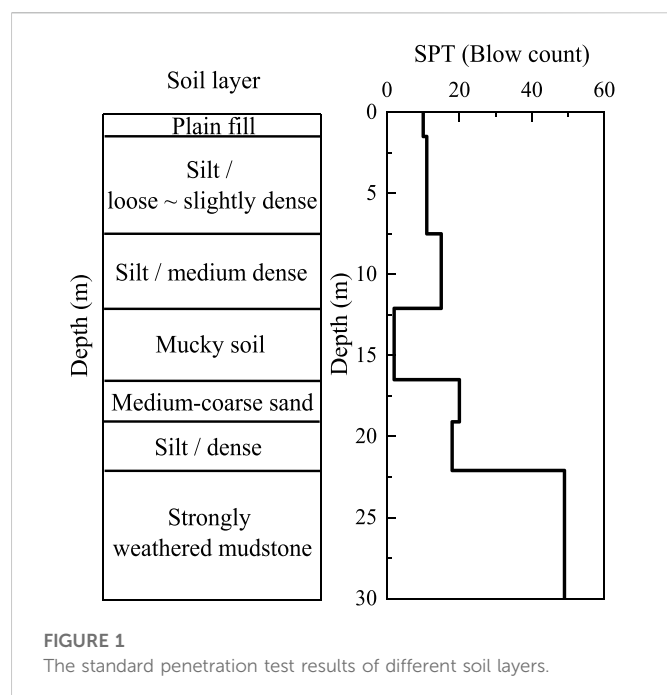
## 1 Introduction

At present, static load test (SLT) and high strain dynamic test (HSDT) are two methods to determine the bearing capacity of base piles (Rausche et al., 1985; Alawneh et al., 2001). Static load test is the most commonly employed technology as the more accurately determination, but it is time-consuming and may be costly for engineering geology (Smith, 1960; Aghayarzadeh et al., 2020; Alwalan and Nagggar, 2020). As a relatively new developed technology, high strain dynamic testing has the advantages of fast, convenient and inexpensive (Heins et al., 2020). In recent years, compared with the traditional static load test, the practice of engineering shows that the error of high strain dynamic test with high strain curve match method (CMM) is within  $\pm 20\%$  (Choe et al., 2002; Long, 2007; Svinkin, 2019). Therefore, it is a widely acknowledged testing technique for pile detection, and is frequently referenced in the ASTM D4945 (ASTM D4945, 2000) as a most basic of test need (Briaud and Tucker, 1984; ASTM D4945, 2000).

Interpretation of HSDT can be accomplished using direct or indirect methods (Chen et al., 2022). The case method adopted by pile driving analyzer (PDA) is an example of the direct method. The PDA is used with the HSDT. It contains a computer-based program for data acquisition and analysis at the field from the case method (Zhao, 2005). The Case Wave Analysis Program (CAPWAP) is applied for an analysis to correlate the dynamic to static capacity of the piles (Ding et al., 2013). It executes the analysis based on the concept of stress

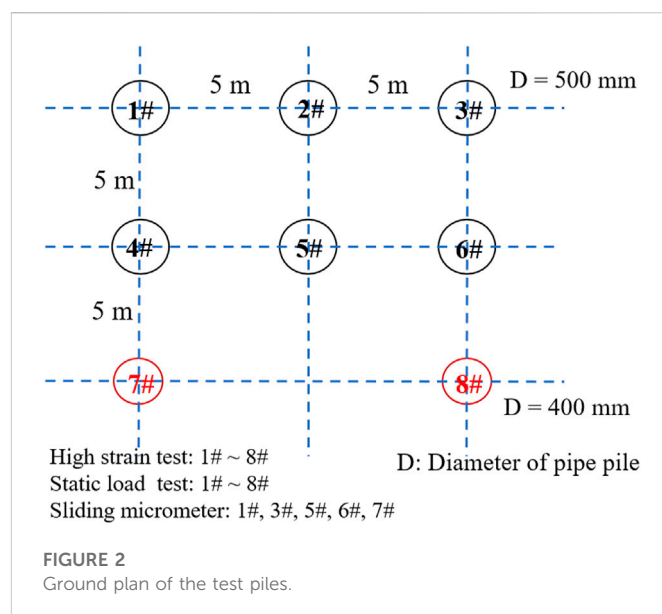
TABLE 1 Soil properties of test site.

Soil layer No	Soil layer	Depth (m)	Deformation modulus (MPa)	Internal friction angle (°)	Cohesion force (°)
①	Plain fill	1.5	2	8	7
②	Silt/Loose ~ slightly dense	6.0	13	25	/
③	Silt/medium dense	4.6	16	28	/
④	Mucky soil	4.4	/	4	6
⑤	Medium-coarse sand	2.6	25	35	/
⑥	Silt/dense	3.0	18	28	/
⑦	Strongly weathered mudstone	6.4	180	45	25



wave propagation with signal matching method to find a reasonable solution (Green and Kightley, 2005a).

Li and Gao (Li and Gao, 2012) tested 56 piles with high strain dynamic test. However, the calculation model of pile-soil was assumed and simplified with the case method (Rajagopal et al., 2012). Considering the pile was an elastic rod with one-dimensional uniform impedance, only the damping of the soil at the toe of pile was taken into account, so the dynamic resistance of the soil at the shaft resistance of pile was disregarded (Likins et al., 1996; Livneh and EL Naggar, 2008). The curve match method not only assumes the rigid soil adjacent to pile but also considers the damping attenuation and deficiency of pile shaft factors (Meyerhof and Murdock, 1953; Gates, 1957; Smith, 1960; Salgado et al., 2017). Mohammed (Mohammed, 2013) examined the difference between high strain dynamic and static load tests of helical piles in cohesive soils. Heins and Grabe (Heins and Grabe, 2019) proposed a new technique based on the finite element method, which accurately captured the key aspects for HSDT results and was capable of deriving the pile bearing capacity. Green and Kightley (Green and Kightley, 2005b) studied the CAPWAP by the theory and engineering application.



For the widespread use of PHC pipe piles in the Chancheng distruct in China, it is crucial to verify the dependability and applicability of HSDT. This paper presents the development and applications of bearing capacity of PHC pipe piles based on HSDT, SLT with sliding micrometer. This paper also presents a new concept of “inflection point” through the curve between shaft resistance and relative displacement of pile-soil. By comparing the error in bearing capacity between SLT and HSDT, the reliability and surveying precision of the curve match method is analyzed, to reasonably determine the design parameters of pile foundation engineering in Chancheng distruct in China.

## 2 Test site and method

### 2.1 Site description

The Chancheng test site is located in Foshan City, Guangdong Province, China. The soil layers consist of plain fill, silty, muddy soil, medium coarse sand, silty, and strongly weathered mudstone from top to bottom. Table 1 gives the soil properties of test site. And the results of standard penetration test (SPT) of various soil layers are depicted in Figure 1.

TABLE 2 Construction parameters of test piles.

Pile	Pile length/m	Pile section parameters		Hammer-driven		Penetration of last three hammer/mm		
		Pile section size/mm	Wall thickness/mm	Hammer weight/kN	Hammering distance/m			
1#	12 + 11	500	125	14	0.43	4.5	3.5	2.5
2#	12 + 11	500	125	14	0.43	4.5	4.8	4.5
3#	12 + 12	500	125	14	0.43	3.0	4.5	4.0
4#	12 + 13	500	125	14	0.43	5.5	5.0	5.0
5#	13 + 12	500	125	14	0.43	4.5	3.5	3.0
6#	13 + 12	500	125	14	0.43	5.5	3.5	3.0
7#	13 + 12	400	95	14	0.25	3.5	3.0	3.0
8#	12 + 13	400	95	14	0.25	5.0	4.5	4.5

## 2.2 Test design

The test contains eight pipe piles with 400 mm or 500 mm diameter. Figure 2 depicts the ground plan of the test piles. The spacing between each pile is 5 m. High strain dynamic tests and static load tests are carried out on piles 1# to 8# piles. For the purpose of analyzing the variation law of the axial force and deformation of pile during the study of static load test, slide micrometers are embedded into the 1#, 3#, 5#, 6#, and 7# piles, and parallel embedded in symmetrical parts.

The 1# and 2# pile length is 23 m, 3# pile length is 24 m, and 4#, 5#, 6#, 7#, and 8# pile length is 25 m. The test piles were driven by D50 diesel hammer pile driver. The construction parameters are shown in Table 2. The hammering can be terminated when the final three hammer penetrations fulfill the specification of the design.

## 2.3 Test method

The high strain dynamic test is done several months after pile installation. The high strain dynamic test employs the eighth generation American-made Pile Driving Analyzer (PDA), free fall hammer hammering, and theodolite testing penetration (Figure 3). Each pile was hammered with an 80 kN hammer at a drop distance of 0.8 m–2.0 m, and four to five times. The hammering distance starts from 0.8 m and gradually increases until the pile end resistance is fully developed. The data sampling time is 200 ms and sampling frequency is 10 kHz. According to the JGJ106-2003 of Chinese technical code for testing of building foundation piles (JGJ106-2003, 2003), two full-bridge strain sensors and two accelerometer sensors are affixed externally at diametrically opposite direction on the pile near ground surface about 1.0 m.

To perform CAPWAP automatic signal matching analysis, good quality high strain dynamic test data are required. An assumption of unknown soil parameters is made and tested by performing an analysis with one of the measured quantities as a top boundary condition. If there is disagreement between the other measurement and its calculated counterpart, the calculation is repeated with a corrected set of soil model parameters.

The static load test is conducted 30 days after the high strain dynamic test. The static load test utilizes the conventional platform stacking method and the slow maintenance load method to measure the settlement of the pile cap via the displacement sensor located on the pile top. The initial stage of loading is 800 kN, and then each subsequent load is raised by 400 kN until the termination loading condition of experiment is reached, and each unloaded stage has a force of 800 kN. After each level of load is applied, the settlement of pile top shall be measured and read according to the 5th, 10th, 20th, 35th, 50th, and 65th minutes, and then measured every 30 min.

Through the incorporated sliding micrometer on the inner side of the pile body (1#, 3#, 5#, 6#, and 7# pile), a cone-shaped measuring ring is mounted on the HPVC measuring pipe every 1 m. The strain of the pile body under various loads of static load test is measured, and the axial force of the pile body of each test section is computed so that friction, end resistance, and pile-soil relative displacement may be determined. Figure 4 depicts the

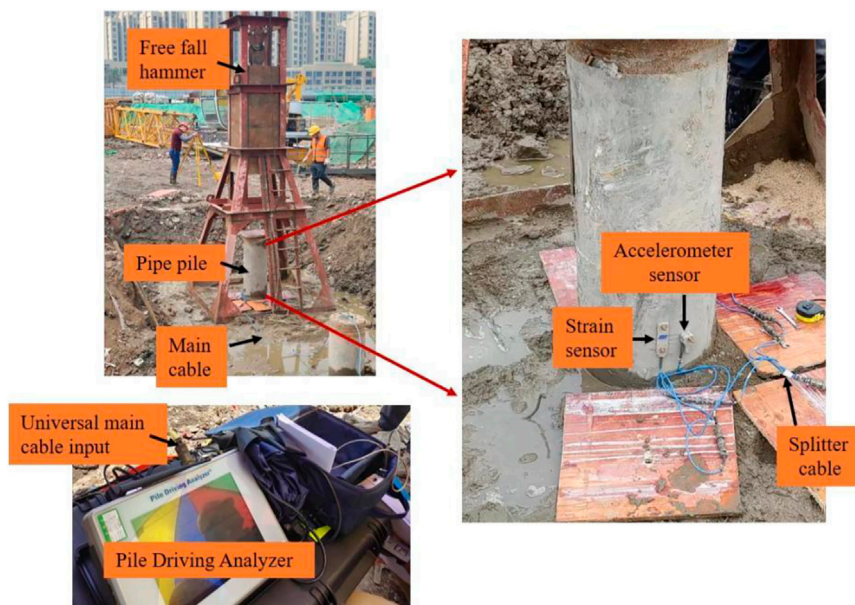


**FIGURE 3**  
The test site of HSDT with PDA.

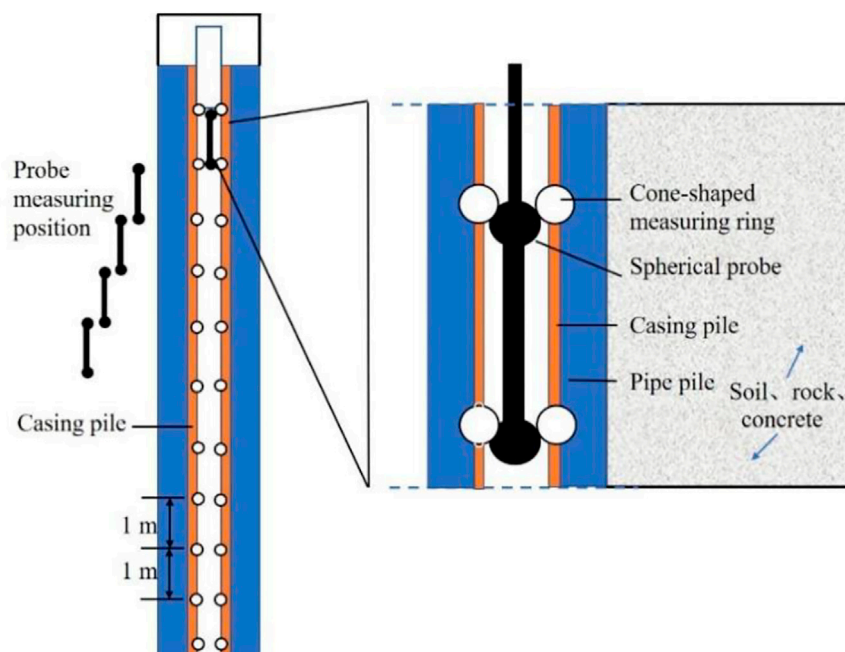


**FIGURE 4**  
Schematic diagram of embedding sliding micrometer.

borehole instrumentation with line measurement instruments (measuring mark and casing).

The upward traveling resistance waves of pile are presented in Figure 5, and the resistance of the upward wave  $F_u$  is depicted in Eq. 1.

$$F_{u2} = \frac{1}{2}R_i + R_d - F_{d1} + \frac{1}{2}R_i \quad (1)$$

where  $R_i$  is shaft resistance,  $R_d$  is the resistance,  $F_{d1}$  is the resistance of the traveling downward wave towards the pile toe at time  $t_1$ . The  $t_1$  is designated as the time when the impact wave passes the sensor

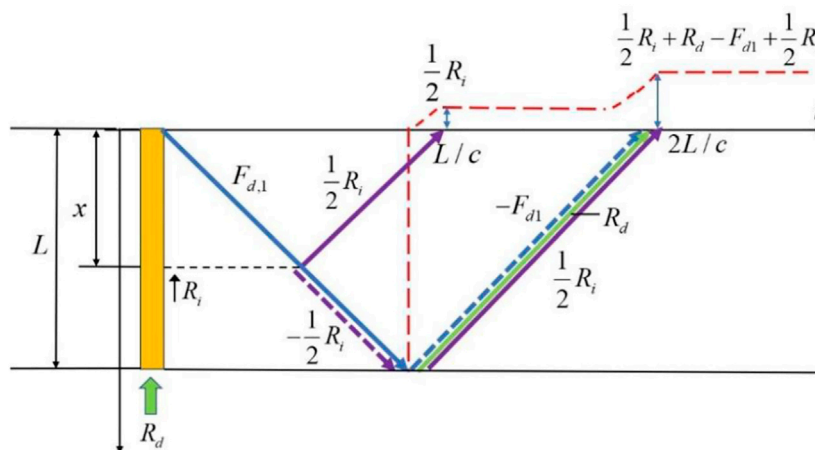


**FIGURE 5**  
The upward traveling resistance waves of pile (Smith, 1960).

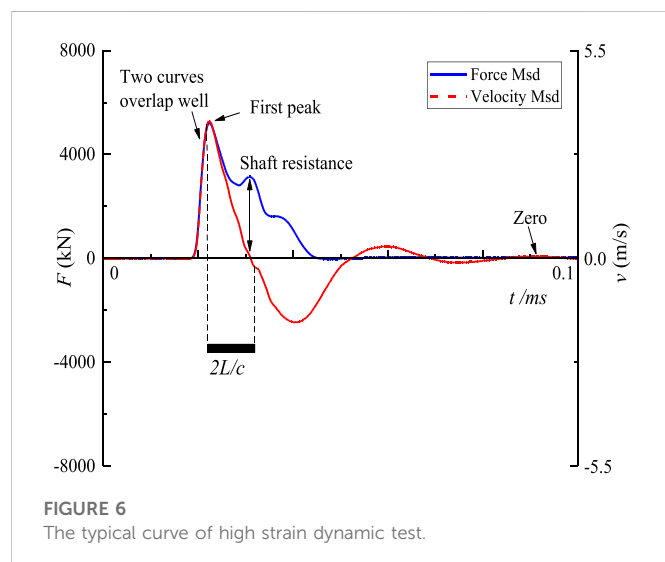


**FIGURE 6**  
The typical curve of high strain dynamic test.

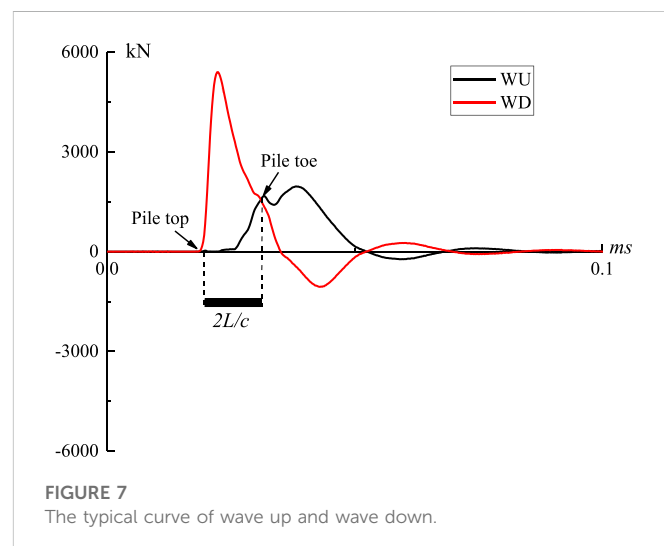


**FIGURE 7**  
The typical curve of wave up and wave down.

**TABLE 3** The ratio of settlement value to pile diameter.

Pile pile	Q/kN	s/mm	D/mm	Ratio (%)
1#	4,400	56.54	500	11.31
2#	3,600	41.17	500	8.23
3#	4,800	52.55	500	10.51
4#	5200	60.81	500	12.16
5#	5200	46.24	500	9.25
6#	5600	56.30	500	11.26
7#	2,400	67.99	400	16.99
8#	3,600	48.43	400	12.11

location and the time  $t_2$  is designated as the time when the toe reflected impact wave returns to the sensor location ( $t_2$  is equal to  $t_1$  plus  $2L/c$ ) (Green and Kightley, 2005a; Zhao, 2005; Ding et al., 2013).

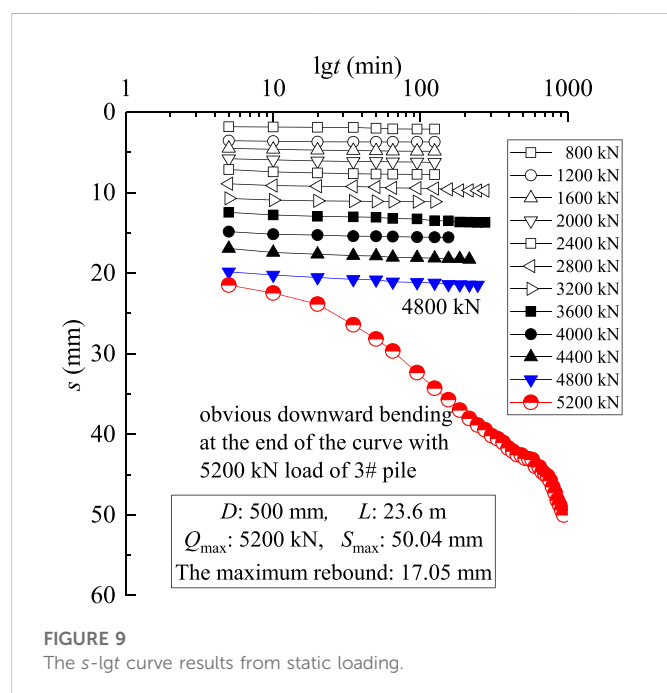
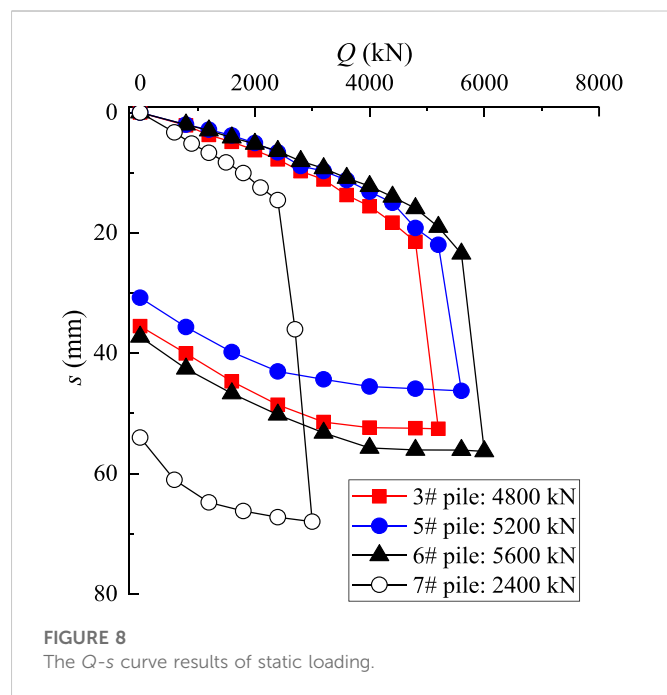
## 3 Analysis of results

### 3.1 High strain dynamic test

Figure 6 depicts the typical curve of HSDT in this site and the results are obtained from with CAPWAP analysis. The high strain dynamic test with CAPWAP analysis performs a wave equation form by using the velocity records as pile-top boundary conditions. The measured (Msd) force value and velocity value with CAPWAP analysis are shown in Figure 6. The cases exhibit a good proportionality between force and velocity impedance at the onset of impact. Two curves overlap well before the first peak, which shows the success of fitting between force and velocity curves. The maximum of force and velocity is 5211.43 kN and 3.63 m/s respectively. For the existence and development of shaft resistance, the two curves are seen clearly to depart sharply after the first peak. And the two curves are seen to depart sharply near the pile toe from the force time history.

Figure 7 shows the typical curves of wave up (WU) and wave down (WD) in the site. The pile top can be considered as the starting point of the

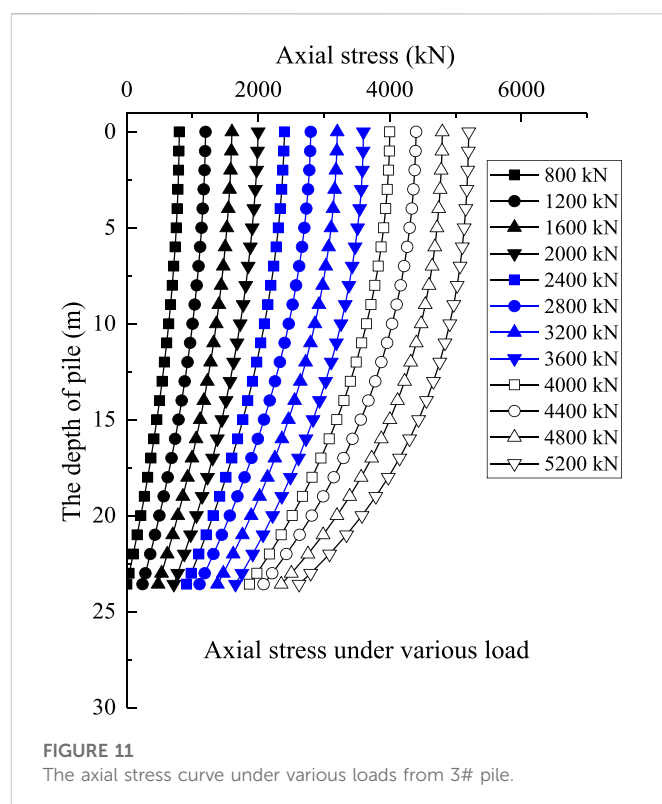
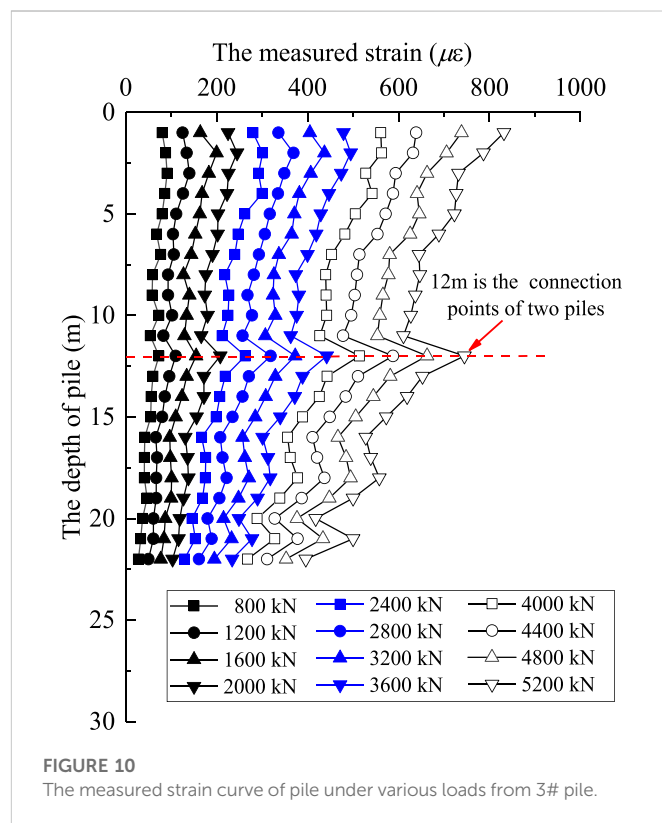




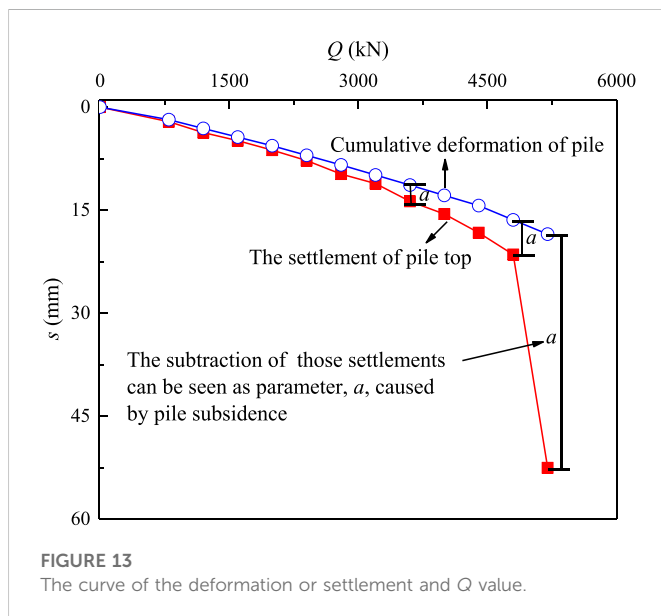
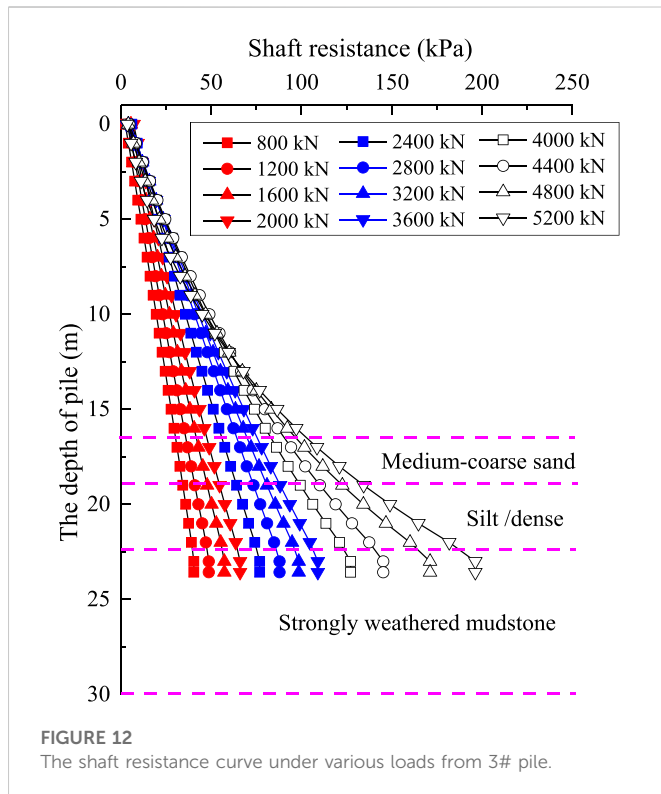
rising of WD, while the pile toe represents the starting point of the falling of WU. The duration of  $2L/c$  is clearly illustrated in Figures 6, 7.

### 3.2 Static loading test

Figure 8 depicts the Q-s curve results of static loading. The 3#, 5#, 6#, and 7# piles have reached the state of failure, and the curves exhibit steep drop characteristics. In addition, the curves demonstrate that the four piles are the typical friction piles. The ultimate bearing capacity of a single pile is the load value at the



starting point of a steep drop section, according to the Chinese building foundation testing code (Briaud and Tucker, 1984). Taking list 3# pile as an example, the beginning of a sharp decline in settling begins below 4,800 kN. The ultimate bearing capacities of 3#, 5#,



6#, and 7# piles are therefore 4,800 kN, 5200 kN, 5600 kN, and 2,400 kN, respectively.

The ratio of settlement value to pile diameter is displayed in Table 3 for all test pipe piles. Extensive practical experience demonstrates that the ultimate load may occur only when the settlement reaches 10% of the pile's diameter (Smith, 1960). The ratio of settlement to pile diameter for the majority of piles exceeds 10%, and the max ratio value is 16.99% from 7# pile. Considering the steep drop characteristics and highly weathered argillaceous siltstone of the pile tip bearing stratum, it can be concluded that the bearing capacity of the foundation was completely developed during the static load test.

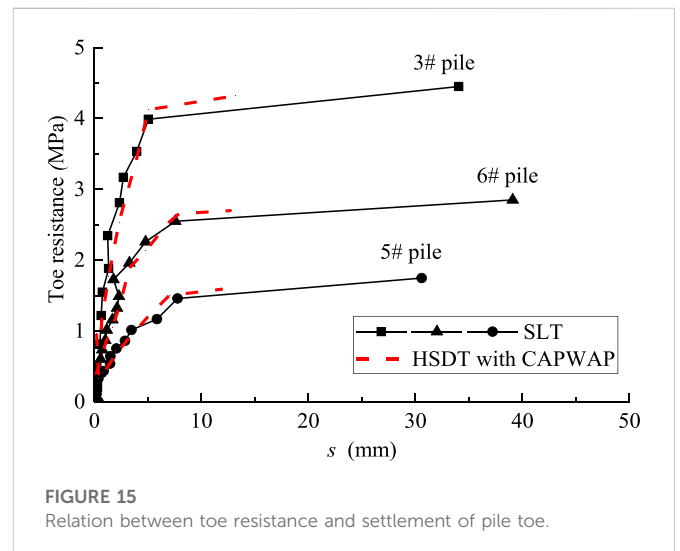
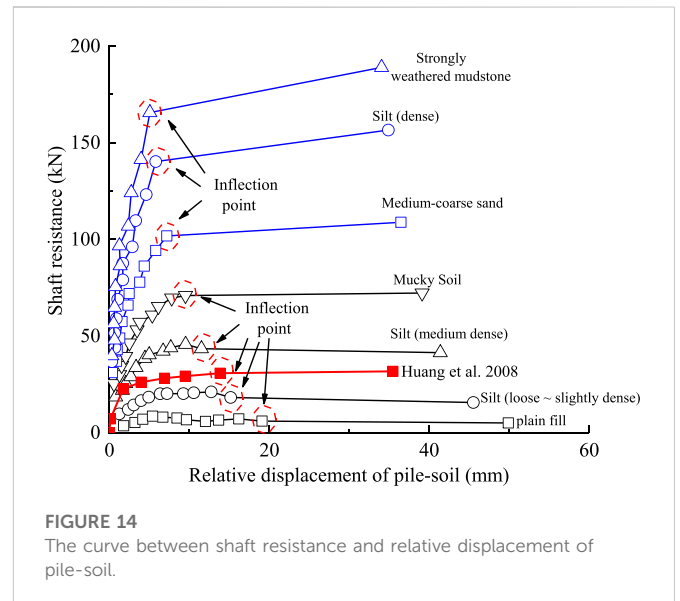


Figure 9 illustrates the  $s$ - $lgt$  curve results of 3# pile from static loading. When the load is increased from 800 kN to 4,800 kN (the twelfth load), the settlement does not decrease appreciably and a steep decline trend do not appear. However, when the load is increased to 5200 kN (the thirteenth load), the curve demonstrates a clear decreasing tendency. Consequently, the ultimate bearing capacity from the  $s$ - $lgt$  curve results is also 4,800 kN, which is equal to the result from the  $Q$ - $s$  curve. During the unloading test, the maximum settlement is 52.55 mm, and the ultimate residual settlement is 35.50 mm. Maximum rebound value is 17.05 mm, and the rate of rebound is 32.45%.

### 3.3 Sliding micrometer

The strain of the pile shaft axis under various loads can be measured continuously by embedding test elements in the pile body. The internal force test of pile body is calculated by the corresponding strain. It can be seen from Figure 10 demonstrates that under the condition of small load (800 kN), the strain change from the pile body to the pile end is minimal.

TABLE 4 Average value of unit friction resistance of each soil layer (kPa).

Soil	Slide micrometer	High strain dynamic test	Code for design of building foundation DBJ15-31-2016	Correction value of code
Plain fill	18	37	20 ~ 28	16 ~ 22
Silt/loose ~ slightly dense	55	38	22 ~ 44	18 ~ 35
Silt/medium dense	94	65	42 ~ 64	42 ~ 64
Mucky soil	119	83	20 ~ 28	21 ~ 29
Medium-coarse sand	137	112	94 ~ 116	107 ~ 125
Silt/dense	185	247	64 ~ 86	72 ~ 96
Strongly weathered mudstone	202	251	160 ~ 240	181 ~ 271

TABLE 5 The contrast from test results by SLT and HSDT.

Pile no.	Max load/kN	Finally settlement/mm	Bearing capacity by SLT/kN	Bearing capacity by HSDT/kN	Contrast/%
1#	5600	56.54	4,400	4,862	10.50
2#	4,000	41.17	3,600	4,131	14.75
3#	5200	52.55	4,800	4,637	-3.39
4#	5600	60.81	5200	5500	5.77
5#	5600	46.24	5200	4,990	-4.04
6#	6,000	56.30	5600	4,910	-12.32
7#	3,000	67.99	2,400	2,300	-4.17
8#	3,900	48.43	3,600	3,400	-5.56

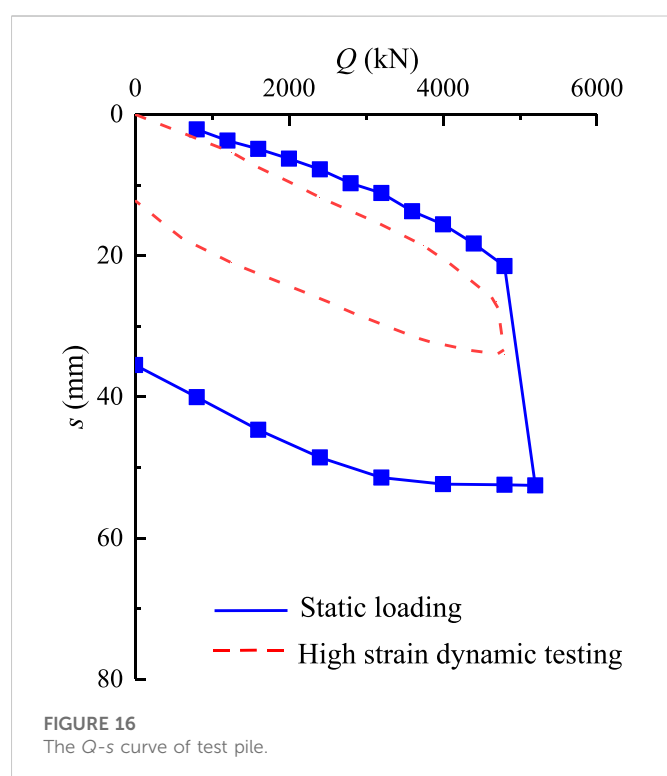
The pile stress is the largest at the pile depth of about 12 m, and the stress at the pile end is the smallest, but the overall stress of the pile body is relatively uniform; as the load on the top of the pile increases, the strain around the pile body tends to be unevenly distributed. When the load on the top of the pile is 5200 kN, the strain at a distance of 12 m from the top of the pile is extremely high, and drops abruptly downward. The construction record indicates that 12 m is the piles' connecting point. When it reaches approximately 18 m and 21 m from pile top, it reaches a small peak, but the measured strain is less than 12 m. It decreases sharply to the minimum at the bottom of the pile, indicating that the pile body begins to enter the plastic stage under high load.

Figure 11 demonstrates that the axial stress of the pile body decreases as the increasing of the test pile depth under the loading of the pile top. This indicates that the pile top load is mainly offset by the pile shaft resistance, which is consistent with the relevant characteristics of friction piles.

The soil strength is reflected by deformation and increases in proportion to the degree of deformation. Likewise, the friction resistance increases as the relative displacement between piles and soil. Figure 12 demonstrates that as the load increases, so does the friction resistance. At different depths of the same soil layer, the friction resistance varies, and the friction resistance of each soil layer increases to varying degrees along the pile depths. In contrast to prior research, in this test the friction resistance in the deep portion of the pile has not decreased, which is mainly due to the hard soil layers of medium coarse sand, silty sand, and severely weathered mudstone.

Before loading 4,800 kN, the load on the pile top is provided by the friction resistance of the pile body, the settlement of the pile is the compression of the pile body, and the toe resistance of the pile is not exerted as shown in Figure 13. With the increase of the load to 4,800 kN, the cumulative deformation and the settlement curves of the pile top are separated, the pile tip begins to subside, and the toe resistance gradually increases with the load.  $a$  is the settlement caused by pile subsidence.

Figure 14 depicts the curve between relative displacement of pile-soil and shaft resistance at the base of each soil layer. The pile shaft resistance is closely related to the relative displacement of the pile-soil. Regardless of the soil layer, the pile shaft resistance increases as the pile-soil relative displacement increases. When the relative displacement of pile-soil reaches a certain extent (Inflection point), the change in pile shaft resistance is negligible, indicating that the pile shaft resistance is fully mobilized. However, the shaft resistance still has an increasing trend, but the increasing trend is small, indicating that the pile shaft resistance has not yet been fully mobilized, such as in the soil layer composed of medium-coarse sand, silt, and strongly weathered mudstone. And this phenomenon is comparable to the research conclusion reached by Huang et al. (2008) (JGJ106-2003, 2003). As a novel notion, the inflection point is crucial for evaluating the relationship between shaft resistance and displacement of pile.



### 3.4 Comparative analysis

Figure 15 depicts the relationship curve between unit toe resistance and toe displacement of 3#, 5# and 6# piles, derived based on the axial stress test results from static load test. In accordance with the rule depicted in Figure 14, soil resistance is proportional to displacement. Under the same displacement, when the pile toe displacement is small, the toe resistance calculated by the high strain dynamic test is less than that calculated by the static load test. However, when the displacement is large, the toe resistance calculated by the high strain dynamic test is higher than that calculated by the static load test. Due to the difference in soil resistance, the settlement calculated by dynamic test is greater than that measured by static load test when the vertical load is small (pile displacement is small), whereas the settlement calculated by dynamic test is smaller than that measured by static load test when the load is large (pile displacement is large).

Table 4 displays the average value of unit friction resistance of each soil layer from each of the five piles (1#, 3#, 5#, 6#, and 7#). The test results of 5 test piles indicate that the unit friction resistance of the upper soil layer measured by a slide micrometer is greater than that measured by a high strain dynamic test, but those of the deeper soil layer tested are smaller than that from the high strain dynamic test; the friction resistance of the soil layer is closely related to its depth.

Figure 16 demonstrates the Q-s curve of the test pile. When the pile top load is small, the settlement calculated by high strain is close to the measured result of static load test; when the pile top load is large, especially when the pile is close to the failure condition, the settlement calculated by high strain dynamic test is obviously less than the static load test result. Table 5 compares the results of the high strain dynamic test and static load test. The errors from high strain dynamic test and static load test are within 15%.

## 4 Conclusion

The bearing capacity of PHC pipe piles in Chancheng district was successfully completed *via* high strain dynamic testing and static load test. This paper investigated a suitable tool HSDT using the PDA and SLT with the sliding micrometer. In Chancheng district of China, CAPWAP analyses by an American-imported PDA tool were successfully completed, and signal matching was accomplished. The following specific conclusions may be drawn.

1. A new concept of “inflection point” is proposed between shaft resistance and relative displacement of pile-soil. The pile shaft resistance increases as the pile-soil relative displacement increases. When the relative displacement of pile-soil increases to a certain extent, that is “Inflection point”, the change of pile shaft resistance is negligible.
2. The relationship between toe resistance and settlement of pile is shown by comparing the SLT and HSDT. when the pile toe displacement is small, the toe resistance calculated by HSDT is lower than that by SLT, while when the displacement is large, the toe resistance calculated by HSDT is higher than that by SLT.
3. CAPWAP analysis were successfully completed and signal matching was achieved. The error between the SLT and HSDT is small, and within the acceptable range of 15%. It indicates that the HSDT could provide suitable results to assess the bearing capacity of PHC pipe piles in Chancheng district.

## Data availability statement

The raw data supporting the conclusions of this article will be made available by the authors, without undue reservation.

## Author contributions

XL is mainly responsible for revising manuscripts, project managements and can be used as the corresponding author. CL is mainly responsible for research methods, data analysis and draft writing, and can be the first author.

## Acknowledgments

Majority of the work presented in this paper was funded by the National Natural Science Foundation of China (Grant No. 41877231).

## Conflict of interest

The authors declare that the research was conducted in the absence of any commercial or financial relationships that could be construed as a potential conflict of interest.

## Publisher's note

All claims expressed in this article are solely those of the authors and do not necessarily represent those of their affiliated

organizations, or those of the publisher, the editors and the reviewers. Any product that may be evaluated in this article, or claim that may be made by its manufacturer, is not guaranteed or endorsed by the publisher.

## References

- Aghayarzadeh, M., Khabbaz, H., Fatahi, B., and Terzaghi, S. (2020). Interpretation of dynamic pile load testing for open-ended tubular piles using finite-element method. *Int. J. Geomechanics* 20 (2), 1–14. doi:10.1061/(ASCE)GM.1943-5622.0001564
- Alawneh, A. S., Nusier, O., Malkawi, A., and Al-Kateeb, M. (2001). Axial compressive capacity of driven piles in sand: A method including post-driving residual stresses. *Can. Geotechnical J.* 38 (2), 364–377. doi:10.1139/t00-104
- Alwalan, M. F., and Naggar, M. E. (2020). Analytical models of impact force-time response generated from high strain dynamic load test on driven and helical piles *comput. geotechnics* 11, 128. doi:10.1016/j.compgeo.2020.103834
- ASTM D4945 (2000). *Standard test method for high-strain dynamic testing of piles*. West Conshohocken, PA, USA: ASTM Int.
- Briaud, J. L., and Tucker, L. (1984). Piles in sand - a method including residual-stresses. *J. geotechnical engineering-ASCE* 110 (11), 1666–1680. doi:10.1061/(ASCE)0733-9410(1984)110:11(1666)
- Chen, R. B., Zhang, J. C., Chen, Z. Y., and Zhang, X. (2022). New mechanical model for evaluating bearing capacity of prestressed pipe piles in soil: Effect of soil layer. *J. Test. Eval.* 50 (3), 1–16.
- Choe, J., Hans, C., and Wold, J. (2002). Pile driving analysis for top hammering and bottom hammering. *J. Geotechnical Geoenvironmental Eng.* 128 (2), 174–182. doi:10.1061/(asce)1090-0241(2002)128:2(174)
- Ding, W., Liu, Q., Wang, B. Y., Sun, K. K., and Sui, F. T. (2013). Determining the pile bearing capacity by the curve match method of high strain dynamic testing. *Appl. Mech. Mater. Trans Tech Publ. Switz.* 438, 1414–1418. doi:10.4028/www.scientific.net/amm.438-439.1414
- Gates, M. (1957). Empirical formula for predicting pile bearing capacity. *Civ. Eng.* 27, 65–66.
- Green, T. A. L., and Kightley, M. L. (2005a). “CAPWAP testing - theory and application,” in Proceedings of the 16th International Conference on Soil Mechanics and Geotechnical Engineering: Geotechnology in Harmony with the Global Environment, Osaka, Japan, 2115–2118.
- Green, T. A. L., and Kightley, M. L. (2005b). CAPWAP testing-theory and application.
- Heins, E., Bienen, B., Randolph, M. F., and Grabe, J. (2020). Effect of installation method on static and dynamic load test response for piles in sand. *Int. J. Phys. Model. Geotechnics* 2 (1), 1–23. doi:10.1680/jphmg.18.00028
- Heins, E., and Grabe, J. (2019). FE-based identification of pile–soil interactions from dynamic load tests to predict the axial bearing capacity. *Acta Geotech.* 14, 1821–1841. doi:10.1007/s11440-019-00804-y
- Huang, L. J., Lin, Y. X., Cai, J., and Wan-qing, Z. (2008). Dynamic and static comparative analyses of settlements of overlength PHC pipe piles. *Rock Soil Mech.* 29 (2), 507–516. doi:10.3901/JME.2008.10.294
- JG106–2003 (2003). *Technical code for testing of building foundation piles*. Beijing China: China Architecture and Building Press. (in Chinese).
- Li, Z. L., and Gao, H. Y. (2012). The comprehensive application of high-low strain test in detecting pile foundations. *Appl. Mech. Mater.* 170, 191–194. doi:10.4028/www.scientific.net/AMM.170-173.1917
- Likins, G., Rausche, F., and Thendean, G. (1996). “CAPWAP correlation studies,” in Proceedings of the Fifth International Conference on the Application of Stress Wave Theory to Piles, Orlando, FL, USA, 447–455.
- Livneh, B., and El Naggar, M. H. (2008). Axial testing and numerical modeling of square shaft helical piles under compressive and tensile loading. *Can. Geotechnical J.* 45 (8), 1142–1155. doi:10.1139/t08-044
- Long, M. (2007). Comparing dynamic and static test results of bored piles. *Geotech. Eng.* 160 (1), 43–49. doi:10.1680/geng.2007.160.1.43
- Meyerhof, G. G., and Murdock, L. J. (1953). An investigation of the bearing capacity of some bored and driven piles in london clay. *Geotechnique* 3, 267–282. doi:10.1680/geot.1953.3.7.267
- Mohammed, S. (2013). Comparison between high strain dynamic and static load tests of helical piles in cohesive soils. *Soil Dyn. Earthq. Eng.* 54, 20–30. doi:10.1016/j.soildyn.2013.07.010
- Rajagopal, C., Solanki, C. H., and Tandel, Y. K. (2012). Comparison of static and dynamic load test of pile. *Electron. J. Geotechnical Eng.* 17, 1905–1914.
- Rausche, F., Goble, G. G., and Likins, G. E. (1985). Dynamic determination of pile capacity. *J. Geotechnical Eng.* 111 (3), 367–383. doi:10.1061/(asce)0733-9410(1985)111:3(367)
- Salgado, R., Zhang, Y. B., Abou-Jaoude, G., Loukidis, D., and Bisht, V. (2017). Pile driving formulas based on pile wave equation analyses. *Comput. Geotechnics* 81, 307–321. doi:10.1016/j.compgeo.2016.09.004
- Smith, E. A. L. (1960). Pile-driving analysis by the wave equation. *J. Soil Mech. Found. Eng.* 98 (9), 917–937. doi:10.1061/TACEAT.0008470
- Svinkin, M. R. (2019). Sensible determination of pile capacity by dynamic methods. *Geotechnical Res.* 6 (1), 1–67. doi:10.1680/jgere.18.00032
- Zhao, H. S. (2005). Errors study on Q-s Curve of pile simulated by high strain dynamic testing method. *Chin. J. rock Mech. Eng.* 24 (12), 2130–2135. doi:10.3321/j.issn:1000-6915.2005.12.021





## OPEN ACCESS

## EDITED BY

Xuelong Li,  
Shandong University of Science and  
Technology, China

## REVIEWED BY

Feng Du,  
China University of Mining and  
Technology, Beijing, China  
Yabin Gao,  
Taiyuan University of Technology, China

## \*CORRESPONDENCE

Xianguang Shang,  
✉ shangxianguang@hpu.edu.cn  
Zhihui Wen,  
✉ wenzhihui@hpu.edu.cn

## SPECIALTY SECTION

This article was submitted to  
Environmental Informatics and Remote  
Sensing,  
a section of the journal  
Frontiers in Earth Science

RECEIVED 06 January 2023

ACCEPTED 02 February 2023

PUBLISHED 13 February 2023

## CITATION

Shang X, Wei J, Wen Z, Shang L and  
Yuan J (2023), Determination of initial  
velocity of gas diffusion under  
temperature control.  
*Front. Earth Sci.* 11:1138828.  
doi: 10.3389/feart.2023.1138828

## COPYRIGHT

© 2023 Shang, Wei, Wen, Shang and  
Yuan. This is an open-access article  
distributed under the terms of the  
[Creative Commons Attribution License  
\(CC BY\)](https://creativecommons.org/licenses/by/4.0/). The use, distribution or  
reproduction in other forums is  
permitted, provided the original author(s)  
and the copyright owner(s) are credited  
and that the original publication in this  
journal is cited, in accordance with  
accepted academic practice. No use,  
distribution or reproduction is permitted  
which does not comply with these terms.

# Determination of initial velocity of gas diffusion under temperature control

Xianguang Shang<sup>1\*</sup>, Jianping Wei<sup>1,2,3</sup>, Zhihui Wen<sup>1,2,3\*</sup>,  
Linwei Shang<sup>4</sup> and Junling Yuan<sup>5</sup>

<sup>1</sup>College of Safety Science and Engineering, Henan Polytechnic University, Jiaozuo, China, <sup>2</sup>State Key Laboratory Cultivation Base for Gas Geology and Gas Control (Henan Polytechnic University), Jiaozuo, China, <sup>3</sup>State Collaborative Innovation Center of Coal Work Safety and Clean-efficiency Utilization, Jiaozuo, China, <sup>4</sup>Chongqing Vocational Institute of Safety and Technology, Chongqing, China, <sup>5</sup>School of Mechanical and Power Engineering, Henan Polytechnic University, Jiaozuo, China

**Introduction:** The initial velocity of gas diffusion ( $\Delta P$ ) of coal is an important index to characterize the outburst risk of coal, and temperature is an important factor affecting the determination of initial velocity of gas diffusion. However, how to control the temperature during  $\Delta P$  determination remains a significant challenge.

**Methods:** In this paper, an experimental system for  $\Delta P$  testing under temperature-controlled conditions was constructed, and the effect of temperature on the  $\Delta P$  determination results was further explored by accurately controlling the temperature of the testing system.

**Results:** The results show that the temperature change will affect the determination result of  $\Delta P$  in the range of 13°C–40°C, and the determination results do not show obvious regularity.

**Discussion:** The main reasons for the analysis are as follows: during the determination of  $\Delta P$ , although the higher the temperature is, the faster the speed of gas diffusion and the greater the amount of gas diffusion and the pressure produced in the first 60 s, but the smaller the amount of gas adsorption before release. There is a situation of mutual offset between the two, resulting in the fluctuation of  $\Delta P$  determination results. It is concluded that the temperature change will affect the determination of the initial velocity of gas diffusion, and when  $\Delta P$  is measured, the temperature of the experimental system should be consistent with the actual temperature of the sampled coal body as far as possible, so as to increase the reliability of the measured results for the prediction of coal and gas outburst. This paper provides an experimental basis for clarifying the industry standard of temperature related to  $\Delta P$ .

## KEYWORDS

gas diffusion, initial velocity, temperature, determination, coal

## 1 Introduction

The initial velocity of gas diffusion of coal is an index that indicates how quickly the coal containing gas changes from adsorption state to free state under the condition of complete exposure. The greater the initial velocity of gas diffusion, the stronger the initial gas release capacity of coal body, and the greater the outburst risk of coal seam (Liu and Wang, 2013; Liang et al., 2018; Sun, 2018). This index has been used as one of the indexes to judge the danger degree of coal and gas outburst in most countries in the world, and has been widely used (AQ1080-2009, 2009; Wang and Shi, 1991; Lu, 1992).

Many scholars have studied the influencing factors of this index and achieved fruitful results (Chen et al., 2012; Meng and Li, 2016; Du et al., 2020; Li et al., 2022; Lu et al., 2022). The effects of adsorption pressure, firmness coefficient, volatile matter, adsorption equilibrium time, and particle size on the initial velocity of gas diffusion have also been studied (Jianning, 2010; Xu and Jiang, 2011; Tan et al., 2012; Xu and Jiang, 2012; Yanwei and Mingju, 2015; Yang et al., 2022). Temperature is one of the important factors. Li et al. (Li and Jiang, 2009) pointed out that there is a quadratic relationship between the initial velocity of gas diffusion and the temperature difference through experiments and curve fitting in the temperature range of 20°C–24°C, and the higher the temperature is, the smaller the initial velocity of gas diffusion is. Guo, (2018) draws the conclusion that the initial velocity of gas diffusion decreases with the increase of temperature in the temperature range of 5°C–30°C through experimental analysis, and points out that the extent of the decrease is related to the initial velocity of gas diffusion of coal sample itself. Ma, (2017) thinks that there is a quadratic function relationship between temperature and initial velocity of gas diffusion in the temperature range of 15°C–35°C, and the initial velocity of gas diffusion increases with the increase of temperature before the extreme point, and decreases with the increase of temperature after the extreme point. Huang et al. (2019) pointed out that the error of the same coal sample is large when the experimental temperature is 10°C–30°C, which is caused by the influence of room temperature, and the follow-up study should fully consider the effect of room temperature on the initial gas diffusion velocity of coal. Guo et al. (2020) pointed out that the initial velocity of gas diffusion does not decrease in a straight line with the increase of temperature, and the change of temperature may affect the internal pressure of gas or the structure of coal matrix.

Although many people at home and abroad have made great contributions to the study of the influence of temperature on the determination results of the initial velocity of gas diffusion, in general, the precise control of temperature during  $\Delta P$  determination has rarely been reported. With the continuous increase of coal mining depth, the phenomenon of coal seam temperature increase occurs in many mines (Zheng et al., 2011), and the influence of temperature factors on coal and gas outburst is increasing. As the main prediction index of coal and gas outburst, the initial velocity of gas diffusion has no clear requirement for temperature in the industry standard for its determination, so there is an urgent need to study the influence of temperature factors on its determination and define the standard.

This paper constructs the  $\Delta P$  determination system under the condition of temperature based on the instrument for measuring the initial velocity of gas diffusion developed by Henan Polytechnic University, and realizes the accurate control of the temperature of the test system. The experiment was carried out strictly according to the technical standard of AQ 1080-2009 (AQ1080-2009, 2009), and the effect of temperature on the initial velocity of gas diffusion was further studied. It is concluded that in the temperature range of 13°C–40°C, the temperature change will affect the determination results of  $\Delta P$ , and the determination results do not show obvious regularity. This paper provides an experimental model and some data support for the further study on the temperature influencing factors of  $\Delta P$  determination.

## 2 Experimental

### 2.1 Coal sample collection

Four coal samples were selected for experiment in this paper in order to make the experimental results comparable. Coal sample 1 is a soft coal collected from the excavation head of 16041 transportation roadway in Jiaozuo Jiulishan Coal Mine, which is numbered JR. Coal sample 2 is hard coal collected from 16021 transportation roadway in Jiaozuo Jiulishan Coal Mine, numbered JY. Coal sample 3 is a soft coal collected from 3101 working face of Hebi No. 8 Coal Mine, which is numbered HR. Coal sample 4 is hard coal collected from 3103 working face of Hebi No. 8 Coal Mine, numbered HY. The specific sampling locations is shown in Figure 1.

In order to fully understand the properties of coal samples, four coal samples were analyzed industrially according to the industrial analysis method of coal (GB/T212-2008). The results are as follows, as shown in Table 1.

### 2.2 Sample preparation

According to the regulations of GB474 and GB477 in China, the collected coal samples were crushed and sieved with particle size of 0.2–0.25 mm. The production process of coal sample is shown in Figure 2. Two specimens are taken from each coal sample, each weighing 3.5 g. Meanwhile, keep the spare coal sample for repeated experimental verification.

### 2.3 Experimental installation

The initial velocity of gas diffusion determination system under temperature-controlled conditions constructed in this paper is mainly composed of five parts: the initial velocity of gas diffusion determination instrument, glass water tank, constant temperature water bath, gas cylinder and vacuum pump. The instrument for measuring the initial velocity of gas diffusion is developed by Henan Polytechnic University. The glass water tank is self-built. Constant temperature water bath is produced by Chongqing Huida Experimental instrument Co., Ltd. Other auxiliary experimental equipment include WY-98B adsorption constant tester, electronic scale, distiller, sealed hammer crusher, mercury thermometer, and so on.

In order to clearly show how to accurately control the temperature of the system, the system model diagram is drawn, as shown in Figure 3. The realization process of temperature control: Appropriate amount of water is injected into the glass tank, and then the well-sealed initial velocity of gas diffusion determination instrument is placed in it to maintain immersion. The constant temperature water bath is connected with the glass water tank, and the temperature of the water in the tank is controlled by the constant temperature water bath, so as to realize the accurate control of the temperature of the  $\Delta P$  determination system. Two thermometers are placed vertically on both sides of the tank to compare and monitor whether the water temperature is stable at the set temperature.

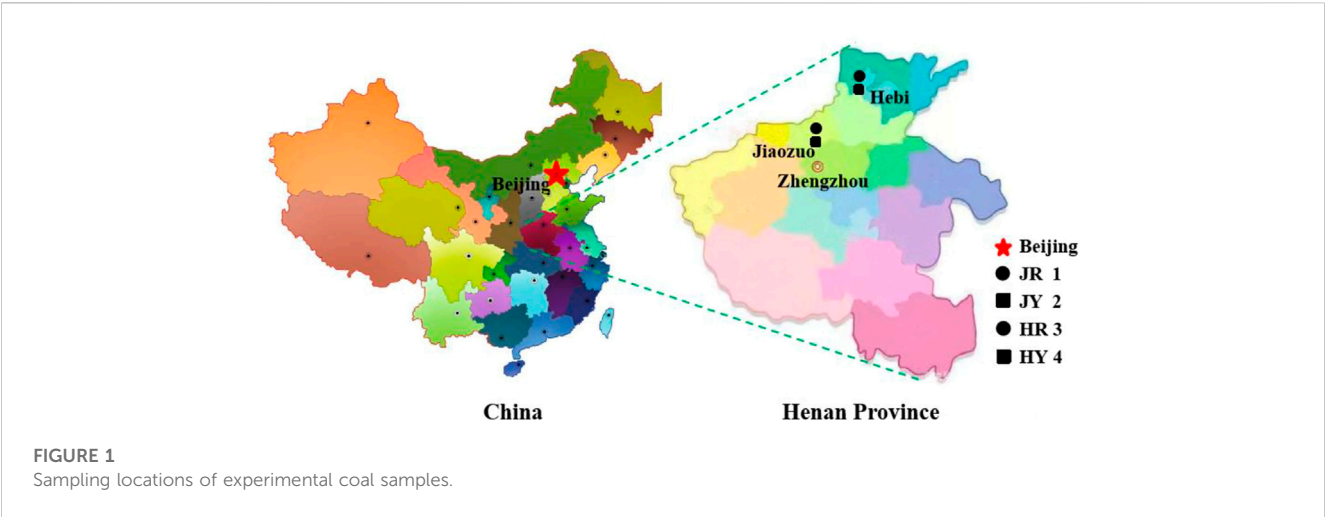


TABLE 1 Basic information and parameters of experimental coal samples.

Sample	Sampling location	$M_{ad}$ (%)	$A_{ad}$ (%)	$V_{daf}$ (%)	$FC_{ad}$ (%)
JR	Jiulishan Mine, Jiaozuo mining area	3.07	11.33	6.28	79.02
JY	Jiulishan Mine, Jiaozuo mining area	2.05	21.1	7.02	69.33
HR	Hebi No. 8 Mine, Hebi mining area	2.2	15.86	11.03	70.46
HY	Hebi No. 8 Mine, Hebi mining area	1.42	9.97	12.42	76.08

Note:  $M_{ad}$ ,  $V_{daf}$  and  $FC_{ad}$  are the moisture, ash, volatile matter, and Fixed Carbon contents on the air-dried basis, respectively.



2.4 Experimental process and results

The experiment was carried out strictly according to the technical standard of AQ 1080-2009 (Liang et al., 2018). In order

to accurately describe the process of the experiment, this paper makes a schematic diagram of the determination system, as shown in Figure 4. The specific experimental process is as follows:

2.4.1 Sample preparation

The coal sample with particle size of 0.2–0.25 mm was prepared according to the 2.2 method. In this experiment, there are 4 coal samples. In order to make the experimental results reliable, two samples are taken from each kind of coal sample, one of which is used as a parallel comparison of coal samples. A total of 8 samples, each sample weighs 3.5 g.

2.4.2 Sample loading

Eight samples were packed in 8 sample bottles by funnel. Sample bottle 1 and 5 are filled with JR, sample bottle 2 and 6 are filled with JY, sample bottle 3 and 7 are filled with HR, and sample bottle 4 and 8 are filled with HY. The latter is the parallel comparison sample of the former.

2.4.3 Temperature selection

The temperature range selected in the experiment is 13°C–40°C. A total of 6 temperature points were selected, which are 13°C, 18.5°C, 23°C, 28°C, 35°C and 40°C. There are three factors to consider: the first is the temperature environment of the coal mine around 20°C in the actual production; the second is the development trend of temperature rising with the increase of mine mining depth; the third is to find the linear law of  $\Delta P$  changing with temperature.

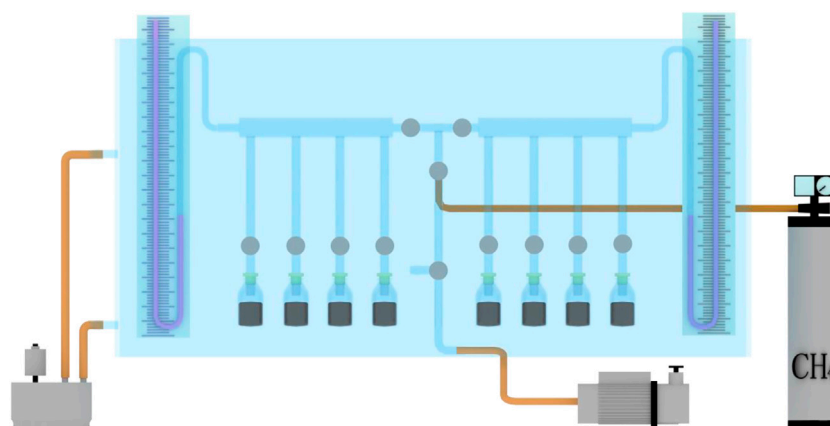


**FIGURE 3**  
System model for measuring the initial velocity of gas diffusion under temperature control.

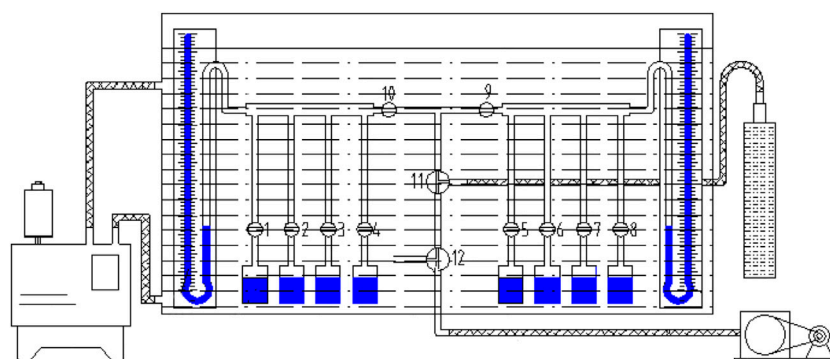


**FIGURE 4**  
The Schematic diagram of  $\Delta P$  determination under temperature condition.

## 2.4.4 Test

**Step 1:** Check the test system, set the first temperature point to be investigated at 13°C, and start heating. Enter the second step after it is constant at 13°C. The temperature of water in the tank was observed by the two thermometers.

**Step 2:** Open all coal sample channels, open valves 9 and 10, rotate three-way valves 11 and 12 to the position where they are connected up and down, and start the vacuum pump to degas the coal sample for 90 min.

**Step 3:** After 90 min of degassing, turn off the vacuum pump, and then rotate valve 11 to connect methane bottles and all coal sample bottles. Gas is charged to make coal samples absorb gas for 90 min, and the charging pressure is maintained at 0.1 MPa.

**Step 4:** Close the methane bottle and all coal sample bottles in order to isolate the coal sample bottle from the methane bottle.

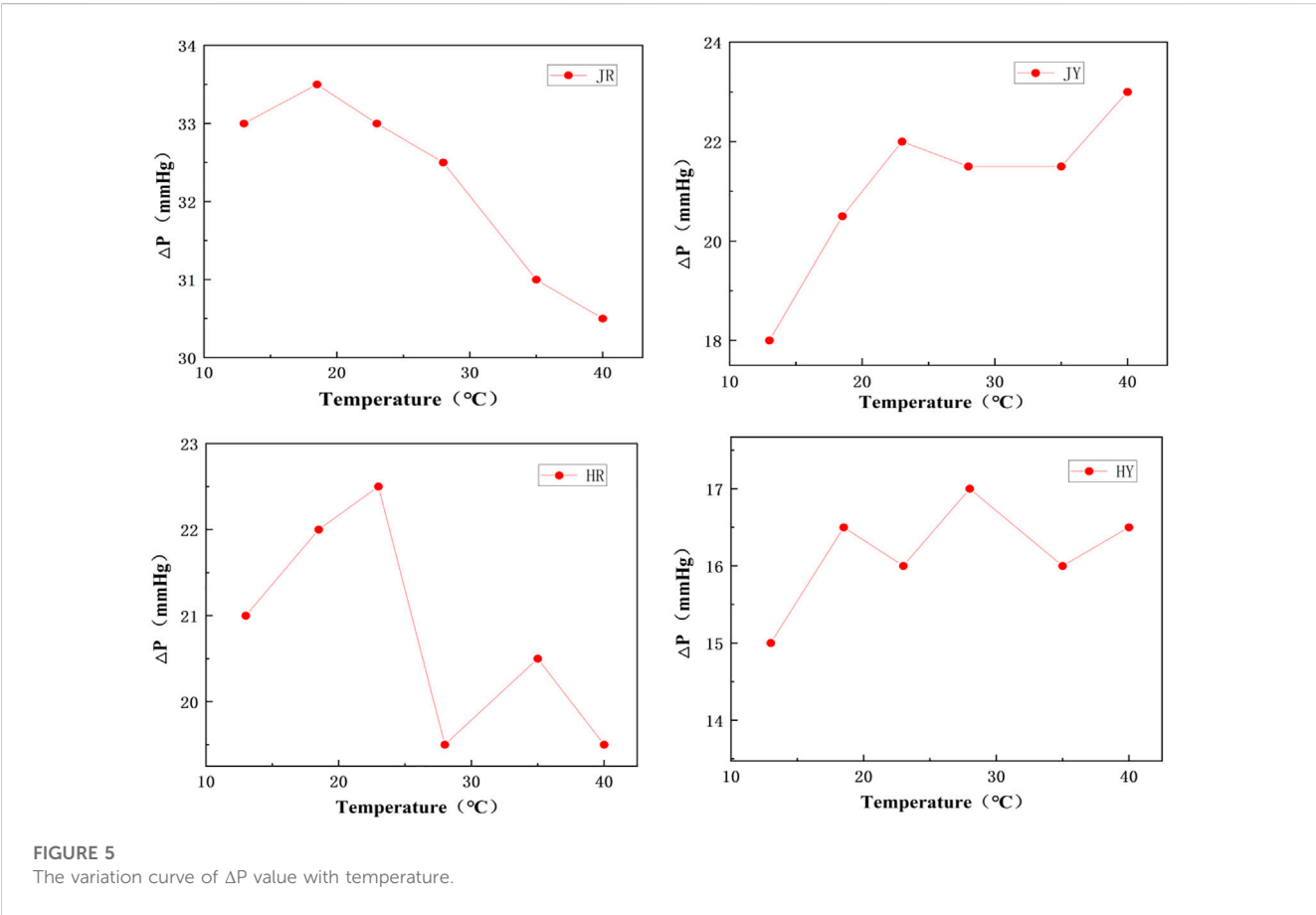
**Step 5:** Rotate the three-way valves 11 and 12 to the position of the upper and lower connection, and start the vacuum pump to degas the dead space of the instrument, so that the liquid level of the mercury column at both ends of the U-shaped mercury column meter is level.

**Step 6:** Close valve 12, stop the vacuum pump, then close valve 10. Open the coal sample bottle 1, start the stopwatch timing when the coal sample bottle is connected to the dead space of the instrument, close valve 1 at 10s, write down the upper and lower liquid level readings of the mercury column meter on the left, and get the  $P_1$  value. Open the valve 1 again at 45 s and close valve 1 again at 60 s, read out the upper and lower liquid level readings of the mercury column meter again, get the  $P_2$  value, and then calculate the  $\Delta P$  value of coal sample 1 at the temperature of 13°C.

**Step 7:** Close the coal sample bottle 1 and complete the coal sample 1 test. Open valve 10 and 12, start the vacuum pump to degas the dead space of the instrument, so that the mercury column surfaces at

TABLE 2 The  $\Delta P$  determination results under temperature condition.

Temperature (°C)	JR (mmHg)	JY (mmHg)	HR (mmHg)	HY(mmHg)
13	33	18	21	15
18.5	33.5	20.5	22	16.5
23	33	22	22.5	16
28	32.5	21.5	19.5	17
35	31	21.5	20.5	16
40	30.5	23	19.5	16.5



both ends of the U-shaped mercury column meter are level. The same method is used to complete the test of coal sample 2, 3 and 4  $\Delta P$  value in turn. The same steps are used to complete the test of  $\Delta P$  values of four parallel coal samples 5, 6, 7 and 8 on the right.

**Step 8:** After all the tests are completed, the difference between the left coal sample and the corresponding right parallel coal sample  $\Delta P$  is calculated. If the difference between the two is greater than 1, the test result of this group is invalid, and the sample is reloaded for testing. If the difference is less than 1, the maximum value of the two will be taken as the determination result of the coal sample. Finally, the determination results of 4 groups of coal samples under 13 °C temperature condition are obtained.

The  $\Delta P$  values of four coal samples at 18.5°C, 23°C, 28°C, 35°C and 40°C are obtained by re-setting the temperature of thermostatic water bath and repeating the above steps. The results are shown in Table 2.

### 3 Discussion and results

#### 3.1 Experimental analysis

From Figure 3 we can see that the instrument for determination of initial velocity of gas diffusion is always immersed in a constant temperature tank in this experiment, the water temperature is



controlled by a thermostatic water bath. The temperature difference is less than 1 °C up and down, and the temperature is relatively constant. The difference between the experimental process and the previous experiments is that when measuring the  $\Delta P$  value at a certain temperature point, the constructed constant temperature system can not only ensure that the temperature of the coal sample is the set temperature, but also ensure that the temperature of the whole test system is constant at the set temperature. It is not affected by room temperature. This scheme greatly improves the reliability and accuracy of the temperature condition in the determination of  $\Delta P$ .

According to the experimental results of 2.4, the variation curves of initial velocity of gas diffusion at different temperatures of JR, JY, HR, and HY are drawn respectively, as shown in Figure 5.

From Figure 5 we can see that in the temperature range of 13°C–40°C, the initial velocity of gas diffusion jumps up and down with the increase of temperature, showing no obvious regularity. From the span, JR is 3, JY is 5, HR is 3, HY is 1.5, compared with the critical value 10, this is enough to affect people's judgment on the risk of coal and gas outburst. From a macro point of view, the initial gas emission rate of soft coal in Jiaozuo Jiulishan Mine and Hebi No. 8 Coal Mine shows a decreasing trend with the increase of temperature, while their corresponding hard coal shows a rising trend. Preliminary judgment: for hard coal, the effect of temperature rise on gas diffusion rate is greater than that on adsorption, while soft coal is the opposite.

## 3.2 Discussion

This paper focuses on the influence of temperature on the determination of the initial velocity of gas diffusion. According to the definition of  $\Delta P$ ,  $\Delta P$  is the difference between the pressure  $P_1$  generated by gas diffusion of coal sample in the first 10 s and the pressure  $P_2$  produced by gas diffusion of coal sample within 45–60 s, provided that the basic measurement conditions such as adsorption equilibrium pressure and particle size remain unchanged. In general, the determination result is reflected in the amount of gas emission in the first 60 s of coal sample, which is related to the gas emission rate and the initial adsorption capacity of coal sample. Therefore, the discussion of the influence of temperature on the initial velocity of gas diffusion becomes the discussion of the influence of temperature on the rate of gas emission and the initial gas adsorption capacity in the first 60 s.

### 3.2.1 Analysis of the influence of temperature on gas diffusion rate

Liu et al. (2013) concluded that the increase of temperature greatly improves the diffusion ability of gas in coal particles by enhancing the activity of methane molecules and strengthening the expansion of pores, especially small pores. Gao, (2013) proved that in the temperature range of 25°C–45°C, under the same pressure condition, the higher the temperature, the greater the rate of gas desorption, and the maximum rate is in the first 60 s, and tends to be consistent after 3 min. Li (Hong, 2011) believes that in the temperature range of 20°C–60°C, under the same pressure, the higher the temperature, the greater the gas desorption rate, and the maximum gas desorption rate is in the first 60 s. He, (2010)

demonstrated that in the temperature range of 10°C–40°C, the higher the temperature, the higher the gas desorption rate and the greater the desorption amount in the same time. Based on the above research, it can be concluded that the higher the temperature, the faster the gas emission rate, and the greater the gas emission amount in the first 60 s, which means that the effect of temperature on the determination results of initial velocity of gas diffusion is positively correlated from the perspective of gas diffusion rate.

### 3.2.2 Analysis of the influence of temperature on initial adsorption amount of gas

Wang et al. (2016); (Zhang et al., 2009); (Chen et al., 1995); (Zhong et al., 2002); (Wang et al., 2011); (Liu et al., 2012); (Cai et al., 2019); (Wang et al., 2022) and others found that the amount of gas adsorption gradually decreased with the increase of temperature. It is generally accepted that the adsorption amount decreases by 8% for a 1 °C temperature increase. Based on the previous research results, from the perspective of gas adsorption, the higher the temperature, the smaller the initial adsorption capacity of coal sample before  $\Delta P$  determination. From this point of view, the effect of temperature on the determination of the initial velocity of gas diffusion is negatively correlated.

### 3.2.3 Analysis of the influence of temperature on gas diffusion pressure

The temperature has an effect on the pressure under the condition of constant diffusion space. The initial velocity of gas diffusion determination instrument used in this paper is of variable volume and pressure type. According to the research results of Lu, (1992),  $\Delta P$  is not only related to the amount of gas diffusion to be measured, but also related to the volume of the dead space of the instrument and the tube diameter of the manometer. The sum of the dead space of the instrument and the space produced by the change of the pressure gauge is the diffusion space of the experimental coal sample. Here, according to the ideal gas state equation ( $PV=nRT$ ), assuming that the diffusion space  $V$  and the gas diffusion quantity  $n$  remain unchanged, it can be seen that the temperature is proportional to the pressure. That is to say, the higher the temperature, the greater the pressure, the greater the corresponding  $p$ -value. Therefore, from this point of view, the change of temperature will directly affect the values of  $P_1$  and  $P_2$ , thus affecting the results of the determination of the initial velocity of gas diffusion.

To sum up, in the process of  $\Delta P$  determination, although the higher the temperature is, the greater the gas diffusion volume and its generating pressure are in the first 60 s, but the smaller the adsorption capacity before release is, and there is a mutual offset between the two cases. Therefore, the measurement results of  $\Delta P$  under different temperature conditions failed to show the corresponding regularity. The analytical results are consistent with the experimental results.

According to the above discussion, it is suggested that the industry standard for the determination of  $\Delta P$  related temperature should be clarified. Reason: In actual production, the actual temperature of coal seams in different mining areas and different depths is different, but most of the experimental measurements are carried out at room temperature (20°C), so the results of  $\Delta P$  may deviate from the real results. In the actual test, not

all laboratories have constant temperature conditions either, and the same coal sample may have different test results in winter and summer, and inconsistent test results in day and night. The result will directly affect people's judgment of coal and gas outburst.

## 4 Conclusion

1. The test system for the initial velocity of gas diffusion under different temperature conditions constructed in this paper provides an experimental reference for further research.
2. The temperature change will affect the  $\Delta P$  determination results in the range of 13°C–40°C, and the results do not show obvious regularity. In the process of  $\Delta P$  determination, the temperature of the experimental system should be kept consistent with the actual temperature of the sampled coal body as far as possible, so as to increase the reliability of the determination results for the prediction of coal and gas outburst.
3. From a macro point of view, hard coal shows an increasing trend of  $\Delta P$  with the increase of temperature, and soft coal shows a decreasing trend. It is preliminarily speculated that the effect of temperature increase on gas diffusion rate of hard coal is greater than the effect on its adsorption, and the opposite is true for soft coal.
4. This paper also provides an experimental basis for clarifying the industry standard for the determination of  $\Delta P$  related temperature. Therefore, the industry standard for determining the temperature of  $\Delta P$  should be defined, in order to increase the comparability and stability of  $\Delta P$  determination results.

## Data availability statement

The original contributions presented in the study are included in the article/Supplementary Material, further inquiries can be directed to the corresponding authors.

## References

- AQ1080-2009 (2009). "State Administration of work safety," in *Determination method for index ( $\Delta P$ ) of initial velocity of diffusion of coal gas*, 12.
- Cai, T., Feng, Z., and Jiang, Y. (2019). Thermodynamic characteristics of methane adsorption of coal with different initial gas pressures at different temperatures[J]. *Adv. Mater. Sci. Eng.* 2019, 4751209.
- Chen, C., Xian, X., and Zhang, D. (1995). The dependence of temperature to the adsorption of methane on anthracite coal and its char[J]. *Coal Convers.* 18 (3), 88–92.
- Chen, X., Cheng, Y., and Wang, L. (2012). Moisture content affected to initial gas emission velocity of different ranking coal[J]. *Coal Sci. Technol.* 40 (12), 62–65.
- Du, F., Wang, K., Zhang, X., Xin, C., Shu, L., and Wang, G. (2020). Experimental study of coal–gas outburst: Insights from coal–rock structure, gas pressure and adsorptivity. *Nat. Resour. Res.* 29, 2481–2493. doi:10.1007/s11053-020-09621-7
- Gao, B. (2013). *Study on gas desorption laws of coal particle at high temperature*[D]. Beijing: China University of Geosciences.
- Guo, P., Gao, J., and Zhang, C. (2020). Research progress and analysis on influence factors of initial velocity of gas emission[J]. *Saf. Coal Mines* 51 (7), 176–182.
- Guo, Z. (2018). Influences of temperature and dissipate space volume on determination of gas initial emission velocity by isobaric variable pressure method [J]. *China Energy Environ. Prot.* 40 (12), 42–44.
- He, Z. (2010). *Research on the impact of temperature on gas desorption law of technically coal*[D]. Jiaozuo: Henan Polytechnic University.
- Hong, Li (2011). *Experimental research on influence of ambient temperature on gas desorption laws of particle coal*[D]. Jiaozuo: Henan Polytechnic University.
- Huang, D., Zhu, H., and Chen, G. (2019). Effect of temperature on initial velocity of coal gas release[J]. *Mod. Min.* 11 (11), 236–262.
- Jianning, K. (2010). Influence study on initial speed of methane diffusion by adsorption pressure[J]. *Saf. Coal Mines* 41 (4), 4–5.
- Li, X., and Jiang, C. (2009). Study on effect of temperature on initial speed of methane emission[J]. *Saf. Coal Mines* 40 (1), 1–3.
- Li, X., Wang, C., Chen, Y., and Li, H. (2022). Influence of temperature on gas desorption characterization in the whole process from coals and its application analysis on outburst risk prediction. *Fuel* 321, 124021. doi:10.1016/j.fuel.2022.124021
- Liang, Y., Wang, F., Luo, Y., and Hu, Q. (2018). Desorption characterization of methane and carbon dioxide in coal and its influence on outburst prediction. *Adsorpt. Sci. Technol.* 36 (7–8), 1484–1495. doi:10.1177/0263617418781903
- Liu, G., Zhang, Z., and Song, Z. (2012). Adsorption experiments on CH<sub>4</sub> under the conditions of high temperature and pressure and equilibrium water[J]. *J. China Coal Soc.* 37 (5), 794–797.
- Liu, J., and Wang, Z. (2013). Relation between metamorphic grade and initial velocity of gas diffusion. *J. Liaoning Tech. Univ. Sci.* 32 (6), 745–748.
- Liu, Y., Jianping, W., and He, Z. (2013). Influence rules and mechanisms of temperature on dynamic process of gas diffusion from coal particles[J]. *J. China Coal Soc.* 38 (S1), 100–105.
- Lu, Z., Wang, L., Lv, M., Lei, Y., Hao, W., and Liu, Q. (2022). Experimental study on coal and gas outburst risk in strong outburst coal under different moisture content[J]. *Front. Earth Sci.* 10, 782372. doi:10.3389/feart.2022.782372

## Author contributions

XS: Conceptualization, funding acquisition, methodology, investigation, writing—original draft, writing—review and editing. JW: Conceptualization, funding acquisition, methodology, writing—review and editing. ZW: Conceptualization, funding acquisition, methodology, investigation, writing—review and editing. LS: Investigation, writing—original draft. JY: Investigation, Writing—original draft.

## Funding

This work was supported by the National Natural Science Foundation of China (Grant No: 51974109), Project funded by China Postdoctoral Science Foundation (2021M700132), Basic Research Funds of Henan Polytechnic University (NSFRF220205).

## Conflict of interest

The authors declare that the research was conducted in the absence of any commercial or financial relationships that could be construed as a potential conflict of interest.

## Publisher's note

All claims expressed in this article are solely those of the authors and do not necessarily represent those of their affiliated organizations, or those of the publisher, the editors and the reviewers. Any product that may be evaluated in this article, or claim that may be made by its manufacturer, is not guaranteed or endorsed by the publisher.

- Lu, Z. (1992). Problems and improvement in determination of initial velocity of gas diffusion  $\Delta P$  [J]. *Industrial Saf. Dust Prot.* (9), 39–41.
- Ma, C. (2017). *Research on calibration technique and device of initial velocity of coal gas measuring device*[D]. Xuzhou, Jiangsu: China University of Mining and Technology.
- Meng, Y., and Li, Z. (2016). Experimental study on diffusion property of methane gas in coal and its influencing factors. *Fuel* 185, 219–228. doi:10.1016/j.fuel.2016.07.119
- Sun, W. (2018). Research on initial speed of methane diffusion on initial gas emission in driving face[J]. *Coal Technol.* 37 (7), 163–164.
- Tan, R., Wang, Z., and Yang, H. (2012). Adsorption equilibrium time affected to initial velocity of gas emission[J]. *Coal Sci. Technol.* 40 (5), 46–48.
- Wang, J., Zhang, L., and Zhao, D. (2011). Effect of temperature and moisture on raw coal adsorption characteristics[J]. *J. China Coal Soc.* 36 (12), 2086–2091.
- Wang, K., Ren, H., Wang, Z., and Wei, J. (2022). Temperature-pressure coupling effect on gas desorption characteristics in coal during low-variable temperature process. *J. Petroleum Sci. Eng.* 211, 110104. doi:10.1016/j.petrol.2022.110104
- Wang, Y., and Shi, B. (1991). Quantitative analysis of influence on  $\Delta P$ -meter measurements[J]. *J. Huainan Min. Inst.* 11 (3), 21–30.
- Wang, Z., Xie, C., and Qi, C. (2016). Inhibitory effect of low temperature on methane diffusion in coal[J]. *J. Saf. Coal Mines* 47 (6), 16–19.
- Xu, L., and Jiang, C. (2012). Influence factors analysis on fastness coefficient and initial speed of methane emission determination[J]. *Coal Technol.* 31 (1), 93–94.
- Xu, L., and Jiang, C. (2011). Study on relation between coal's volatility and initial speed of methane emission[J]. *Saf. Coal Mines* 42 (7), 21–22.
- Yang, X., Wang, G., Du, F., Jin, L., and Gong, H. (2022). N<sub>2</sub> injection to enhance coal seam gas drainage (N<sub>2</sub>-ECGD): Insights from underground field trial investigation[J]. *Energy* 239, 122247. doi:10.1016/j.energy.2021.122247
- Yanwei, L., and Mingju, L. (2015). Effect of particle size on difference of gas desorption and diffusion between soft coal and hard coal[J]. *J. China Coal Soc.* 40 (3), 579–587.
- Zhang, T., Xu, H., and Li, S. (2009). The effect of temperature on the adsorbing capability of coal[J]. *J. China Coal Soc.* 34 (6), 802–805.
- Zheng, G., Luan, Y., and Bai, L. (2011). Discussion on the zonations of shallow geothermal energy resources in China[J]. *City Geol.* 6 (1), 12–16.
- Zhong, W., Zheng, Y., and Yuan, Z. (2002). The adsorption capability of coal under integrated influence of temperature and pressure and predicted of content quantity of coal bed gas[J]. *J. China Coal Soc.* 27 (6), 581–585.



## OPEN ACCESS

## EDITED BY

Zhibo Zhang,  
University of Science and Technology  
Beijing, China

## REVIEWED BY

Juan Zhang,  
Chongqing University, China  
Guansheng Qi,  
Shandong University of Science and  
Technology, China

## \*CORRESPONDENCE

Xingpan Zhu,  
✉ zhuxingpan126@163.com

## SPECIALTY SECTION

This article was submitted to  
Environmental Informatics and Remote  
Sensing,  
a section of the journal  
Frontiers in Earth Science

RECEIVED 06 January 2023

ACCEPTED 16 February 2023

PUBLISHED 02 March 2023

## CITATION

Zhu X and Wen H (2023), Numerical  
simulation study on the influence of air  
leakage on oxygen concentration in  
goafs of fully mechanized caving mining  
with shallow buried and large  
mining height.  
*Front. Earth Sci.* 11:1138925.  
doi: 10.3389/feart.2023.1138925

## COPYRIGHT

© 2023 Zhu and Wen. This is an open-  
access article distributed under the terms  
of the [Creative Commons Attribution  
License \(CC BY\)](https://creativecommons.org/licenses/by/4.0/). The use, distribution or  
reproduction in other forums is  
permitted, provided the original author(s)  
and the copyright owner(s) are credited  
and that the original publication in this  
journal is cited, in accordance with  
accepted academic practice. No use,  
distribution or reproduction is permitted  
which does not comply with these terms.

# Numerical simulation study on the influence of air leakage on oxygen concentration in goafs of fully mechanized caving mining with shallow buried and large mining height

Xingpan Zhu<sup>1,2\*</sup> and Hu Wen<sup>1</sup>

<sup>1</sup>College of Safety Science and Engineering, Xi'an University of Science and Technology, Xi'an, Shaanxi, China, <sup>2</sup>Shaanxi Coal and Chemical Industry Group Yubei Coal Industry Co., Ltd., Yulin, Shaanxi, China

In order to reveal the influence of air leakage on oxygen concentration in goafs of fully mechanized caving mining with a shallow buried and high mining height, the air leakage of No.122108 working face in Caojiatan coal mine in different seasons was tested by the SF<sub>6</sub> tracer gas test method. Based on the result of the air leakage test, the “three zones” of spontaneous combustion in the goaf were simulated using Ansys Fluent fluid dynamics software, and the simulated result was compared with that of the field test. The result shows that the vertical air leakage of the working face is serious, the wind speed is high, and the air leakage rate is up to 86.96%. The air leakage rate is higher in winter and lower in summer. The air leakage intensity decreases from the air inlet side to the air return side through the middle of the goaf. The range of the oxidation heating zone of the goaf is 98–245 m on the air inlet side and 33–96 m on the air return side. The numerical simulation result is well consistent with the field test data. The research conclusion can guide fire prevention and the extinguishing of No.122108 working face and lay a foundation for the prevention and control of spontaneous fire in goafs of fully mechanized caving mining with a shallow buried and high mining height.

## KEYWORDS

shallow buried and high mining height, SF<sub>6</sub> tracer gas, air leakage, oxygen concentration, numerical simulation, coal spontaneous combustion

## 1 Introduction

There are many kinds of complex mine disasters. coal spontaneous combustion is one of the most serious mine disasters (Querol et al., 2011; Liu et al., 2019; Zheng et al., 2019; Liu et al., 2020; Onifade and Genc, 2020; Jin et al., 2021; Kuai, 2021), which can easily cause casualties, environmental pollution, and property loss (Deng et al., 2017; Wu et al., 2018; Li et al., 2019; Song et al., 2020). According to the data, fire accidents caused by coal spontaneous combustion account for more than 90% of the total mine fires (Ma et al., 2022), and coal spontaneous combustion in goafs comprise over 60% of total mine spontaneous combustion (Su et al., 2016; Wen et al., 2017). In the process of mining, the roof of the coal bed in goafs will be pressed periodically; therefore, the roof will break and

sink, and the cracks will be connected with goafs. For shallow buried coal beds, even the surface will experience local collapse, and rock cracks will penetrate the surface and goafs and form air leakage channels, thus creating air leakage and an oxygen supply environment for goafs (Li W. et al., 2022). When special geological conditions are encountered in the process of mining, the speed of mining slows down, and a certain thickness of the loose coal body is left behind in goafs, which will inevitably cause spontaneous combustion of coal left in goafs. Therefore, it is of great significance to study and master the distribution of air leakage flow fields in goafs of fully mechanized caving mining with a shallow buried and high mining height in order to realize the control of spontaneous combustion in goafs.

The SF<sub>6</sub> tracer gas measurement method is a reliable technique for measuring air leakage in mines, which is used to determine air leakage channels and air leakage in goafs (Wang et al., 2014; Zhu et al., 2016). Researchers at home and abroad have carried out a lot of research studies and practices on air leakage using the SF<sub>6</sub> tracer gas measurement method. Tian et al. (2020) measured the air leakage in goafs of the U-type ventilation working face in the Wenzhuang Coal Mine using the SF<sub>6</sub> tracer gas method. The results showed that there were many air leakage channels in goafs of this working face, and the air leakage velocity at the interface between the hydraulic support and goafs was high. Zhao et al. (2016) used the SF<sub>6</sub> tracer gas instantaneous release method to analyze the air leakage from surface cracks in the fully mechanized cave mining with a shallow buried and high mining height of the Pingshuo mine area, determining parameters of surface air leakage and proposing comprehensive prevention and control measures according to the air leakage test result. Wu (2020) used SF<sub>6</sub> tracer gas measurement method to measure the air leakage velocity in the goaf of the Xiegou coal mining face and obtained the main air leakage interval of the goaf.

Due to the complexity of residual coal and porosity distribution in goafs, determining air leakage flow fields in goafs and “three zones” of spontaneous combustion in goafs by means of field measurement and experimental study is limited. To some extent, numerical simulation can make up for the deficiency of field measurement and carry out reasonable and accurate physical simulation of air leakage flow fields in goafs (Kurnia et al., 2014; Tang et al., 2016; Zhang and Ji, 2016; Liu et al., 2022). Based on the unsteady state simulation method, Zuo et al. (2021) divided “three zones” of coal spontaneous combustion in goafs by analyzing the relationship between working face mining and coal spontaneous combustion under the condition of low air leakage velocity in goafs. Li et al. (2019), by establishing a numerical model, determined the three-dimensional spontaneous combustion risk area in goafs. The results showed that the “spontaneous combustion zones” in goafs became wider along the vertical height and the spontaneous combustion risk area turned larger. Shi et al. (2014) simulated the variation law of oxygen concentration in goafs during the mining of a fully mechanized caving mining face by the computational fluid dynamics (CFD) method. Hu and Liu (2021) took a fully mechanized caving mining face in the Yindonggou Coal Mine as the research object and combined numerical simulation with actual conditions to accurately divide the distribution range of “three zones” of spontaneous combustion in goafs. The simulation result was in agreement with the measured one. Based on the method of numerical simulation and field measurement, Xing (2021) studied

the influence of surface air leakage in shallow thick coal beds on coal spontaneous combustion in goafs and obtained the distribution of “three zones” in goafs and the distribution law of the oxygen concentration field. In addition, a coal mine fire monitoring device was used for field verification.

At present, most scholars have only studied the law of air leakage in one time dimension. Due to the change of seasons, many environmental factors such as climate, temperature difference, and atmospheric pressure are changed, which causes the coal seam to trigger the “gasp effect.” Based on the research studies carried out at home and abroad, this study takes No.122108 working face of Caojiatan coal mine as the research object and uses the SF<sub>6</sub> tracer gas to measure the air leakage of this working face in summer, autumn, winter, and spring. Based on the measured result of the air leakage, fluid dynamics software Ansys Fluent is used to simulate the “three zones” of spontaneous combustion in goafs, and the simulation result is compared with the field measurement. The research conclusion can lay a foundation for the prevention and control of spontaneous fire in goafs of fully mechanized caving mining with a shallow buried and high mining height. It is hoped that it can guide the fire prevention and extinguishing work of a similar working face in Caojiatan coal mine.

The subsequent sections of this paper are organized as follows: Section 2 introduces the overview of the working face. Air leakage measurement of the SF<sub>6</sub> tracer gas and analysis of results are elaborated in Section 3. Section 4 is dedicated to the theoretical basis of simulation in the goaf, parameter setting of the numerical model of the goaf, and the numerical simulation result and analysis. Field verification is explained in Section 5. Finally, conclusions are given in Section 6.

## 2 Overview of the working face

No. 122108 working face is located in the second coal face in the east of the 12th panel of the 2<sup>-2</sup> coal bed in Caojiatan coal mine, and the mined coal bed belongs to the type I spontaneous combustion coal bed. The coal dust is explosive with the absolute gas emission of 2.90 m<sup>3</sup>/min and relative gas emission of 0.10 m<sup>3</sup>/t. The working face is adjacent to the goaf of No.122106 working face in the north, with a strike length of 5,966 m and an inclined length of 280 m. The working face adopts the longwall backward mining method and integrates the fully mechanized caving mining technology. The caving method is used to treat the goaf. The average coal thickness of the working face is 10 m, the designed mining height is 6 m, the coal caving height is 4 m, and the ratio of mining to caving is 1:0.67. The coal mining machine cuts coal in two directions, and the end is cut obliquely with a length not less than 59.7 m and a depth of 865 mm. The roadway layout of the mining working face is shown in Figure 1.

## 3 Air leakage measurement of the SF<sub>6</sub> tracer gas

### 3.1 Air leakage measurement principle of the SF<sub>6</sub> tracer gas

SF<sub>6</sub> does not exist in natural stones and has good stability and testability (Zheng et al., 2022). Therefore, this study uses the SF<sub>6</sub> tracer



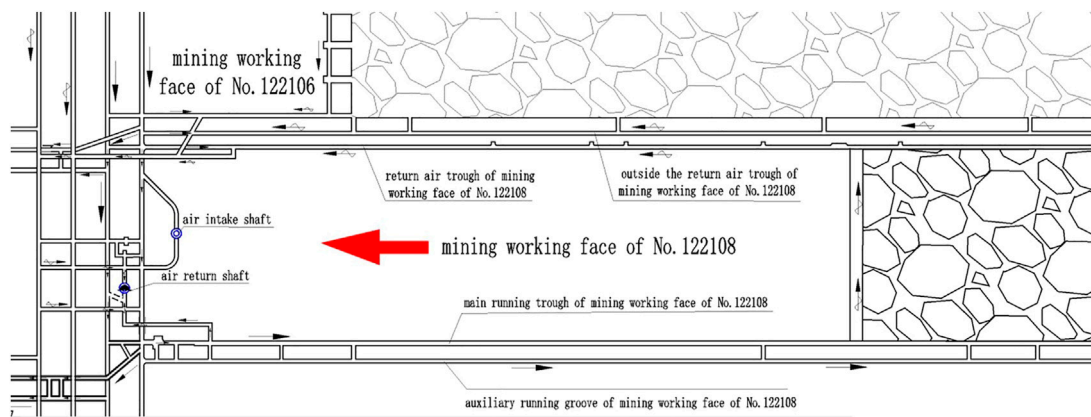


**FIGURE 1**  
Roadway layout of the mining working face.

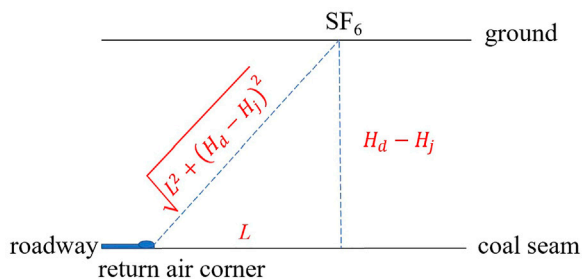


**FIGURE 2**  
Schematic diagram of air leakage rate calculation ( $L$  is the horizontal distance between the tracer gas release point and the working face, and  $H_d$  and  $H_j$  represent the elevation of the tracer gas release point and monitoring point in the mine, respectively).

gas to detect the air leakage. When there is an air leakage channel,  $SF_6$  will pass through and can be detected at the air outlet; otherwise, it must not be detected from the air return side.

This study measures the distribution of surface air leakage channels by the  $SF_6$  tracer gas pulse release method and tests surface air leakage of No.122108 working face in spring, summer, autumn, and winter *in situ*. In order to ensure the accuracy and reliability of the field test, this paper measures twice a quarter. This study measures the  $SF_6$  gas released from the surface, which is tested, and the air return corner of the working face is measured to analyze the distribution law of air leakage channels on the surface and the air leakage and transfusion parameters.

The vertical air leakage rate from the surface to the goaf is calculated quantitatively by the release time of the tracer gas on the surface, the appearance time of the tracer gas in the mine, and the relative position between the release point and the working face. The air leakage rate can be expressed as follows (Tian et al., 2022):

$$V = \frac{d}{t}, \quad (1)$$

where  $V$  is the air leakage rate,  $d$  is the distance between the tracer gas release point and the corner of the working face, and  $t$  refers to time interval.

Due to irregular air flow to the formation in cracks, the maximum air leakage rate and the minimum air leakage rate can be determined by calculating the longest and shortest straight line distances, respectively. As shown in Figure 2, the formula for calculating the maximum and minimum air leakage rates can be obtained as follows.

$$V_{max} = \frac{L + (H_d - H_j)}{t}, \quad (2)$$

$$V_{min} = \frac{\sqrt{L^2 + (H_d - H_j)^2}}{t}, \quad (3)$$

where  $V_{max}$  and  $V_{min}$  are the maximum and minimum air leakage rates, respectively.

### 3.2 Air leakage measurement scheme in the goaf

In this measurement, the instantaneous release mode is adopted to conduct field observation and investigation on the surface subsidence area of the working face at different times (winter: 16 January 2021; spring: 11 March 2021; summer: 27 June 2021; and autumn: 16 September 2021). In addition, a “two-way” chute with a relatively large air leakage and good communication with the working face and the position with large cracks under periodic pressure of the working face are selected as tracer gas release points on the surface. The  $SF_6$  tracer gas is used to test the distribution of surface air leakage channels, and the release amount is 32 L. The selected release point position is shown in Figure 3.

### 3.3 Analysis of results

The portable  $SF_6$  gas detector is adopted to test the return wind 20 m from the return wind corner of No.122108 working face on the surface and in the mine in different seasons. The ambient temperature, air pressure, working face wind speed,  $SF_6$  appearance time, and duration are recorded, and then the air leakage from the surface to No.122108 working face is measured.

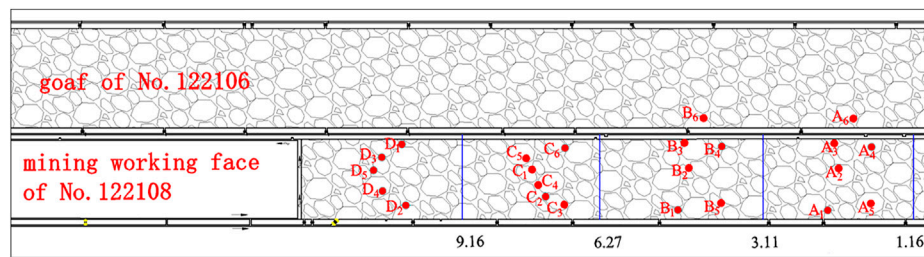


FIGURE 3

SF<sub>6</sub> release point position (A, B, C, and D represent winter, spring, summer, and autumn, respectively). The numbers 1 to 6 represent the position of the SF<sub>6</sub> tracer gas measuring point.

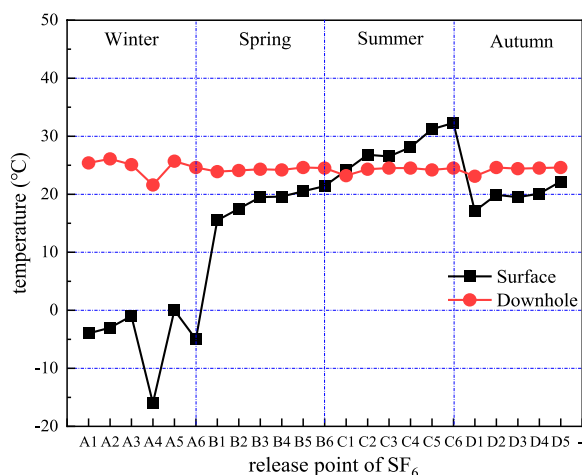


FIGURE 4

Change of surface and downhole temperatures in different seasons.

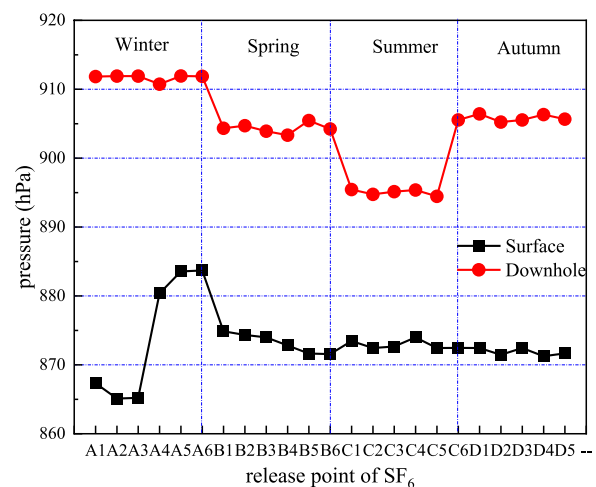


FIGURE 5

Change of surface and downhole air pressures in different seasons.

### 3.3.1 Change of surface and downhole ambient temperatures and air pressure in different seasons

As can be observed in Figures 4, 5, the largest temperature difference in winter reaches 37.7°C, the surface temperature is below zero, and the smallest temperature difference in summer is only 0.9°C. Because of the change of seasons, the surface temperature is greatly different, and the change of air temperature leads to the change of air density, forming the phenomenon that the atmospheric pressure in winter is higher than that in summer. The downhole is a semi-closed environment where the change of temperature and atmospheric pressure is small, thus forming an evident temperature difference in the downhole. As shown in Figure 5, the maximum air pressure difference is 40.37 hPa in winter and 22.47 hPa in summer. The difference between spring and autumn is small due to climatic characteristics.

### 3.3.2 Leakage rate

In combination with the crack survey in the surface collapse area, tracer gas release in different positions, and downhole observation, the vertical air leakage in No.122108 working face of

Caojiatan coal mine is qualitatively and quantitatively analyzed to find the characteristics and law of the formation of surface cracks and air leakage channels. The change of the air leakage rate of each measuring point in different seasons is obtained by calculation, as shown in Figure 6. The result shows that the vertical air leakage of No.122108 working face in Caojiatan coal mine is serious, the wind speed is high, air leakage exists in 20 of 23 measuring points, and the air leakage rate is up to 86.96%. As can be observed in Figure 6, the air leakage rate also varies significantly with the seasonal change. Due to the large temperature difference in winter, the air pressure difference between the surface and downhole is large, the air leakage is serious, and the maximum air leakage rate at A<sub>5</sub> measuring point reaches 0.1614 m/s. The air leakage rate is generally higher in winter than in the other three seasons, and the air leakage rate is the lowest in summer because the temperature in winter is low, the air shrinks, the density increases, and the weight of the air column per unit area and the air pressure goes up. Therefore, in winter, the maximum air leakage rate ranges from 0.1003 to 0.1614 m/s, the average flow rate is 0.1022 m/s, the minimum air leakage rate is 0.0717–0.1145 m/s, and the average flow rate is 0.5377 m/s. It is the opposite in summer.

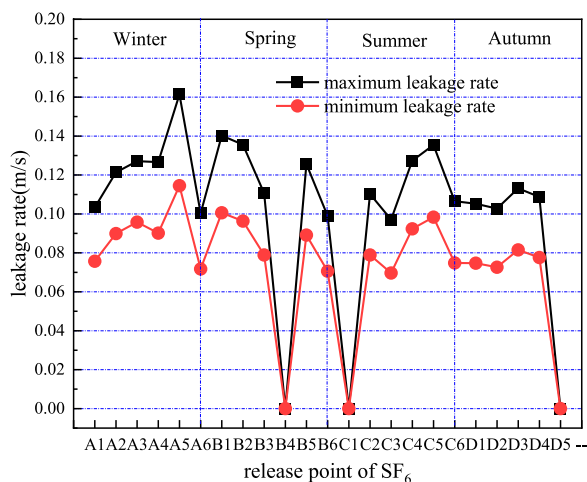


FIGURE 6

Change of the air leakage rate at each release point in different seasons.

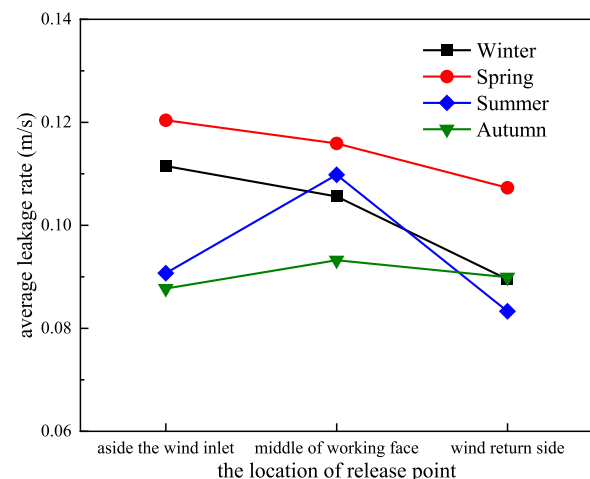


FIGURE 8

Distribution of the average air leakage flow rate of the measuring points at different positions in the surface crack working face in four seasons.

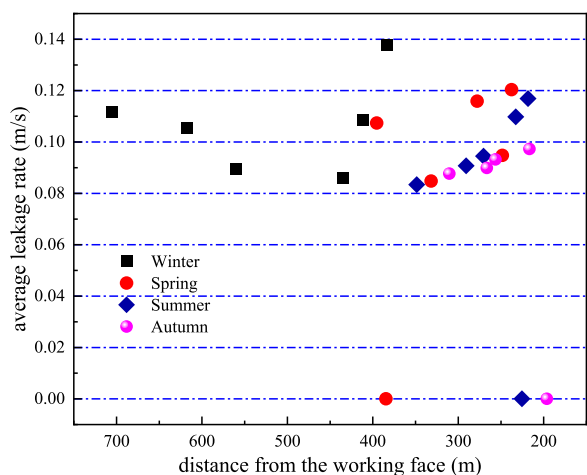


FIGURE 7

Change of the average air leakage rate with the working face distance.

The air pressure decreases, and the downhole negative pressure decreases. In summer, the maximum air leakage rate ranges from 0 to 0.1354 m/s, the average flow rate is 0.0961 m/s, the minimum air leakage rate ranges from 0 to 0.0983 m/s, and the flow rate is 0.0670 m/s. Seasonal changes result in the difference of pressure between the surface and downhole, and the air leakage is serious in winter when the negative pressure increases.

Figure 7 shows the change of the average air leakage rate with the working face distance. It can be observed that the air leakage rate is smaller when the measuring point is far away from the working face. On the contrary, the air leakage rate is larger when the distance from the working face is closer. This is because the surface cracks at the measuring point far away from the working face are relatively few due to a series of environmental factors such as long subsidence time

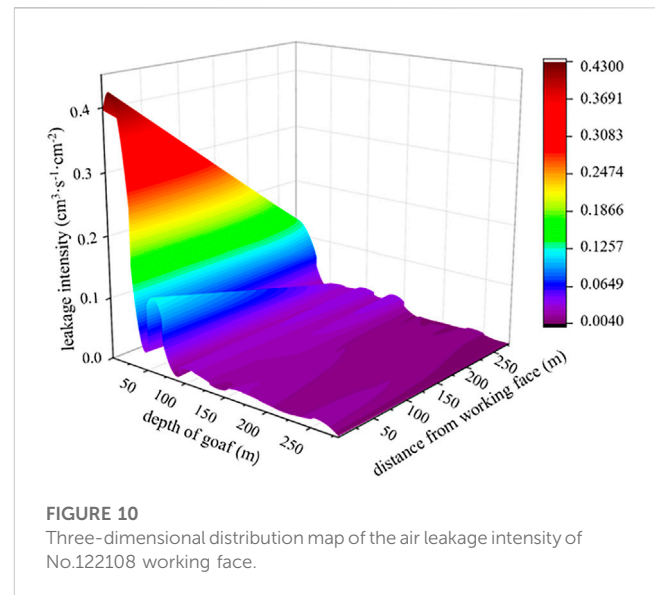
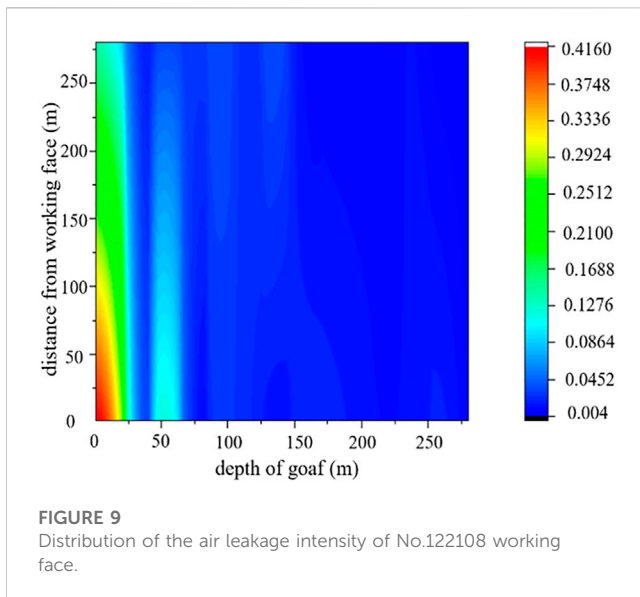
and surface soil filling, and the wind leakage speed of the cracks is relatively small; the surface cracks at the measuring point near the working face are relatively more for a good development condition due to the initial formation of the subsidence area, and the wind leakage speed of the cracks is relatively large. According to the results of field investigation and test, the transfusion through the surface to the goaf is not uniform due to serious air leakage in the large crack zone in some subsidence areas and the small cracks with little or no air leakage. There are many extended large cracks on the surface; the maximum width of cracks is 0.03–0.09 m, and the length of cracks is 23–35 m. These large cracks are highly likely to have serious air leakage and need to be buried in time.

Figure 8 shows the distribution of the average air leakage flow rate on the air inlet side, air return side, and measuring point in the middle of the working face in four seasons. It can be observed that the air leakage flow rate on the inlet side is relatively large, while that on the return side is relatively small.

### 3.3.3 Distribution of air leakage intensity

The main methods for calculating the air leakage intensity of a loose coal body include the air flow calculation method, Darcy differential algorithm, air network solution algorithm, and oxygen concentration calculation method (Deng et al., 1999). Theoretically, the first three methods can accurately calculate the air leakage intensity and distribution of a loose coal body. However, due to the limitation of accuracy of the current wind and pressure measurement technology and practical conditions of roadway, it is difficult to implement the practical application of calculating the air leakage intensity of a loose coal body. The error is large, so they are seldom used in the field. The fourth method is simple and accurate; it calculates the air leakage intensity using the measured oxygen concentration.

The oxygen concentration measurement method is through the actually measured oxygen concentration distribution to push back the air leakage intensity. The idea is to assume a kind of air leakage



law and calculate the air leakage intensity according to the oxygen consumption rate of coal at the temperature by measuring the oxygen concentration at a certain point in a loose coal body. The air leakage intensity is taken as the initial value, and the change of the system air pressure is considered (mainly the change of hot air pressure caused by the change of coal temperature); then, the dynamic change law of air leakage intensity can be obtained.

Assuming that the air leakage flows only along one dimension, when the air leakage intensity in a loose coal body is constant, the relationship between the air leakage intensity and oxygen concentration can be obtained [as shown in Formula 4 (Zuo et al., 2018)]:

$$\bar{Q}(\bar{x}_i) = \frac{V_{O_2}^0 (x_{i+1} - x_i)}{C_{O_2}^0 \ln \frac{C_{O_2}^i}{C_{O_2}^{i+1}}}, \quad (4)$$

where  $C_{O_2}^0$  is the oxygen concentration of the fresh air flow and is set as  $9.375 \times 10^{-6} \text{ mol/cm}^3$ ;  $V_{O_2}^0(T)$  is the oxygen consumption rate when the experimentally determined coal temperature is  $T$  and the oxygen concentration is 21% and is set as  $\text{mol}/(\text{s} \cdot \text{cm}^3)$ ;  $\bar{Q}(\bar{x}_i)$  is the air leakage intensity at  $\bar{x}_i$  in the goaf and is  $\text{cm}^3/(\text{s} \cdot \text{cm}^2)$ ;  $x_{i+1}$  and  $x_i$  are, respectively, the distance between two points of the goaf and the working face, m.

According to the field observation data, the horizontal distribution map and three-dimensional distribution map of the air leakage intensity in different positions inside the goaf are established as shown in Figures 9, 10. As can be observed in Figures 9, 10, the air leakage intensity is highest on the air inlet side of the goaf, second highest in the middle of the goaf, and lowest on the air return side. Therefore, the air leakage intensity decreases from the air inlet side to the air return side through the middle of the goaf. At about 50 m from the air inlet side to the working face, the air leakage intensity has a peak value and is higher than the surrounding points, which should be due to the existence of the auxiliary chute and connection roadway at the wind inlet side so that the air leakage is relatively large. According to the analysis result of air leakage intensity, the air leakage is serious on the air inlet side, which should be the key area of fire prevention and extinguishing work.

## 4 Numerical simulation analysis

### 4.1 Theoretical basis of simulation in the goaf

After the working face is mined, the roof strata will collapse one after another. Therefore, the goaf is filled with broken rock and the loose coal body, and the cracks between the broken rock and the loose coal body are very abundant in the goaf. For the purpose of simulation calculation, we consider the loose coal body and rock as homogeneous porous media. It is assumed that 1) spontaneous combustion occurs in residual coal in the goaf; 2) heat exchange occurs between residual coal and the surrounding air; and 3) heat released by the chemical reaction enhances the transfusion process between the substances and intensifies heat and mass transfer.

#### 4.1.1 Mathematical equation of gas concentration in the goaf

The pore distribution in loose coal is usually large, and large pores will cause the gas to leak easily. The air leakage rate causing spontaneous coal combustion is very small ( $0.001\text{--}0.5 \text{ cm}^3 \text{ s}^{-1}$ ) under the actual conditions, and the air leakage distribution is a function of time and space. In order to study the influence of surface air leakage on coal spontaneous combustion in the goaf, the control equation of the key characteristic parameter  $O_2$  of coal spontaneous combustion is established.

The migration of  $O_2$  in porous media includes diffusion and transfusion. According to Fick's law, the diffusion of air components is from high concentration to low concentration. In the given calculation area,  $O_2$  transfusion should conform to Darcy's law, and the air leakage intensity in the transfusion model only needs to consider the air leakage through the unit area of loose coal. The equation for the mass balance of  $O_2$  can be expressed as follows:

$$\bar{Q}_x \frac{\partial C_{O_2}}{\partial x} + \bar{Q}_y \frac{\partial C_{O_2}}{\partial y} + \bar{Q}_z \frac{\partial C_{O_2}}{\partial z} = D_x \frac{\partial^2 C_{O_2}}{\partial x^2} + D_y \frac{\partial^2 C_{O_2}}{\partial y^2} + D_z \frac{\partial^2 C_{O_2}}{\partial z^2} - V_{O_2}(T), \quad (5)$$

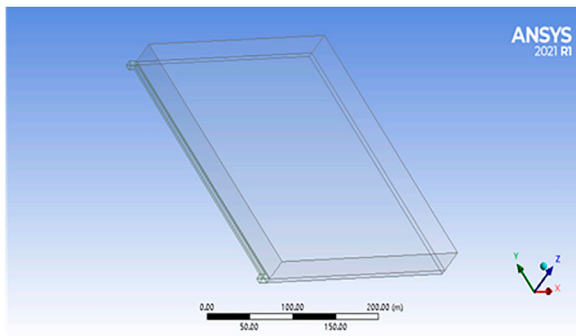


**FIGURE 11**  
Three-dimensional model of the goaf.

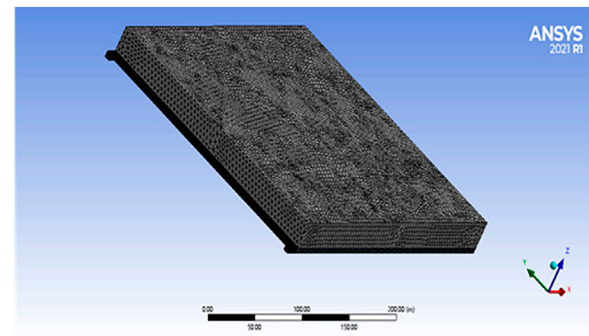


**FIGURE 12**  
Three-dimensional model of grid division.

where  $\bar{Q}$  is air leakage intensity of the goaf;  $\bar{Q}_x$ ,  $\bar{Q}_y$ , and  $\bar{Q}_z$  are air leakage intensity components in the  $x$ ,  $y$ , and  $z$  directions, respectively;  $C_{O_2}$  is the concentration of  $O_2$ ;  $D$  is diffusion coefficient;  $D_x$ ,  $D_y$ , and  $D_z$  are diffusion coefficients of  $O_2$  in  $x$ ,  $y$ , and  $z$  directions, respectively;  $V_{O_2}(T)$  is the oxygen consumption rate of coal, when the  $O_2$  volume fraction is  $C_{O_2}$  and the oxygen consumption rate is proportional to  $O_2$  volume fraction.

#### 4.1.2 Governing equation of the flow field in the goaf

In the normal production of the mine, it is assumed that the transfusion, diffusion, and chemical reaction in the combustion space proceed smoothly, and the total mass of air remains unchanged. If the temperature of the goaf is basically kept constant, the governing equation of the flow field in the goaf can be obtained as follows (Li Y. C. et al., 2022):

$$\begin{cases} \frac{\partial}{\partial x} \left( k_x \frac{\partial H}{\partial x} \right) + \frac{\partial}{\partial y} \left( k_y \frac{\partial H}{\partial y} \right) + \frac{\partial}{\partial z} \left( k_z \frac{\partial H}{\partial z} \right) = 0 \\ \bar{Q}_x \frac{\partial C}{\partial x} + \bar{Q}_y \frac{\partial C}{\partial y} + \bar{Q}_z \frac{\partial C}{\partial z} = D_x \frac{\partial^2 C}{\partial x^2} + D_y \frac{\partial^2 C}{\partial y^2} + D_z \frac{\partial^2 C}{\partial z^2} - V(T) \\ \bar{Q} = -\frac{k}{\mu} \nabla H \\ V(T) = \frac{C}{C_0} V_0(T) \end{cases}, \quad (6)$$

where  $H$  is the pressure and  $k$  is the absolute permeability; if the permeability of the goaf is isotropic,  $k_x = k_y = k_z$ ;  $\mu$  is the air viscosity coefficient;  $C_0$  is the mass concentration of  $O_2$  in air;  $V_0(T)$  is the standard oxygen consumption rate.

## 4.2 Parameter setting of the numerical model of the goaf

### 4.2.1 Numerical model

In accordance with the actual condition of No.122108 working face, a three-dimensional model of the goaf of the working face is established. The depth of the goaf is set to 400 m, the inclined length

of the working face is set to 280 m, the thickness of floating coal along the inlet and return air chute is set to 5.71 m, the thickness of floating coal in the middle of the goaf is 0.85 m, and the rock on floating coal is 10-m thick. The origin of coordinates is located at the innermost end of the goaf. The direction pointing to the air outlet is the  $x$ -axis-positive direction, the direction pointing to the working face is the  $y$ -axis-positive direction, and the upward direction is the  $z$ -axis-positive direction. The calculation area grids are divided into structured grids. In the floating coal, the step length is 1 m in  $x$ ,  $y$ , and  $z$  directions, the step length in the rock is 4 m, and there are 1,523,756 grids. The three-dimensional model and grid division are shown in Figures 11, 12.

### 4.2.2 Boundary conditions

The setting of boundary conditions is the key of the numerical simulation solution. Only when the conditions are reasonable and close to the actual conditions can the accurate flow field distribution be calculated.

In the model area studied, it is assumed that the air inlet lane, air return lane, and working face surface are boundaries in this area. The wind speed and gas concentration involved in these boundaries are the boundary conditions to be considered in the model. In addition, it is assumed that that rest of the surface in the area has a wall property. Due to the presence of this wall, the permeation effect of the gas will not be possible. Therefore, based on the aforementioned assumptions, the boundary conditions for transfusion and diffusion in the model area are defined as follows.

- (1) Assuming that the temperature in the goaf does not change and the pressure at both ends of the working face remains stable, it is a steady-state transfusion problem, namely,  $\frac{dC}{dt} = 0$ .
- (2) On the wall,  $\bar{Q} = 0$ .

Assuming that the gas enters the goaf in a steady-state transfusion mode, the air inlet is set to the velocity inlet, the speed is set to 2.4 m/s, and the air outlet boundary is set to out flow. The goaf is set as the porous medium area of air flow. The porosity, viscous resistance coefficient, inertia resistance coefficient, and oxygen consumption rate are compiled into the solution program by UDF programming. In that process of model



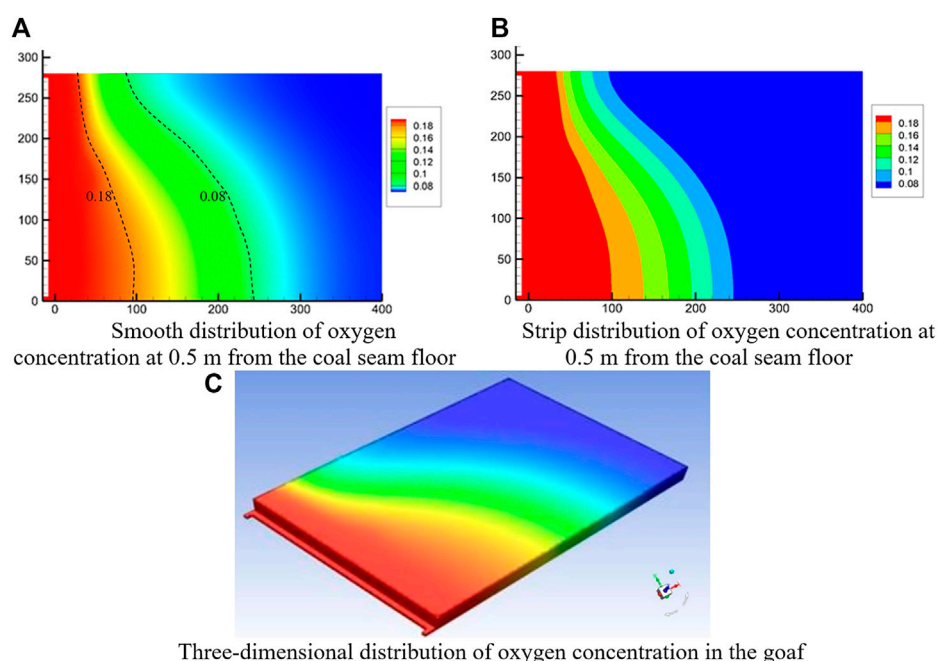


FIGURE 13

Distribution of oxygen concentration in the goaf. (A) Smooth distribution of oxygen concentration at 0.5 m from the coal seam floor. (B) Strip distribution of oxygen concentration at 0.5 m from the coal seam floor. (C) Three-dimensional distribution of oxygen concentration in the goaf.

solution, the energy equation and the component transport model are opened.

### 4.3 Numerical simulation result and analysis

Based on the aforementioned model, the distribution of oxygen concentration in the goaf is obtained as shown in Figure 13. Figures 13A, B show, respectively, smooth distribution and stripe distribution of oxygen concentration at a distance of 0.5 m from the coal seam floor, and Figure 13C shows three-dimensional distribution of the oxygen concentration in the goaf.

It can be observed from Figures 13A–C that oxygen concentration in the goaf of Caojiatan coal mine is 18% at 98 m from the air inlet side to the working face and 8% at 245 m; similarly, oxygen concentration on the air return side is at 33 and 96 m. The comparison shows that oxygen concentration on the air inlet side of the goaf decreases more slowly than that on the air return side, oxygen concentration distribution at the same depth is different, and oxygen concentration at the inlet side is greater than that at the return side.

## 5 Field verification

The oxygen concentration result obtained by the simulation is compared with the field observation result as shown in Figures 14, 15.

As can be observed intuitively from Figures 14, 15, the oxygen concentration data obtained by numerical simulation show a

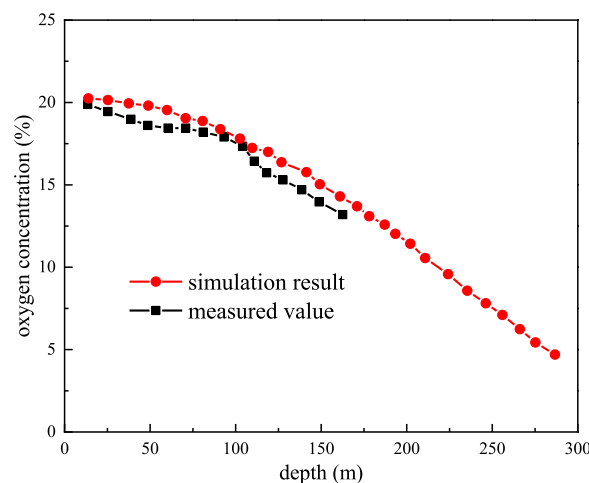
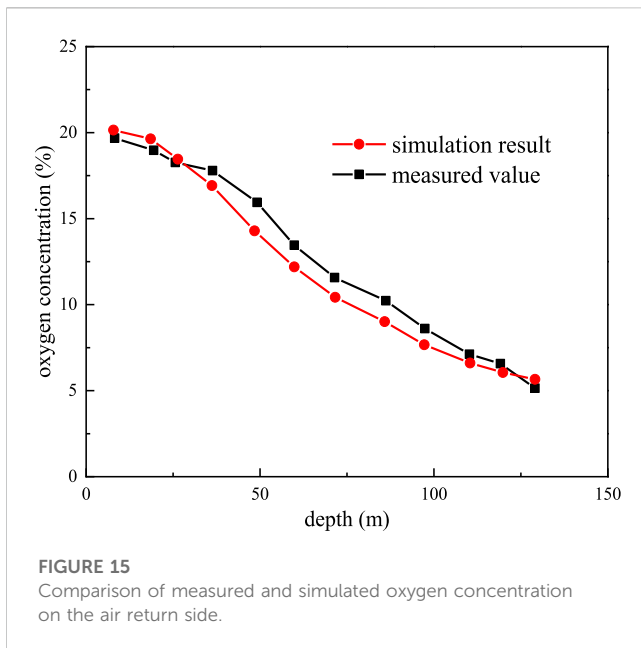


FIGURE 14

Comparison of measured and simulated oxygen concentration on the air inlet side.

decreasing trend as a whole along with the extension of the deep part of the goaf, while the measured data show a slight fluctuation and decreasing trend. This is due to the error in field measurement and the influence of air leakage in the goaf. Generally speaking, the numerical simulation and the field data are well anastomotic. Considering the results of field observation and simulation, in order to eliminate the hidden danger of coal spontaneous combustion fully



mechanized caving face, it is necessary to enlarge the monitoring range of the dangerous area in the goaf. Therefore, assuming that the thickness of floating coal is enough to gather heat, it can be preliminarily judged that the coal spontaneous combustion risk is high in the goaf of No.122108 fully mechanized caving face in Caojiatan coal mine in the range of 98–245 m from the air inlet side and 33–96 m from the air return side.

## 6 Conclusion

This study takes No.122108 working face of Caojiatan coal mine as the research object and uses the SF<sub>6</sub> tracer gas to measure the air leakage of the working face in different seasons. Based on the result of air leakage measurement, the “three zones” of spontaneous combustion in the goaf are simulated using Ansys Fluent fluid dynamics software, and the simulation result is compared with the field measurement. The main conclusions are as follows.

- (1) The vertical air leakage in No.122108 working face is serious, with high wind speed and air leakage rate up to 86.96%. The air leakage intensity decreases from the air inlet side to the air return side through the middle of the goaf.
- (2) The air leakage rate of No.122108 working face is generally higher in winter than that in other three seasons and the lowest

in summer. When the measuring point is far away from the working face, the air leakage rate is small, and when the measuring point is near the working face, the air leakage rate is large.

- (3) The oxygen concentration in the goaf of No.122108 fully mechanized caving face is 18% at 98 m on the air inlet side and 8% at 245 m and 33 and 96 m on the air return side, respectively. The decrease speed of oxygen concentration on the intake side of the goaf is slower than that on the return side. The oxygen concentration distribution at the same depth is different and that on the inlet side is greater than that on the return side.
- (4) The numerical simulation and the field data are well anastomotic. In order to eliminate the hidden danger of coal spontaneous combustion in the goaf of No.122108 fully mechanized caving face, it is necessary to enlarge the monitoring range of the dangerous area in the goaf.

## Data availability statement

The raw data supporting the conclusion of this article will be made available by the authors, without undue reservation.

## Author contributions

Investigation, methodology, and writing-original draft were completed by the author XZ. Formal analysis, supervision, and final draft were completed by the author HW.

## Conflict of interest

Author XZ was employed by the company Shaanxi Coal and Chemical Industry Group Co., Ltd., Yubei Coal Industry.

The remaining author declares that the research was conducted in the absence of any commercial or financial relationships that could be construed as a potential conflict of interest.

## Publisher's note

All claims expressed in this article are solely those of the authors and do not necessarily represent those of their affiliated organizations, or those of the publisher, the editors, and the reviewers. Any product that may be evaluated in this article, or claim that may be made by its manufacturer, is not guaranteed or endorsed by the publisher.

## References

- Wu, W. Q. (2020). Three zones fire prevention and extinguish technology for fully mechanized caving face of Gaoyang Coal Mine. *Shanxi Coking Coal Sci. Technol.* 44(9), 23–26–26.
- Deng, J., Xu, J. C., Wang, C. Y., and Lv, Z. Q. (1999). Methods for calculating specific air-leakage in loose coal of fully mechanized longwall top-coal caving face. *J. China Coal Soc.* 24 (5), 502–506. doi:10.13225/j.cnki.jccs.1999.05.014
- Deng, J., Li, B., Xiao, Y., Ma, L., Wang, C. P., Wang, B. L., et al. (2017). Combustion properties of coal gangue using thermogravimetry- Fourier transform infrared spectroscopy. *Appl. Therm. Eng.* 116, 244–252. doi:10.1016/j.applthermaleng.2017.01.083
- Hu, J. T., and Liu, Z. G. (2021). Numerical simulation of spontaneous combustion “Three zones” in goaf of Yindonggou 110201 fully mechanized working face based on FLUENT. *Coal Technol.* 40 (8), 111–115. doi:10.13301/j.cnki.ct.2021.08.028
- Jin, Y. F., Yan, L., Liu, Y., and Li, C. S. (2021). The spatiotemporal changes of oxygen consumption rate and heat release intensity during coal spontaneous combustion. *Int. J. Heat Technol.* 39 (4), 1287–1293. doi:10.18280/ijht.390427

- Kuai, D. L. (2021). Distribution law of three spontaneous combustion zones in the goaf area of a fully mechanized working face under high ground temperature. *Environ. Earth Sci. Res. J.* 8 (2), 86–90. doi:10.18280/eesrj.080204
- Kurnia, J. C., Sasmito, A. P., and Mujumdar, A. S. (2014). CFD simulation of methane dispersion and innovative methane management in underground mining faces. *Appl. Math. Model.* 38 (14), 3467–3484. doi:10.1016/j.apm.2013.11.067
- Li, C. Y., and Zhang, L. L. (2019). Study on distribution law of spontaneous combustion “three zones” in goaf of fully mechanized mining face with large mining height. *IOP Conf. Ser. Earth Environ. Sci.* 358, 032041. doi:10.1088/1755-1315/358/3/032041
- Li, J. L., Lu, W., Cao, Y. J. Z., Kong, B., and Zhang, Q. S. (2019). Method of pre-oxidation treatment for spontaneous combustion inhibition and its application. *Process Saf. Environ. Prot.* 131 (C), 169–177. doi:10.1016/j.psep.2019.08.013
- Li, W., Qiang, F. W., Yang, C. F., and Quan, Y. P. (2022). Numerical simulation study on “three zones” of spontaneous combustion in goaf of fully mechanized mining face. *Shaanxi Coal* 4, 38–42.
- Li, Y. C., Huang, Y. L., Wu, Y. B., Guo, Y. C., Sun, T. Y., Liu, Y. H., et al. (2022). Study on the development law of surface cracks in extra-thick coal seam mining in Loess Gully region. *Min. Res. Dev.* 42 (6), 68–73. doi:10.13827/j.cnki.kyyk.2022.06.030
- Liu, W. Y., Wen, H., and Guo, J. (2019). Inhibition mechanism of LDHs on coal spontaneous combustion based on thermogravimetric analysis. *Int. J. Heat Technol.* 37 (2), 589–596. doi:10.18280/ijht.370229
- Liu, Y., Wen, H., Guo, J., Jin, Y. F., Wei, G. M., and Yang, Z. W. (2020). Coal spontaneous combustion and N<sub>2</sub> suppression in triple goafs: A numerical simulation and experimental study. *Fuel* 271, 117625. doi:10.1016/j.fuel.2020.117625
- Liu, Z. Z., Jiang, S., Tian, B., Zhu, K., and Lin, W. H. (2022). Mining subsidence monitoring based on InSAR method fusing multi-threshold target. *Acadlore Trans. Geosci.* 1 (1), 22–32. doi:10.56578/atg010104
- Ma, L. Y., Zhang, Y. L., Wang, J., Wang, J. F., and Zhou, C. S. (2022). Fire-prevention characteristics of an active colloid prepared from stimulated fly ash component. *ACS Omega* 7, 1639–1647. doi:10.1021/ACSOMEGA.1C03299
- Onifade, M., and Genc, B. (2020). A review of research on spontaneous combustion of coal. *J. Min. Sci. Technol. Engl. Ed.* 30 (3), 303–311. doi:10.1016/j.ijmst.2020.03.001
- Querol, X., Zhuang, X., Font, O., Izquierdo, M., Alastuey, A., Castro, I., et al. (2011). Influence of soil cover on reducing the environmental impact of spontaneous coal combustion in coal waste goafs: A review and new experimental data. *Int. J. Coal Geol.* 85 (1), 2–22. doi:10.1016/j.coal.2010.09.002
- Shi, G. Q., Hu, F. K., Wang, D. M., and Wang, S. L. (2014). Unsteady simulation on distribution of three zones for spontaneous combustion in goaf areas. *J. China Univ. Min. Technol.* 43 (2), 189–194. doi:10.13247/j.cnki.jcmt.2014.02.014
- Song, Z. Y., Huang, X. Y., Jiang, J. C., and Pan, X. H. (2020). A laboratory approach to CO<sub>2</sub> and CO emission factors from underground coal fires. *Int. J. Coal Geol.* 219, 103382. doi:10.1016/j.coal.2019.103382
- Su, H. T., Zhou, F. B., Song, X. L., Shi, B. B., and Sun, S. H. (2016). Risk analysis of coal self-ignition in longwall gob: A modeling study on three-dimensional hazard zones. *Fire Saf. J.* 83, 54–65. doi:10.1016/j.firesaf.2016.04.002
- Tang, M. Y., Jiang, B. Y., Zhang, R. Q., Yin, Z. Q., and Dai, G. L. (2016). Numerical analysis on the influence of gas extraction on air leakage in the gob. *J. Nat. Sci. Eng.* 33, 278–286. doi:10.1016/j.jngse.2016.05.006
- Tian, Y., Yang, C. H., Sun, Q. J., Chang, K. K., and Guo, Z. L. (2020). Air leakage law in goaf of the working face using U-type ventilation. *Coal Eng.* 52 (12), 132–136. doi:10.11799/ce202012028
- Wang, H. Y., Feng, C., Geng, L., Yu, B., Cui, X. L., and Chen, M. Z. (2014). Study on air leakage in underground coal fire based on energy level and tracer test. *J. Saf. Sci. Technol.* 10 (1), 118–123. doi:10.11731/j.issn.1673-193x.2014.01.020
- Wen, H., Yu, Z. J., Fan, S. X., Zhai, X. W., and Liu, W. Y. (2017). Prediction of spontaneous combustion potential of coal in the gob area using CO extreme concentration: A case study. *Combust. Sci. Technol.* 189, 1713–1727. doi:10.1080/00102202.2017.1327430
- Wu, Z. Y., Hu, S. S., Jiang, S. G., He, X. J., Shao, H., Wang, K., et al. (2018). Experimental study on prevention and control of coal spontaneous combustion with heat control inhibitor. *J. Loss Prev. Process Indust.* 56, 272–277. doi:10.1016/j.jlp.2018.09.012
- Xing, Z. (2021). Numerical simulation study on the influence of surface air leakage in shallow thick coal seam on coal spontaneous combustion in goaf. *Industry Mine Automation* 47 (2), 80–87. doi:10.13272/j.issn.1671-251x.2020100018
- Zhang, Z., and Ji, S. F. (2016). Numerical simulation of particle/monolithic two-stage catalyst bed reactor with beds-inter-space distributed dioxygen feeding for oxidative coupling of methane. *Comput. Chem. Eng.* 90, 247–259. doi:10.1016/j.compchemeng.2016.04.036
- Zhao, Q. F., He, H. R., Zhang, J. W., Zhang, J. G., and Wang, Y. H. (2016). Surface air leakage of fully-mechanized top coal caving mining in shallow depth seam affected to abandoned coal spontaneous combustion and control. *Coal Sci. Technol.* 44 (3), 65–69. doi:10.13199/j.cnki.cst.2016.03.013
- Zheng, X. Z., Wang, X. L., Guo, J., Zhang, D., and Wang, B. Y. (2019). Experimental study on CH<sub>4</sub> displacement from coal seam fractured by liquid CO<sub>2</sub>. *Int. J. Heat Technol.* 37 (1), 212–218. doi:10.18280/ijht.370126
- Zheng, L. W., Ao, K., Yuan, Q., Li, Z., Wang, X., and Zhou, X. (2022). Study on the reference material of sulfur hexafluoride (SF<sub>6</sub>) and application on quantitative analysis of oil-gas field tracer. *China Meas. Test* 48 (3), 66–71. doi:10.11857/j.issn.1674-5124.2021100172
- Zhu, J. F., Xu, Y. M., Guo, W. J., and Duan, J. M. (2016). Using potential energy measurement and SF<sub>6</sub> tracer gas to detect air leakage in complicated goaf. *J. North China Inst. Sci. Technol.* 13 (4), 30–34.
- Zuo, Q. L., Li, J. S., and Zhang, Z. H. (2018). Dynamic change of air leakage intensity of loose coal in goaf after fully-mechanized top coal caving without pillar mining. *Coal Sci. Technol. Mag.* 4, 1–4. doi:10.19896/j.cnki.mtkj.2018.04.001
- Zuo, Q. L., Li, J. S., and Wang, Y. J. (2021). Distribution law for the danger area for spontaneous coal combustion in a dynamic goaf with low air leakage speed. *Therm. Sci.* 25 (5A), 3229–3237. doi:10.2298/TSCI200602308Z



## OPEN ACCESS

## EDITED BY

Zhibo Zhang,  
University of Science and Technology  
Beijing, China

## REVIEWED BY

Chenchen Wang,  
China University of Mining and  
Technology, Beijing, China  
Botao Li,  
Xi'an University of Science and  
Technology, China

## \*CORRESPONDENCE

Yuyang Shang,  
✉ 15991220977@163.com

## SPECIALTY SECTION

This article was submitted to  
Environmental Informatics and Remote  
Sensing,  
a section of the journal  
Frontiers in Earth Science

RECEIVED 29 December 2022

ACCEPTED 01 March 2023

PUBLISHED 10 March 2023

## CITATION

Shang Y (2023), Experimental research on  
the water precipitation performance of  
polymer colloid and fly ash colloid and  
their applications as fire extinguishing  
materials in mines.

*Front. Earth Sci.* 11:1133732.

doi: 10.3389/feart.2023.1133732

## COPYRIGHT

© 2023 Shang. This is an open-access  
article distributed under the terms of the  
[Creative Commons Attribution License  
\(CC BY\)](https://creativecommons.org/licenses/by/4.0/). The use, distribution or  
reproduction in other forums is  
permitted, provided the original author(s)  
and the copyright owner(s) are credited  
and that the original publication in this  
journal is cited, in accordance with  
accepted academic practice. No use,  
distribution or reproduction is permitted  
which does not comply with these terms.

# Experimental research on the water precipitation performance of polymer colloid and fly ash colloid and their applications as fire extinguishing materials in mines

Yuyang Shang<sup>1,2\*</sup>

<sup>1</sup>College of Safety Science and Engineering, Xi'an University of Science and Technology, Xi'an, Shaanxi, China, <sup>2</sup>Shaanxi Key Laboratory of Prevention and Control of Coal Fire, Xi'an University of Science and Technology, Xi'an, Shaanxi, China

In this paper, polymer colloid and fly ash colloid fire extinguishing materials are selected. Through experimental preparation and water precipitation characteristics research, colloid fire extinguishing materials and optimal concentration ratio suitable for Binchang mining area are selected to effectively control the fire area. The results show that, the higher the concentration of polymer colloidal powder mixed with water, the shorter the gelling time. After the fly ash is mixed with the gelling agent and water, when the concentration ratio of fly ash to water remains the same, the greater the concentration of the gelling agent, the shorter the gelling time. After the colloid is left standing for 24 h, the smaller the concentration is, the more water is precipitated, and the higher the water precipitation rate is. Through comparison, it was found that when the polymer colloid was selected as the fire extinguishing material, with the concentration ratio of polymer colloid material to water being 3.5%–4%: 96.5%–96%, effective control could be achieved over the fire zones in the goaf of Binchang mine. The research is of great reference value for the control of mine fires.

## KEYWORDS

spontaneous combustion of coal, polymer colloid, fly ash colloid, water precipitation characteristics, fire zone management

## 1 Introduction

China is rich in coal resources, with its output and consumption being among the world's highest (Qi and Kuan, 2011). The disasters in mines are complex and of various types, and fires caused by spontaneous combustion of coal are one of the most serious mine disasters (Querol et al., 2011; Liu et al., 2020; Onifade and Genc, 2020), which can easily cause casualties, environmental pollution and property losses (Deng et al., 2017; Wu et al., 2018; Li et al., 2019; Song et al., 2020). Data show that fire incidents caused by spontaneous combustion of coal account for more than 90% of the mine fires (Su et al., 2016; Ma et al., 2022). With the improvement of the safety level of coal mines, the spontaneous combustion of coal seams is mainly managed by the principle of “prevention first and

prevention and treatment combined” (Zhang, 2018; Liu et al., 2022), which has put forward higher requirements for the fire extinguishing materials used in mines.

At present, grouting technology is the most widely used technology to inhibit coal spontaneous combustion because of its low cost (Colaizzi, 2004; Wen et al., 2017). The grouting technology mainly includes slurry grouting, gel, three-phase foam, polymer colloids and other materials (Liang et al., 2016). Domestic and foreign researchers have carried out a lot of research on the grouting technology and its application in fire extinguishment, and achieved certain results. Based on the existing prevention and control measures taken in Lijiata Coal Mine, Chen (2020) proposed an emergency response plan for preventing spontaneous combustion of coal by using fly ash thickened colloid to wrap the broken coal body and block the leaking air. Li et al. (2005) applied the fire prevention and extinguishing technology of pipe-network-type composite colloid injection to successfully control the large fire zone with complicated air leakage situation in Shuangyashan Dongrong No.3 Mine, which ensured the normal use of the rail going up the mountain and the safety of the whole mine. Wang et al. (2017) developed a control plan based on fly ash colloid grouting according to the characteristics of the spontaneous combustion of coal in the Ewirgol Coal Mine, which helped successfully extinguish the natural fires in this mine. Yang et al. (2020) found that the fly ash composite colloid isolation technology can be used to quickly deal with the complex fire zones in Huashan Mine and the spreading and escalating fires there. In response to the signs of spontaneous combustion of coal pillars in the main tunnel of Huangling No. 2 Coal Mine in Shaanxi Province, Yan (2015) used the polymer colloid fire prevention technology to effectively deal with abnormal high-temperature areas. Shi et al. (2018) analyzed the potential application of the optimal concentration of surfactant in stabilizing fly ash suspension to delay coal spontaneous combustion.

Fly ash used for grouting fire extinguishing can play the role of isolation, encapsulation and cooling (Zhao et al., 2019). Polymer colloid has the comprehensive characteristics of water retention, cooling, plugging and inhibition (Zhang et al., 2011). The interface properties of fly ash and polymer colloid material matrix are different. Most researchers at home and abroad only study the fire extinguishing technology for a certain material. In this paper, the water precipitation and water loss of two kinds of fire extinguishing materials, the polymer colloid fire extinguishing agent and the fly ash colloid fire extinguishing agent, after being placed at different concentrations for 24 h are studied experimentally. The optimal fire extinguishing material and its concentration ratio suitable for Binchang mining area are selected, and the amount of glue injected into the filling roadway is calculated. The reasonable injection process is adopted. The research conclusion can play a good role in controlling the spontaneous combustion of loose accumulation coal in underground goaf.

The subsequent sections of this paper are organized as follows: Section 2 introduces the overview of the fire zones. Grouting of ignition points in the working face for fire extinguishment is elaborated in Section 3. Section 4 is dedicated to the experimental study. Discussion is evaluated in Section 5. And Section 6 describes the implementation of the fire prevention and extinguishment project. Finally, conclusions are given in Section 7.

## 2 Overview of the fire zones

Binchang Mine Field is located in the north of Taiyu anticline, in which the main minable coal seams are prone to spontaneous combustion of coal. In the mines of this mine field, the fully mechanized top coal caving is mostly adopted for the coal mining, resulting in large amount of float coal in the goafs, so it is necessary to focus on preventing the fires caused by spontaneous combustion of float coal in the goaf. The coal seam structure in the mining area is complex, with developed endogenous fissures, and the coal seam thickness is 12 m. In the process of tunnel excavation, due to the local high pressure of the mine, the top coal body is relatively broken, forming air leakage ways which constantly supply oxygen, which has made it possible for heat storage. When the temperature in the deep part of top coal is above 60°C, the CO concentration will continue to increase and gradually spread along the working face. Therefore, it can be judged that there are abnormal high-temperature areas in the mine field, which have high risks of spontaneous combustion of coal.

## 3 Grouting of ignition points in the working face for fire extinguishment

### 3.1 Problems and solutions

The design and good application of mine fire prevention and control is a complex, systematic process. At present, there are some problems in the fire prevention and extinguishment technology and equipment adopted in Binchang Mine Field and the basic research on spontaneous combustion, specifically as follows: 1) with the increase of mining depth, the mining process suffers more obvious disturbances, and the geothermal gradient increases significantly, but there is little research on the coupling effect of the spontaneous combustion of deep coal seams under the influence of hot air pressure; 2) in terms of monitoring and early warning, China lacks an integrated fire monitoring and warning system against both internal and external causes, and it is imperative to establish such an integrated monitoring and prevention technology system for coal mine fires that organically combines early fire monitoring and warning and expert decision-making and analysis; 3) in terms of fire control, besides high costs, the current fireproof materials are not pertinent enough to completely control the high-temperature areas, resulting in frequent re-ignitions, and the professional equipment used by personnel are not intelligent enough; 4) in terms of emergency rescue of mine fires, there has been a lack of explosion hazard detection and control technologies in semi-enclosed areas and special monitoring equipment for opening and closing of fire zones to deal with the wide range of and complex situations involved in the chain reaction disasters caused by fires; 5) facing the worldwide problem—detection of hidden fire sources, the drilling method used is costly and wasteful. The isotope radon measurement method can be easily affected by air leakage, and the remote sensing method is also susceptible to surface radiation, lithology and geological structures of overlying strata.

So far, China has made great progress in the monitoring and early warning of mine fires, the management of mine fires, the emergency rescue of fire incidents, the comprehensive evaluation



methods for fire hazards resulting from internal and external causes in coal mines based on the Internet big data platform, and the corresponding management platform technologies and equipment: 1) in terms of emergency rescue, small instruments such as gas analyzers for detection of coal mine disasters have been developed, among which, the portable infrared coal temperature monitoring device can provide *in-situ* monitoring and analysis underground, and the developed gas explosion-proof material can achieve the explosion risk prediction and rapid protection against the catastrophic environment of fire zones. 2) in terms of fire prevention and control, the technologies of monitoring the ignition points in hidden areas by electronic control and infrared remote sensing methods have been developed, and new types of aerosol and foam inhibitors and microorganisms have also been worked out for fire extinguishment, large-aperture fire-fighting drilling equipment have been developed against large-aperture and loose coal bodies, short-distance composite inert gas cooling and air plugging technologies have been explored for shallow buried coal seams, and rapid cooling and fire-extinguishing equipment and technologies, for high-temperature coal bodies.

### 3.2 Management plan

The coal seam in the affected working face has an inclination length of 220 m and a thickness of 12 m, the length of the mining area is 3 m, and that of the venting area is 9 m, with 40 m not topped. The overall bottom length of the drill holes is 6 m, and there are three rows of drill holes. According to the conditions of the goaf, the grouting technology was adopted, which can effectively control the spontaneous combustion of loose coal body in the goaf.

The polymer colloid has the advantages of fast gelation speed, simple process and less corrosive to the equipment, which can effectively improve the water content in the fire extinguishing agent and greatly improve the fire extinguishing efficiency. The fly ash gelling agent can accumulate a large amount of water after swelling in water, so that the mixed slurry has great heat storage capacity and good thermal stability. After dehydration, it can be stored in water again, which has a good effect in preventing and controlling coal seam spontaneous combustion fire. Therefore, polymer colloid fire extinguishing agent and fly ash colloid fire extinguishing agent were selected.

## 4 Experimental study

### 4.1 Experimental principle

In this experiment, polymer colloid fire extinguishing agent and fly ash colloid fire extinguishing agent are used to control the spontaneous combustion fire of loose accumulation coal in underground goaf. After grouting in the goaf, the loose coal in the lower layer of the accumulation body is wrapped by the water precipitation of the colloid, and the heat in the loose coal-fired body is replaced by the good thermal conductivity of the water, and the colloid deposited in the upper layer is used to absorb the



**FIGURE 1**  
Polymer colloid fire extinguishing agent.

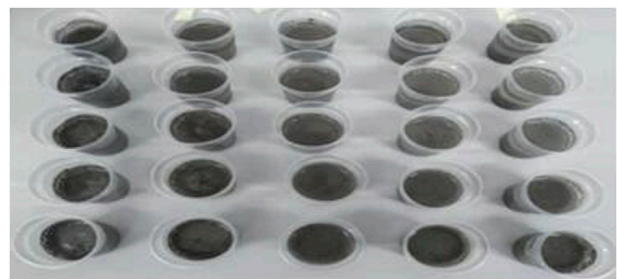


**FIGURE 2**  
Fly ash colloid fire extinguishing agent.

replacement heat. Through these two experiments, the heat in the loose self-fired coal body is removed to achieve a good cooling effect.

### 4.2 Process of the experiment

#### 4.2.1 Experimental materials

The experimental materials required for the preparation of polymer colloid and fly ash colloid fire extinguishment agents are shown in [Table 1](#).

#### 4.2.2 Steps of the experiment

The steps for the preparation of polymer colloid and fly ash colloid fire extinguishing agents are shown in [Table 2](#).

[Figure 3](#) and [Figure 4](#) compare the water precipitation performance of polymer colloid and fly ash colloid fire extinguishing agents with different concentrations, respectively. It can be clearly seen that when the concentrations are different, the water precipitation of the polymer colloid and the fly ash colloid fire extinguishing agents is quite obvious.

### 4.3 Experimental results

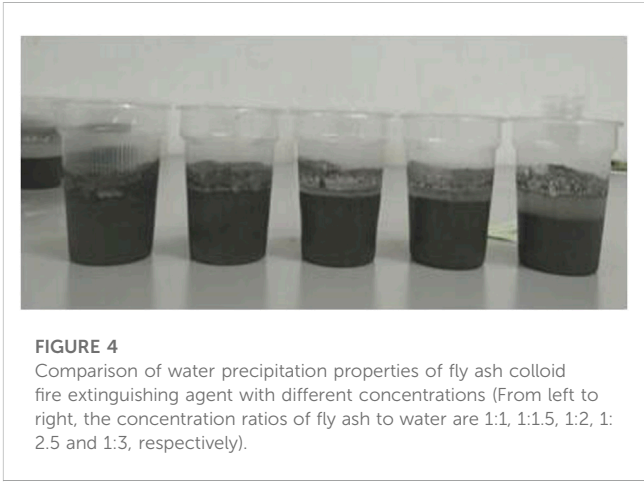
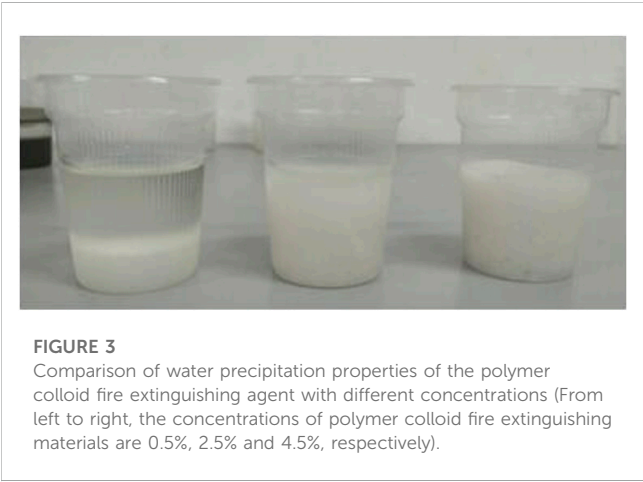
All colloids can retain water—they can make a certain amount of water retained in the colloidal network framework and lose its fluidity. The colloid fire extinguishing agent makes full use of the

TABLE 1 Experimental materials required for preparation of polymer colloid and fly ash colloid fire extinguishing agents.

	Preparation of polymer colloid fire extinguishing agent	Preparation of fly ash colloid fire extinguishing agent
Experimental materials	Polymer colloid fire extinguishing agent (as shown in Figure 1), water, disposable clear plastic cups, a stopwatch, and glass rods	Gelling agent, water, disposable clear plastic cups, a stopwatch, glass rods, and fly ash (as shown in Figure 2)

TABLE 2 Steps for the preparation of polymer colloid and fly ash colloid fire-extinguishing agents.

	Preparation of polymer colloid fire extinguishing agent	Preparation of fly ash colloid fire extinguishing agent
Steps of the experiment	1) Prepare the raw materials required for the experiment, such as polymer colloid fire extinguishing material, disposable clear plastic cups, and glass rods.	1) Prepare the raw materials required for the experiment, such as gelling agent, disposable clear plastic cups, glass rods, and fly ash, etc.
	2) Keep the concentration range of the polymer colloid fire extinguishing material at 0.5%–5%, and mix it with water. Set control groups for the polymer colloid powder by increasing its concentration at a rate of 0.5%, and prepare 100 g of solution for each group.	2) Keep the concentration range of the gelling agent at 0.06%–2%, and mix it with water and fly ash. Set control groups for the gelling agent by increasing its concentration at a rate of 0.5%, and prepare 100 g of solution for each group.
	3) Prepare the polymer colloid fire extinguishing solution with a concentration of 0.5%, where the required mass of the polymer colloid fire extinguishing material is 0.5g, and the required volume of water is 99.5 ml.	3) Prepare the solution at a fly ash to water ratio of 1:1, and add 0.06% gelling agent solution, which requires 0.06 g of gelling agent, 49.97 ml of water and 49.97 g of fly ash.
	4) Weigh the required substances with an electronic balance, pour them into the clear plastic cups, and label them separately for easy identification.	
	5) Weigh 99.5 ml of water with a measuring cylinder, and pour the polymer colloid powder into the water, stir while pouring it to make it thoroughly mixed, until it becomes colloidal, and record the gelling time.	5) Weigh 49.97 ml of water with a measuring cylinder, pour the gelling agent into the water, stir while pouring it to make it thoroughly mixed, until it becomes colloidal, and record the gelling time.
	6) Mix all the group thoroughly and record the time, and then record the quality of the colloid every 1 h, 2 h, 5 h, and 24 h, and observe the changing trend of the colloid quality; after 24 h, record the volume of water precipitated.	6) Mix all the group thoroughly and record the time, and then record the quality of the colloid every 1 h, 2 h, 18 h and 24 h, and observe the changing trend of the colloid quality; after 24 h, record the volume of water precipitated.



water retention property to extinguish fires with water and also makes up for the shortcoming of flowing water, that is, it is highly fluid and unable to extinguish fires at high places such as the tops of the tunnels and working faces. The more stable the structure of the colloid, the greater the force between the colloid and water, and the slower the water loss rate at a high temperature, which is very conducive to prevention and extinguishment of coal mine fires. If the water loss rate of the colloid is too high, the colloid structure will be unstable and have a shorter useful life, making it difficult to achieve the desired fire-extinguishment effect. The calculation of water loss rate and water precipitation rate of colloidal materials is

helpful to study the water retention properties of the two colloidal materials.

The formula for calculating the water loss rate is as follows:

$$Y = \frac{M_1}{M_2} \tag{1}$$

where,  $Y$  is the water loss rate of the polymer colloid fire extinguishing agent,  $M_1$  is the mass reduction, and  $M_2$  is the total mass.

The formula for calculating the water precipitation rate is as follows:

TABLE 3 Calculation results of the water loss rate and water precipitation rate of the polymer colloid fire extinguishing agent.

Group	Concentration of the polymer colloid fire extinguishing material/%	Water/%	Gelling time/s	Residual mass/g				Water loss rate/%	Drainage/mm	Total volume/%	Drainage rate/%
				1 h	2 h	5 h	24 h				
1	0.5	99.5	56	99.82	99.71	99.46	97.69	2.31	35	53	66.04
2	1.0	99.0	47	99.62	99.60	99.36	97.59	2.41	27	52	51.92
3	1.5	98.5	34	99.78	99.66	99.42	97.78	2.22	21	50	42.00
4	2.0	98.0	31	99.75	99.60	99.36	97.75	2.25	16	48	33.33
5	2.5	97.5	29	99.93	99.90	99.80	98.22	1.78	11	51	21.57
6	3.0	97.0	19	99.69	99.65	99.45	97.90	2.10	6	52	11.54
7	3.5	96.5	13	99.96	99.94	99.83	98.26	1.74	3	51	5.88
8	4.0	96.0	12	99.94	100.05	99.83	98.26	1.74	0	50	0.00
9	4.5	95.5	8	99.33	99.38	99.16	97.52	2.48	0	49	0.00
10	5.0	95.0	6	99.91	99.94	99.70	97.94	2.06	0	50	0.00

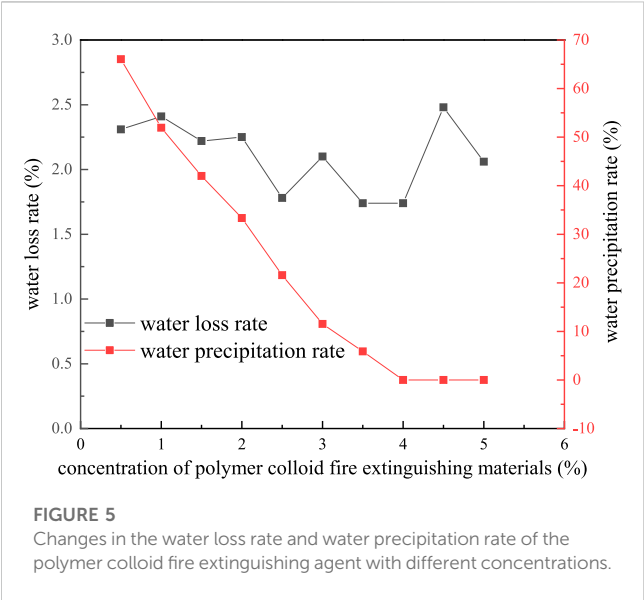


FIGURE 5 Changes in the water loss rate and water precipitation rate of the polymer colloid fire extinguishing agent with different concentrations.

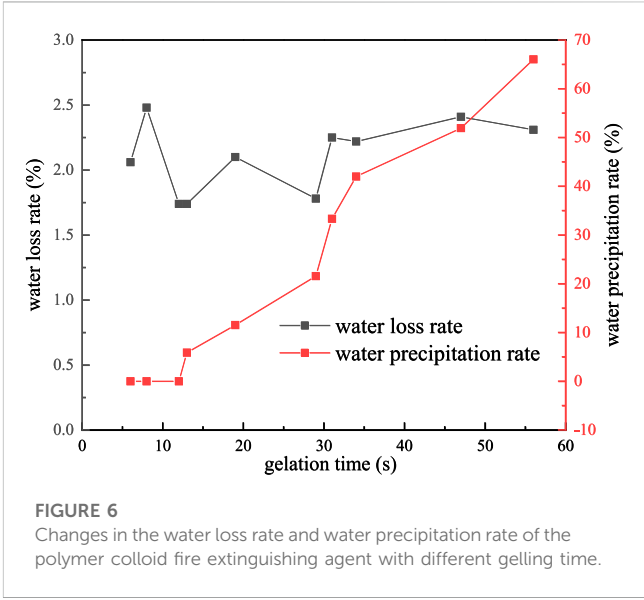


FIGURE 6 Changes in the water loss rate and water precipitation rate of the polymer colloid fire extinguishing agent with different gelling time.

$$P = \frac{V_1}{V_2} \tag{2}$$

where,  $P$  is the water precipitation rate of the polymer colloid fire extinguishing agent,  $V_1$  is the mass reduction, and  $V_2$  is the total mass.

4.3.1 Water loss rate/water precipitation rate of the polymer colloid fire extinguishing agent

According to Eq. 1 and Eq. 2, the calculation results of the water loss rate and water precipitation rate of the polymer colloid fire extinguishing agent are shown in Table 3.

Figure 5 shows the changes of water loss rate and water precipitation rate of the polymer colloid fire extinguishing agent with different concentrations, and the effect of gelling time of polymer colloid fire extinguishing material on water loss rate and

water precipitation rate is shown in Figure 6. It can be seen from Figure 5 and Figure 6: 1) After the polymer colloid powder was mixed with water, the higher the concentration, the shorter the gelling time. 2) After the colloid was left standing for 24 h, the smaller the concentration, the more the water precipitated, and the higher the water precipitation rate. 3) When the concentration of the polymer colloid fire extinguishing material was 4.5% and the concentration of water 95.5%, the water loss rate was the highest—2.48%, indicating that its water retention performance was the worst. When the concentration of the polymer colloid fire extinguishing material was 3.5% and the concentration of water 96.5%, or when the concentration of the polymer colloid fire extinguishing material was 4% and the concentration of water 96%, the water loss rate was the lowest—1.74%, indicating that its water retention performance reached the best level. According to the

TABLE 4 Calculation results of the water loss rate and water precipitation rate of the fly ash colloid fire extinguishing agent.

Fly ash: water	Fly ash/%	Water/%	Gelling agent/%	Gelling time/s	Residual mass/g				Water loss rate/%	Water precipitation/mm	Total volume/%	Water precipitation rate/%
					1 h	2 h	18 h	24 h				
1:1	49.97	49.97	0.06	51	99.43	99.31	97.86	97.04	2.96	1.00	3.0	33.3
	49.72	49.72	0.56	35	99.40	99.27	97.94	97.13	2.87	0.40	3.9	10.3
	49.50	49.50	1.00	25	98.63	98.47	97.14	96.39	3.61	0.05	3.9	1.3
	49.25	49.25	1.50	18	97.58	97.40	96.13	95.47	4.53	0.02	4.4	0.5
	49.00	49.00	2.00	15	98.58	98.43	97.08	96.40	3.60	0.01	4.0	0.3
1:1.5	39.98	59.96	0.06	55	99.41	99.31	97.97	97.23	2.77	1.70	2.9	58.6
	39.78	59.66	0.56	37	99.73	99.61	98.34	97.56	2.44	0.80	3.6	22.2
	39.60	59.40	1.00	27	99.54	99.37	98.08	97.32	2.68	0.20	3.9	5.2
	39.40	59.10	1.50	21	99.87	99.70	98.46	87.75	2.25	0.10	3.8	2.6
	39.20	58.80	2.00	20	99.51	99.43	98.14	97.43	2.57	0.05	4.0	1.3
1:2	33.31	66.62	0.06	57	99.47	99.34	97.97	97.23	2.77	2.10	2.3	91.3
	33.15	66.29	0.56	38	97.71	97.58	96.28	95.56	4.44	0.60	3.3	19.2
	33.00	66.00	1.00	31	99.72	99.55	98.33	97.64	2.36	0.50	3.7	14.2
	32.83	65.67	1.50	22	99.72	99.56	98.26	97.67	2.33	0.40	4.0	10.0
	32.67	65.33	2.00	20	99.54	99.43	98.16	97.44	2.56	0.40	4.2	9.5
1:2.5	28.55	71.39	0.06	63	99.48	99.36	97.91	97.12	2.88	2.10	2.6	81.6
	28.41	71.03	0.56	51	99.71	99.60	98.33	97.62	2.38	1.50	3.0	50.0
	28.29	70.71	1.00	35	99.57	99.46	98.25	97.56	2.44	1.20	3.2	34.5
	28.14	70.36	1.50	27	99.61	99.49	98.26	97.58	2.42	0.90	3.2	28.1
	28.00	70.00	2.00	22	99.16	99.02	97.67	96.94	3.06	0.90	3.4	26.4
1:3	24.99	74.95	0.06	75	99.66	99.58	98.08	97.28	2.72	2.20	3.0	73.3
	24.86	74.58	0.56	58	99.70	99.57	98.19	97.52	2.48	1.90	3.1	61.3
	24.75	74.25	1.00	37	99.88	99.66	98.40	97.72	2.28	1.60	3.4	47.1
	24.63	73.88	1.50	28	99.65	99.47	98.12	97.41	2.59	1.20	3.5	34.3
	24.50	73.50	2.00	24	99.15	98.99	97.57	96.82	3.18	1.00	3.6	27.8

experimental results, it can also be found that the polymer colloid after gelation has the following properties: 1) lower water loss and better water precipitation. 2) higher fluidity before gelation, and water precipitation after gelation, making it able to seal fluids.

4.3.2 Water precipitation rate/water loss rate of the fly ash colloid fire extinguishing agent

According to Eq. 1 and Eq. 2, the calculation results of the water loss rate and the water precipitation rate of the fly ash colloid fire extinguishing agent are displayed in Table 4.

Figure 7 is the variation curves of the gelling time with the concentration of the gelling agent under different concentration ratios of fly ash and water. As can be observed in Figure 7, after the fly ash was mixed with the gelling agent and water, when the concentration ratio of fly ash and water remained the same, the greater the concentration of the gelling agent, the shorter the gelling

time. When the concentration of the gelling agent remained the same, the greater the concentration of water mixed with fly ash, the longer the gelling time. The changes in the water loss rate and water precipitation rate under different concentration ratios of fly ash to water are shown in Figure 8. After the colloid was left standing for 24 h, the smaller the concentration, the more water precipitated, and the higher the water precipitation rate. Through comparison of the water loss rate and water precipitation rate under different concentration ratios, it can be found that when the concentration ratio of fly ash to water was 1:1, and the concentrations of fly ash and water were both 49.25%, the water loss rate reached the maximum—4.53%, but the water precipitation rate was 0.5%, which was not the lowest level, indicating that its water retention performance was not the best. When the concentration ratio of fly ash to water was 1:1.5, the concentration of fly ash was 39.40%, and the concentration of water 59.10%, the water loss rate was the

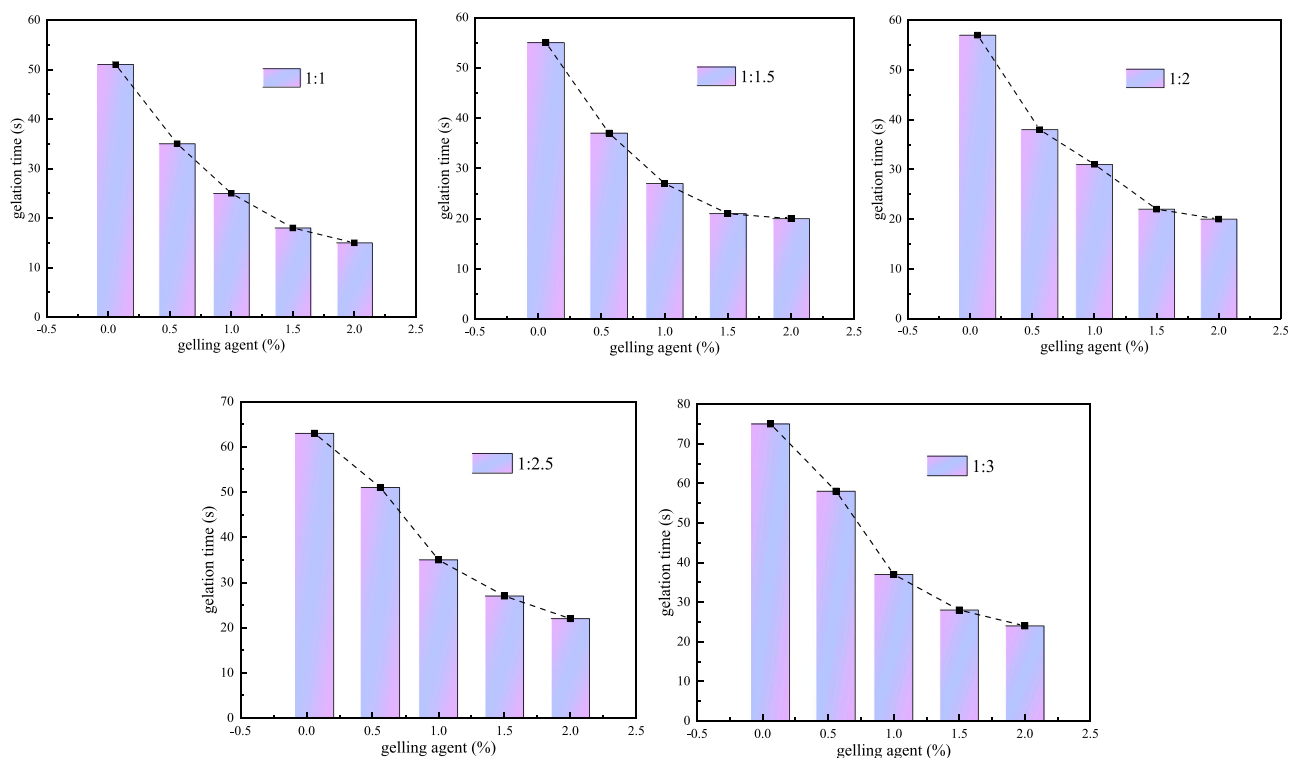


FIGURE 7

Variation curves of the gelling time with the concentration of the gelling agent under different concentration ratios of fly ash and water.

smallest—2.25%, but the water precipitation rate was 2.6%, which was not the highest, indicating that its water retention performance was not the best, either.

## 5 Discussion

Based on the two experimental results, we can make the following analysis and discussion: 1) When the polymer colloid to water concentration ratio in the polymer colloid fire extinguishing agent is 4.5%:95.5%, the water loss rate is the highest and the water retention is the poorest. However, when the concentration ratio is 3.5%–4%:96.5%–96%, the water loss rate is the lowest and the water retention is the best. 2) When the concentration ratio is 5%:95%, the gelling time is the shortest, but its water retention is not the best. When the concentration ratio of the two is 0.5%:95%, the gelling time is the longest, but the effect is not obvious, and the water retention effect is not the best, either. 3) In the experiment where the fly ash was mixed with water and gelling agent, it can also be found that when the ratio of fly ash, water and gelling agent leads to the shortest or longest gelling time, the water retention may not be the best or the worst.

Both polymer colloid and fly ash colloid fire extinguishing agents have their own advantages. The fly ash colloid material has been used for a longer time, and has the advantages of low price, non-toxicity and good permeability, but it also has its disadvantages—large consumption, long gelling time, inability to be accumulated in high places, poor fluidity, easiness to block

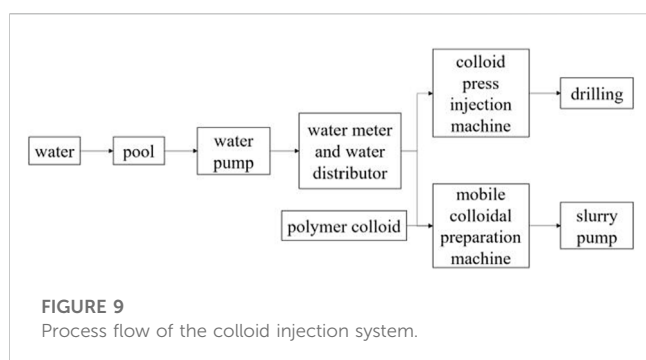
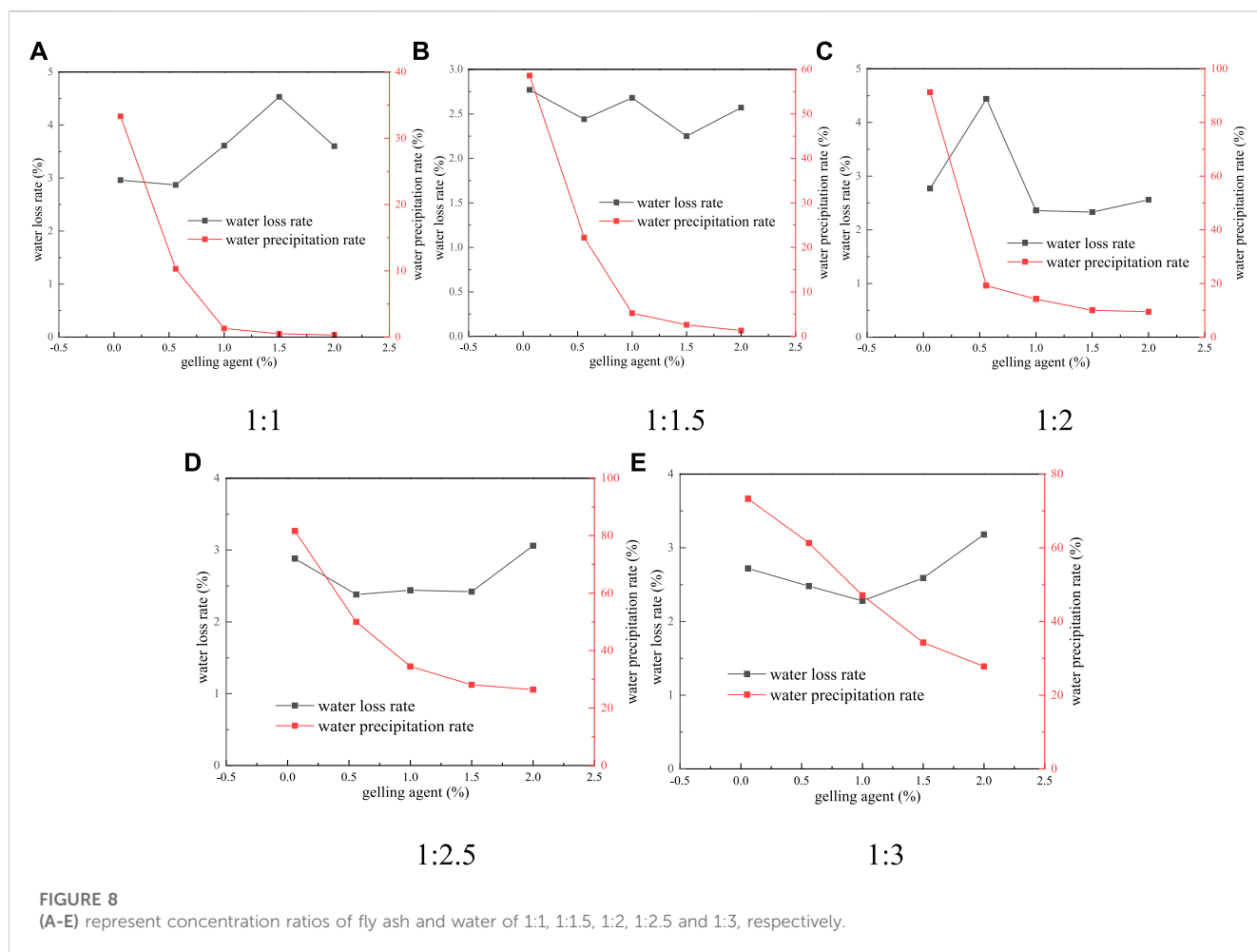
pipelines and easy cracking of the gel layer. While the polymer gel material has good fluidity, good fire prevention and extinguishment effect, and high strength of the gel layer, but it is more costly. In the traditional fly ash slurry, water only adheres to the surface of the fly ash particles, and since the fly ash slurry has no three-dimensional network structure, the water retention performance of the traditional fly ash slurry is poor. Through comparison of the advantages and disadvantages of the two types of materials, the polymer colloid fire extinguishing agent was finally chosen to effectively control the spontaneous combustion of loose coal in the goaf of Binchang mining area.

## 6 Implementation of the fire prevention and extinguishment project

### 6.1 Colloid injection system and process

The grouting and colloid injection system mainly consist of the ground portable grouting and colloid injection fire prevention and fire extinguishing system developed by the coal fire disaster prevention innovation team at Xi'an University of Science and Technology, supported by the portable fire prevention and extinguishment devices for mine use. The project was implemented in a targeted manner. The process flow of the colloid injection system is shown in Figure 9. The structure and function principle of the portable fire prevention and extinguishment devices for mine use are presented in Figure 10.





## 6.2 Design and arrangement of glue injection drilling

The colloid injection project used “polymer colloid” as the main fire extinguishing medium. Based on the distance of 5 m between the top of the two boreholes, it can be calculated that about 44 boreholes should be drilled, and each borehole must be drilled into the goaf. The total amount of colloid injected was calculated as follows: 9 (goaf)  $\times$  220 (inclination length of the working face)  $\times$  6 (overall bottom length of the drilling holes)  $\times$  1.5 (fill factor) = 17,820 m<sup>3</sup>,

and the colloid injection volume for each drilling hole was about 405 m<sup>3</sup>. Through 44 fire extinguishing boreholes, polymer colloid fire extinguishing agent was poured from high to low to fill the loose coal in the goaf to achieve cooling and oxygen barrier.

In order to achieve the desired effect of colloid injection, the fire extinguishing holes must be arranged with the underground goaf as the center. By reference to the detection results of the fire zones, the drilling positions should be arranged above the goaf and the tunnel if possible, and avoid coal pillars. The holes should be finished at the bottom plate of the coal seam, which was to be injected with colloid. In order to first control the fire sources deep in the fire zones, the holes should be arranged on the ground from east to west and south to north, with deep holes first and then shallow ones.

## 6.3 Notes for injection process

- (1) Before the colloid injection, the air volume of the affected working face was adjusted first, and the air volume was reduced from 230 m<sup>3</sup>/s to 180 m<sup>3</sup>/s to reduce the air leakage to the roof of coal seam. Considering the fluidity of the colloid, the direct injection into the float coal on the roof may cause the polymer colloid to flow into the tunnel, leading to the fall of the

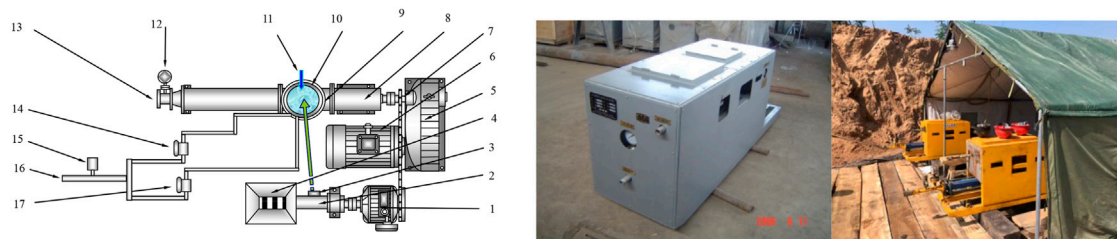


FIGURE 10

1-belt speeder, 2-polymer fire extinguishing agent quantitative feeding assembly, 3-colloid material outlet, 4-material tank, 5-reducer, 6-explosion-proof motor, 7-transmission chain, 8-screw pump, 9-screw pump inlet (mixture box), 10-ring water curtain tube, 11-water glass entrance, 12-seismic pressure gauge, 13-screw pump outlet, 14-hand wheel water valve "a", 15-water flowmeter, 16-water inlet, 17-hand wheel water valve "b".

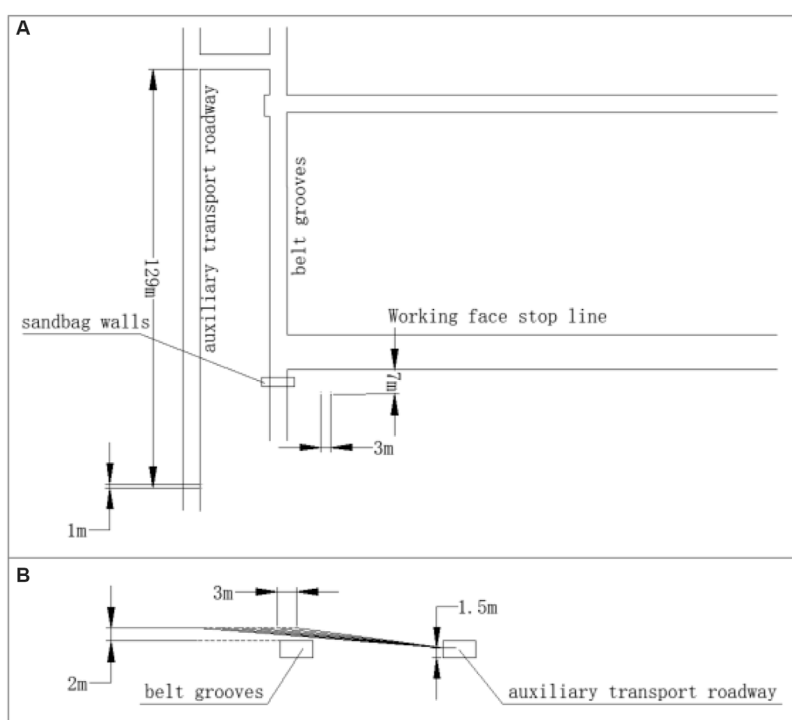


FIGURE 11

Schematic diagram of the inlet end injection (A) and (B) are the top view and main view of glue injection drilling construction, respectively).

- top coal and creating larger voids, thereby affecting the fire extinguishing effect. Therefore, it is necessary to spray cement mortar on the two sides and roof of the tunnel within the fire zone first, and then densely drill holes in the roof of the tunnel to ensure the effectiveness of the colloid injection process.
- (2) The colloid injection equipment was placed in the tunnel near the fire source, and through control of the valve, the colloid was injected alternately, so as to ensure the continuity of colloid injection. Then the two base solutions were pushed into the mixer by two mud pumps to make the two solutions evenly mixed, and then into the colloid injection holes through the colloid output pipes. Injection can be carried out into two holes at the same time.
  - (3) For a situation where the coal has spontaneously ignited and there is an open flame, the polymer colloid is required to form a gel quickly after being mixed at the sprayer outlet. Therefore, it is necessary to use two feeding systems of the same model to transport the two raw materials A and B to the ignition site, and mix them with the sprayer to quickly form a gel to cover the fire zone.
  - (4) During colloid injection into the holes, in a large goaf, the parameters of colloid injection should be adjusted in time to minimize the consumption of colloid provided that the desired effect can be achieved. During the colloid injection, there should be technical construction personnel both above surface and underground to make timely adjustments to any abnormal

situations that occur and record the adjustments. For different areas, the colloid filling process is slightly different, and adjustments should be made according to the actual situation.

## 6.4 Application of polymer colloid fire extinguishing materials during the withdrawal period

By injecting polymer colloid material into the air inlet end of the goaf, the cracks of the residual coal in the roof are blocked to form a colloid isolation zone to prevent air leakage to the upper part of the goaf. At the same time, the colloid isolation zone and the loess isolation wall at the air inlet end form a plugging barrier together, and the plugging effect is more obvious. Figure 11 is the schematic diagram of the inlet end injection.

A grouting pipe with a diameter of 108 mm and a one-inch injection pipe are embedded in the isolation wall, and polymer colloids are poured into the wall to seal the inlet end of the inner side of the isolation wall.

The polymer colloid material integrates the properties of plugging, cooling, resistance and consolidation of water, and solves the problem of slurry leakage and loss in traditional grouting. It is suitable for underground sealing plugging and large-area glue injection fire prevention and extinguishing such as final mining line and goaf. In view of the field situation of the working face in Binchang mining area, the polymer colloid fire prevention and extinguishing technology is adopted. Practice has proved that the gel injection effect is good.

## 7 Conclusion

This paper selected two kinds of fire extinguishment materials—polymer colloid and fly ash colloid, and conducted experimental research on the water precipitation and water loss of the above two types of colloids after 24-h standing at different concentrations, and the polymer colloid fire extinguishing material is used in Binchang mining area. The following conclusions are drawn:

- (1) After the polymer colloid powder is mixed with water, the higher the concentration, the shorter the gelling time. After the colloid is left standing for 24 h, the smaller the concentration is, the more water is precipitated, and the higher the water precipitation rate is. The water loss of the polymer colloid is lower after gelation, and on the other hand, the water precipitation is better. It is more fluid before gelation, and precipitates water after gelation
- (2) After the fly ash is mixed with the gelling agent and water, when the concentration ratio of fly ash and water remains the same, the greater the concentration of the gelling agent, the shorter the

gelling time. When the concentration of the gelling agent remains the same, the higher the concentration of water mixed with the fly ash, the longer the gelling time.

- (3) Through comparison of the water precipitation and water loss performance of the two materials and their respective advantages and disadvantages, the polymer colloid fire extinguishing agent was selected to effectively control the spontaneous combustion of loose coal in the goafs of a mine in Binchang mining area.
- (4) The colloid injection process mainly consisting of ground mobile grouting and colloid injection system was adopted for fire prevention and extinguishment in a mine of Binchang mining area, supported by portable colloid injection devices. A total of 44 holes were arranged, with a colloid injection of 405 m<sup>3</sup> into each hole, to fill the loose coal bodies in the goafs, which achieved cooling and oxygen barrier, and effectively prevented and extinguished fires in the fire zones. In the future, we can work hard on material ratio and optimization, and continue to explore new fire extinguishing materials or composite colloidal materials suitable for fire prevention and extinguishing in Binchang mining area.

## Data availability statement

The original contributions presented in the study are included in the article/supplementary material, further inquiries can be directed to the corresponding author.

## Author contributions

The author confirms being the sole contributor of this work and has approved it for publication.

## Conflict of interest

The author declares that the research was conducted in the absence of any commercial or financial relationships that could be construed as a potential conflict of interest.

## Publisher's note

All claims expressed in this article are solely those of the authors and do not necessarily represent those of their affiliated organizations, or those of the publisher, the editors and the reviewers. Any product that may be evaluated in this article, or claim that may be made by its manufacturer, is not guaranteed or endorsed by the publisher.

## References

- Chen, K. (2020). *Study on preparation of fly ash thickened colloid and fire-extinguishing properties*. China University of Mining and Technology. Beijing, China.
- Colaizzi, G. J. (2004). Prevention, control and/or extinguishment of coal seam fires using cellular grout. *Int. J. coal Geol.* 59 (1-2), 75–81. doi:10.1016/j.coal.2003.11.004

- Deng, J., Li, B., Xiao, Y., Ma, L., Wang, C. P., Lai-Wang, B., et al. (2017). Combustion properties of coal gangue using thermogravimetry-Fourier transform infrared spectroscopy. *Appl. Therm. Eng.* 116, 244–252. doi:10.1016/j.applthermaleng.2017.01.083
- Li, J. L., Lu, W., Cao, Y. J., Kong, B., and Zhang, Q. S. (2019). Method of pre-oxidation treatment for spontaneous combustion inhibition and its application. *Process Saf. Environ. Prot.* 131, 169–177. doi:10.1016/j.psep.2019.08.013
- Li, Q. J., Zhang, X. H., Fan, X. Y., and Feng, D. Q. (2005). Application of fly ash composite colloid fire prevention technology in Dongrong No. 3 Mine. *Min. Saf. Environ. Prot.* 32 (2), 45–47. doi:10.1111/j.1744-7909.2005.00136.x
- Liang, Y. T., Hou, X. J., Luo, H. Z., Tian, F. C., and Yu, G. S. (2016). Development countermeasures and current situation of coal mine fire prevention and extinguishing in China. *Coal Sci. Technol.* 44 (6), 1–6. doi:10.13199/j.cnki.cst.2016.06.001
- Liu, Y., Wen, H., Guo, J., Jin, Y., Wei, G., and Yang, Z. (2020). Coal spontaneous combustion and N<sub>2</sub> suppression in triple goafs: A numerical simulation and experimental study. *Fuel* 271, 117625. doi:10.1016/j.fuel.2020.117625
- Liu, Z. Z., Jiang, S., Tian, B., Zhu, K., and Lin, W. H. (2022). Mining subsidence monitoring based on InSAR method fusing multi-threshold target. *Acadlore Trans. Geosciences* 1 (1), 22–32. doi:10.56578/atg010104
- Ma, L., Zhang, Y., Wang, J., Wang, J., and Zhou, C. (2022). Fire-prevention characteristics of an active colloid prepared from stimulated fly ash component. *ACS omega* 7 (2), 1639–1647. doi:10.1021/acsomega.1c03299
- Onifade, M., and Genc, B. (2020). A review of research on spontaneous combustion of coal. *Int. J. Min. Sci. Technol.* 30 (3), 303–311. doi:10.1016/j.ijmst.2020.03.001
- Qi, Z., and Kuan, G. (2011). Exploration on the relationship between coal resource and China's economy development: The ANLYSIS based on econometric model. *Value Eng.* 30 (9), 171–172. doi:10.14018/j.cnki.cn13-1085/n.2011.09.017
- Querol, X., Zhuang, X., Font, O., Izquierdo, M., Alastuey, A., Castro, I., et al. (2011). Influence of soil cover on reducing the environmental impact of spontaneous coal combustion in coal waste gobs: A review and new experimental data. *Int. J. Coal Geol.* 85 (1), 2–22. doi:10.1016/j.coal.2010.09.002
- Shi, Q., Qin, B., Bi, Q., and Qu, B. (2018). Fly ash suspensions stabilized by hydroxypropyl guar gum and xanthan gum for retarding spontaneous combustion of coal. *Combust. Sci. Technol.* 190 (12), 2097–2110. doi:10.1080/00102202.2018.1491845
- Song, Z., Huang, X., Jiang, J., and Pan, X. (2020). A laboratory approach to CO<sub>2</sub> and CO emission factors from underground coal fires. *Int. J. Coal Geol.* 219, 103382. doi:10.1016/j.coal.2019.103382
- Su, H. T., Zhou, F. B., Song, X. L., Shi, B. B., and Sun, S. H. (2016). Risk analysis of coal self-ignition in longwall gob: A modeling study on three-dimensional hazard zones. *Fire Saf. J.* 83, 54–65. doi:10.1016/j.firesaf.2016.04.002
- Wang, Y. C., Liu, Y. F., and Guo, J. (2017). Application of fly-ash compound gel technique for coal spontaneous combustion prevention in roadway fire control. *Coal Technol.* 36 (5), 196–198. doi:10.13301/j.cnki.ct.2017.05.074
- Wen, H., Yu, Z., Fan, S., Zhai, X., and Liu, W. (2017). Prediction of spontaneous combustion potential of coal in the gob area using CO extreme concentration: A case study. *Combust. Sci. Technol.* 189 (10), 1713–1727. doi:10.1080/00102202.2017.1327430
- Wu, Z., Hu, S., Jiang, S., He, X., Shao, H., Wang, K., et al. (2018). Experimental study on prevention and control of coal spontaneous combustion with heat control inhibitor. *J. Loss Prev. Process Industries* 56, 272–277. doi:10.1016/j.jlp.2018.09.012
- Yan, Z. (2015). Shanxi Huangling Application of fire prevention technology with polymer colloid in Huangling No.2 colliery. *Jiangxi Coal Sci. Technol.* 3, 45–47.
- Yang, P., Liang, G. D., Yu, G. S., Zhang, X. Q., and Duan, T. (2020). Application of fly ash colloid isolation control technology in complex fire area of Huashan Mine. *Saf. Coal Mines* 51 (8), 82–86. doi:10.13347/j.cnki.mkaq.2020.08.016
- Zhang, D., Cai, W. W., Zou, Y., and Shi, Q. Q. (2011). Analysis of polymer gel fire-fighting technology principle and development situation. *Coal Technol.* 30 (11), 252–254.
- Zhang, L. (2018). Application of fire prevention beam tube monitoring technology for in fully mechanized coal working face of close distance coal seam. *Coal Eng.* 50 (S1), 100–102.
- Zhao, Z. Z., Zhang, Z. Q., and Huang, Y. Y. (2019). Research and application on fire preventing and fly ash grouting technology of coal ash grouting in Hongliu Coal Mine. *China coal.* 45 (10), 66–69. doi:10.19880/j.cnki.ccm.2019.10.013



## OPEN ACCESS

## EDITED BY

Xuelong Li,  
Shandong University of Science and  
Technology, China

## REVIEWED BY

Yu Xuguang,  
Tangshan Vocational and Technical  
College, China  
Rulong Bn,  
Guilin University of Technology, China

## \*CORRESPONDENCE

Wanjiang Wang,  
✉ wangwanjiang@xju.edu.cn

## SPECIALTY SECTION

This article was submitted to  
Environmental Informatics  
and Remote Sensing,  
a section of the journal  
Frontiers in Earth Science

RECEIVED 09 February 2023

ACCEPTED 10 March 2023

PUBLISHED 21 March 2023

## CITATION

Wang K, Wang W and Huang L (2023),  
Study on heat exchange of groundwater  
under complex geological conditions in  
karst area of south China.  
*Front. Earth Sci.* 11:1162303.  
doi: 10.3389/feart.2023.1162303

## COPYRIGHT

© 2023 Wang, Wang and Huang. This is  
an open-access article distributed under  
the terms of the [Creative Commons  
Attribution License \(CC BY\)](#). The use,  
distribution or reproduction in other  
forums is permitted, provided the original  
author(s) and the copyright owner(s) are  
credited and that the original publication  
in this journal is cited, in accordance with  
accepted academic practice. No use,  
distribution or reproduction is permitted  
which does not comply with these terms.

# Study on heat exchange of groundwater under complex geological conditions in karst area of south China

Kun Wang<sup>1</sup>, Wanjiang Wang<sup>1\*</sup> and Lidong Huang<sup>2</sup>

<sup>1</sup>College of Civil Engineering and Architecture, Xinjiang University, Urumqi, China, <sup>2</sup>Turpan Nenghui New Energy Company, Turpan, China

This paper takes a groundwater source heat pump in the region as the research object and based on field research, experimental tests combined with comparative analysis, the data on its operation is monitored and analyzed in terms of operation, energy saving, and environment. The results show that the cooling temperatures of the test rooms were all below 26°C, the average coefficient of performance of the units was 4.61–4.93 and the average coefficient of performance of the system was 3.08–3.27. In addition, compared to conventional water-cooled chillers, 466 tons of standard coal could be saved in one cooling season, resulting in a reduction of 1,150.8 tons of carbon dioxide emissions, 9.3 tons of sulfur dioxide emissions and 4.7 tons of dust emissions. The savings in operating costs are 793,000 RMB. This shows that the groundwater source heat pump has good energy efficiency and economy. The research results obtained in this paper provide a reference for improving energy efficiency and optimizing the operation of the groundwater source heat pump system. It is of great significance to the application of groundwater source heat pump systems in areas with complex geological environments.

## KEYWORDS

karst area, complex geological conditions, utilization of groundwater resources, heat exchange, energy consumption analysis

## 1 Introduction

The richer the water content of the site in the complex geological distribution area, the better the water conductivity, the greater the thermal conductivity of the rock mass, and the more conducive to improving the heat transfer effect (Liu et al., 2020a). But at the same time, there are more factors that affect development. According to DZ/T 225-2009 Code for Exploration and Evaluation of Shallow Geothermal Energy, the suitability zoning of shallow geothermal energy water source heat pump mainly considers the lithology, distribution, burial depth, thickness, water abundance, permeability, water temperature, water quality, water level dynamic changes, water source protection, and geological disasters of the aquifer (Zhou et al., 2022c).

The groundwater source heat pump system is a heat pump technology that uses groundwater as a low-level heat source or sinks to heat and cool buildings in winter and summer respectively (Ma et al., 2010). As a branch of ground source heat pumps, it is known as a 21st-century technology characterized by energy saving and environmental protection, and it plays an indispensable role in achieving China's "double carbon" target, reducing energy consumption, and protecting the ecological environment.



As early as the 1940s, the application of the groundwater source heat pump system in public buildings in the United States, whereas the development in China occurred somewhat later. The associated technologies of groundwater source heat pumps were not developed and deployed in China until the 1950s, and in the 1980s, groundwater source heat pump technology research progressed gradually (Peng, 2013). Up till now, the ground source heat pump technology has been quite developed, with a great number of engineering projects domestically and internationally, the technology has been widely adopted and promoted (Sanner et al., 2003; Liu et al., 2020b; Li et al., 2021a; Biglia et al., 2021; Gao et al., 2021; Sang et al., 2022). The impacts of various parameters on the performance of the groundwater source heat pump system were investigated in Kim and Nam, (2016). The results show that the groundwater level and temperature have the greatest impact on the performance of the groundwater source heat pump system, followed by submersible pumps and heat exchangers (Kim and Nam, 2016). Moreover, factors such as water flow rate (Zhou et al., 2022a), performance parameters (Sang et al., 2022), porous medium (Na and Xia, 2021), layout of pumping and recharge wells (Wen et al., 2022; Yan et al., 2023) and pipe corrosion (Luo et al., 2022) play significant role. Obviously, a great number of researchers also offer optimization strategies for groundwater source heat pump systems (Nam and Ooka, 2010; Lu et al., 2015; Zhu et al., 2015; Zhen et al., 2017; Liu et al., 2019; Li et al., 2021b; Zhang et al., 2022). Park et al. (2020) developed an optimization model of groundwater source heat pump, which can calculate the optimal pumping and irrigation speed of groundwater source heat pump system, maximize system efficiency, and have excellent economic and environmental benefits. Zhou et al. (2022b) proposed recycling groundwater, and the results shown that the performance of groundwater source heat pump systems could be greatly enhanced and water wasted minimized. Park et al. (2021) proposed a simulation optimization approach, a model that can determine the optimal well location and pump/injection rate to find the best installation and operation strategy for the system. Halilovic et al. (2022) proposed a strategy for optimizing the hair of the well layout of groundwater source heat pump systems to maximize the utilization of thermal potential of groundwater. Zhou et al. (2022a) investigated the economics of ground source heat pump systems with various flow control methods and highlighted the significance of variable flow regulation methods for enhancing thermal and economic performance. Luo and Ma, (2022) proposed an integrated management strategy for system operation that significantly improved thermal efficiency and coefficient of performance in comparison to the conventional model. Granryd, (2010) derived a relational equation for the optimal flow rate, on the basis of which the evaporator and condenser flow rates were optimized to maximize the COP of the system. Zhao et al. (2003) established an optimization mathematical model with economic cost as the objective function, according to which the optimal matching is obtained between each component of the system, resulting in a significant improvement in heat

pump performance. Kang et al. (2017) investigated a new groundwater source heat pump system optimization method to make the system more energy efficient and demonstrated that the compressor power was reduced, the system's energy efficiency was enhanced, and the total annual cost was reduced compared to the conventional groundwater source heat pump system. Wang et al. (2019) suggested a new groundwater source heat pump with pre-conditioner, and the study proved that the new groundwater source heat pump has excellent energy saving performance. Ma and Xia, (2017) proposed an optimization technique in which the optimization variable is the heat exchanger discharge temperature and the overall goal of the optimization is to minimize the system power consumption while meeting the required heating and cooling demands of the building. The results demonstrate that the optimization strategy is effective in reducing energy consumption.

These articles combine theory with practice, analyze the performance of the GWHP system, expound the influencing factors of system performance, and put forward the optimization model. However, there is a lack of research on the benefits of the corresponding groundwater source heat pump system. In this paper, the operation of the groundwater source heat pump system in four residential community was monitored over a 3-day period during the cooling season and the data tested to show that these systems met the design requirements. The data is also analyzed to calculate the performance coefficients of the heat pump system, to classify it according to national codes, and to provide a brief analysis of the reasons for the decline in system and unit performance. The energy-saving, environmental and economic benefits of these systems are also analyzed based on the data, revealing the energy-saving and environmental friendliness of the groundwater source heat and heat pump system. It provides a reference for improving energy efficiency and optimizing the operation of the groundwater source heat pump system. It is of great significance to the application of groundwater source heat pump systems in complex geological environment areas.

## 2 Project overview and testing scheme

### 2.1 Project overview

In this study, the GWHP system is located in the karst area of south China. According to the literature content (Wang et al., 2011), in the project area, the aquifer permeability coefficient is 10.42–18.17 m/d, the unit water inflow of a single well is 5.59–10.20 L/sm, the maximum recharge volume of a single well is 70 m<sup>3</sup>/h, and the groundwater recharge volume is 12,539,500 m<sup>3</sup>/a. The underground water is buried 60–115 m deep, and the temperature of the underground water is maintained at about 18°C and is not affected by the outside air temperature. The heat pump systems in the four residential communities were put into use in 2012 with an air conditioning area of approximately 116,500 m<sup>2</sup>, 135,600 m<sup>2</sup>, 187,500 m<sup>2</sup>, and 111,300 m<sup>2</sup> respectively. The building floors in the community are five floors, with a height of 3 m and a utility room on the top

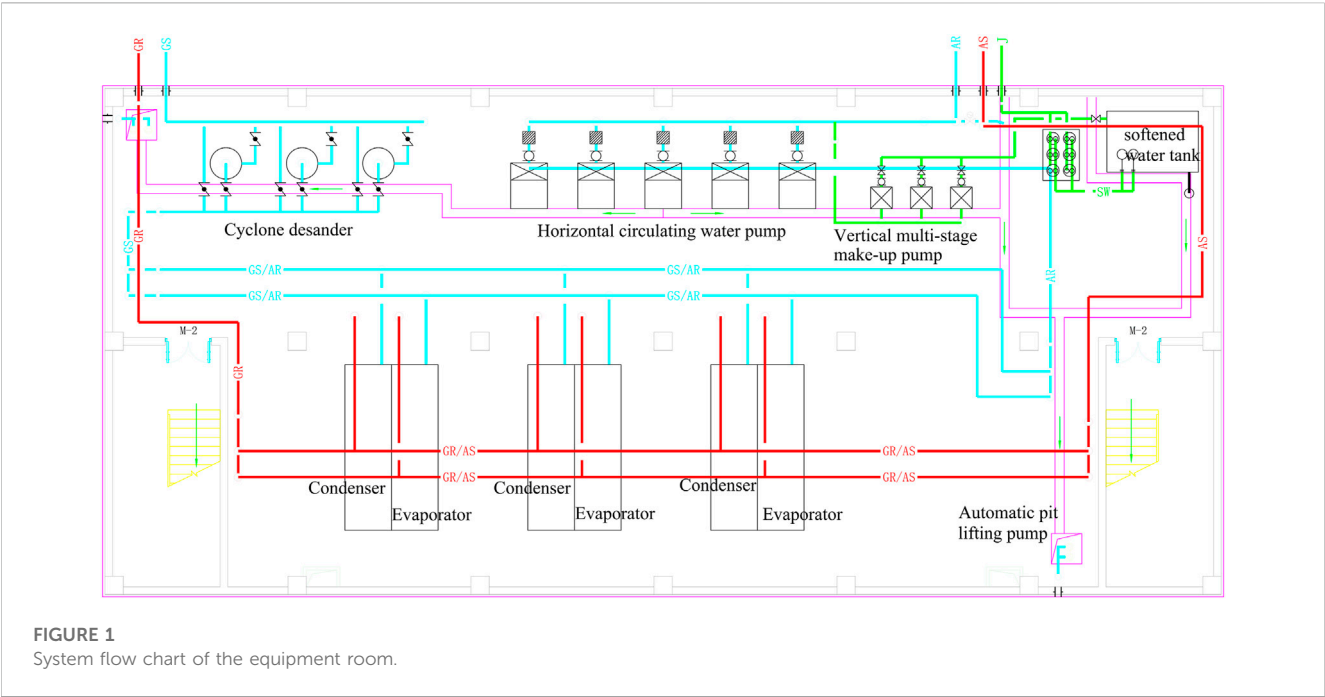


FIGURE 1  
System flow chart of the equipment room.

TABLE 1 Main equipment parameters of GWHP system.

Community	Device name	Model/Specification	Performance parameters	Number
A	Ground source heat pump unit	CVHG780	Rated cooling capacity:2981kW; input power:483 kW	3
	Air conditioning circulating pump	DEW/250–400A/4	V=500 m <sup>3</sup> /h; H=44m; N=90 kW	3
		DEW/250–315A/4	V=550 m <sup>3</sup> /h; H=28m; N=55 kW	2
B	Ground source heat pump unit	CVHG780	Rated cooling capacity:2981kW; input power:483 kW	3
	Air conditioning circulating pump	DEW/250–400A/4	V=500 m <sup>3</sup> /h; H=44m; N=90 kW	3
		DEW/250–315A/4	V=550 m <sup>3</sup> /h; H=32m; N=75 kW	2
C	Ground source heat pump unit	CVHG780	Rated cooling capacity:2532kW; input power:396 kW	3
	Air conditioning circulating pump	DEW/250–400A/4	V=500 m <sup>3</sup> /h; H=44m; N=90 kW	3
		DEW/250–315A/4	V=500 m <sup>3</sup> /h; H=32m; N=75 kW	2
D	Ground source heat pump unit	CVHG1100	Rated cooling capacity:3436kW; input power:549 kW	3
	Air conditioning circulating pump	DEW/300–400A/4	V=500 m <sup>3</sup> /h; H=38m; N=90 kW	3
		DEW/300–315A/4	V=637 m <sup>3</sup> /h; H=28m; N=75 kW	2

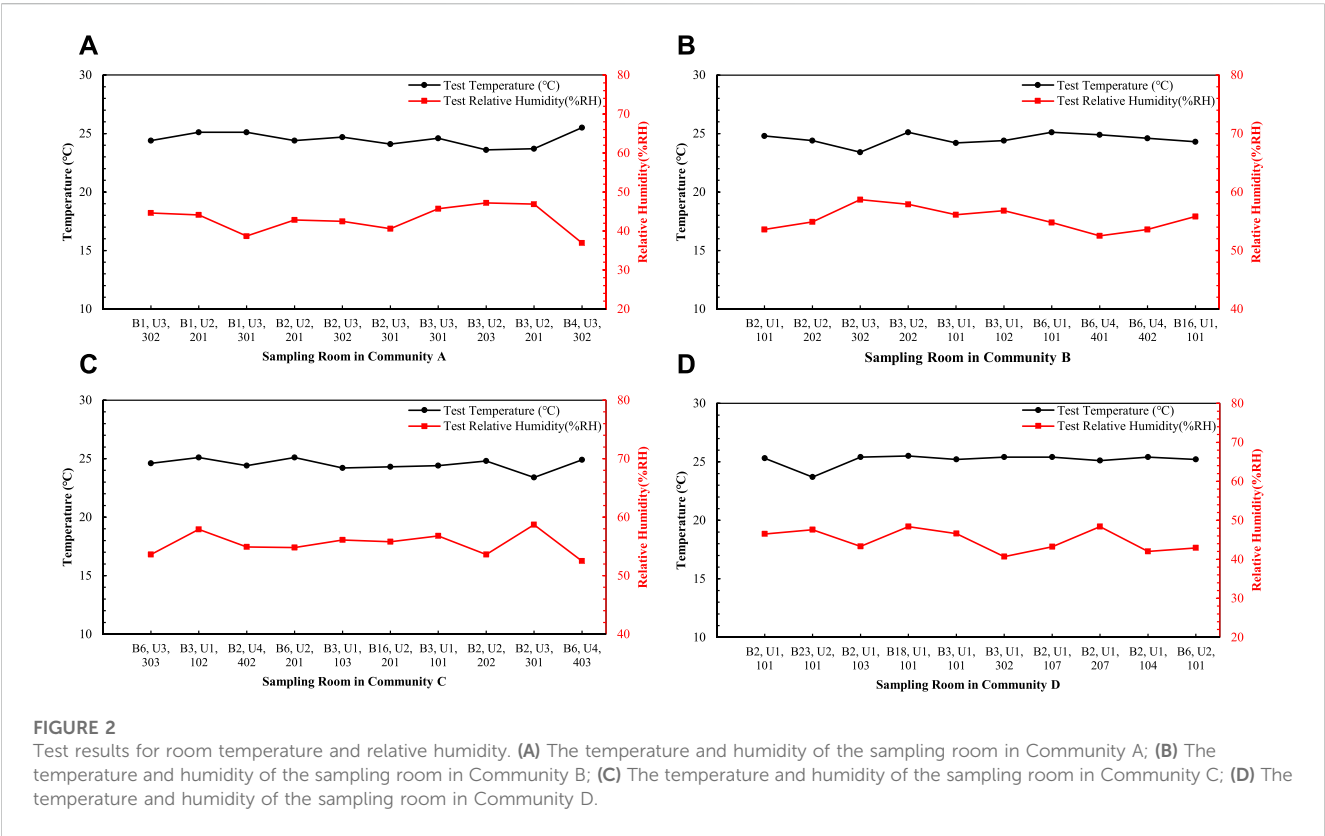
floor. The owner determines the form of the building’s final heating, which is typically fan coils or radiant floor systems. The groundwater level is around –100m, and the groundwater is extracted from the ground by pumping wells, passing through a cyclone desander for preliminary water treatment, and then entering the heat pump unit for heat exchange before being returned to the ground via a recharge well (Wang et al., 2011; Hou et al., 2017; Liu et al., 2022). Figure 1 depicts the equipment room’s system flow diagram. Table 1 displays the equipment configuration and main equipment parameters.

## 2.2 Testing scheme

According to the requirements of the GB/T 50,801-2013 *Evaluation Standards for Renewable Energy Building Application Projects* (Ministry of Housing and Urban-Rural Development of the People’s Republic of China, 2013) and the *Guidelines for the Measurement and Evaluation of Renewable Energy Building Application Demonstration Projects* (Ministry of Housing and Urban-Rural Development of the People’s Republic of China, 2008) (hereinafter referred to as the Evaluation Standards and

TABLE 2 Test meter.

Serial number	Name and model	Range	Accuracy
1	Ultrasonic flowmeter (FLCS1012)	Φ50~Φ400	0.02 m/s,±1.0%
2	Temperature and humidity recorder (RHLOG-T-H)	-25~+55°C,0-100%RH	±0.3°C,±5%RH
3	Thermometer (HM34)	-20~+60°C,0-90%RH	±0.3°C,±2%RH
4	Temperature measurement system (34970A)	0-100°C	±0.2°C
5	Clamp electrometer (PROVA6600)	0-2000A,0-600V	±2.0%
6	Three-phase power analyzer (HIOKI3469-20)	0-5000A,150-600V	±0.1%,±0.2%



Guidelines) regarding the test contents of the heat pump system, the operation of the groundwater source heat pump system in these residential area was evaluated during the cooling season. The test contents mainly include inlet and outlet water temperature and water flow on the ground-source-side and the user-side, the input power of the system and water pumps, and the air temperature inside and outside of the test room. The main test instruments are shown in Table 2.

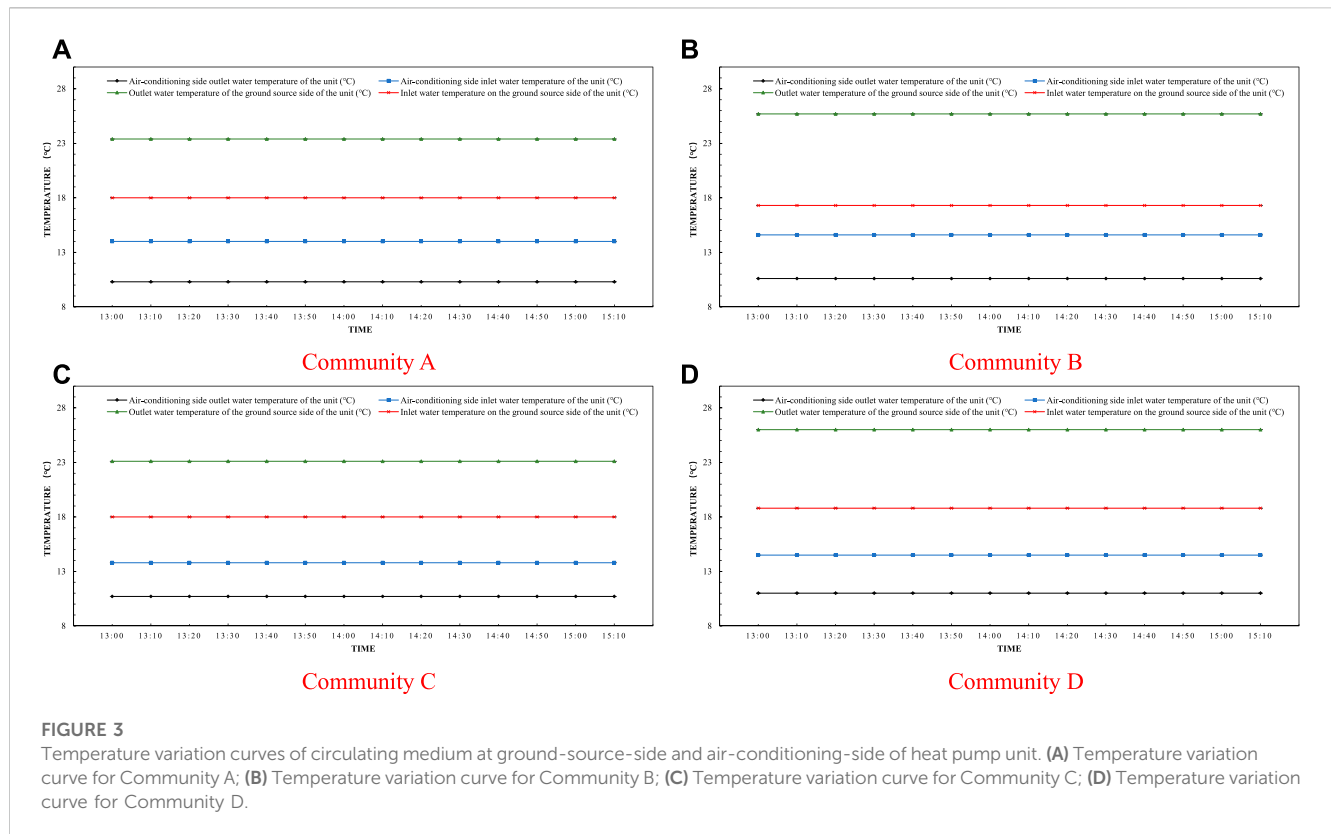
The test methods are mainly for the instrument to automatically record data and manually read real-time operational parameters at regular intervals. Use the ultrasonic flowmeter to measure the inlet and outlet flow of the ground source side and the inlet and outlet flow of the user side, and the temperature measurement system to measure the inlet and outlet water temperature of the ground source side and the inlet and outlet water temperature of the user side. The analyzer measures the power consumption of the heat pump unit and the water pump. The

indoor and outdoor air temperatures were measured by a thermometer. When measuring the outdoor temperature, hang the autograph away from the building to avoid the influence of heat dissipation of the building, and avoid direct solar radiation, which will affect the accuracy of the measurement. The indoor temperature test is carried out after the heat pump system continues to operate normally, and the temperature test points are positioned 1.5 m above the ground and far away from the influence of the indoor heat source.

### 3 Analysis of test results

#### 3.1 Temperature

The heat pump system provides cooling to four communities, and 10 rooms in each community were sampled for temperature and



humidity testing. The sampling results show that the indoor temperature and humidity test values in each room meet the design requirements, and the cooling guarantee rate is 100%. The specific test results are shown in Figure 2.

The temperature outside of the test rooms can reach a maximum of 34.5°C, and the average temperature was 25.4°C during testing. From Figure 2 it can be concluded that the average maximum indoor temperature of the test rooms is 25.5°C, which is below the design cooling requirement limit. Meanwhile, the average temperature inside of the test rooms is 24.5°C, which has a good cooling effect.

## 3.2 Cooling capacity and coefficient of performance

### 3.2.1 Heat pump unit performance test results

Test the water temperature and water flow of the supply and return on the ground-source-side and air-conditioning-side of the heat pump, as well as the electricity consumed by the heat pump unit during testing. And then, the average cooling capacity of the heat pump unit and the cooling performance coefficient of the heat pump unit can be calculated according to the following formula.

The average cooling capacity of the groundwater source heat pump unit during the test period is calculated as follows:

$$Q = V\rho c\Delta t_w / 3600 \quad (1)$$

where  $Q$  is average heating (cooling) capacity of the unit during the test,  $V$  is the average flow rate of air conditioning side of heat pump unit,  $\rho$  is the average density of water,  $c$  is the average constant

pressure specific heat of water,  $\Delta t_w$  is the temperature difference between the inlet and outlet water on the air-conditioning-side.

During the test period, the heating/cooling performance coefficient of the heat pump unit can be calculated according to the test results as follows:

$$COP = \frac{Q}{N_i} \quad (2)$$

where  $COP$  is the heating (cooling) performance coefficient of the heat pump unit,  $Q$  is average heating (cooling) capacity of the unit during the test,  $N_i$  is average input power of the unit during the test.

After measurement, the temperature changes of supply and return water on the ground-source-side and the user-side of the heat pump unit with time are derived. The specific results are shown in Figure 3. As can be seen in Figure 3, the water supply and return temperatures on the ground source and user sides of the four communities remained constant during the test. The supply and return water temperatures on the ground source side of the four communities were stable and unchanged, thus the ground source heat exchange effect was stable. The system uses a constant frequency circulation pump and the water flow rate on the user side is constant. While the temperature difference between the supply and return water on the user side of the system is constant, according to eq. 1, the cooling capacity of the unit under test is constant during the test period and the unit operates stably. In addition, the maximum temperature difference between the supply and return water on the customer side of the four systems is only 4°C, and the average temperature difference between the supply and return water is 3.7°C. It can be seen that the system

**TABLE 3 Refrigeration performance test results under actual operating conditions.**

Test items	Community A	Community B	Community C	Community D
Air-conditioning side outlet water temperature of the unit (°C)	10.3	10.6	10.7	11.0
Air-conditioning side inlet water temperature of the unit (°C)	14.0	14.6	13.8	14.5
The outlet water temperature of the ground source side of the unit (°C)	23.4	25.7	23.1	26.0
Inlet water temperature on the ground source side of the unit (°C)	18.0	17.3	18	18.8
Air conditioner side flow of unit (m³/h)	410.0	430.0	560.1	510.0
Ground source side flow of the unit (m³/h)	350.1	245.5	394.1	298.0
Unit cooling capacity (kW)	1768.0	2013.2	2004.6	2,113.3
Unit average input power (kW)	358.3	425.1	415.5	458.1
Unit average performance coefficient (kW/kW)	4.93	4.74	4.82	4.61

Notes: The average performance coefficient of unit cooling = unit cooling capacity/unit input power.

**TABLE 4 Performance test results of heat pump system under actual operating conditions.**

Test items	Community A	Community B	Community C	Community D
Total cooling capacity of the system (kWh)	39,333.7	31,759.2	46,488.4	50,541.7
Total system power consumption (kWh)	12,789.8	9,936.0	14,215.3	16,425.1
Heat pump unit power consumption (kWh)	8,337.8	6,956.8	9,883.3	12,069.1
Circulating water pump power consumption (kWh)	4,452	2,979.2	4,332	4,356
System Cooling Average Coefficient of Performance (kWh/kWh)	3.08	3.20	3.27	3.08

Notes: 1) The total power consumption of the system = the power consumption of the heat pump unit + the power consumption of the circulating water pump.

2) System cooling average performance coefficient = total system cooling capacity/system total power consumption.

adopts the “large flow rate and small temperature difference” operation mode. The corresponding “large temperature difference and small flow rate” operation mode is more conducive to reducing the system transmission and distribution energy consumption as well as improving the system energy efficiency ratio.

According to the measured data combined with the calculation formula, the average cooling performance coefficients of the four units during the test period were 4.93, 4.74, 4.82, and 4.61 respectively, and the specific test results are shown in Table 3. Based on the information of the equipment parameters of the heat pump units in Table 1, it can be calculated that the rated cooling performance coefficient of the heat pump units can reach more than 6, while the actual operating effect is only 70%–80% of the design working condition. This may be due to the long-term operation of the equipment, the heat exchange equipment and pipes of the heat pump unit have problems such as corrosion, oxidation and scaling, resulting in the heat exchange efficiency of the heat pump unit being reduced, thus making the cooling performance coefficient of the unit not high.

### 3.2.2 Heat pump system performance test results

On the basis of the test results, the typical seasonal system performance coefficient of the system is calculated by the following formula:

$$COP_s = \frac{Q_s}{\sum N_i + \sum N_j} \quad (3)$$

where  $Q_s$  is the total heating (cooling) capacity of the system during the test,  $\sum N_i$  is the total electricity consumed by the heat pump unit during the system test,  $\sum N_j$  is the total power consumed by the pump during system test.

The total heating (cooling) capacity of the system during the test is calculated according to the following formula:

$$Q_s = \sum_{i=1}^n q_i \Delta T_i \quad \text{and} \quad q_i = V_i \rho c \Delta T_i / 3600 \quad (4)$$

where  $q_i$  is the cooling capacity of the heat pump system in a certain period of time,  $\Delta T_i$  is the duration of a period of time,  $V_i$  is the average water flow on the air-conditioning-side of the system in a certain period of time,  $\Delta T_i$  is the temperature difference between the inlet and outlet water on the air-conditioning-side in a certain period of time.

Test the water temperature, flow rate, and power consumption of the system on the air-conditioning-side of the system. From the test data, the performance coefficient of the groundwater source heat pump system is calculated. The average coefficient of performance for each system during testing was 3.08, 3.20, 3.27, and 3.08. The specific test results are presented in Table 4, and the proportion of power consumption of the system is depicted in Figure 4.

The calculation concludes that the average coefficient of performance of the GWHP system was 3.08, 3.20, 3.27 and 3.08 respectively, which meets the requirements of the limit value in the “Evaluation Standard” (Table 5). Furthermore, given that the



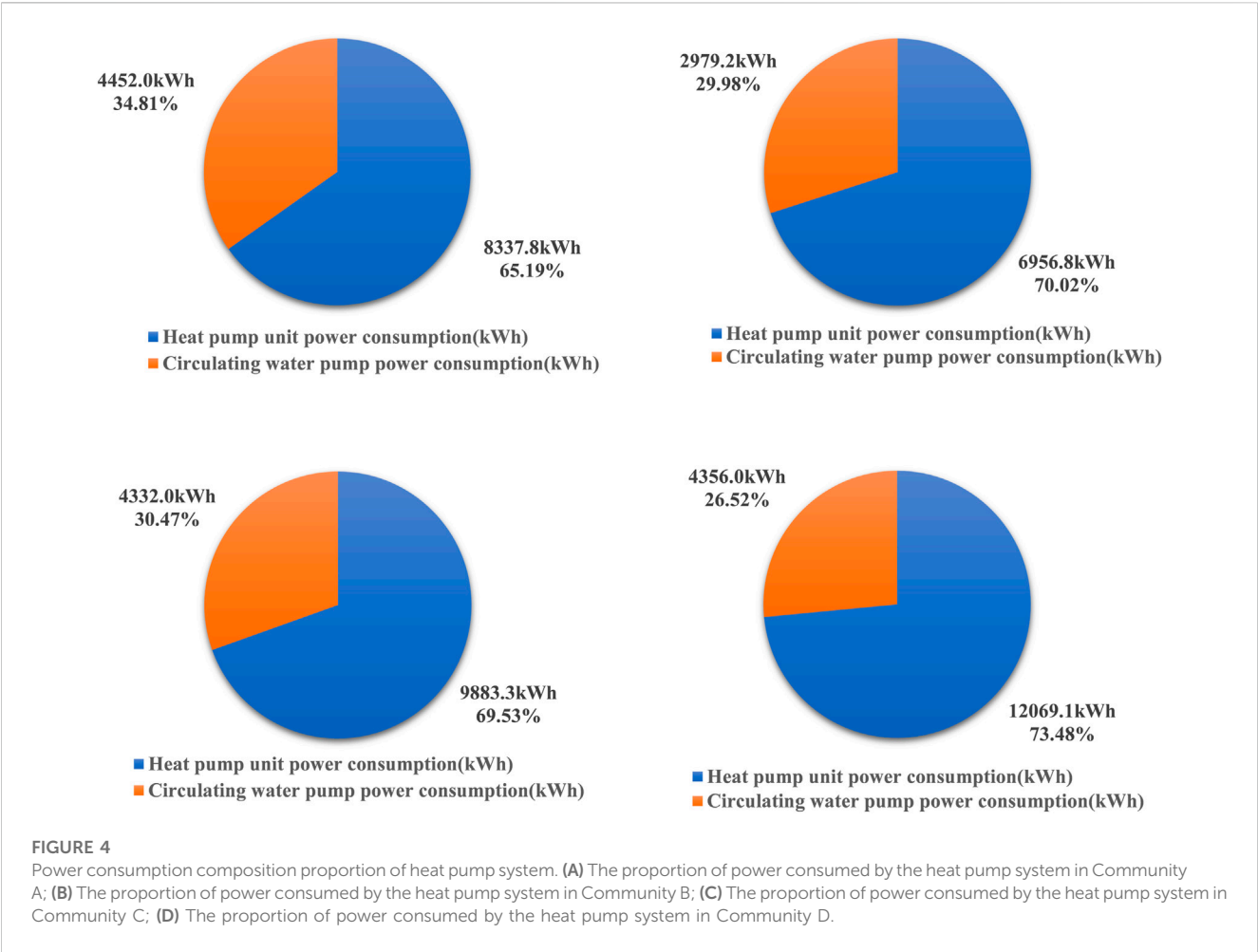


TABLE 5 Limits of performance coefficient of GWHP.

	System cooling energy efficiency ratio EER <sub>sys</sub>	System heating performance coefficient COP <sub>sys</sub>
Limit values	≥3.0	≥2.6

TABLE 6 Performance level division of GWHP system.

Working condition	Level 1	Level 2	Level 3
Cooling Energy Efficiency Ratio	EER <sub>sys</sub> ≥3.9	3.9>EER <sub>sys</sub> ≥3.4	3.4>EER <sub>sys</sub> ≥3.0

“Evaluation Standard” divides the performance of the GWHP system into 3 grades (Table 6), with level 1 being the highest, the performance coefficients of the GWHP systems in the test communities all belong to Level 3. However, comparing Tables 5, 6, the performance of this groundwater source heat pump system just meets the limit value requirements and is among the lowest levels in the classification of the code. Analysis of the reasons, the system after a long time of operation, heat exchanger performance decline, compressor performance deterioration, pipeline scaling or corrosion, and other reasons, leading to the energy efficiency of the system isn’t very ideal.

Nevertheless, the specific reasons for the degradation of system performance still need to be corroborated by subsequent studies.

Tested and calculated, the test of the underground water source heat pump units revealed an average performance coefficient of 4.61–4.93, the performance coefficient of 3.08–3.27 for the heat pump systems, and a system average that is 32%–38% lower than the average crew. What effect is formed by Figure 4 heat pump power consumption ratio is: the power consumption of the water pump is relatively large, accounting for about 27%–35% of the total power consumption, which leads to the reduction of the system performance coefficient.

### 4 Benefit analysis

#### 4.1 Energy saving benefit analysis

Calculate the coal saving of the GWHP system in comparison to the conventional water-cooled chiller, and analyze the energy saving

**TABLE 7 Cumulative cooling load calculation table of air conditioning in summer.**

Temperature band (°C)	Hours (h)	Outdoor temperature (°C)	Cooling load (kW)	Cumulative cooling load (kWh)
26–28	361	27	529.55	191,165.9
28–30	344	29	1,588.64	546,490.9
30–32	337	31	2,647.73	892,284.1
32–34	305	33	3,706.82	1,130,579.5
34–36	282	35	4,765.91	1,343,986.4
36–38	235	37	5,825.00	1,368,875.0
38–40	152	39	6,884.09	1,046,381.8
40–42	95	41	7,943.18	754,602.3
42–44	38	43	9,002.27	342,086.4
44–46	1	45	10,061.36	10,061.4
Total				7,626,513.6

**TABLE 8 Cumulative cooling load statistics table.**

	Community A	Community B	Community C	Community D
Cumulative cooling load (kWh)	7,626,513.6	8,876,869.1	12,274,431.8	7,286,102.7

**TABLE 9 Conventional energy substitution calculation table.**

Community	Cooling method	Cooling load (kWh)	Annual power consumption (kWh)	Converted total coal consumption (tce)	Coal saving (tce)
A	Groundwater Source Heat Pump	7,626,513.6	2,479,843.5	1,001.6	98.5
	Conventional water-cooled chillers	7,626,513.6	2,723,754.9	1,100.4	
B	Groundwater Source Heat Pump	8,876,869.1	2,886,410.1	1,166.1	114.7
	Conventional water-cooled chillers	8,876,869.1	3,170,310.4	1,280.8	
C	Groundwater Source Heat Pump	12,274,431.8	3,991,164.5	1,612.4	158.6
	Conventional water-cooled chillers	12,274,431.8	4,383,725.7	1771.0	
D	Groundwater Source Heat Pump	7,286,102.7	2,369,155.2	957.1	94.1
	Conventional water-cooled chillers	7,286,102.7	2,602,179.5	1,051.3	

benefit of the GWHP system. The energy consumption of the system only includes the power consumption. The actual power consumption can be measured by a clamp-type electric power meter and a three-phase power analyzer. The conversion rate of electric energy and primary energy is taken as 0.404 (Li et al., 2023).

According to the Guidelines, the temperature-frequency method is used to calculate the cumulative annual loads of a building, based on the measured cooling loads of the system and actual meteorological parameters during testing. The so-called temperature-frequency method assumes a linear relationship

TABLE 10 Calculation table of CO<sub>2</sub>, SO<sub>2</sub>, and dust emission reduction.

Community	Standard coal saving (ton/year)	CO <sub>2</sub> emission reduction (ton/year)	SO <sub>2</sub> emission reduction (ton/year)	Dust emission reduction (ton/year)
A	98.5	243.3	1.97	0.99
B	114.7	283.3	2.29	1.15
C	158.6	391.7	3.17	1.59
D	94.1	232.4	1.88	0.94

between the envelope load (including solar and differential temperature loads) and the outdoor temperature, calculates the load at various temperatures based on this linear relationship, and multiplies it by the number of hours at that temperature to determine the cooling and heating loads at that temperature (Long, 1992).

The BIN weather parameter is utilized for load calculation by temperature and frequency method. The meteorological parameters are sorted out according to hourly values given by the annual outdoor dry bulb temperature or random weather model of a certain place. Taking 2°C as a temperature interval, the number of hours occurring in each temperature interval is calculated, namely, the time and frequency table of temperature (Song and Wang, 2015).

The summer building cooling load is calculated as follows:

$$Q_{OUT} = \frac{t_N - t_{OUT}}{t_N - t_{EJ}} \times Q_{EJ} \quad (5)$$

where  $Q_{OUT}$  is building cooling load at outdoor temperature  $t_{OUT}$ ,  $Q_{EJ}$  is building cooling load at outdoor temperature  $t_{EJ}$ ,  $t_N$  is building summer interior design temperature,  $t_{EJ}$  is building summer design outdoor temperature.

The procedure for calculating the cooling load of the research area is outlined below. The detailed calculation process is described using Community A as an example. The meteorological parameters of the typical meteorological year in the test area are selected as the BIN meteorological parameters. The outdoor design temperature is 40.3°C, the design cooling load is 7,572.5 kW, the outdoor temperature is selected according to the typical annual data, and the design temperature inside of the buildings is 26°C. Calculated according to the above formula, the cumulative cooling load of the building in the cooling season is 7,626,513.6 kWh. The specific summer cumulative air-conditioning cooling load calculation table is shown in Table 7 and the cumulative summer air conditioning cooling loads for each community are shown in Table 8. The formula for calculating the electricity consumption of the GWHP, system in the whole cooling season is as follows:

$$E_H = \frac{\sum Q_H}{COP_{SH}} \quad (6)$$

where  $E_H$  is electricity consumption of heat pump system in cooling season,  $\sum Q_H$  is the cumulative cooling load of the building throughout the year.

Comparing the GWHP system with a conventional water-cooled chiller. The performance coefficient of the conventional chilled water-cooled unit is 2.8. The comparison outcomes are presented in Table 9.

From this calculation, it is concluded that the groundwater source heat pump system saves 0.85 kgce/m<sup>2</sup> in summer compared with the conventional water-cooled chiller system, and the energy saving effect is remarkable.

## 4.2 Environmental benefit analysis

Based on the results of the annual conventional energy substitution amount for the project, the annual conventional energy substitution amount for each system is 98.5 tons, 114.7 tons, 158.6 tons and 94.1 tons. According to the “Guidelines” and “Evaluation Standards” on environmental benefits, the emission reductions of carbon dioxide, sulfur dioxide, and dust are calculated respectively. The calculation methods are as follows:

Carbon dioxide emission reduction is calculated according to the following formula:

$$Q_{CO2} = 2.47Q_{bm} \quad (7)$$

where  $Q_{CO2}$  is Carbon dioxide emission reduction,  $Q_{bm}$  is standard coal saving, 2.47 is Carbon dioxide emission factor.

Sulfur dioxide emissions are calculated according to the following formula:

$$Q_{SO2} = 0.02Q_{bm} \quad (8)$$

where  $Q_{SO2}$  is Sulfur dioxide emission reduction,  $Q_{bm}$  is standard coal saving, 0.02 is SO<sub>2</sub> emission factor for standard coal.

Dust emission reduction is calculated according to the following formula:

$$Q_{FC} = 0.01Q_{bm} \quad (9)$$

where  $Q_{FC}$  is dust emission reduction,  $Q_{bm}$  is standard coal saving, 0.01 is dust emission factor.

From the calculations in Table 10, it can be concluded that the CO<sub>2</sub> reduction, SO<sub>2</sub> reduction, and dust reduction in a cooling season in this test area are 2.09 kg/m<sup>2</sup>, 0.02 kg/m<sup>2</sup> and 0.01 kg/m<sup>2</sup> respectively. The implementation of the GWHP system has clear implications for air pollution control and environmental conservation.

### 4.3 Economic benefit analysis

In light of the energy consumption analysis results, the power consumption of the heat pump system in the cooling season is 21.29 kWh/m<sup>2</sup>, and the power consumption of the traditional chilled water system is 23.38 kWh/m<sup>2</sup>, representing a savings of 2.1 kWh/m<sup>2</sup>. Combined with the paid electricity price standard of the project (0.567 yuan/kWh for this project), the cost of utilizing the GWHP system for cooling in the summer of the four communities is at least 793,000 yuan cheaper than that of using the traditional cold-water system.

## 5 Conclusion

This paper tests the GWHP system in residential quarters and analyzes the performance, energy saving, environmental protection and economic benefits of the system. The result of the study are as follows.

- (1) On the basis of the test and evaluation of the groundwater source heat pump heating and cooling project in the residential communities, the groundwater source heat pump technology is effectively applied, and the indoor effect of cooling meets the design and specification requirements, and the heat pump unit and system operate stably.
- (2) The average cooling performance factor of the four heat pump units is 4.61–4.93, while the average cooling performance factor of the heat pump systems is 3.08–3.27. The average energy efficiency ratio of the heat pump systems is 32%–38% lower than that of the units. The main reason is that the electricity consumption of the water pump accounts for a large proportion, which leads to the reduction of the performance coefficient of the system. Frequency conversion measures should be taken for the circulating water pump to reduce the power consumption of the water pump and improve the coefficient of performance of the system.
- (3) Compared with traditional water-cooled chillers, the four GWHP systems tested can save a total of 466 tons of standard coal, reduce 1,150.8 tons of carbon dioxide emissions, 9.3 tons of sulfur dioxide emissions and 4.7 tons of dust emissions in one cooling season, showing obvious energy and environmental benefits, while reducing operating costs by RMB 793,000, which has certain economic benefits.

Through the analysis, it can be seen that the groundwater source heat pump system offers significant energy-saving benefits, environmental benefits, and economic benefits. Within the

current worldwide situation, the promotion of this technology is of crucial practical importance. Moreover, without improving its control strategy, this work conducts simply a performance test and benefit analysis of a GWHP system in a residential area, this part of the content needs to be expanded and enhanced.

## Data availability statement

The original contributions presented in the study are included in the article/supplementary material, further inquiries can be directed to the corresponding author.

## Author contributions

Conceptualization, KW and WW; data curation, KW; formal analysis, KW and WW; funding acquisition, WW; investigation, KW; methodology, KW, WW, and LH; project administration, LH; resources, KW, WW, and LH; software, KW; supervision, WW; validation, KW, WW, and LH; visualization, KW; writing—original draft, KW and WW; writing—review and editing, KW and WW.

## Acknowledgments

The author would like to thank Turpan Nenghui New Energy Co., Ltd. for providing relevant data on the groundwater source heat pump system.

## Conflict of interest

LH was employed by Turpan Nenghui New Energy Company. The remaining authors declare that the research was conducted in the absence of any commercial or financial relationships that could be construed as a potential conflict of interest.

## Publisher's note

All claims expressed in this article are solely those of the authors and do not necessarily represent those of their affiliated organizations, or those of the publisher, the editors and the reviewers. Any product that may be evaluated in this article, or claim that may be made by its manufacturer, is not guaranteed or endorsed by the publisher.

## References

- Biglia, A., Ferrara, M., and Fabrizio, E. (2021). On the real performance of groundwater heat pumps: Experimental evidence from a residential district. *Appl. Therm. Eng.* 192, 116887. doi:10.1016/j.applthermaleng.2021.116887
- Gao, B., Zhu, X. Y., Yang, X. J., Yuan, Y. P., Yu, N. Y., and Ni, J. (2021). Operation performance test and energy efficiency analysis of ground-source heat pump systems. *J. Build. Eng.* 41, 102446. doi:10.1016/j.jobbe.2021.102446
- Granryd, E. (2010). Analytical expressions for optimum flow rates in evaporators and condensers of heat pumping systems. *Int. J. Refrigeration-Revue Int. Du Froid* 33 (7), 1211–1220. doi:10.1016/j.ijrefrig.2010.05.009
- Halilovic, S., Bottcher, F., Kramer, S. C., Piggott, M. D., Zosseder, K., and Hamacher, T. (2022). Well layout optimization for groundwater heat pump systems using the adjoint approach. *Energy Convers. Manag.* 268, 116033. doi:10.1016/j.enconman.2022.116033

- Hou, X. Y., Chen, S. J., and Tang, W. I. (2017). "Research on green building eco-city in turpan new energy demonstration zone," in *Construction science and technology*, 42–44. doi:10.16116/j.cnki.jskj.2017.17.008
- Kang, Z., Zhou, X., Zhao, Y., Wang, R., and Wang, X. (2017). Study on optimization of underground water source heat pump. *Procedia Eng.* 205, 1691–1697. doi:10.1016/j.proeng.2017.10.353
- Kim, J., and Nam, Y. (2016). A numerical study on system performance of groundwater heat pumps. *Energies* 9 (1), 4. doi:10.3390/en9010004
- Li, X. L., Chen, S. J., Liu, S. M., and Li, Z. H. (2021a). AE waveform characteristics of rock mass under uniaxial loading based on Hilbert-Huang transform. *J. Central South Univ.* 28 (6), 1843–1856. doi:10.1007/s11771-021-4734-6
- Li, X. L., Chen, S. J., Wang, S., Zhao, M., and Liu, H. (2021b). Study on *in situ* stress distribution law of the deep mine: Taking linyi mining area as an example. *Adv. Mater. Sci. Eng.* 2021, 5594181–5594211. doi:10.1155/2021/5594181
- Li, X. L., Zhang, X. Y., Shen, W. L., Zeng, Q. D., Chen, P., Qin, Q. Z., et al. (2023). Research on the mechanism and control technology of coal wall sloughing in the ultra-large mining height working face. *Int. J. Environ. Res. Public Health* 20 (1), 868. doi:10.3390/ijerph20010868
- Liu, H. Y., Zhang, B. Y., Li, X. L., Liu, C. W., Wang, C., Wang, F., et al. (2022). Research on roof damage mechanism and control technology of gob-side entry retaining under close distance gob. *Eng. Fail. Anal.* 138, 106331. doi:10.1016/j.engfailanal.2022.106331
- Liu, S. M., Li, X. L., Wang, D. K., and Zhang, D. M. (2020a). "Investigations on the mechanism of the microstructural evolution of different coal ranks under liquid nitrogen cold soaking," in *Energy sources part a-recovery utilization and environmental effects*, 1–17. doi:10.1080/15567036.2020.1841856
- Liu, S. M., Li, Y. W., Xu, W., Yin, H., Gao, J., Jin, G. Y., et al. (2019). Performance and feasibility study of hybrid ground source heat pump system assisted with cooling tower for one office building based on one Shanghai case. *Energy* 173, 28–37. doi:10.1016/j.energy.2019.02.061
- Liu, Z. J., Zhang, Y. L., Xu, W., Yang, X. Y., Liu, Y. W., and Jin, G. Y. (2020b). Suitability and feasibility study on the application of groundwater source heat pump (GWSHP) system in residential buildings for different climate zones in China. *Energy Rep.* 6, 2587–2603. doi:10.1016/j.egy.2020.09.015
- Liong, W. D. (1992). "Using BIN parameters for building energy consumption analysis," in *Heating ventilating and air conditioning*, 6–11.02
- Lu, S. L., Qi, Y. F., Cai, Z., and Li, Y. R. (2015). Optimization model analysis of centralized groundwater source heat pump system in heating season. *Front. Energy* 9 (3), 343–361. doi:10.1007/s11708-015-0372-8
- Luo, J., and Ma, X. N. (2022). An integrated strategy for the improvement of thermoeconomic performance of a GWHP system. *Appl. Therm. Eng.* 213, 118777. doi:10.1016/j.applthermaleng.2022.118777
- Luo, J., Pei, K. H., and Li, P. J. (2022). Analysis of the thermal performance reduction of a groundwater source heat pump (GWHP) system. *Eng. Fail. Anal.* 132, 105922. doi:10.1016/j.engfailanal.2021.105922
- Ma, Z. L., Yao, Y., Jiang, Y. Q., and Ni, L. (2010). *Theoretical basis and practice of heat pump technology application*. Beijing: China Construction Industry Press.
- Ma, Z., and Xia, L. (2017). Model-based optimization of ground source heat pump systems. *Energy Procedia* 111, 12–20. doi:10.1016/j.egypro.2017.03.003
- Ministry of Housing and Urban-Rural Development of the People's Republic of China (2013). *Evaluation standard for application of renewable energy in building: GB/T 50801-2013*. Beijing: China Architecture and Building Press.
- Ministry of Housing and Urban-Rural Development of the People's Republic of China (2008). *Guidelines for evaluation of renewable energy building Application Demonstration projects*. Beijing: China Architecture and Building Press.
- Na, W., and Xia, Q. Y. (2021). Influence of different porous media and groundwater-source heat pump operation modes on thermal breakthrough in energy extraction area. *Heat. Vent. Air Cond.* 51 (07), 104–110.
- Nam, Y., and Ooka, R. (2010). Numerical simulation of ground heat and water transfer for groundwater heat pump system based on real-scale experiment. *Energy Build.* 42 (1), 69–75. doi:10.1016/j.enbuild.2009.07.012
- Park, D. K., Kaown, D., and Lee, K. K. (2020). Development of a simulation-optimization model for sustainable operation of groundwater heat pump system. *Renew. Energy* 145, 585–595. doi:10.1016/j.renene.2019.06.039
- Park, D., Lee, E., Kaown, D., Lee, S. S., and Lee, K. K. (2021). Determination of optimal well locations and pumping/injection rates for groundwater heat pump system. *Geothermics* 92, 102050. doi:10.1016/j.geothermics.2021.102050
- Peng, Y. M. (2013). *Simulation analysis of ground water heat pumps system and operation optimization research*. Master's Thesis (Hefei University of Technology).
- Sang, J. M., Liu, X., Liang, C. Z., Feng, G. H., Li, Z. H., Wu, X. H., et al. (2022). Differences between design expectations and actual operation of ground source heat pumps for green buildings in the cold region of northern China. *Energy* 252, 124077. doi:10.1016/j.energy.2022.124077
- Sanner, B., Karytsas, C., Mendrinou, D., and Rybach, L. (2003). Current status of ground source heat pumps and underground thermal energy storage in Europe. *Geothermics* 32 (4-6), 579–588. doi:10.1016/S0375-6505(03)00060-9
- Song, T., and Wang, W. J. (2015). Application and analysis of BIN method in Urumqi region. *Heat. Vent. Air Cond.* 45 (05), 39–43.
- Wang, Z. H., Xiang, X. Y., and Pan, Y. L. (2011). *Hydrogeological report of groundwater and surface water ground source heat pump project in Xincheng District, Turpan City, Xinjiang*. Urumqi: Water Conservancy and Hydropower Survey and Design Institute Geological Survey Research Institute.
- Wang, Z. W., Wang, L., Ma, A. H., Liang, K. F., Song, Z., and Feng, L. W. (2019). Performance evaluation of ground water-source heat pump system with a fresh air preconditioner using ground water. *Energy Convers. Manag.* 188, 250–261. doi:10.1016/j.enconman.2019.03.061
- Wen, T., Cui, X. Z., and Fan, Y. (2022). Optimal layout of pumping and recharging wells for ground-source heat pump. *J. Yangtze River Sci. Res. Inst.* 39 (01), 23–31+38.
- Yan, B. Z., Xu, W. J., Li, Y. H., Sun, J., Bi, P., Li, Y., et al. (2023). Optimal layout of pumping and recharging wells for groundwater source heat pump and parameter sensitivity. *J. Jilin Univ. (Earth Sci. Ed.)* 53 (01), 218–229. doi:10.13278/j.cnki.jjuese.20210222
- Zhang, Z. L., Zhang, H. J., Xie, B., and Zhang, X. T. (2022). Energy scheduling optimization of the integrated energy system with ground source heat pumps. *J. Clean. Prod.* 365, 132758. doi:10.1016/j.jclepro.2022.132758
- Zhao, Y., Zhang, S. G., and Xun, L. (2003). Cost-effective optimal design of groundwater source heat pumps. *Appl. Therm. Eng.* 23 (13), 1595–1603. doi:10.1016/S1359-4311(03)00110-8
- Zhen, J. L., Lu, J., Huang, G. Q., and Zhang, H. Y. (2017). Groundwater source heat pump application in the heating system of Tibet Plateau airport. *Energy Build.* 136, 33–42. doi:10.1016/j.enbuild.2016.12.008
- Zhou, K., Mao, J. F., Li, Y., Zhang, H., Chen, S. Y., and Chen, F. (2022a). Thermal and economic performance of horizontal ground source heat pump systems with different flowrate control methods. *J. Build. Eng.* 53, 104554. doi:10.1016/j.job.2022.104554
- Zhou, M. L., Cai, F., and Arai, K. (2022b). Cyclic use of groundwater: An innovative way to improve performance of a groundwater source heat pump system during a cooling period. *J. Build. Eng.* 51, 104325. doi:10.1016/j.job.2022.104325
- Zhou, X. M., Wang, S., Li, X. L., Meng, J. J., Li, Z., Zhang, L. H., et al. (2022c). Research on theory and technology of floor heave control in semicool rock roadway: Taking longhu coal mine in qitaihe mining area as an example. *Lithosphere* 2022, 3810988. doi:10.2113/2022/3810988
- Zhu, N., Hu, P. F., Wang, W., Yu, J. M., and Lei, F. (2015). Performance analysis of ground water-source heat pump system with improved control strategies for building retrofit. *Renew. Energy* 80, 324–330. doi:10.1016/j.renene.2015.02.021





## OPEN ACCESS

## EDITED BY

Xuelong Li,  
Shandong University of Science and  
Technology, China

## REVIEWED BY

Lei Shi,  
China University of Mining and  
Technology, China  
Junlong Sun,  
Kunming University of Science and  
Technology, China

## \*CORRESPONDENCE

Ruiyuan Zhang,  
✉ 1532272557@qq.com

## SPECIALTY SECTION

This article was submitted to  
Environmental Informatics  
and Remote Sensing,  
a section of the journal  
Frontiers in Earth Science

RECEIVED 11 February 2023

ACCEPTED 10 March 2023

PUBLISHED 23 March 2023

## CITATION

Zhang Y, Zhang R, Yu C, Luo H and  
Deng Z (2023), Study on shear  
characteristics of calcareous sand with  
different particle size distribution.  
*Front. Earth Sci.* 11:1163930.  
doi: 10.3389/feart.2023.1163930

## COPYRIGHT

© 2023 Zhang, Zhang, Yu, Luo and Deng.  
This is an open-access article distributed  
under the terms of the [Creative  
Commons Attribution License \(CC BY\)](#).  
The use, distribution or reproduction in  
other forums is permitted, provided the  
original author(s) and the copyright  
owner(s) are credited and that the original  
publication in this journal is cited, in  
accordance with accepted academic  
practice. No use, distribution or  
reproduction is permitted which does not  
comply with these terms.

# Study on shear characteristics of calcareous sand with different particle size distribution

Yongtao Zhang<sup>1,2</sup>, Ruiyuan Zhang<sup>1\*</sup>, Chengcheng Yu<sup>1</sup>,  
Huiwu Luo<sup>1</sup> and Zhiqiang Deng<sup>1</sup>

<sup>1</sup>CCCC Second Harbor Engineering Co., Ltd., Wuhan, China, <sup>2</sup>Tongji University, Shanghai, China

For the island and reef project formed by filling calcareous sand, the problems of wide particle size distribution (PSD) and complex mechanical properties have to be faced. Therefore, in order to provide basic mechanical parameters for the construction of the island and reef project, triaxial shear tests were carried out on calcareous sands with five different typical PSDs. The results showed that as particle gradation became narrower, the axial strain corresponding to the strain-softening point all showed a decreasing trend and their differences gradually decreased; the confining pressure has a significant impact on the volumetric deformation modulus of calcareous sand with a wide PSD. The cohesion of calcareous sand showed a positive correlation with non-uniformity and curvature coefficients, while the variation of an internal friction angle showed a parabolic law; the internal friction angle also changes in the parabola with the change of fine particle contents. Furthermore, by establishing the PFC3D discrete element model, it was found that the numerical simulation results were in good agreement with the test results, which verifies the feasibility of the numerical simulation and the rationality of the mesoscopic parameter calibration. It was discovered that the wider the particle gradation range, the greater the axial strain corresponding to the critical coordination number; the sample with a narrow gradation interval was more likely to present a rotating displacement field to form a penetrating shear band. This study can provide design parameters for stability analysis of high and steep slopes in calcareous sand sites.

## KEYWORDS

calcareous sand, particle size distribution, triaxial test, shear strength, discrete element

## 1 Introduction

Calcareous sand (Hongbing et al., 2006) is widely distributed in the Maldives and other islands, which is a kind of carbonate sediment obtained after experiencing long-term immersion in calcium carbonate solution; it has the characteristics of irregular shape (Liu and Wang, 1998; Smith and Cheung, 2003), numerous pores (Xu et al., 2022), easy cementation (Meng et al., 2014), and breakage (Hu, 2008; Donohue et al., 2009). In terms of the particularity of calcareous sand, a series of studies have been carried out, including physical and mechanical properties (Lade et al., 2010; Lv et al., 2017; Giretti et al., 2020; Xu et al., 2020), dynamic properties (Morsy et al., 2019; Zhou et al., 2019; Liu et al., 2020), engineering properties (Yue et al., 2017; Rui et al., 2021), calcareous sand concrete (Ma et al., 2019; Wang et al., 2020), and microbial cementation (Liu et al., 2019; Xiao et al., 2019). The research results showed that the engineering mechanical properties of calcareous sand are very different from those of common continental sediments (Jiang et al., 2015; Wang et al.,

2017a). Because of the “Belt and Road Initiative” policy, numerous island and reef projects are being planned, where the construction sites are often formed by blowing and filling calcareous sand (Wang et al., 2011; Wang et al., 2021). When the island and reef underground engineering is excavated, it will face the problem of slope stability analysis, especially some high and steep slopes. At the same time, due to the wide distribution of particles in the calcareous sand site formed by hydraulic reclamation, the shear strength of different graded calcareous sand slopes is different (Coop, 1990; Ma et al., 2022), which brings difficulties to the slope stability analysis. Therefore, it is necessary to conduct an in-depth research on the shear characteristics of calcareous sand (Ding et al., 2021).

The shear characteristics of calcareous sand have been extensively studied; it has been observed that particle gradation (Hassanlourad et al., 2014; Rezvani et al., 2021), confining pressure (Fahey, 2021), and particle breakage (Jingping et al., 1997; Zhang and Luo, 2020) have an impact on the shear strength of calcareous sand. For particle gradation, significant attention has been paid to the influence of particle size (Bagherzadeh-Khalkhali and Mirghasemi, 2009; Cao et al., 2020; Kuang et al., 2021), uniformity coefficient (Liang et al., 2022), average particle size (Giang et al., 2017; Wang et al., 2017b), fine particle content (Shen et al., 2021), and particle group content (Ata et al., 2018; Shen et al., 2018; Yang et al., 2020; Fan et al., 2021) on the shear strength of calcareous sand. Chen et al. (2022) carried out triaxial shear tests to study the effect of gradation on the particle breakage and mechanical properties of coral sand. However, the grading range of prepared coral sand samples is very narrow, which cannot fully reflect the shear characteristics of hydraulic fill calcareous sand at the project site. It can be observed that although there are some achievements in the research on the influence of particle gradation on the shear characteristics of calcareous sand, they are partial and not comprehensive enough to reflect the shear characteristics of fully classified calcareous sand (gravel sand, coarse sand, medium sand, fine sand, and silt) under wide grading.

In this research, wide graded and fully classified calcareous sand was taken as the research object, and five kinds of typically graded calcareous sand, which can represent calcareous gravel sand, calcareous coarse sand, calcareous medium sand, calcareous fine sand, and calcareous silt, were selected to conduct the triaxial drainage shear test; thus, the change rules of strength characteristics, volumetric deformation characteristics, and the impact of grading on strength indexes were analyzed. Furthermore, the 3D discrete element model was established to conduct a mesoscopic study of the shear characteristics of calcareous sand so as to clarify the basic mechanical characteristics of the calcareous sand site, which also provides reasonable mechanical

parameters for stability analysis of high and steep slopes in island and reef engineering.

## 2 Materials and methods

### 2.1 Test material

According to the Code for Geotechnical Investigation of Water Transport Engineering (Partial Revision)—Geotechnical Investigation of Coral Reef (Draft) (CCCC Second Harbor Engineering Survey and Design Institute, 2022), the calcareous sandy soil is divided into calcareous gravel sand, calcareous coarse sand, calcareous medium sand, calcareous fine sand, and calcareous silty sand, as shown in Table 1. This paper considered the coral sandy soil revealed by the engineering geology of the coral reef area in the Maldives as the research object, and five kinds of typically graded calcareous sand (respectively representing calcareous gravel sand, calcareous coarse sand, calcareous medium sand, calcareous fine sand, and calcareous silty sand) were selected through field sampling, in order to avoid the particle size effect; particles with the size of more than 5 mm were removed, but the reserved particle groups are <0.075 mm, 0.075–0.1 mm, 0.1–0.25 mm, 0.25–0.5 mm, 0.5–1 mm, 1–2 mm, and 2–5 mm, as shown in Figure 1. The particle analysis test results are shown in Figure 2. According to particle grading curves, the calculated controlled particle size and grading index are shown in Table 2.

### 2.2 Test scheme

#### 2.2.1 Test apparatuses

The strain control triaxial tester was used in this test. The sample diameter is 50 mm, and the height is 100 mm. The maximum axial force is 100 kN, and the maximum axial displacement can reach 50 mm. The confining pressure is provided by the air pump, where the confining pressure range is 0–16 MPa, and the back pressure control is 0–4 MPa. The pore water pressure, axial strain, axial displacement, and other parameters are automatically recorded by the computer.

#### 2.2.2 Sample preparation

The saturated sample is the key to this test. The main process of the test is as follows:

- (1) Pour the weighed calcareous sand into the rubber membrane three times, and compact the sand sample with a slender rod to achieve the required dry density of 1.45 g/cm<sup>3</sup>.

TABLE 1 Classification of coral reef debris.

Coral reef detritus		Particle size distribution
Calcareous sandy soil	Calcareous gravel sand	Mass of particles with a particle size greater than 2 mm accounts for 25%–50% of the total mass
	Calcareous coarse sand	Mass of particles with a particle size greater than 0.5 mm exceeds 50% of the total mass
	Calcareous medium sand	Mass of particles with a particle size greater than 0.25 mm exceeds 50% of the total mass
	Calcareous fine sand	Mass of particles with a particle size greater than 0.075 mm exceeds 85% of the total mass
	Calcareous silt	Mass of particles with a particle size greater than 0.075 mm exceeds 50% of the total mass

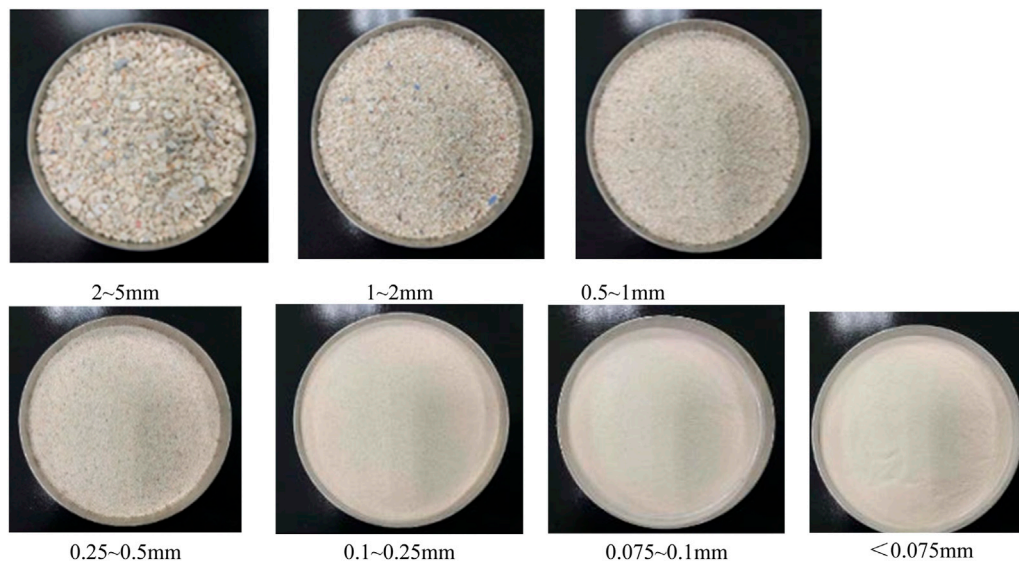


FIGURE 1

Calcareous sand of each grain group: 2~5 mm, 1~2 mm, 0.5~1 mm, 0.25~0.5 mm, 0.1~0.25 mm, 0.075~0.1 mm, and below 0.075 mm.

- (2) Apply a confining pressure of 10–20 kPa through a computer, pass CO<sub>2</sub> into the sample through the small hole in the center of the sample base for about 1 h, and maintain the pressure at about 10 kPa.
- (3) Open the water inlet valve to allow water to enter the sample from the bottom of the sample, and the water head saturation is completed until the water continuously flows out of the drain valve.
- (4) Apply back pressure to saturate the sample and maintain the confining pressure greater than the back pressure of 30 kPa to prevent the rubber membrane from being damaged by excessive back pressure until the water no longer flows into the sample.
- (5) When the saturation degree  $S_r$  is detected to be more than 0.95, saturation is completed; the next step is the shear test.

### 2.2.3 Sample shearing

Under the confining pressure values of 25 kPa, 50 kPa, 100 kPa, and 200 kPa, a total of 20 groups of triaxial consolidation drainage

shear tests were performed on five kinds of calcareous sand mentioned previously. When the axial strain of the sample reaches 15%, the test is terminated and the shear rate is 0.3 mm/min.

## 3 Experiment results

### 3.1 Strength characteristics

The deviatoric stress–strain curves of five calcareous sand samples are shown in Figure 3. It can be observed that under confining pressure ( $\sigma_3 = 25 \sim 200$  kPa), these curves all show strain-softening characteristics (Huodong et al., 2018). As the axial strain increased, the sustained deviator stress continuously increased (Yamamuro and Lade, 1996) but decreased after reaching the peak value. Under low confining pressure ( $\sigma_3 = 25 \sim 50$  kPa), the curve slope did not significantly decrease after increasing, and the strain-softening phenomenon was not evident. With confining pressure increasing to ( $\sigma_3 = 100 \sim 200$  kPa), the strain-softening phenomenon became more evident. This is because, under low horizontal stress, the particle breakage phenomenon (Lade et al., 1996) is not evident, but the particles were broken to different degrees as the confining pressure increased (Desrosiers and Silva, 2002; Yu, 2018), during which as the content of fine particles increased, the calcareous gravel sand changed into calcareous silt (Figures 3A, B, C, D, E), making some fine particles play the role of “ball” on the surface of the coarse particles; thus, the coarse particles became easier to slip, forming a relatively evident shear band, and make the stress–strain curve exhibit evident strain-softening phenomena. Moreover, it can also be observed that with the increase of the confining pressure, the axial strain corresponding to the peak stress continuously increased, that is, the starting position of strain-softening moved backwards; moreover, as the calcareous sand particles gradually became finer, these axial strains

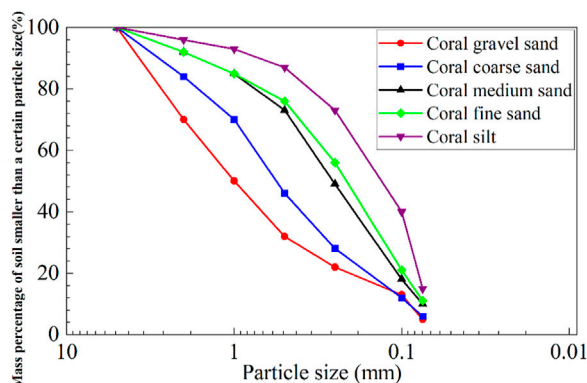
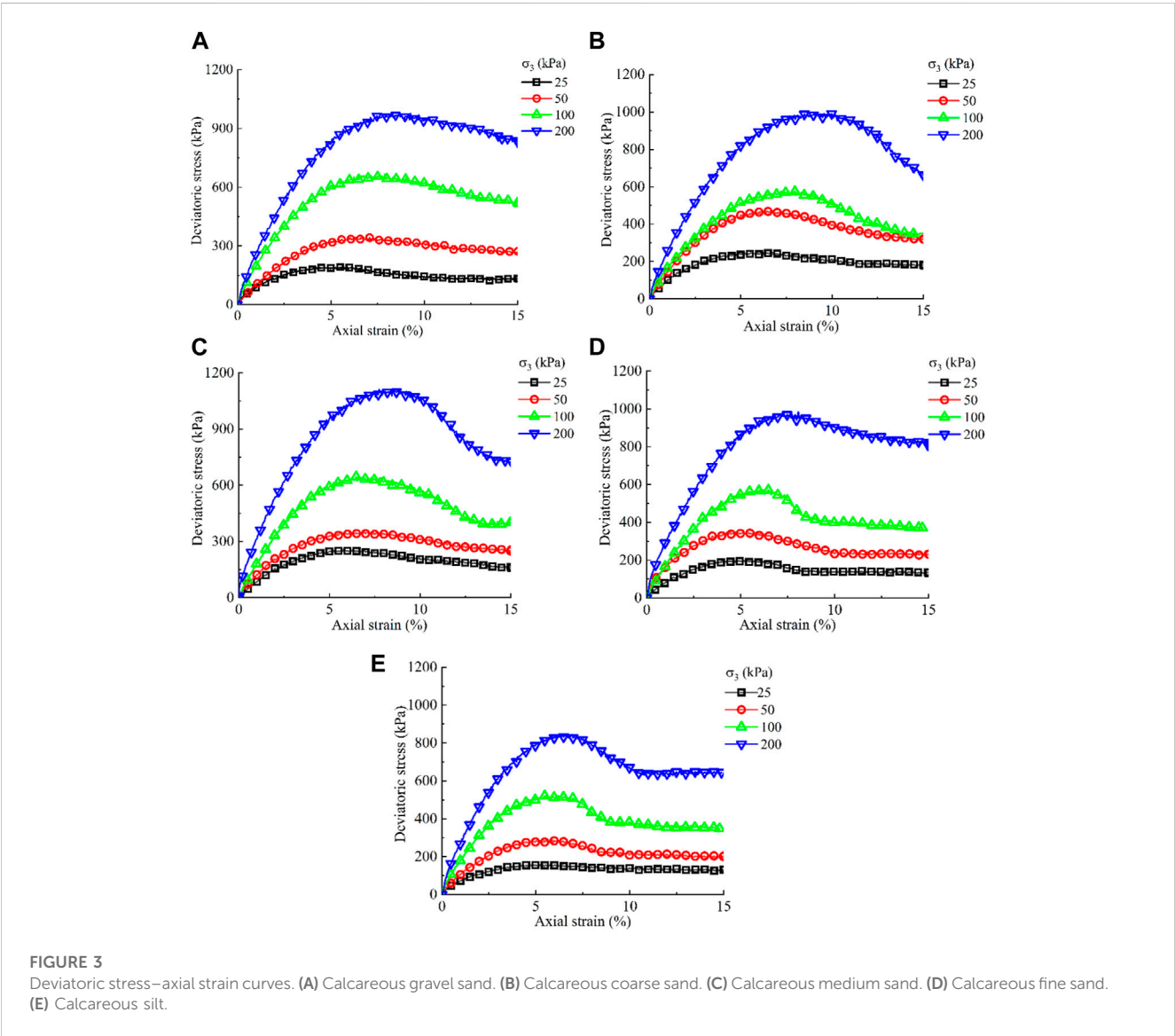


FIGURE 2

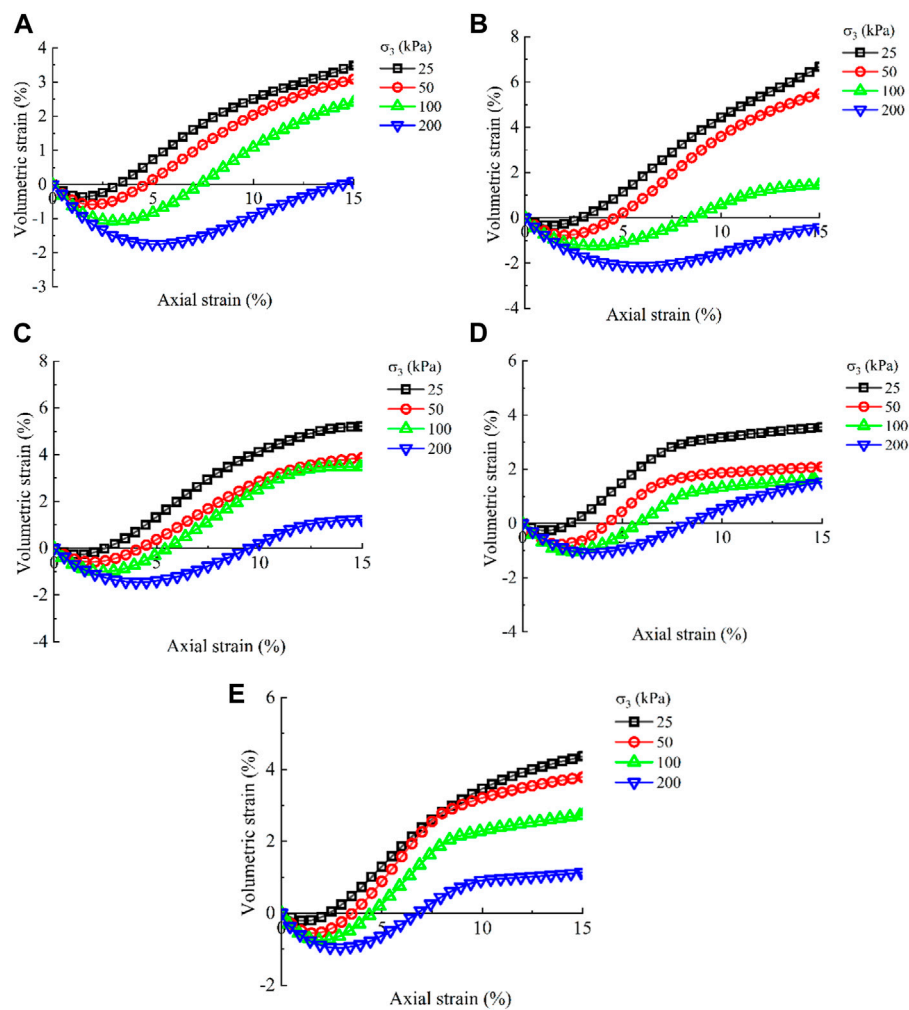
PSD curves.

TABLE 2 Physical property index of calcareous sand.

Parameter	Calcareous gravel sand	Calcareous coarse sand	Calcareous medium sand	Calcareous fine sand	Calcareous silt
$d_{10}$	0.09	0.09	0.08	0.08	0.08
$d_{30}$	0.45	0.28	0.16	0.14	0.09
$d_{50}$	1.00	0.58	0.26	0.22	0.15
$d_{60}$	1.50	0.80	0.36	0.30	0.20
Non-uniformity coefficient $C_u$	16.67	8.70	4.80	4.00	2.67
Curvature coefficient $C_c$	1.50	1.07	0.95	0.87	0.54



under each confining pressure decreased and the difference between them gradually became smaller. This is because as calcareous gravel sand changed into calcareous silty sand, the particle size distribution (PSD) gradually became worse and the interlocking effect between particles decreased, making particles more prone to shear. Figure 3E shows that for calcareous silt, the difference in the axial strain corresponding to the four peak stresses was very small; this is because the increase of fine particles in calcareous silt makes the



**FIGURE 4**  
Volumetric strain–axial strain curve of calcareous sand. (A) Calcareous gravel sand. (B) Calcareous coarse sand. (C) Calcareous medium sand. (D) Calcareous fine sand. (E) Calcareous silt.

particle not easy to break and slip, which results in the whole decrease of the axial strain corresponding to the strain-softening point and the decrease of deviation between them. Figure 3 shows that when the axial strain of calcareous gravel sand, calcareous coarse sand, and calcareous medium sand reached 15%, the deviatoric stress still remained unstable, while that of the axial strain of calcareous fine sand and calcareous silty sand reached 15%; the deviatoric stress of the axial strain gradually became stable, especially for calcareous silty sand; this indicates that for the fine-grained sample, the strain is small and it will maintain its stable residual strength after strain-softening occurs.

### 3.2 Deformation characteristics

As the relationship between the volumetric strain and axial strain of five kinds of calcareous sand shown in Figure 4, these calcareous sand forms all showed volumetric deformation characteristics of the first shear compression and then shear dilatancy, which means that

with the increase of the axial strain, the shear compression became more evident, the shear compression rate gradually decreased, and then the shear dilatancy appeared, with first increase and then decrease of shear dilatancy rates. With calcareous gravel sand changing to calcareous silt, their gradation range became narrower and the decreasing amplitude of the shear dilatancy rate was large, indicating that the shear dilatancy rate decreased and the volumetric deformation showed a stable trend. With the increase of the confining pressure from 50 kPa to 200 kPa, the volumetric strain curve changed significantly, especially for calcareous gravel sand and calcareous coarse sand, suggesting that the confining pressure has a significant impact on the volume change modulus of calcareous sand with a wide PSD. This is because the coarse particles are irregular in shape with many edges and corners, and porosity was compressed and some coarse particles were crushed as the strain increased; furthermore, the increase in the axial strain caused the particles to slip as a whole, presenting the volumetric characteristics of shear dilatancy. With the increase of confining pressure, the coarse particles in calcareous sand were partially crushed, resulting in the



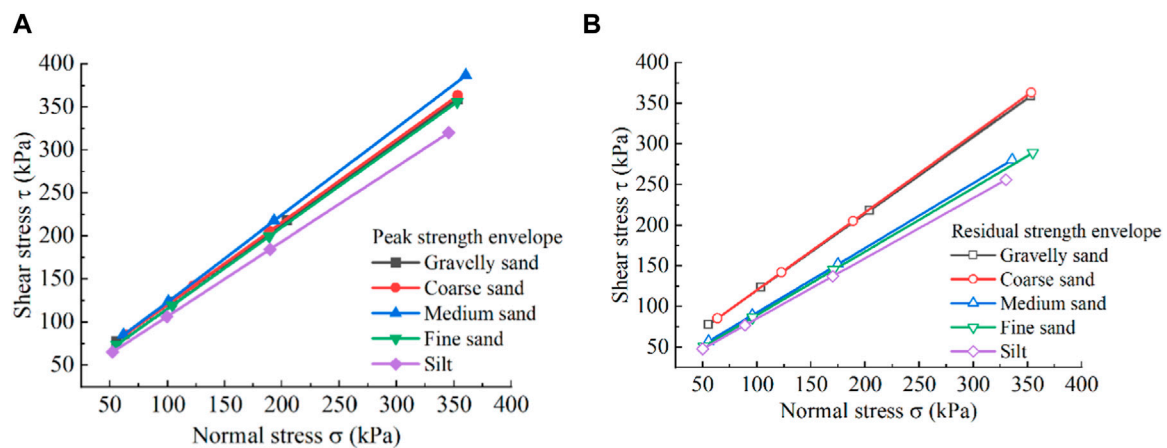


FIGURE 5  
 $\sigma$ - $\tau$  envelope. (A) Peak  $\sigma$ - $\tau$  envelope. (B) Residual  $\sigma$ - $\tau$  envelope.

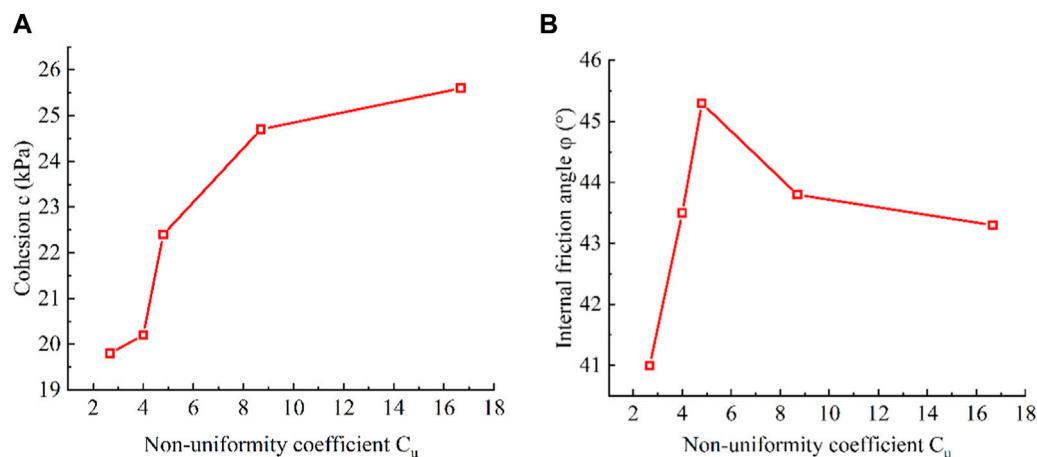


FIGURE 6  
Relationship between  $C_u$  and cohesion and the internal friction angle. (A) Relationship between  $C_u$  and cohesion. (B) Relationship between  $C_u$  and the internal friction angle.

sample being compressed to a greater extent. Therefore, the volumetric strain curve was significantly different from that under low confining pressure. It can also be observed that with the increase in the confining pressure, the axial strain corresponding to the change point from shear compression to shear dilatancy increased continuously, which indicates that the increase in confining pressure compressed pores and crushed particles, delaying the shear dilatancy.

### 3.3 The effect of PSD on the strength index

According to the Mohr-Coulomb strength criterion, the  $\sigma$ - $\tau$  envelope is obtained, as shown in Figure 5, based on which the shear strength parameters can be obtained. The peak internal friction angle of calcareous sand was in the range of  $41^\circ$ – $45.3^\circ$ , the bite force was in the range of 19.8 kPa–25.6 kPa, the residual internal

friction angle was in the range of  $36.6^\circ$ – $38.5^\circ$ , and the residual bite force was in the range of 10.9 kPa–15.9 kPa.

In order to further investigate the impact of the gradation index on shear strength, the curves reflecting the relationship between the non-uniformity coefficient  $C_u$ , curvature coefficient  $C_c$  and cohesion, and the internal friction angle were drawn and are shown in Figures 6, 7.

According to the test results, it can be observed that cohesion increased with the increase of  $C_u$  and  $C_c$ . Previous research shows that the basic shape of particles is similar in calcareous soil with different particle sizes, but the particle size will change with particle groups varying, and the proportion of particles with different shapes in each particle group is also different. In coarse calcareous sand, the particle shape is mostly flaky and branched and the interlocking effect between particles is easy to form. Table 1 shows that as  $C_u$  of calcareous silt increased to  $C_u$  of calcareous gravel sand,  $C_c$  also increased, so the sample gradually met the requirements of  $C_u \geq 5$  and  $C_c = 1$ –3,

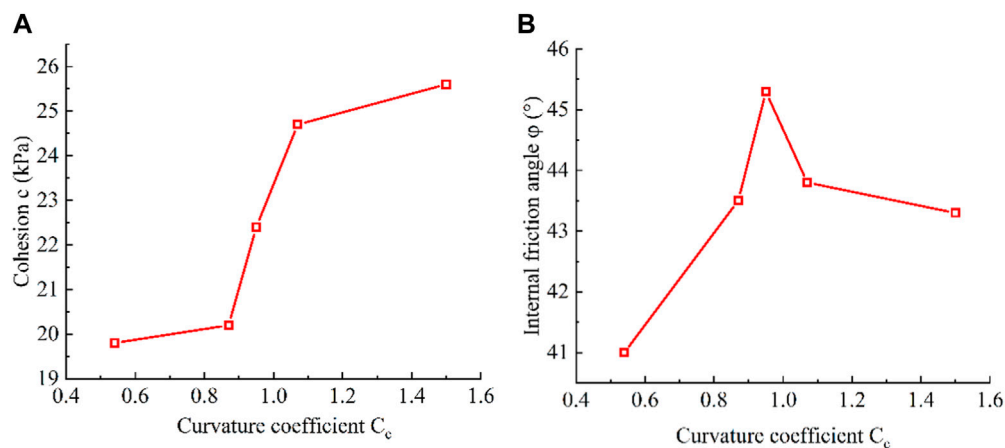


FIGURE 7

Relationship between  $C_c$  and cohesion and the internal friction angle. (A) Relationship between  $C_c$  and cohesion. (B) Relationship between  $C_c$  and the internal friction angle.

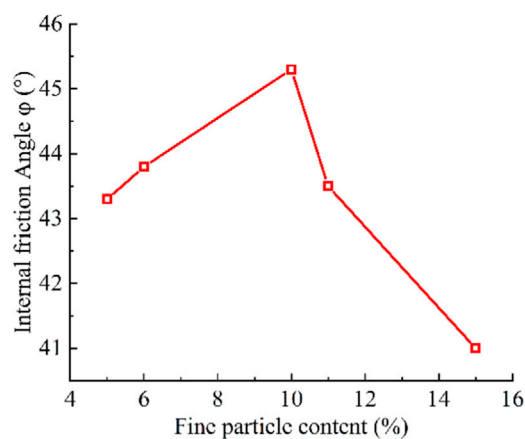


FIGURE 8

Relationship curve between the fine particle content and internal friction angle.

“ball” effect appeared in calcareous sand, reducing the internal friction angle. Therefore, corresponding to the peak internal friction angle, there is a limit value for the content of fine particles. In order to further quantify the limit value of fine particle contents and clarify the effect of fine particle contents on the internal friction angle of calcareous sand, the relationship between fine particle contents and internal friction angles is plotted and shown in Figure 8.

Figure 8 shows that there was a limit value of 10% for the fine content, which means when the fine content was 10%, the internal friction angle reached the maximum value; when the content of fine particles was less than 10%, the internal friction angle gradually increased; when the fine content was greater than 10%, the internal friction angle decreased.

Based on qualitative analysis, the test data were fitted to quantitatively reflect the impact of the particle size of calcareous sand on the strength index; the following formulas can be used to accurately calculate and evaluate the strength characteristics of calcareous sand with different PSDs. Figures 9–11 show the fitting relationships between  $C_u$  and cohesion,  $C_c$  and cohesion, and fine particle content and internal friction angle; the determination coefficients of the fitting formulas are all above 0.95, indicating a high reliability.

$$y = -12.2 \cdot e^{\left(-\frac{x}{4.5}\right)} + 26, \quad (1)$$

$$R^2 = 0.95,$$

$$y = 25.5 + \frac{-5.8}{1 + e^{\left(\frac{x-1}{0.05}\right)}}, \quad (2)$$

$$R^2 = 0.99,$$

$$y = 40.9 + 5.2 \cdot e^{-0.5 \cdot \left(\frac{x-8.3}{2.4}\right)^2}, \quad (3)$$

$$R^2 = 0.96.$$

suggesting a continuous good gradation, and the filling, extrusion, and occlusion of particles were enhanced. With the particle size increasing, the content of large-particle calcareous sand became higher and the occluding effect between particles was continuously strengthened, while the apparent cohesion was generated by the occluding effect of particles; so, with the increase of non-uniformity and curvature coefficients, calcareous sand showed a higher cohesion.

It can also be observed that with the decrease of  $C_u$  and  $C_c$ , the internal friction angle first increased and then decreased. This is because as calcareous gravel sand changed into calcareous silt,  $C_u$  and  $C_c$  gradually decreased and particles gradually became uniform and poorly graded, during which the content of coarse particles decreased, and the content of fine particles gradually increased; thus, more fine particles fill pores to intensify the contact between particles, making the friction angle gradually increase. However, with further increase in the content of fine particles, fine particles started to play a role in lubrication and the

## 4 Discrete element simulation (Wang et al., 2018)

Bardet and Proubet (1991) and Bardet and Proubet (1992) simulated the evolution law of shear bands in granular materials

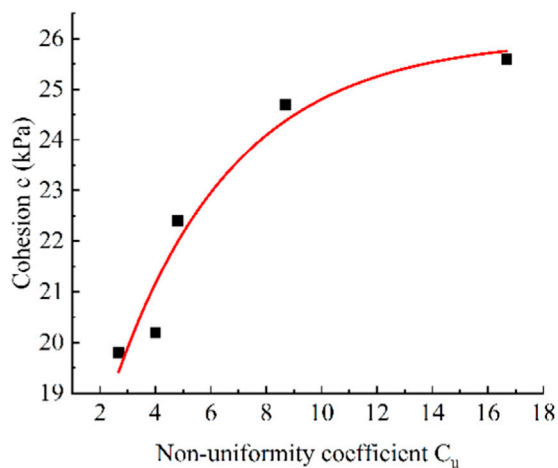


**FIGURE 9**  
Fitted relationship curve between  $C_u$  and cohesion.

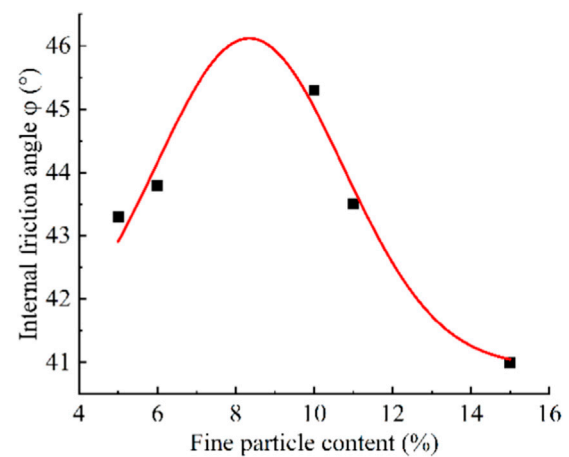


**FIGURE 11**  
Fitted relationship curve between the fine particle content and internal friction angle.

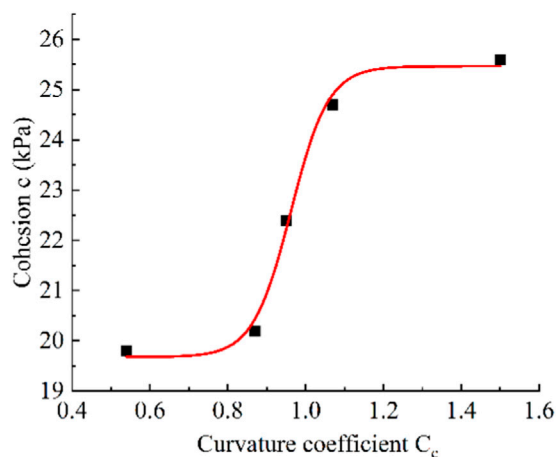


**FIGURE 10**  
Fitted relationship curve between  $C_c$  and cohesion.

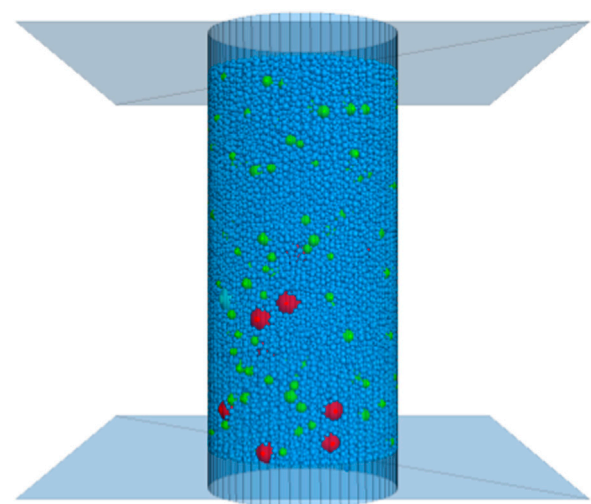


**FIGURE 12**  
Numerical sample.

from a two-dimensional perspective. In order to overcome the limitation of a two-dimensional plane, PFC3D (Cundall and Strack, 1979; Cundall, 2001) was adopted to model calcareous sands with different PSDs and explore the interaction between particles from a three-dimensional perspective, which provides a powerful tool for revealing the shear behavior of calcareous sand from the mesoscopic level.

## 4.1 Numerical sample preparation

Referring to the existing numerical test results, the method of expanding particle sizes has a small impact on the mechanical behavior of the material (Belheine et al., 2009; Evans and Valdes, 2011); in this paper, the particle size was uniformly enlarged

3.5 times; the numerical sample is shown in Figure 12, and the numerical test process is as follows:

- (1) According to the PSD in the laboratory test, a model of the sample in a cylinder with a diameter of 50 mm and a height of 100 mm was established, which had the same PSD. In this sample model, the generated particles are as follows: 28,013 particles for calcareous gravel sand, 39,715 particles for calcareous coarse sand, 59,915 particles for calcareous medium sand, 61,983 particles for calcareous fine sand, and 70,362 particles for calcareous silt.
- (2) The particle sample was generated according to the initial porosity, and the wall was preloaded with a certain pressure to obtain a uniform and dense sample.

TABLE 3 Mesoscopic parameters of a numerical sample.

Sand type	Friction force	Normal contact stiffness/ MN·m <sup>-1</sup>	Stiffness ratio	Effective modulus/GPa	Cohesion/ MPa	Friction angle/(°)
Calcareous gravel sand	0.5	100	1.0	0.1	0.32	43.3
Calcareous coarse sand	0.5	100	1.0	0.1	0.26	43.8
Calcareous medium sand	0.5	100	1.0	0.1	0.3	45.3
Calcareous fine sand	0.5	100	1.0	0.1	0.28	43.5
Calcareous silt	0.5	100	1.0	0.1	0.22	41.0

- (3) The contact between particles was set as the parallel bonding model “linearpbond,” and relevant parameters were assigned to realize the bond between particles.
- (4) The displacement of particles was reset, and then a relative velocity was applied to the upper and lower walls to realize triaxial shear numerical sample loading.

## 4.2 Calibration of mesoscopic parameters

In this paper, parallel bonding was used to simulate the bonding force between calcareous sand particles. The parallel bond model can describe the constitutive characteristics between the cemented particles, where the spring group with constant normal and tangential stiffness is distributed on the contact surface. When the displacement or force between particles exceeds the critical value, the parallel bonding model will fail to induce a fracture. In the discrete element numerical simulation, mesoscopic parameters, such as contact stiffness and friction coefficient, need to be calibrated. Referring to previous numerical tests (Thompson et al., 2009; Stratton and Wensrich, 2010), the normal stiffness in this paper is 100 MN/m, and the particle stiffness ratio is 1.0, which meets the range of 1.0–1.5 recommended by Goldenberg and Goldhirsch (2005). According to the results of indoor tests, the internal friction angle of calcareous sand was 45°, and the cohesion, effective modulus, and other mesoscopic parameters were calibrated according to the stress–strain curve in the laboratory test, as shown in Table 3.

## 5 Numerical simulation results

### 5.1 Comparison with indoor tests

Figure 13 shows the comparison between the numerical simulation results and the test results of calcareous silt; it can be observed that they are in good agreement, and the feasibility of the numerical simulation and the rationality of the calibration of mesoscopic parameters are verified. On this basis, the numerical simulation results can be further analyzed. Figure 14 shows the failure pattern in the numerical calculation and the indoor test of

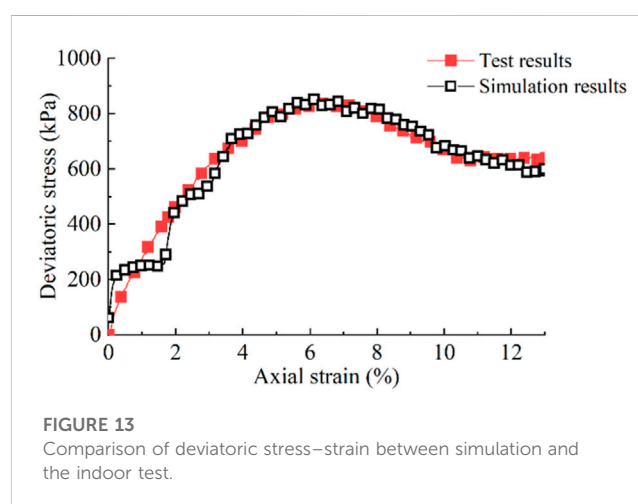


FIGURE 13 Comparison of deviatoric stress–strain between simulation and the indoor test.

### 5.2 Coordination number evolution

The coordination number reflects the average number of contacts per ball and can be defined as follows:

$$C_n = \frac{\sum_{N_{\text{grain}}} n_i^c}{N_{\text{grain}}} \quad i = 1, 2, \dots, N_{\text{grain}}. \quad (4)$$

Under the impact of load, the rearrangement of calcareous sand particles is the fundamental reason for the shear compression and dilatancy, and their sliding and rotation will cause the change of the coordination number. Figure 15 shows the change curve of the coordination number of five types of calcareous sand during shearing. As a whole, with the increase of the axial strain, the coordination number first increased and then decreased, existing as a critical coordination number; this is because, with the increase of the axial load, the volume of calcareous sand is compressed, resulting in an increase in the number of contact between particles and an increase in the coordination number. With the further increase of the axial

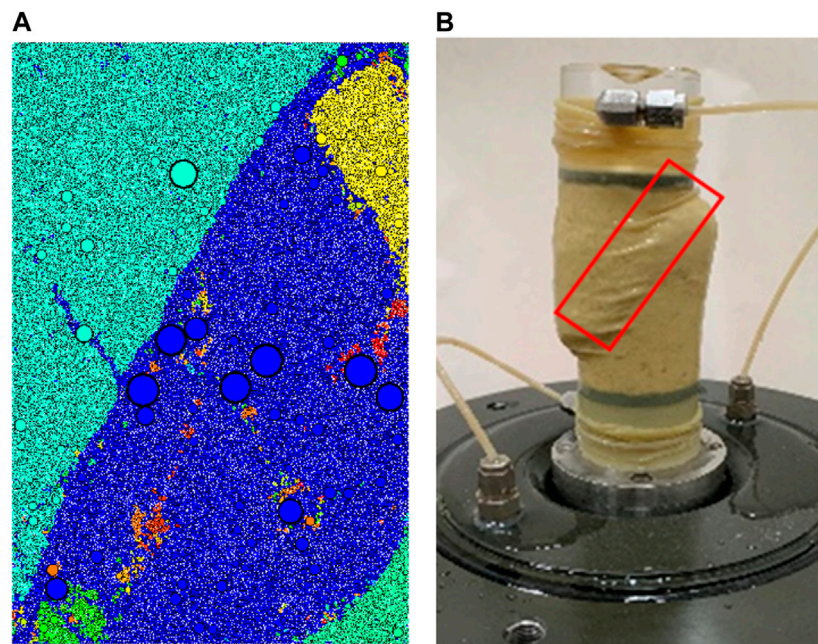


**FIGURE 14**  
Comparison of the shear band between simulation and the indoor test. (A) Numerical simulation of the shear band. (B) Shear band for an indoor test.

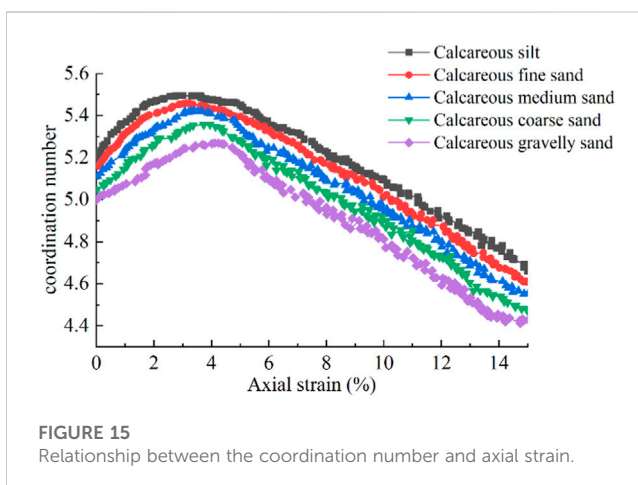


**FIGURE 15**  
Relationship between the coordination number and axial strain.

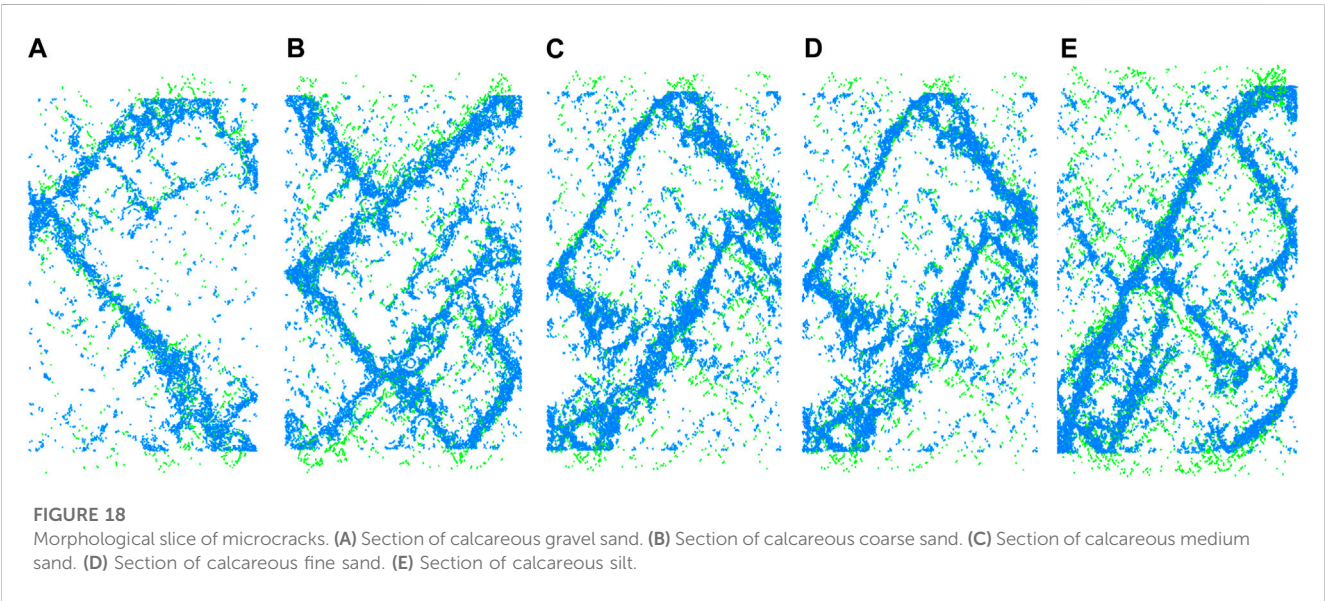
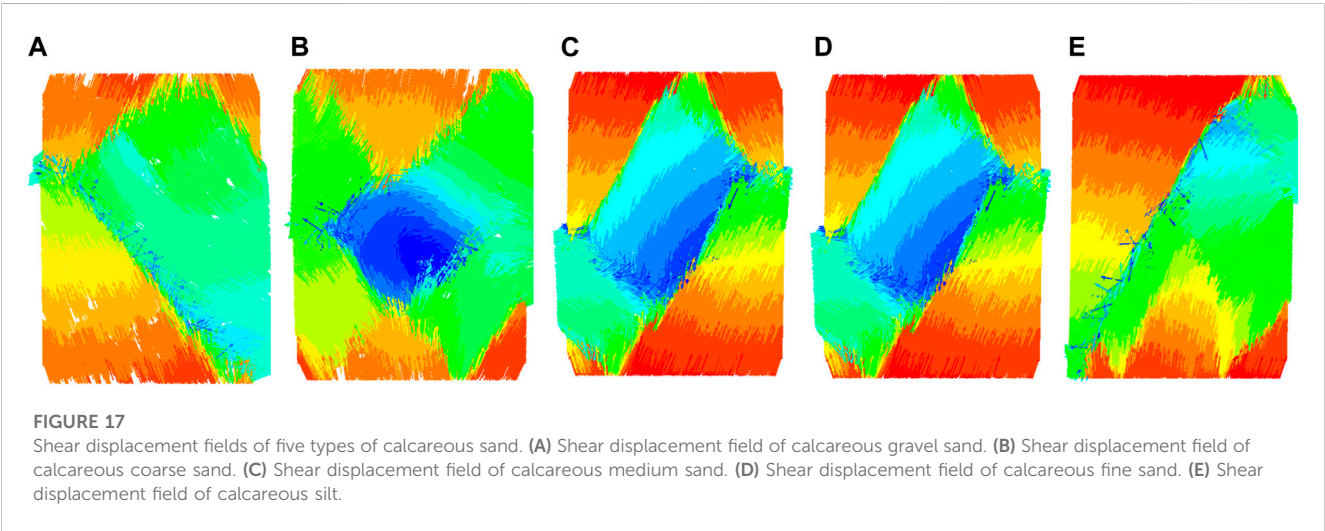
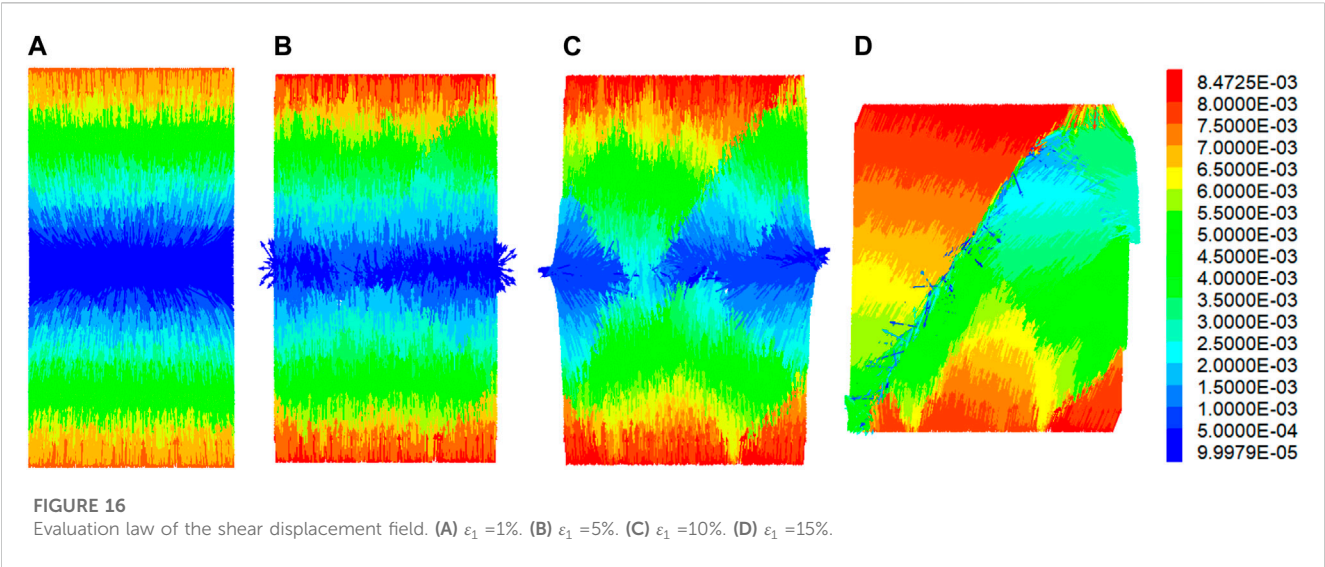
strain, the sample exhibited a shear slip, the number of contact between particles decreased, and the sample showed shear dilatancy. It can be observed that with calcareous gravel sand changing into calcareous silt, the coordination number increased significantly and the axial strain corresponding to the critical coordination number decreased gradually from 5% to 3%. This is because as the PSD gradually became worse, embedding and occluding between the particles were weakened, making the shear slip more likely to occur. This is consistent with the shear law obtained from the laboratory test. The change of the coordination number also explains the volume change mechanism of the first shear compression and then shear dilatancy of calcareous sand in the mesoscale.

### 5.3 Developmental law of the shear displacement field

To further analyze the formation and characteristics of the shear band in the sample, the development and change of a displacement field were revealed by slicing the cylindrical sample. Figure 16 shows the development process of the shear displacement field under a confining pressure of 200 kPa. Figures 16A,B show the particle displacement field with a small axial strain. With the increase of the axial strain, the displacement of particles at the top and bottom gradually increased and the particles in the middle of the sample began to show a trend of horizontal outward shear dilatancy; however, the displacement field corresponding to the peak strength was not reached, and there was no shear band. As the peak strength was reached with the increase of the axial strain. Figure 16C showed a more evident shear band, and the shear dilatancy of the sample was further enhanced. At the same time, an evident and concentrated shear zone is shown in Figure 16D, and the movement direction of particles in the shear zone was almost distributed between  $0^\circ$  and  $360^\circ$ , indicating that the particles in the shear zone have slipped and turned over, which explains the formation mechanism of the macroscopic shear fracture zone from a microscopic perspective.

In order to further compare the shear zone evolution of these five types of calcareous sand, their shear displacement fields are observed, as shown in Figure 17. It can be observed that as grain gradation decreased (Figures 17A, B, C, D, E), the particles gradually became finer and the rotating blue displacement field gradually appeared in the sample; moreover, the displacement field in the calcareous medium sand (calcareous fine sand) was significantly larger than that of the calcareous coarse sand; this is the primary





condition of forming shear bands. With the further increase of the rotational displacement field, a fully penetrating shear slip band was formed as that of calcareous silt, as shown in Figure 17E. If the rotational displacement field is not formed, the specimen may exhibit local shear failure and form a local shear band, as shown in Figure 17A. Due to small differences in sample gradation, calcareous medium sand and calcareous fine sand showed similar displacement fields.

## 5.4 Analysis of microcrack evolution

Figure 18 shows the morphological slice of microcracks in five types of calcareous sand after triaxial shear, where blue represents the microcrack formed by shear failure and green represents the microcrack formed by tensile failure. It can be observed that the obvious shear failure zone is accompanied by partial tension cracks on the shear crack zone, which indicates that the bond failure between particles is caused by both the shear and tension effects, particularly by shear failure. At the same time, it can also be observed that in the samples with wide PSDs, such as calcareous gravel sand, the content of coarse particles is high and the distribution of shear bands is relatively irregular and more scattered; this is because the particles have strong impingement and occlusion, making the penetrating shear bands difficult to form; moreover, the coarse particles may limit the extension and penetration of the shear zone.

## 6 Conclusion

In this paper, the shear characteristics of calcareous sand with five PSDs were studied using the triaxial drainage shear test and the influence of PSD on the shear properties of calcareous sand is discussed in detail. The following conclusions can be drawn.

- (1) During triaxial drained shear tests, as the PSD became narrow, this axial strain decreased and the difference between the five types of calcareous sand decreased. As the PSD became narrow, the deviator stress of the sample tended to be stable earlier and the residual strength remained stable. The peak internal friction angle of calcareous sand is in the range of 41–45.3°, and the bite force is in the range of 19.8–25.6 kPa; the residual internal friction angle is in the range of 36.6–38.5°, and the residual bite force is in the range of 10.9–15.9 kPa. With the calcareous gravel sand changing into calcareous silt, the particles gradually became finer and the volumetric deformation exhibits a stable trend. With the increase of confining pressure, the occurrence of shear dilatancy was delayed.
- (2) After comparing the PSD of five types of calcareous sand, it was found that the cohesion of the sample increases with the increase of the non-uniformity coefficient  $C_u$  and curvature

coefficient  $C_c$ , while the internal friction angle first increased and then decreased, showing a parabolic variation law. The internal friction angle varied with the fine particle content in a parabola and reached the maximum value when the fine particle content was 10%. The formulas fitting the relationship between the non-uniformity coefficient  $C_u$ , curvature coefficient  $C_c$ , fine particle contents, and strength parameters were obtained, and the strength index of calcareous sand can be calculated and evaluated, with high accuracy.

- (3) With PSD becoming wider, the coordination number decreased, but the axial strain point corresponding to the critical coordination number continued to increase. With the decrease in particle gradation, the particles gradually became finer and the rotating blue displacement field gradually appeared in the sample. With further increase of the rotating displacement field, a complete shear slip zone was formed. With the widening of particle gradation, the content of coarse particles increased and the distribution of shear bands became relatively irregular and more dispersed.

## Data availability statement

The original contributions presented in the study are included in the article/Supplementary Material; further inquiries can be directed to the corresponding author.

## Author contributions

Methodology, YZ and HL; validation, RZ; formal analysis, RZ and HL; writing—original draft, RZ and CY; writing—review and editing, RZ; supervision, HL and ZD; and project administration, YZ. All authors have read and agreed to the published version of the manuscript.

## Conflict of interest

All authors were employed by CCCC Second Harbor Engineering Co., Ltd.

## Publisher's note

All claims expressed in this article are solely those of the authors and do not necessarily represent those of their affiliated organizations, or those of the publisher, the editors, and the reviewers. Any product that may be evaluated in this article, or claim that may be made by its manufacturer, is not guaranteed or endorsed by the publisher.

## References

- Ata, A., Salem, T. N., and Hassan, R. (2018). Geotechnical characterization of the calcareous sand in northern coast of Egypt. *Ain Shams Eng. J.* 9, 3381–3390. doi:10.1016/j.jasej.2018.03.008
- Bagherzadeh-Khalkhali, A., and Mirghasemi, A. A. (2009). Numerical and experimental direct shear tests for coarse-grained soils. *Particle Technology* 7, 83–91. doi:10.1016/j.partic.2008.11.006
- Bardet, J., and Proubet, J. (1991). A numerical investigation of the structure of persistent shear bands in granular media. *Geotechnique* 41, 599–613. doi:10.1680/geot.1991.41.4.599
- Bardet, J., and Proubet, J. (1992). Shear-band analysis in idealized granular material. *J. Eng. Mech.* 118, 397–415. doi:10.1061/(asce)0733-9399(1992)118:2(397)

- Belheine, N., Plassiard, J.-P., Donzé, F.-V., Darve, F., and Seridi, A. (2009). Numerical simulation of drained triaxial test using 3D discrete element modeling. *Comput. Geotechnics* 36, 320–331. doi:10.1016/j.compgeo.2008.02.003
- Cao, P., Jiang, M.-j., and Ding, Z.-j. (2020). Effects of particle size on mechanical behaviors of calcareous sand under triaxial conditions. *Jpn. Geotech. Soc. Spec. Publ.* 8, 182–187. doi:10.3208/jgssp.v08.c54
- CCCC Second Harbor Engineering Survey and Design Institute (2022). *JTS133. Code for geotechnical investigation of water transport engineering (partially revised) - coral reef geotechnical investigation [S]*. Beijing: Beijing People's Communications Press.
- Chen, Y. Y., Tang, Y., Guan, Y. F., Liu, R. M., Han, X., and Zhao, X. Q. (2022). Study on the mechanical properties of coral sands with different particle gradations. *Mar. Georesources Geotechnol.*, 1–12. doi:10.1080/1064119x.2022.2037112
- Coop, M. (1990). The mechanics of uncemented carbonate sands. *Géotechnique* 40, 607–626. doi:10.1680/geot.1990.40.4.607
- Cundall, P. A. (2001). A discontinuous future for numerical modelling in geomechanics? *Proc. institution Civ. engineers-geotechnical Eng.* 149, 41–47. doi:10.1680/geng.2001.149.1.41
- Cundall, P. A., and Strack, O. D. (1979). A discrete numerical model for granular assemblies. *geotechnique* 29, 47–65. doi:10.1680/geot.1979.29.1.47
- Desrosiers, R., and Silva, A. J. (2002). Strength behavior of marine sands at elevated confining stresses. *Mar. Georesources Geotechnol.* 20, 1–19. doi:10.1080/106411902753556834
- Ding, Z., He, S.-H., Sun, Y., Xia, T.-D., and Zhang, Q.-F. (2021). Comparative study on cyclic behavior of marine calcareous sand and terrigenous siliceous sand for transportation infrastructure applications. *Constr. Build. Mater.* 283, 122740. doi:10.1016/j.conbuildmat.2021.122740
- Donohue, S., O'sullivan, C., and Long, M. (2009). Particle breakage during cyclic triaxial loading of a carbonate sand. *Géotechnique* 59, 477–482. doi:10.1680/geot.2008.t.003
- Evans, T. M., and Valdes, J. R. (2011). The microstructure of particulate mixtures in one-dimensional compression: Numerical studies. *Granul. Matter* 13, 657–669. doi:10.1007/s10035-011-0278-z
- Fahey, M. (2021). “The response of calcareous soil in static and cyclic triaxial tests,” in *Engineering for calcareous sediments* (Boca Raton: CRC Press), 61–68.
- Fan, K., Zheng, Y., Baudet, B. A., and Cheng, Y. P. H. (2021). Investigation of the ultimate particle size distribution of a carbonate sand. *Soils Found.* 61 (6), 1708–1717. doi:10.1016/j.sandf.2021.10.002
- Giang, P. H. H., Van Impe, P., Van Impe, W., Menge, P., Cnudde, V., and Haegeman, W. (2017). Effects of particle characteristics on the shear strength of calcareous sand. *Acta Geotech. Slov.* 14, 77–89.
- Giretti, D., Fioravante, V., Been, K., Dickenson, S., Mesri, G., and Kane, T. (2020). Mechanical properties of a carbonate sand from a dredged hydraulic fill. *Geotechnique* 70 (10), 937–942. doi:10.1680/jgeot.18.d.014
- Goldenberg, C., and Goldhirsch, I. (2005). Friction enhances elasticity in granular solids. *Nature* 435, 188–191. doi:10.1038/nature03497
- Hassanlourad, M., Salehzadeh, H., and Shahnazari, H. (2014). Drained shear strength of carbonate sands based on energy approach. *Int. J. Geotechnical Eng.* 8, 1–9. doi:10.1179/1938636213z.000000000050
- Hongbing, Y., Zongxun, S., and Cheng, T. (2006). *Physical and mechanical properties of coral sand in the Nansha Islands*.
- Hu, B. (2008). *Research on the particle breakage mechanical characteristics and constitutive model of calcareous sand under triaxial conditions*. Wuhan, China: Institute of Rock and Soil Mechanics, Chinese Academy of Sciences.
- Huodong, C., Houzhen, W., Qingshan, M., Zhibing, W., and Zheng, F. (2018). The study on stress-strain-strength behavior of calcareous sand with particle breakage. *工程地质学报* 26, 1490–1498.
- Jiang, L., Fan, J., Wang, Z., and Huo, Z. (2015). Mechanical property of calcareous sand under action of compaction. *Glob. Geol.* 18, 183–187.
- Jingping, W., Yao, C., and Zhigang, L. (1997). Influence of particle breakage on the deformation and strength properties of calcareous sands. *Chin. J. Geotechnical Eng.* 19.
- Kuang, D., Long, Z., Guo, R., and Yu, P. (2021). Experimental and numerical investigation on size effect on crushing behaviors of single calcareous sand particles. *Mar. Georesources Geotechnol.* 39 (5), 543–553. doi:10.1080/1064119x.2020.1725194
- Lade, P. V., Nam, J., and Liggio, C. D., Jr (2010). Effects of particle crushing in stress drop-relaxation experiments on crushed coral sand. *J. Geotechnical Geoenvironmental Eng.* 136 (3), 500–509. doi:10.1061/(asce)gt.1943-5606.0000212
- Lade, P. V., Yamamuro, J. A., and Bopp, P. A. (1996). Significance of particle crushing in granular materials. *J. Geotechnical Eng.* 122, 309–316. doi:10.1061/(asce)0733-9410(1996)122:4(309)
- Liang, K., Chen, G., and Dong, Q. (2022). “Small-strain shear modulus of coral sand with various particle size distribution curves,” in *Proceedings of the 4th international conference on performance based Design in earthquake geotechnical engineering (beijing 2022)*. Editors L. Wang, J.-M. Zhang, and R. Wang (Cham: Springer International Publishing), 2054–2072.
- Liu, C., and Wang, R. (1998). Preliminary research on physical and mechanical properties of calcareous sand. *Rock Soil Mech.* 19, 32–37.
- Liu, H., Zeng, K., and Zou, Y. (2020). Particle breakage of calcareous sand and its correlation with input energy. *Int. J. Geomechanics* 20 (2), 04019151. doi:10.1061/(asce)gm.1943-5622.0001541
- Liu, L., Liu, H., Stuedlein, A. W., Evans, T. M., and Xiao, Y. (2019). Strength, stiffness, and microstructure characteristics of biocemented calcareous sand. *Can. Geotechnical J.* 56 (10), 1502–1513. doi:10.1139/cgj-2018-0007
- Lv, Y., Li, F., Liu, Y., Fan, P., and Wang, M. (2017). Comparative study of coral sand and silica sand in creep under general stress states. *Can. Geotechnical J.* 54 (11), 1601–1611. doi:10.1139/cgj-2016-0295
- Ma, L., Li, Z., Liu, J., Duan, L., and Wu, J. (2019). Mechanical properties of coral concrete subjected to uniaxial dynamic compression. *Constr. Build. Mater.* 199, 244–255. doi:10.1016/j.conbuildmat.2018.12.032
- Ma, W., Qin, Y., Zhao, K., and Chen, G. (2022). Comparisons on liquefaction behavior of saturated coral sand and quartz sand under principal stress rotation. *Mar. Georesources Geotechnol.* 40, 235–247.
- Meng, Q.-S., Yu, K.-F., Wang, R., Qin, Y., Wei, H.-Z., and Wang, X.-Z. (2014). Characteristics of rocky basin structure of yongshu reef in the southern south China sea. *Mar. Georesources Geotechnol.* 32, 307–315. doi:10.1080/1064119x.2013.764553
- Morsy, A. M., Salem, M. A., and Elmamlouk, H. H. (2019). Evaluation of dynamic properties of calcareous sands in Egypt at small and medium shear strain ranges. *Soil Dyn. Earthq. Eng.* 116, 692–708. doi:10.1016/j.soildyn.2018.09.030
- Rezvani, R., Nabizadeh, A., and Amin Tutunchian, M. (2021). The effect of particle size distribution on shearing response and particle breakage of two different calcareous soils. *Eur. Phys. J. Plus* 136, 1008–1016. doi:10.1140/epjp/s13360-021-01871-5
- Rui, S., Wang, L., Guo, Z., Zhou, W., and Li, Y. (2021). Cyclic behavior of interface shear between carbonate sand and steel. *Acta Geotech.* 16, 189–209. doi:10.1007/s11440-020-01002-x
- Shen, J., Wang, X., Wang, X., Yao, T., Wei, H., and Zhu, C. (2021). Effect and mechanism of fines content on the shear strength of calcareous sand. *Bull. Eng. Geol. Environ.* 80, 7899–7919. doi:10.1007/s10064-021-02398-w
- Shen, Y., Zhu, Y., Liu, H., Li, A., and Ge, H. (2018). Macro-meso effects of gradation and particle morphology on the compressibility characteristics of calcareous sand. *Bull. Eng. Geol. Environ.* 77, 1047–1055. doi:10.1007/s10064-017-1157-6
- Smith, D. A., and Cheung, K. F. (2003). Settling characteristics of calcareous sand. *J. Hydraulic Eng.* 129, 479–483. doi:10.1061/(asce)0733-9429(2003)129:6(479)
- Stratton, R., and Wensrich, C. (2010). Modelling of multiple intra-time step collisions in the hard-sphere discrete element method. *Powder Technol.* 199, 120–130. doi:10.1016/j.powtec.2009.12.008
- Thompson, N., Bennett, M. R., and Petford, N. (2009). Analyses on granular mass movement mechanics and deformation with distinct element numerical modeling: Implications for large-scale rock and debris avalanches. *Acta Geotech.* 4, 233–247. doi:10.1007/s11440-009-0093-4
- Wang, L., Jiang, X., Liu, H., Zhang, Z., and Xiao, Y. (2018). “DEM investigation of fracture characteristics of calcareous sand particles under dynamic compression,” in *Proceedings of China-europe conference on geotechnical engineering: Volume 1* (Springer), 247–251.
- Wang, X.-Z., Jiao, Y.-Y., Wang, R., Hu, M.-J., Meng, Q.-S., and Tan, F.-Y. (2011). Engineering characteristics of the calcareous sand in nansha islands, south China sea. *Eng. Geol.* 120, 40–47. doi:10.1016/j.enggeo.2011.03.011
- Wang, X.-Z., Wang, X., Jin, Z.-C., Meng, Q.-S., Zhu, C.-Q., and Wang, R. (2017). Shear characteristics of calcareous gravelly soil. *Bull. Eng. Geol. Environ.* 76, 561–573. doi:10.1007/s10064-016-0978-z
- Wang, X.-Z., Wang, X., Jin, Z.-C., Zhu, C.-Q., Wang, R., and Meng, Q.-s. (2017). Investigation of engineering characteristics of calcareous soils from fringing reef. *Ocean. Eng.* 134, 77–86. doi:10.1016/j.oceaneng.2017.02.019
- Wang, X., Ding, H., Meng, Q., Wei, H., Wu, Y., and Zhang, Y. (2021). Engineering characteristics of coral reef and site assessment of hydraulic reclamation in the South China Sea. *Constr. Build. Mater.* 300, 124263. doi:10.1016/j.conbuildmat.2021.124263
- Wang, Y., Huang, J., Wang, D., Liu, Y., Zhao, Z., and Liu, J. (2020). Experimental study on hygrothermal characteristics of coral sand aggregate concrete and aerated concrete under different humidity and temperature conditions. *Constr. Build. Mater.* 230, 117034. doi:10.1016/j.conbuildmat.2019.117034
- Xiao, P., Liu, H., Stuedlein, A. W., Evans, T. M., and Xiao, Y. (2019). Effect of relative density and biocementation on cyclic response of calcareous sand. *Can. Geotechnical J.* 56 (12), 1849–1862. doi:10.1139/cgj-2018-0573

- Xu, D. S., Huang, M., and Zhou, Y. (2020). One-dimensional compression behavior of calcareous sand and marine clay mixtures. *Int. J. Geomechanics* 20 (9), 04020137. doi:10.1061/(asce)gm.1943-5622.0001763
- Xu, L.-J., Wang, X.-z., Wang, R., Zhu, C.-q., and Liu, X.-p. (2022). Physical and mechanical properties of calcareous soils: A review. *Mar. Georesources Geotechnol.* 40, 751–766. doi:10.1080/1064119x.2021.1927270
- Yamamuro, J. A., and Lade, P. V. (1996). Drained sand behavior in axisymmetric tests at high pressures. *J. Geotechnical Eng.* 122, 109–119. doi:10.1061/(asce)0733-9410(1996)122:2(109)
- Yang, S., Shen, X., Liu, H., Ge, H., and Rui, X. (2020). Gradation affects basic mechanical characteristics of Chinese calcareous sand as airport subgrade of reefs. *Mar. Georesources Geotechnol.* 38 (6), 706–715. doi:10.1080/1064119x.2019.1614122
- Yu, F. (2018). Particle breakage in triaxial shear of a coral sand. *Soils Found.* 58, 866–880. doi:10.1016/j.sandf.2018.04.001
- Yue, Q., Qingshan, M., Ren, W., Siqian, H., and Yuting, Z. (2017). Model experimental research on uplift single pile in calcareous sand of South China Sea. *Mar. Georesources Geotechnol.* 35 (5), 653–660. doi:10.1080/1064119x.2016.1215362
- Zhang, J., and Luo, M. (2020). Dilatancy and critical state of calcareous sand incorporating particle breakage. *Int. J. Geomechanics* 20, 04020030. doi:10.1061/(asce)gm.1943-5622.0001637
- Zhou, X. Z., Chen, Y. M., Li, W. W., and Liu, H. L. (2019). Monotonic and cyclic behaviors of loose anisotropically consolidated calcareous sand in torsional shear tests. *Mar. Georesources Geotechnol.* 37 (4), 438–451. doi:10.1080/1064119x.2018.1449274





## OPEN ACCESS

## EDITED BY

Xuelong Li,  
Shandong University of Science and  
Technology, China

## REVIEWED BY

Zihan Liu,  
The University of Hong Kong, Hong Kong  
SAR, China  
Xinxin Fang,  
China Coal Research Institute, China

## \*CORRESPONDENCE

Mingming He,  
✉ hemingming@xaut.edu.cn

## SPECIALTY SECTION

This article was submitted to  
Environmental Informatics  
and Remote Sensing,  
a section of the journal  
Frontiers in Earth Science

RECEIVED 20 February 2023

ACCEPTED 17 March 2023

PUBLISHED 13 April 2023

## CITATION

Zhang Y, Zhao J, Xiao Z, Gao Y, Cui S,  
Cheng D, He M, Fang C, Xue H and Zhao Y  
(2023), Estimation of mechanics  
parameters of rock in consideration of  
confining pressure using monitoring  
while drilling data.  
*Front. Earth Sci.* 11:1169712.  
doi: 10.3389/feart.2023.1169712

## COPYRIGHT

© 2023 Zhang, Zhao, Xiao, Gao, Cui,  
Cheng, He, Fang, Xue and Zhao. This is an  
open-access article distributed under the  
terms of the [Creative Commons  
Attribution License \(CC BY\)](https://creativecommons.org/licenses/by/4.0/). The use,  
distribution or reproduction in other  
forums is permitted, provided the original  
author(s) and the copyright owner(s) are  
credited and that the original publication  
in this journal is cited, in accordance with  
accepted academic practice. No use,  
distribution or reproduction is permitted  
which does not comply with these terms.

# Estimation of mechanics parameters of rock in consideration of confining pressure using monitoring while drilling data

Yonghao Zhang<sup>1</sup>, Jianbin Zhao<sup>1</sup>, Zhanshan Xiao<sup>1</sup>, Yanwu Gao<sup>1</sup>,  
Shitao Cui<sup>1</sup>, Daojie Cheng<sup>1</sup>, Mingming He<sup>2\*</sup>, Chaoqiang Fang<sup>1</sup>,  
Haifang Xue<sup>3</sup> and Ying Zhao<sup>4</sup>

<sup>1</sup>Geological Research Institute, China National Logging Corporation, Beijing, China, <sup>2</sup>State Key Laboratory of Eco-hydraulics in Northwest Arid Region, Xi'an University of Technology, Xi'an, China, <sup>3</sup>Qinghai Xihu Expressway Management Co., Ltd., Xining, China, <sup>4</sup>School of Highway, Chang'an University, Xi'an, China

During the drilling process, high-strength rock can lead to various issues such as drilling suppression, bit wear, and increased operational costs. To ensure safe and efficient drilling operations, it is crucial to accurately predict the strength parameters of the rock and recommend modifications to operational procedures. This paper proposes a low-cost and fast measurement method for predicting the strength parameters of rock in the field. To evaluate the effectiveness of this method, a drilling process monitoring experiment was conducted on sandstone, limestone, and granite. The experiment studied the effect of confining pressure on the response of cutting with an impregnated diamond bit. By analyzing the relationship between the thrust force, torque force, and penetration depth under different confining pressures, the researchers developed an analytical model for drilling that considers confining pressure, compressed crushed zone, and bit geometry. The results show that the confining pressure has a significant effect on the cutting response. As the confining pressure increases, the thrust force, torque force, and penetration depth at the cutting point also increase. Furthermore, a new measurement method was proposed to determine the strength parameters, such as cohesion, internal friction angle, and unconfined compressive strength. The estimated strength parameters for the three rock types using the drilling method were in good agreement with those of the standard laboratory test, with an error range of 10%. This method of estimating rock strength parameters is

**Abbreviations:**  $\alpha$ , rake angle of drill bit;  $A$ , cutting area of the drilling bit;  $C$ , cohesion of intact rock;  $F_t$ , tangential force;  $F_n$ , thrust force;  $F_n^c$ , normal components of the cutting force;  $F_t^c$ , tangential components of the cutting force;  $F_w^c$ , normal components of the friction force;  $F_w$ , tangential components of the friction force in the front end of diamond particle;  $F^b$ , normal force in the back end of diamond particle;  $F^f$ , frictional force between the diamond particle and rock sides;  $k$ , number of drill bits;  $P_f$ , confining pressure;  $P_m$ , fluid column pressure in the drilling hole;  $v$ , drilling speed;  $w$ , rotation speed;  $\tau_0$ , shear stress of the crushed zone;  $\sigma_0$ , principal stress of the crushed zone;  $\phi'$ , friction angle of the crushed zone;  $\sigma_2$ , normal stress in the fracture surface;  $\tau_2$ , shear stress in the fracture surface;  $\phi$ , internal friction angle of intact rock;  $\theta$ , rock-bit contact angle;  $\psi$ , propagating angle of the crushed zone;  $\tau$ , total shear stress of rock fragment;  $\sigma$ , total normal stress of rock fragment;  $\beta$ , angle of shear plane in the back of the blade;  $\sigma_1$ , normal stress caused by the ground stress;  $\tau_2$ , shear stress caused by the ground stress.



a practical tool for engineers. It can continuously and quickly obtain the drilling parameters of *in-situ* rocks.

#### KEYWORDS

advanced prediction, analytical model, rock strength parameters, drilling process monitoring, confining pressure

## 1 Introduction

The projected economic growth is expected to drive global energy demands to reach 20,679 million tons of oil equivalent by 2040, with 28% coming from oil and 23% from natural gas (Chong et al., 2016; Yang et al., 2019). The supply of the global energy market is heavily influenced by hydrocarbon resources, and the development of drilling technology has enabled deeper hydrocarbon resources to be explored to meet the growing energy demand worldwide (Li et al., 2016; Vedachalam et al., 2016). However, as boreholes become deeper, drilling efficiency tends to decrease, posing significant challenges that need to be addressed to promote drilling efficiency. The mechanical properties of the rock, such as strength parameters, significantly affect drilling efficiency, and high-strength rock during the drilling process can lead to drilling suppression, drilling bit wear, and high operational costs. To avoid such adverse effects, accurately predicting the strength parameters of rock during the drilling process and recommending effective modifications to operational procedures are essential for maintaining safer and more efficient drilling operations.

The unconfined compressive strength (UCS) test, which requires well-prepared samples, is time-consuming, costly, and a destructive procedure, making it challenging to determine the strength parameters of rock in the field (Kalantari et al., 2018). To overcome these limitations, indirect methods such as the point load test, scratch test, Schmidt hammer test, and block punch test have been developed for UCS determination (Palassi and Emami, 2014; Naeimipour et al., 2018). However, these methods have some limitations when it comes to evaluating the complex field conditions and related effects on field rock (Palassi and Emami, 2014). They provide only limited information about rock and may not accurately reflect the properties of field rock (Richard et al., 2012). In recent years, drilling has emerged as a promising technique for measuring rock strength parameters in the field. This method allows for fast and continuous measurement of field rock strength during the drilling process. Moreover, it is applied as a quasi-nondestructive field method and easily facilitated because of non-sampling and simple movement (Kalantari et al., 2018). Researchers have developed several methods for estimating rock strength based on forces limit equilibrium and energy equilibrium (Merchant, 1945; Evans, 1962; Nishimatsu, 1972; Roxborough and Philips, 1975; Nakajima and Kinoshita, 1979; Hoover and Middleton, 1981; Detournay and Defourny, 1992; Wojtanowicz and Kuru, 1993; Gerbaud et al., 2006; Franca, 2010; Hareland, 2010; Chiaia et al., 2013). However, except for Nakajima and Kinoshita's model and Gerbaud' model, the crushed zone has not been considered in the proposed relations between the drilling data and rock strength. To address this issue, Kalantari et al. (2018) developed an analytical model to estimate rock strength parameters using a T-shaped drag

bit. Several other researchers (Karasawa et al., 2002a; b; Ohno et al., 2004; Bingham, 1964; Wolcott and Bordelon, 1993; Hoberock and Bratcher, 1996; Burgess and Less, 1985; Pessier and Fear, 1992; Warren, 1987; Lia and Itakura, 2012) have used various approaches to determine the UCS of rock during the drilling process based on the specific energy by Teale (1965). Analytical models based on energy equilibrium can easily resolve the problem of the crushed zone during the drilling process. However, the explicit relationship between the confining pressure and the response of drilling in the field has not been well-established, particularly in the deep rock mass.

In this study, an experiment was conducted to monitor the drilling process of sandstone, limestone, and granite, in order to investigate how the confining pressure affects the response of cutting with an impregnated diamond bit. The relationships between thrust force, torque force, and penetration depth were analyzed for different confining pressures. An analytical model was developed to take into account the effects of gravity, the compressed crushed zone, and the bit geometry on drilling. Furthermore, an advanced method was proposed to predict the cohesion, internal friction angle, and unconfined compressive strength of sandstone, limestone, and granite. The resulting unconfined compressive strength values obtained from the proposed method were compared with test results obtained in the laboratory.

## 2 Model

During the drilling process monitoring, the bottom of drilling hole is affected by the confining pressure and fluid column pressure in the drilling hole as well as the applied force of the bit. In the drilling process, due to the continuous downward and forward movements of diamond particle in impregnated diamond bit, the crushed zone in front of the diamond particle is formed as shown in Figure 1A. For a diamond particle, assume that the diamond particle is a pentahedron as shown in Figure 1B. When the rock on both sides of the diamond particle occurs shear failure, the geometry and mechanism of the acting force of bit is shown in Figure 1. In the failure surface, the shear stress and normal stress caused by the ground stress, pore pressure and fluid column pressure can be expressed as

$$\tau_1 = \frac{1}{2}(P_f - P_m) \sin 2\beta \quad (1)$$

$$\sigma_1 = \frac{1}{2}(P_f + P_m) - \frac{1}{2}(P_f - P_m) \cos 2\beta \quad (2)$$

Where  $\beta$  is the angle of shear plane in the back of the blade,  $P_f$  is the confining pressure,  $P_m$  is the fluid column pressure in the drilling hole.



$$\tau - \sigma \tan \varphi = \frac{F^h}{A} \cos(a + \beta) + \frac{1}{2}(P_f - P_m) \sin 2\beta - \frac{F^h}{A} \sin(a + \beta) \tan \varphi - \frac{1}{2}(P_f + P_m) \tan \varphi + \frac{1}{2}(P_f - P_m) \cos 2\beta \tan \varphi \quad (15)$$

If  $\tau - \sigma \tan \varphi$  is replaced with the cohesion  $C$  in Eq. 14, and after some algebraic manipulation in Eq. 15, the normal force  $F^h$  in the back end of diamond particle can be calculated as

$$F^h = \frac{[C - \frac{1}{2}(P_f - P_m) \sin 2\beta + \frac{1}{2}(P_f + P_m) \tan \varphi - \frac{1}{2}(P_f - P_m) \cos 2\beta \tan \varphi] A \cos \varphi}{\cos(a + \varphi + \beta) \cos \beta} \quad (16)$$

To obtain the minimum value of  $F^h$ , the value of  $\beta$  can be calculated as

$$\frac{\partial F^h}{\partial \beta} = 0 \quad (17)$$

$$\beta = \frac{\pi}{4} - \left( \frac{a + \varphi}{2} \right) \quad (18)$$

The minimum value of  $F^h$  can be calculated as

$$F^h = \frac{[2C - (P_f - P_m) \cos(a + \varphi) + (P_f + P_m) \tan \varphi - (P_f - P_m) \sin(a + \varphi) \tan \varphi] A \cos \varphi}{\cos(a + \varphi)} \quad (19)$$

## 2.2 No. 2 crushed zone

Now, considering the No. 2 crushed zone (see Figure 1B), the tangential and normal components of the cutting force can be calculated as

$$F_t^c = A\sigma_o + A\tau_o \tan a \quad (20)$$

$$F_n^c = A\sigma_o \tan a + A\tau_o \quad (21)$$

After some algebraic manipulation, the shear strength  $\tau_o$  and hydrostatic pressure  $\sigma_o$  in the No. 2 crushed zone can be obtained from Eqs 20, 21:

$$\sigma_o = \frac{F_t^c - \tan F_n^c}{A - A \tan^2 a} \quad (22)$$

$$\tau_o = \frac{F_n^c - F_t^c \tan a}{A - A \tan^2 a} \quad (23)$$

Shear tractions,  $\tau'$ , and normal tractions,  $\sigma'$ , can be calculated as

$$\sigma' = \sigma_o \sin^2 \psi - \tau_o \cos \psi \sin \psi \quad (24)$$

$$\tau' = \sigma_o \cos \psi \sin \psi + \tau_o \sin^2 \psi \quad (25)$$

$\psi$  is the angle of the cutting plane in front of the blade. Considering the real stress characteristics of rock at the bottom of drilling core, the total normal stress and total shear stress in the fracture surface can be calculated as

$$\sigma = \sigma_1 + \sigma' \quad (26)$$

$$\tau = \tau_1 + \tau' \quad (27)$$

The values of  $\tau$  and  $\sigma$  from Eqs 26, 27 are assigned in the Mohr-Coulomb criterion of rock (Eq. 14), then we have

$$\begin{aligned} \sigma_o \cos \psi \sin \psi + \tau_o \sin^2 \psi + \frac{1}{2}(P_f - P_m) \sin 2\psi \\ = \sigma_o \sin^2 \psi - \tau_o \cos \psi \sin \psi \end{aligned}$$

$$+ \frac{1}{2}(P_f + P_m) - \frac{1}{2}(P_f - P_m) \cos 2\psi - P_p + C \quad (28)$$

According to Eqs 7, 28, the cohesion can be obtained as

$$\begin{aligned} C = \sigma_o [\cos \psi \sin \psi + \tan \varphi' \sin^2 \psi - \sin^2 \psi \tan \varphi + \tan \varphi' \cos \psi \sin \psi \tan \varphi] \\ + \frac{1}{2}(P_f - P_m) \sin 2\psi - \frac{1}{2}(P_f + P_m) \tan \varphi \\ + \frac{1}{2}(P_f - P_m) \cos 2\psi \tan \varphi \end{aligned} \quad (29)$$

Equation 29 is derived in respect to  $\psi$  to obtain the minimum value of  $\sigma_o$ . Then the value of  $\psi$  can be calculated as

$$\frac{\partial \sigma_o}{\partial \psi} = 0 \quad (30)$$

$$\psi = \frac{\pi}{4} - \left( \frac{\varphi' - \varphi}{2} \right) \quad (31)$$

The minimum values of  $\sigma_o$  and  $\tau_o$  are obtained as

$$\sigma_o = \frac{[2C - (P_f - P_m) \sin(\varphi' - \varphi) + (P_f + P_m) \tan \varphi - (P_f - P_m) \cos(\varphi' - \varphi) \tan \varphi] \cos(\varphi' - \varphi)}{(1 + \tan \varphi \tan \varphi') [\cos(\varphi' - \varphi) - \sin^2(\varphi' - \varphi) + \sin(\varphi' - \varphi)]} \quad (32)$$

$$\tau_o = \frac{[2C - (P_f - P_m) \sin(\varphi' - \varphi) + (P_f + P_m) \tan \varphi - (P_f - P_m) \cos(\varphi' - \varphi) \tan \varphi] \cos(\varphi' - \varphi) \tan \varphi'}{(1 + \tan \varphi \tan \varphi') [\cos(\varphi' - \varphi) - \sin^2(\varphi' - \varphi) + \sin(\varphi' - \varphi)]} \quad (33)$$

## 2.3 Relationship of $F_t$ and $F_n$

Now, considering the normal and tangential acting forces in diamond particle as well as Eqs 3–6, 20, 21, the tangential forces  $F_t$  and normal forces  $F_n$  can be obtained as

$$F_t = A\sigma_o + A\sigma_o \tan \varphi' \tan a + F_n^w \tan \theta - F^h \cos a + 2F^h \tan \theta \quad (34)$$

$$F_n = A\sigma_o \tan a + A\sigma_o \tan \varphi' + F_n^w + 3F^h \sin a \quad (35)$$

After some algebraic manipulation from Eqs 34, 35, the relationship between the tangential forces  $F_t$  and normal forces  $F_n$  can be obtained as

$$F_t = F_n \tan \theta + A\sigma_o [1 + \tan \varphi' \tan a - (\tan a + \tan \varphi') \tan \theta] + 2F^h \tan \theta - 3F^h \sin a \tan \theta \quad (36)$$

Where  $A=Bh/2$ ,  $B$  is the shape parameters of the drill bit.  $F^h$  and  $\sigma_o$  can be calculated using Eqs 19, 32, respectively. For an impregnated diamond bit, when penetration rate and rotation speed are  $v$  and  $w$ , respectively, the depth of penetration per rotation  $h$  can be calculated as (Kalantari et al., 2019)

$$h = \frac{2v}{60kw} \quad (37)$$

Where  $k$  is the number of drill bits.

Equation 36 shows that the normal force  $F_n$  and tangential force  $F_t$  are affected by cutting and friction during drilling process that occurs simultaneously, and they are dependent on each other. The slope of this equation (Eq. 36) is dependent on the contact friction angle between the diamond particle end wearing face. Many drilling experimental results from researchers also show a linear relationship between the normal

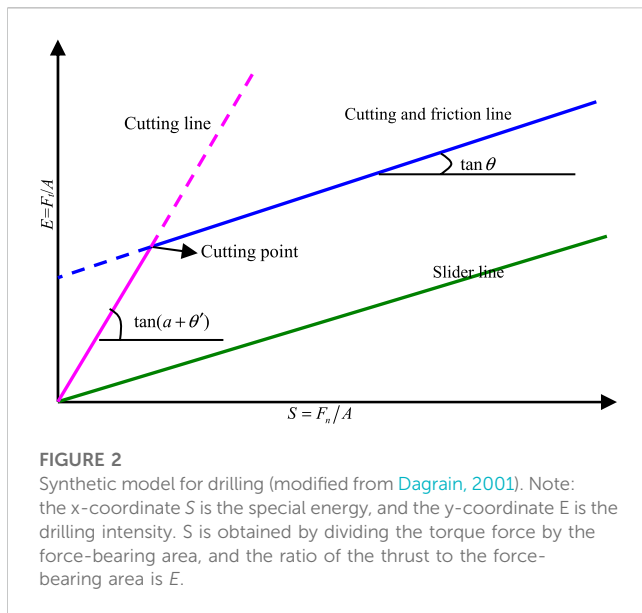


FIGURE 2

Synthetic model for drilling (modified from Dagrain, 2001). Note: the x-coordinate  $S$  is the special energy, and the y-coordinate  $E$  is the drilling intensity.  $S$  is obtained by dividing the torque force by the force-bearing area, and the ratio of the thrust to the force-bearing area is  $E$ .

and tangential acting forces during the rock penetration process (Teale, 1965; Detournay and Defourny, 1992; Kalantari et al., 2018; 2019). The intersection of the two paths was mostly located in the cutting point, including cutting and friction (Dagrain, 2001) (see Figure 2). When the friction and cutting is performed simultaneously including the pure cutting and the friction between the diamond particle and rock sides, the linear of  $F_t$ - $F_n$  in the impregnated diamond bit represents the theoretically pure cutting for  $F_n=0$  (see Eq. 36).

For low thrust force (below the cutting point), the value of the friction force  $F_t^w$  between the diamond particle and rock bottom sides is negligible. The normal force of the impregnated diamond bit is transferred to the compressed zone. In this case, Eqs 34, 35 can be rewritten as

$$F_t = A\sigma_o + A\sigma_o \tan \varphi' \tan a - F^h \cos a + 2F^h \tan \theta \quad (38)$$

$$F_n = A\sigma_o \tan a + A\sigma_o \tan \varphi' + 3F^h \sin a \quad (39)$$

By substituting Eqs 32, 33 into Eqs 38, 39, the axial force  $F_n$  and tangential force  $F_t$  can be calculated as

$$F_t = \frac{A[2C - (P_f - P_m) \sin(\varphi' - \varphi) + (P_f + P_m) \tan \varphi - (P_f - P_m) \cos(\varphi' - \varphi) \tan \varphi] (1 + \tan \varphi' \tan a) \cos(\varphi' - \varphi)}{(1 + \tan \varphi \tan \varphi') [\cos(\varphi' - \varphi) - \sin^2(\varphi' - \varphi) + \sin(\varphi' - \varphi)]} + \frac{A[2C - (P_f - P_m) \cos(a + \varphi) + (P_f + P_m) \tan \varphi - (P_f - P_m) \sin(a + \varphi) \tan \varphi] \cos \varphi (2 \tan \theta - \cos a)}{\cos(a + \varphi)} \quad (40)$$

$$F_n = \frac{A[2C - (P_f - P_m) \sin(\varphi' - \varphi) + (P_f + P_m) \tan \varphi - (P_f - P_m) \cos(\varphi' - \varphi) \tan \varphi] (\tan a + \tan \varphi') \cos(\varphi' - \varphi)}{(1 + \tan \varphi \tan \varphi') [\cos(\varphi' - \varphi) - \sin^2(\varphi' - \varphi) + \sin(\varphi' - \varphi)]} + \frac{3A[2C - (P_f - P_m) \cos(a + \varphi) + (P_f + P_m) \tan \varphi - (P_f - P_m) \sin(a + \varphi) \tan \varphi] \cos \varphi \sin a}{\cos(a + \varphi)} \quad (41)$$

The linear of  $F_t$ - $A$  and  $F_n$ - $A$  are dependent on the contact friction ( $\theta$ ) in the side of diamond particle, frictional angle ( $\varphi'$ ) between the intact rock and compressed crushed zone, the rake angle ( $a$ ) of the diamond particle, and internal friction angle of intact rock ( $\varphi$ ). The value of  $F_t/F_n$  is a constant as follows (Kalantari et al., 2018; 2019)

$$\frac{F_t}{F_n} = \frac{1}{\tan(a + \theta')} = \text{constant} \quad (42)$$

For high thrust force (beyond the cutting point), the relationship between the normal force  $F_n$  and tangential force  $F_t$  is dependent of the contact friction ( $\theta$ ) in the side of diamond particle, frictional angle ( $\varphi'$ ), internal friction angle of intact rock ( $\varphi$ ), and the rake angle ( $a$ ) of the diamond particle. The normal force of diamond particle from the impregnated diamond bit is transferred to rock due to the created cross-sectional area. Hence, using Eq. 42, the friction appears in drilling with the impregnated diamond bit. In the diamond particle, the friction between the diamond particle end and side wearing face and rock, acting as a resistant force, plays an important part in the cutting process.

According to Eqs 41, 42, for high thrust force (beyond the cutting point) the contact friction ( $\theta$ ) in the side of diamond particle, frictional angle ( $\varphi'$ ), and the rake angle of the diamond particle ( $a$ ) are dominant factors. For the diamond core bit, the shape of each diamond particle impregnated in the bit is irregular, resulting in the difficulty and limitation of the measurement of the rake angle of each diamond particle. For a diamond core bit (see Figure 1A), due to the irregular shape of diamond grains in bit, we cannot accurately measure the rake angle ( $a$ ) of the diamond particle, and assume that it is an unknown parameter. We can use the following five steps to predict the strength parameters of rock:

- (1) According to Eq. 42, we can calculate the value of  $a + \theta'$  using the experimental results of the linear  $F_t$ - $F_n$  relation for low thrust force (below the cutting point). According to Eq. 36, the value of the contact friction ( $\theta$ ) using the experimental results of the linear  $F_t$ - $F_n$  relation for low thrust force. The contact friction angle  $\theta'$  of the diamond particle side wearing face and the contact friction angle  $\theta$  are almost the same in cutting and friction process (Kalantari et al., 2018). Then, the rake angle ( $a$ ) can be obtained according to Eqs 36, 42.
- (2) The slope of linear Eqs 39, 41, 42 in low thrust force are an important factor. Using the obtained rake angle ( $a$ ) and the contact friction ( $\theta'$ ) from the slope of  $F_t$ - $F_n$  curve in high thrust force, after some algebraic manipulation from Eqs 24, 25, the value of  $\varphi'$  can be calculated as

$$\varphi' = \arctan \frac{\tan(a + \theta') - \tan a}{1 - \tan a \tan(a + \theta')} \quad (43)$$

- (3) Using the estimated friction angle ( $\varphi'$ ) from Eq. 43, the internal friction angle ( $\varphi$ ) of rock can be calculated as (Kerisel, 1975; Gerbaud et al., 2006)

$$\varphi = \tan^{-1} \left( \frac{2}{\pi} \tan \varphi' \right) \quad (44)$$

- (4) These slopes in Eq. 41 can be obtained from the plotted drilling data ( $F_n$ - $h$ ) in low thrust force (below the cutting point) in the impregnated diamond bit. Using the parameters ( $\theta$ ,  $\varphi'$ ,  $\varphi$ , and  $a$ ) obtained from the steps (1)~(3) and the slope of  $F_n$ - $h$ , the cohesion  $C$  can be calculated according to Eq. 41. By utilizing the slope values from Eqs 36, 41, 42, along with Eqs 43, 44, we can accurately determine the values of five parameters ( $\theta$ ,  $\varphi'$ ,  $\varphi$ ,  $a$ , and  $C$ )

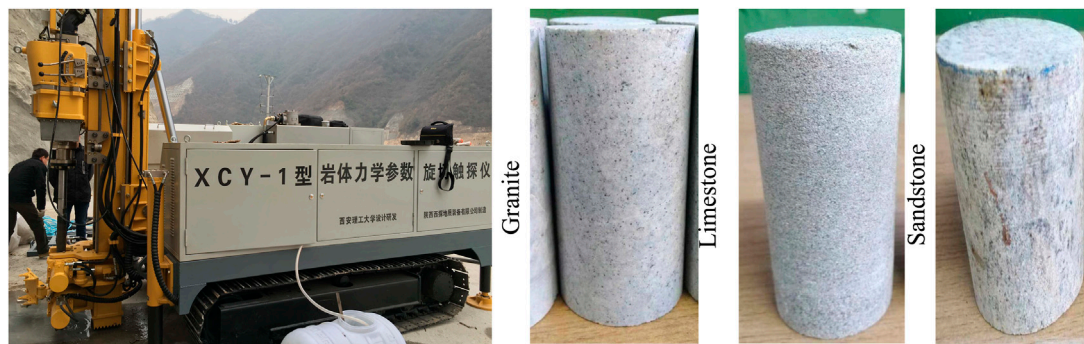


**FIGURE 3**  
An overview of the drilling process monitoring apparatus (DPM) and part of drilled rock sample.

- (5) Now using the obtained  $C$  and  $\varphi$  from the proposed method, the unconfined compressive strength of rock ( $R_c$ ) is calculated as (Kalantari et al., 2018)

$$R_c = \frac{2C \cos \varphi}{1 - \sin \varphi} \quad (45)$$

Where  $R_c$  is the unconfined compressive strength of intact rock.

### 3 Drilling equipment

A drilling process monitoring apparatus, known as the DPM (Drilling Monitoring Process) (see Figure 3), has been developed to predict the strength of the rock in the field (He et al., 2019). With an inner diameter of 60 mm, outer diameter of 70 mm, and drilling depth of 50 m, the DPM is capable of continuous measurement and recording of drilling operational data, including thrust force, torque, penetration rate, rotation speed, drilling depth, and penetration depth per rotation. As drilling depth increases, the DPM automatically saves the drilling operational data in an Excel file. The DPM has a maximum collection ability of 500 data points per second, enabling accurate storage of several hundred sets of drilling data. The digital drilling experimental equipment can provide the maximum power of 1050 W and the maximum rotation speed of 800 r/min. In this experiment, the control parameters are the rotation speed ( $\omega$ ) and the penetration rate ( $v$ ), while the thrust force and torque are obtained as the drilling response. An impregnated diamond bit is used as the drill bit in the DPM, which allows for drilling in the field with high accuracy and precision.

### 4 Discussion

After conducting a study, it is essential for authors to discuss the results and their interpretation based on previous studies and working hypotheses. The discussion should include the implications of the findings in the broader context and explore their significance.

In this study, a drilling test using an impregnated diamond bit with an outer diameter of 70 mm and an inner diameter of 60 mm is performed, as depicted in Figure 1A. The drilling parameters, including the penetration rate and rotation speed, are varied for each rock type. The penetration rates for limestone, granite, marble, and sandstone are set in the range of 0.1–1.2 mm/min, and the rotation speeds are set in the range of 200–600 rpm for each rock type. The experiments are carried out on hard, medium, and weak rocks, such as granite, limestone, and sandstone. The cohesion and internal friction angle of each rock type are measured in the laboratory, following the ISRM standard.

Figure 4 displays the plots of the relationship between thrust force and penetration depth per rotation for sandstone, limestone, and granite under different confining pressures. Similarly, Figure 5 illustrates the relationship between torque force and penetration depth per rotation for each rock type under varying confining pressures. In the cutting process and the cutting and friction process, the thrust and torque forces linearly increase with the penetration depth per rotation. When low thrust and torque forces are applied on three rock types, the thrust and torque forces gradually increase with the depth of penetration per rotation. At a critical value defined as the cutting point by Lhomme (1999), the forces reach a maximum limit and cease to increase with further penetration depth per rotation. At shallow penetration depths, the friction force between the diamond particle and rock bottom sides is negligible and any increase in cutting force is due to the increase of penetration depth per rotation before it reaches the critical penetration depth (Detournay et al., 2008; Zhou and Detournay, 2014). Beyond the critical value of the penetration depth, the normal component of frictional force reaches a stable value and a limited value of the effective contact stress has also occurred (Rostamsowlat, 2018). In this stage, the incremental cutting response is governed by the pure cutting of the diamond particle. These findings from the impregnated diamond bit are consistent with those of other types of bits (Adachi, 1996; Dagrain, 2006; Detournay et al., 2008; Rostamsowlat et al., 2018).

In addition, the relationship between the thrust force, torque force, and critical penetration depth at the cutting point is affected by the confining pressure ( $P_f$ ), as shown in Table 1. The confining



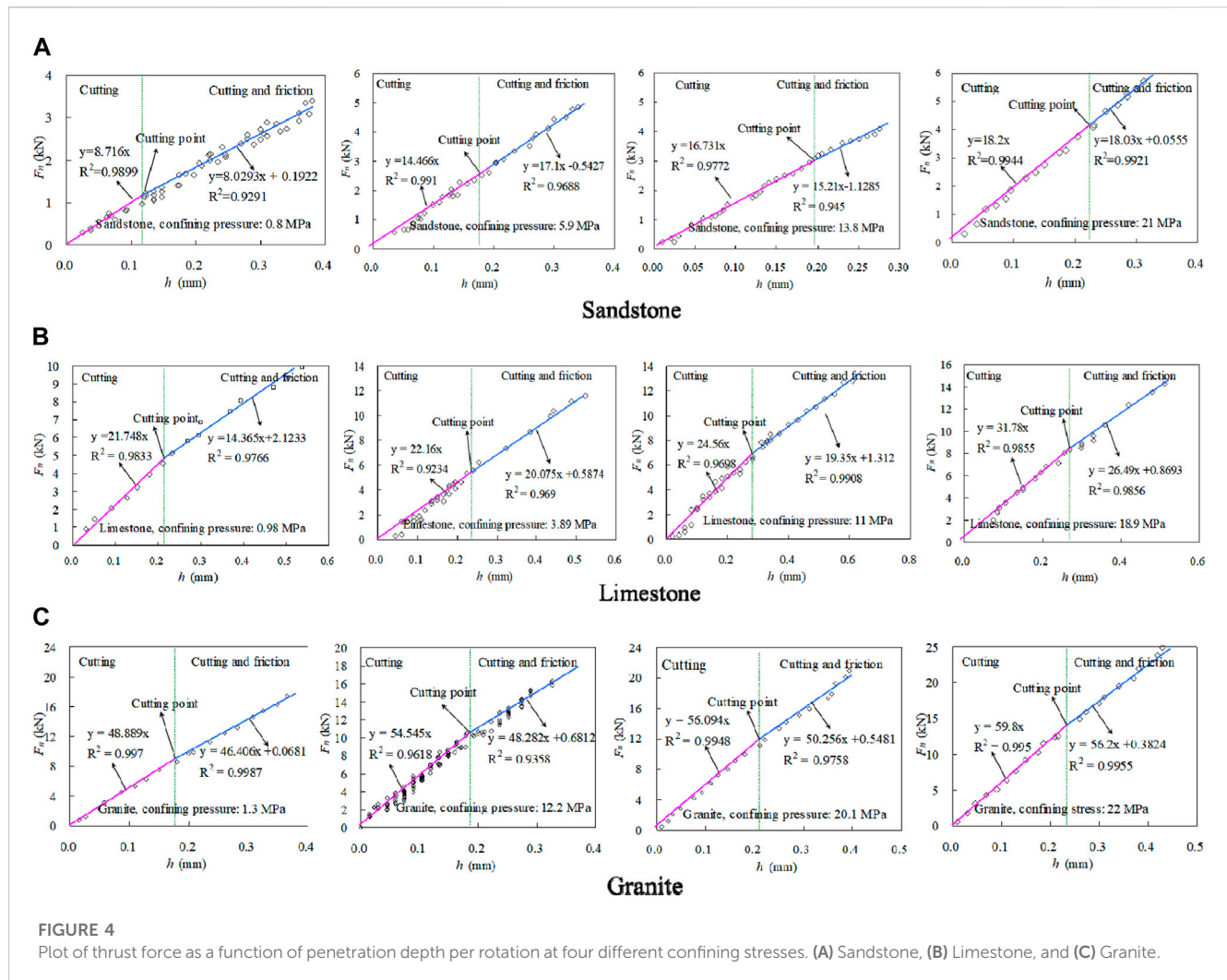


FIGURE 4

Plot of thrust force as a function of penetration depth per rotation at four different confining stresses. (A) Sandstone, (B) Limestone, and (C) Granite.

pressure was varied between 0.8 MPa and 22 MPa, resulting in critical penetration depth ranges of 0.123–0.228 mm for sandstone, 0.233–0.255 mm for limestone, and 0.181–0.215 mm for granite. The cutting point for each rock type is influenced by the confining pressure during the drilling process, which can be seen in the slope variation of the  $F_n \sim h$  and  $F_t \sim h$  relationships in the cutting process and the cutting and friction process. The study's findings indicate that the confining pressure ( $P_f$ ) has a significant impact on the cutting response of the impregnated diamond bit in both cutting and cutting and friction regimes, as illustrated in Figures 4, 5. The confining pressure can affect the elastic and elastoplastic regimes of frictional contact, depending on the two regimes of frictional contact (Rostamsowlat et al., 2018).

Figure 6 depicts the torque force versus thrust force plots for sandstone, limestone, and granite. The cutting point, which depends on the predominance of the cutting process, varies with different confining pressures in the  $F_t/F_n$  relation of the impregnated diamond bit. The data points of the  $F_t/F_n$  relation follow a linear path with a low slope in the friction process, while points on another path follow the same path as the  $F_t/F_n$  linear relation if the drilling is dominated by the cutting process (Dagrain, 2001). For the impregnated diamond bit, the data obtained between these two

paths of the  $F_t/F_n$  linear relation represent a combination of friction and cutting processes, as shown in Table 1. Most of the data points from the two paths were located in the cutting point under different confining pressures. It is evident that the role of the cutting process and friction process depends on the confining pressure. In other words, the slope of the  $F_t \sim F_n$  linear relation varies with the confining pressure in the drilling process. As the confining pressure increases, the penetration depth increases with high thrust force and cutting force, which are provided simultaneously.

During the drilling process using an impregnated diamond bit, the diamond particles on the bit penetrate into the rock and create a penetration depth. As the bit rotates, it cuts through the rock, while the slope of the  $F_t \sim F_n$  linear equation is determined by the contact friction and the intercept value is dependent on the penetration depth. This relationship is affected by various factors such as the crushed zone, rock properties, bit geometric parameters, and confining pressure, as demonstrated in Eq. 36. Through a least-squares regression, the correlation between the thrust force and torque force in the cutting and friction process can be plotted as a linear curve, as illustrated in Figure 6; Table 1. The correlation coefficients of the curves are almost always greater than 0.95. Consequently, the slopes of the trend lines can be determined,

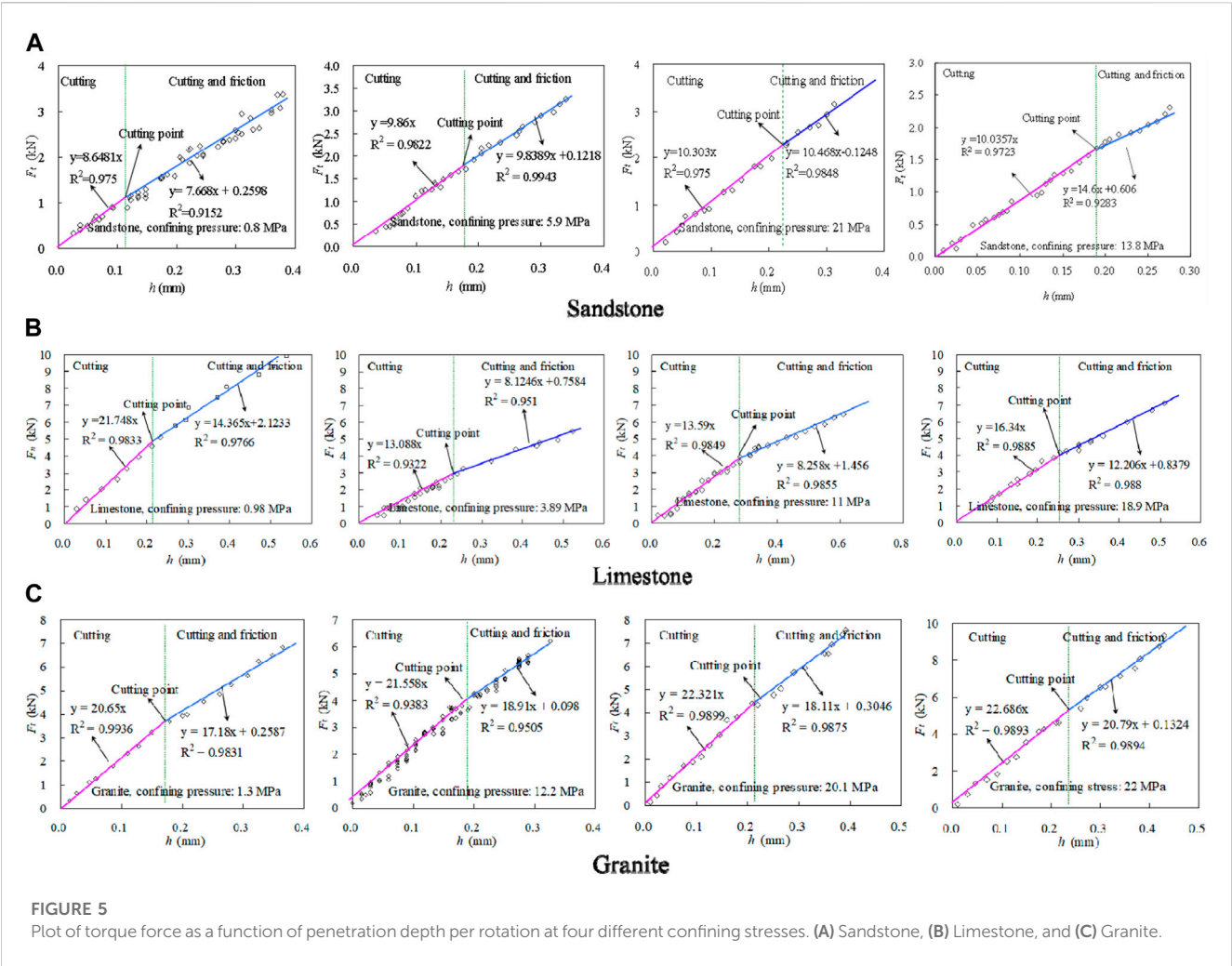


TABLE 1 Rocks parameters obtained from drilling tests.

Rock types	$P_f$ (MPa)	$\tan\theta$	$1/\tan(a+\theta')$	$a$ (°)	Slope of Eq. 41	Cutting point			$\varphi$ (°)	$C$ (MPa)	$R_c$ (MPa)
						$F_n$	$F_t$	$h$			
sandstone	0.8	0.810	0.980	5.79	8.7	1.16	1.06	0.123	33.1	6.2	22.7
	5.9	0.578	0.702	5.04	14.5	2.51	1.68	0.184	44.2	8.6	40.8
	13.8	0.529	0.560	1.38	16.7	2.95	1.71	0.192	49.5	9.9	54.0
	21	0.530	0.550	0.86	18.3	3.95	2.28	0.228	49.8	11.4	62.2
Limestone	0.98	0.530	0.560	1.32	21.7	5.12	2.84	0.233	49.5	11.4	61.9
	3.89	0.512	0.551	1.72	22.6	5.56	2.95	0.241	50.3	11.8	65.2
	11	0.486	0.540	2.46	24.6	6.47	3.94	0.248	51.4	12.8	73.2
	18.9	0.460	0.510	2.29	31.0	8.05	4.18	0.255	53.0	15.8	94.8
Granite	1.3	0.386	0.422	1.78	48.9	9.85	3.98	0.181	58.1	18.9	132.6
	12.2	0.377	0.394	0.86	54.5	10.69	4.21	0.193	59.1	21.0	151.9
	20.1	0.373	0.383	0.52	55.1	11.22	4.42	0.206	59.5	21.4	156.6
	22	0.371	0.380	0.46	59.8	12.51	4.61	0.215	59.6	23.1	169.9

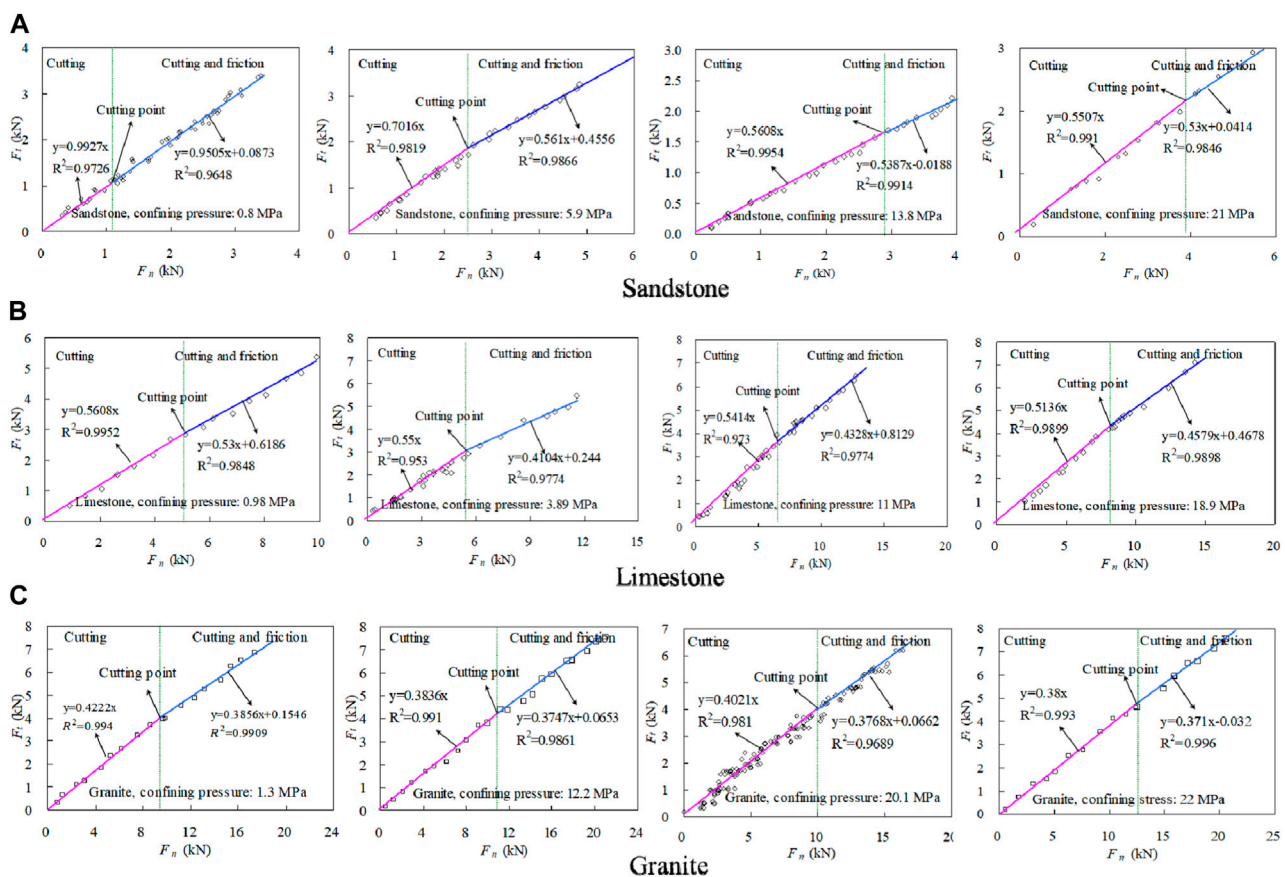


FIGURE 6

Plot of torque force as a function of thrust force at four different confining stresses. (A) Sandstone, (B) Limestone, and (C) Granite.

with one slope attributed to the cutting process and the other slope representing the cutting and friction process. Furthermore, the slopes of the trend lines from the cutting and friction process exhibit higher values at relatively low confining pressure. The obtained slopes of the  $F_t \sim F_n$  linear curves for both cutting and cutting with friction processes, as shown in Figure 6, can be used to determine the rock parameters through the established model. This model yields the frictional angle, the dilation angle, and the internal friction angle of the rocks. Figures 4, 5 depict significant variations in torque and thrust forces concerning the depth of penetration during the cutting process. Through a least-squares regression of the torque and thrust forces *versus* the depth of penetration per rotation for both cutting and friction processes, a linear curve is obtained for the diamond core bit, as shown in Figures 4, 5, with correlation coefficients ( $R^2$ ) greater than 0.95, satisfying Eqs 36, 41. Moreover, the obtained slopes of the linear  $F_n \sim h$  curves during the drilling process can be used to calculate the cohesion of the rock, as presented in Table 1. The unconfined compressive strength of the rock ( $R_c$ ) can then be obtained from Eq. 45, also shown in Table 1. The drilling tests under different confining pressures have yielded results for the strength of sandstone, limestone, and granite, which agree well with those from standard tests, with an error within 10%, as illustrated in Figure 7.

The irregular shape of diamond particles in impregnated diamond bits makes it challenging to determine the rake angle of the particles. However, the slope of the  $F_t/F_n$  linear curves for cutting and friction processes can be used to calculate the rake angle  $\alpha$  for the three types of rock using Eqs 36, 42. Table 1 shows the slopes of trend lines for cutting and friction processes in sandstone, limestone, and granite. The side wearing face of the diamond particles has nearly the same values of and during cutting and friction processes (Li et al., 2016). By replacing with in Eqs 36, 42, the rake angle  $\alpha$  can be estimated, which is considered negligible for the estimated results (Bingham, 1964; Roxborough and Phillips, 1975; Hibb and Flom, 1978; Karasawa and Misawa, 1992; Li et al., 1993; Richard et al., 1998; Sinor et al., 1998). Using Eqs 36, 41–45, the rock strength can be estimated. The parameters and confining pressure are related to the rock strength. The effect of parameter on the estimated cohesion is negligible at low confining pressure when the range of is  $30^\circ \sim 70^\circ$ , which is close to the internal friction angles of all natural rocks, as shown in Figure 8. However, for high confining pressure ( $P_f > 30$  MPa) and low range, the effect of parameter on the estimated cohesion must be considered. The proposed method can practically estimate the strength parameters of rock, although there might be slight overestimation or underestimation of the strength for the three rock types, making the method reliable for estimating strength parameters.

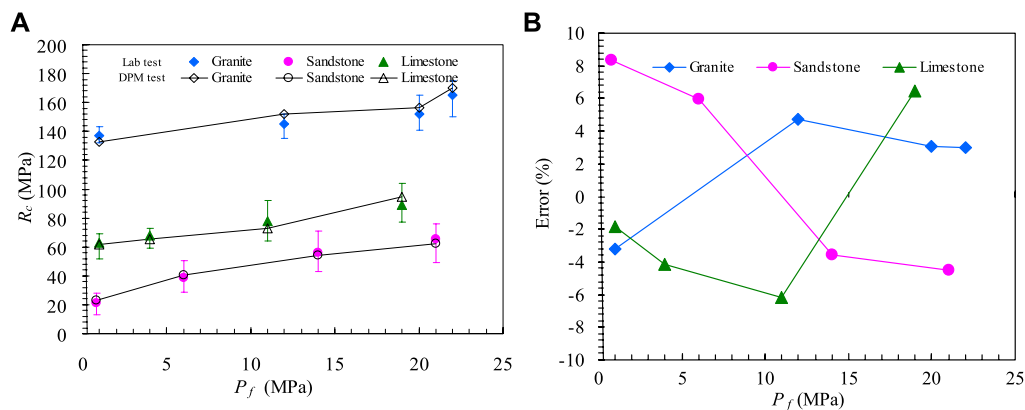


FIGURE 7

The obtained results for the strength of sandstone, limestone and granite from the drilling tests. (A) the strength result (B) the strength error.

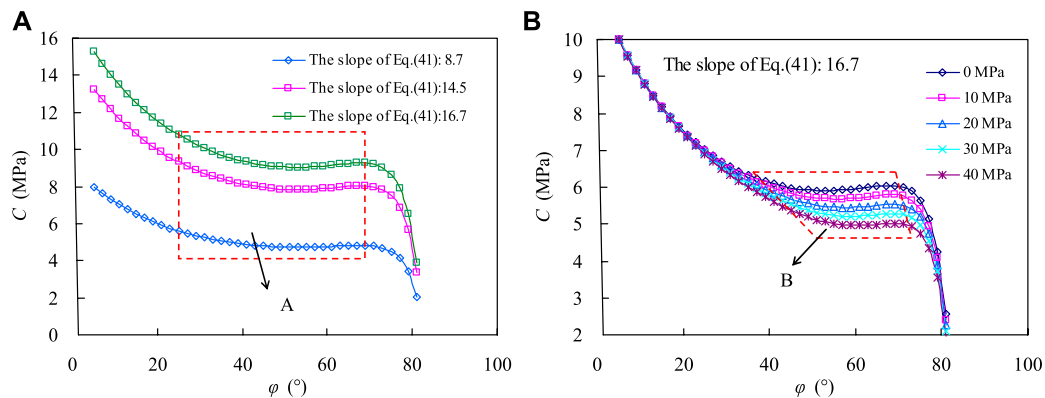


FIGURE 8

Variations of the estimated cohesion from the internal friction angle. (A) Different confining pressures (B) different fluid column pressures.

## 5 Conclusion

This study conducted a drilling process monitoring experiment to investigate the effect of confining pressure on cutting response with an impregnated diamond bit on sandstone, limestone, and granite.

- (1) The relationship between thrust force, torque force, and penetration depth was analyzed for both cutting and friction regimes under varying confining pressures.
- (2) An analytical model, which accounted for gravity effects, compressed crushed zones, and bit geometry, was developed. Results for high, medium, and weak strength rock suggest that drilling with an impregnated diamond bit involves two simultaneous processes of rock cutting and frictional contact, with the dominant role depending on the cutting point. Confining pressure was found to significantly affect the

cutting response in both regimes, with increased thrust force, torque force, and penetration depth at the cutting point under higher confining pressure.

- (3) Furthermore, a new field measurement method was proposed to determine cohesion, internal friction angle, and unconfined compressive strength of sandstone, limestone, and granite. The estimated strength values for the three rock types using this drilling technique are in good agreement with those of standard laboratory tests. The results demonstrate that the estimated strength of rocks is within an accepted error range of 10% compared to the results from standard tests. The drilling method provides a number of advantages over conventional tests, including high-resolution and continuous field measurement of rock strength parameters. With minimum requirements for test preparation, this practical method shows great potential for field applications in rock engineering.



## Data availability statement

The original contributions presented in the study are included in the article/supplementary material, further inquiries can be directed to the corresponding author.

## Author contributions

YoZ, JZ, and MH contributed to conception and design of the study. ZX organized the database. YG and YiZ performed the statistical analysis. SC and HX wrote the first draft of the manuscript. DC, MH, and CF wrote sections of the manuscript. All authors contributed to manuscript revision, read, and approved the submitted version.

## Funding

This research is financially supported by the Key R&D and Transformation Plan of Qinghai Province (2021-SF-167).

## References

- Adachi, J. I. (1996). *Frictional contact in rock cutting with blunt tools*. Civil Engineering, University of Minnesota. M. Sc Thesis.
- Bingham, M. G. (1964). How rock properties are related to drilling. *Oil Gas. J.* 62 (50), 94–101.
- Burgess, T. M., and Less, W. G. (1985). “Measuring the wear of milled tooth bits using MWD torque and weight-on-bit,” in *Proceedings of the drilling conference SPE/IADC* (New Orleans, 453–462).
- Chiaia, B., Borri-Brunetto, M., and Carpinteri, A. (2013). Mechanical modelling of the mechanics of core drilling in geomaterials. *Mach. Sci. Technol.* 17, 1–25. doi:10.1080/10910344.2012.747881
- Chong, Z. R., Yang, S. H. B., Babu, P., Linga, P., and Li, X. S. (2016). Review of natural gas hydrates as an energy resource: Prospects and challenges. *Appl. Energy* 162, 1633–1652. doi:10.1016/j.apenergy.2014.12.061
- Dagrain, F. (2006). *Etude des mecanismes de coupe des roches avec couteaux Uses Approche des mecanismes de frottement sous les couteaux par le concept du troisième corps*. Faculté Polytechnique de Mons. Ph.D Thesis.
- Dagrain, F. (2001). *Influence of the cutter geometry in rock cutting: An experimental approach*. University of Minnesota. M. Sc Thesis.
- Detournay, E., and Defourny, P. (1992). A phenomenological model for the drilling action of drag bits. *Int. J. Rock Mech. Min. Sci.* 29, 13–23. doi:10.1016/0148-9062(92)91041-3
- Detournay, E., Richard, T., and Shepherd, M. (2008). Drilling response of drag bits: Theory and experiment. *Int. J. Rock Mech. Min. Sci.* 45, 1347–1360. doi:10.1016/j.ijrmms.2008.01.010
- Evans, I. (1962). “A theory on the basic mechanics of coal ploughing,” in *Proceedings of international symposium on mining research* (London 2, 761–798).
- Franca, L. F. P. (2010). Drilling action of roller-cone bits: Modeling and experimental validation. *J. Energy Resour. Technol.* 132, 1–9. doi:10.1115/1.4003168
- Gerbaud, L., Menand, S., and Sellami, H. (2006). “PDC Bits: All comes from the cutter rock interaction,” in *Proceedings of the IADC/SPE drilling conference held in miami, 2* (Florida, USA, 21–23).
- Hareland, G. A. (2010). “Drilling rate model for roller cone bits and its application,” in *Proceedings of the CPS/SPE international oil & gas conference and exhibition in China held in beijing, China*, 8–10.
- He, M. M., Li, N., Zhang, Z. Q., Yao, X. C., Chen, Y. S., and Zhu, C. H. (2019). An empirical method for determining the mechanical properties of jointed rock mass using drilling energy. *Int. J. Rock Mech. Min. Sci.* 116, 64–74. doi:10.1016/j.ijrmms.2019.03.010
- Hibb, L. E. J., and Flom, D. G. (1978). Diamond compact cutter studies for geothermal bit design. *J. Press. Vessel Tech.* 100 (4), 406–416. doi:10.1115/1.3454488
- Hoferock, L., and Bratcher, G. J. (1996). A new approach for determining *in-situ* rock strength while drilling. *J. Energy Resour. Technol.* 118, 249–255. doi:10.1115/1.2793870
- YZ, JZ, ZX, YG, SC, DC, and CF was employed by the company Geological Research Institute, China National Logging Corporation; HX was employed by the company Qinghai Xihu Expressway Management Co., Ltd.
- The remaining authors declare that the research was conducted in the absence of any commercial or financial relationships that could be construed as a potential conflict of interest.
- Hoover, E. R., and Middleton, J. N. (1981). Laboratory evaluation of PDC drill bits under high-speed and high-wear conditions. *J. Petro Tech.* 33 (12), 2316–2321. doi:10.2118/10326-pa
- Kalantari, S., Baghbanan, A., and Hashemolhosseini, H. (2019). An analytical model for estimating rock strength parameters from small-scale drilling data. *J. Rock Mech. Geotech. Eng.* 104, 135–145. doi:10.1016/j.jrmge.2018.09.005
- Kalantari, S., Hashemolhosseini, H., and Baghbanan, A. (2018). Estimating rock strength parameters using drilling data. *Int. J. Rock Mech. Min. Sci.* 104, 45–52. doi:10.1016/j.ijrmms.2018.02.013
- Karasawa, H., and Misawa, S. (1992). Laboratory testing to design PDC bits for geothermal well drilling. *Drilling Technology. Am. Soc. Mech. Eng. (ASME)* 40, 135–141.
- Karasawa, H., Ohno, T., Kosugi, M., and Rowley, J. C. (2002b). Methods to estimate the rock strength and tooth wear while drilling with roller-bits-part 1: Milled-Tooth Bits. *J. Energy Resour. Technol.* 24, 125–132. doi:10.1115/1.1482405
- Karasawa, H., Ohno, T., Kosugi, M., and Rowley, J. C. (2002a). Methods to estimate the rock strength and tooth wear while drilling with roller-bits-part 2: Insert bits. *J. Energy Resour. Technol.* 124, 133–140. doi:10.1115/1.1482406
- Kerisel, J. (1975). *Cours de mécanique des sols*. Paris: Ecole National Des Ponts Et Chaussées. (in French).
- Lhomme, T. (1999). *Frictional contact at a rock-tool interface: An experimental study*. University of Minnesota. M. Sc Thesis.
- Li, X., Hood, M., and Find, X. X. (1993). *Wear and damage to PDC bits*, 3. Society of Petroleum Engineers Journal, 267–294.
- Li, X. S., Xu, C. G., Zhang, Y., Ruan, X. K., Li, G., and Wang, Y. (2016). Investigation into gas production from natural gas hydrate: A review. *Appl. Energy* 172, 286–322. doi:10.1016/j.apenergy.2016.03.101
- Lia, Z., and Itakura, K. (2012). An analytical drilling model of drag bits for evaluation of rock strength. *Soils Found.* 52 (2), 216–227. doi:10.1016/j.sandf.2012.02.002
- Merchant, M. E. (1945). Basic mechanics of the metal cutting process. *J. Appl. Phys.* 66, 168–175. doi:10.1115/1.4009380
- Naeimipour, A., Rostami, J., Buyuksagis, I. S., and Frough, O. (2018). Estimation of rock strength using scratch test by a miniature disc cutter on rock cores or inside boreholes. *Int. J. Rock Mech. Min. Sci.* 107, 9–18. doi:10.1016/j.ijrmms.2018.03.020
- Nakajima, I., and Kinoshita, S. (1979). Theoretical studies on cutting force of rock fracture mechanism in rock cutting. *J. Min. Metall. Inst. Jpn.* 95, 49–55. doi:10.2473/shigentozai1953.95.1092\_49
- Nishimatsu, Y. (1972). The mechanics of rock cutting. *Int. J. Rock Mech. Min. Sci.* 9, 261–270. doi:10.1016/0148-9062(72)90027-7
- Ohno, T., Karasawa, H., Kosugi, M., and Rowley, J. C. (2004). Proposed practical methods to estimate rock strength and tooth wear while drilling with roller-cone bits. *J. Energy Resour. Technol.* 126, 302–310. doi:10.1115/1.1794696

## Conflict of interest

## Publisher's note

All claims expressed in this article are solely those of the authors and do not necessarily represent those of their affiliated organizations, or those of the publisher, the editors and the reviewers. Any product that may be evaluated in this article, or claim that may be made by its manufacturer, is not guaranteed or endorsed by the publisher.



- Palassi, M., and Emami, V. (2014). A new nail penetration test for estimation of rock strength. *Int. J. Rock Mech. Min. Sci.* 66, 124–127. doi:10.1016/j.ijrmms.2013.12.016
- Pessier, R. C., and Fear, M. J. (1992). “Quantifying common drilling problems with mechanical specific energy and a bit-specific coefficient of sliding friction,” in *Proceedings of the 67<sup>th</sup> annual technical conference and exposition of the SPE*, 4–7 (Washington, DC, 373–387).
- Richard, T., Dagrain, F., Poyol, E., and Detournay, E. (2012). Rock strength determination from scratch tests. *Eng. Geol.* 147–148, 91–100. doi:10.1016/j.enggeo.2012.07.011
- Richard, T., Detournay, E., Drescher, A., Nicodeme, P., and Fourmaintraux, D. (1998). “The scratch test as a means to measure strength of sedimentary rocks,” in *Proceedings of the SPE/ISRM rock mechanics in petroleum engineering* (Society of Petroleum Engineers), 15–22.
- Rostamsowlat, I., Akbari, B., and Evans, B. (2018). Analysis of rock cutting process with a blunt PDC cutter under different wear flat inclination angles. *J. Petro Sci. Eng.* 171, 771–783. doi:10.1016/j.petrol.2018.06.003
- Rostamsowlat, I. (2018). Effect of cutting tool properties and depth of cut in rock cutting: An experimental study. *Rock Mech. Rock Eng.* 51 (6), 1715–1728. doi:10.1007/s00603-018-1440-2
- Roxborough, F. F., and Philips, H. R. (1975). Rock excavation by disc cutter. *Int. J. Rock Mech. Min. Sci.* 12 (12), 361–366. doi:10.1016/0148-9062(75)90547-1
- Sinor, L. A., Powers, J. R., and Warren, T. M. (1998). “The effect of PDC cutter density, back rake size and speed on performance,” in *Proceedings of the IADC/SPE drilling conference* (Society of Petroleum Engineers). No. SPE-39306-MS.
- Teale, R. (1965). The concept of specific energy in rock drilling. *Int. J. Rock Mech. Min. Sci.* 2, 245–273. doi:10.1016/0148-9062(65)90016-1
- Vedachalam, N., Ramesh, S., Srinivasalu, S., Rajendran, G., Ramadass, G., and Atmanand, M. (2016). Assessment of methane gas production from Indian gas hydrate petroleum systems. *Appl. Energy* 168, 649–660. doi:10.1016/j.apenergy.2016.01.117
- Warren, T. M. (1987). Penetration rate performance of roller cone bits. *SPE Drill. Eng.* 2, 9–18. doi:10.2118/13259-pa
- Wojtanowicz, A. K., and Kuru, E. (1993). Mathematical modeling of PDC bit drilling process based on a single-cutter mechanics. *J. Energy Resour. Technol.* 115, 247–256. doi:10.1115/1.2906429
- Wolcott, D. S., and Bordelon, D. R. (1993). “Lithology determination using downhole bit mechanics data,” in *Proceedings of the 68th annual technical conference and exhibition of the SPE*, 3–6 (Houston, Texas, 769–778).
- Yang, M., Luo, D. Y., Chen, Y. H., Li, G., Tang, D. Q., and Meng, Y. F. (2019). Establishing a practical method to accurately determine and manage wellbore thermal behavior in high-temperature drilling. *Appl. Energy* 238, 1471–1483. doi:10.1016/j.apenergy.2019.01.164
- Zhou, Y., and Detournay, E. (2014). “Analysis of the contact forces on a blunt PDC bit,” in *ARMA 14-7351, 48th US rock mechanics/geomechanics symposium* (ARMA).



## OPEN ACCESS

## EDITED BY

Xuelong Li,  
Shandong University of Science  
and Technology, China

## REVIEWED BY

Jiuyang Huan,  
Yangzhou Polytechnic Institute, China  
Yonggang Zhang,  
Tongji University, China

## \*CORRESPONDENCE

Haoteng Wang,  
✉ Ironhookbrother@gmail.com

## SPECIALTY SECTION

This article was submitted to  
Environmental Informatics  
and Remote Sensing,  
a section of the journal  
Frontiers in Earth Science

RECEIVED 20 February 2023

ACCEPTED 17 March 2023

PUBLISHED 13 April 2023

## CITATION

Li X, Wang H, Zhao Y, Xue H and Li L  
(2023), Experimental investigation into  
rock burst proneness of rock materials  
considering strain rate and size effect.  
*Front. Earth Sci.* 11:1169750.  
doi: 10.3389/feart.2023.1169750

## COPYRIGHT

© 2023 Li, Wang, Zhao, Xue and Li. This is  
an open-access article distributed under  
the terms of the [Creative Commons  
Attribution License \(CC BY\)](#). The use,  
distribution or reproduction in other  
forums is permitted, provided the original  
author(s) and the copyright owner(s) are  
credited and that the original publication  
in this journal is cited, in accordance with  
accepted academic practice. No use,  
distribution or reproduction is permitted  
which does not comply with these terms.

# Experimental investigation into rock burst proneness of rock materials considering strain rate and size effect

Xiaobin Li<sup>1,2,3</sup>, Haoteng Wang<sup>4\*</sup>, Ying Zhao<sup>5</sup>, Haifang Xue<sup>3</sup> and  
Lingyun Li<sup>3</sup>

<sup>1</sup>School of Civil Engineering, Chongqing University, Chongqing, China, <sup>2</sup>Qinghai Traffic Construction Management Co., Ltd., Xining, China, <sup>3</sup>Qinghai Xihu Expressway Management Co., Ltd., Xining, China, <sup>4</sup>State Key Laboratory of Eco-hydraulics in Northwest Arid Region, Xi'an University of Technology, Xi'an, China, <sup>5</sup>School of Highway, Chang'an University, Xi'an, China

In deep rock engineering, evaluating the likelihood of rock burst is imperative to ensure safety. This study proposes a new metric, the post-peak dissipated energy index, which accounts for strain rate and size effects in assessment of the rock burst proneness of a rock mass. To investigate rock burst proneness, conventional compression tests were conducted on limestone and slate samples with different length to diameter (L/D) ratios (ranging from 0.3 to 1.5) at four different strain rates (0.005, 0.01, 0.5, and 1.0 s<sup>-1</sup>). Based on the testing observations, the actual rock burst proneness was classified into three categories (no risk, low risk, and high risk). A new criterion was also established using the post-peak dissipated energy index, which is the ratio of elastic energy to total dissipated energy. The impact of the strain rate and L/D ratio on rock burst proneness was analyzed. The results indicated that increased strain rates cause a strong hardening effect, leading to staged growth of rock burst proneness. However, the rock burst proneness decreases non-linearly with the increasing L/D ratio. The accuracy of the proposed criterion was validated by comparison with existing criteria, demonstrating that the energy-based index ensures a reliable evaluation of the rock burst proneness of a rock mass. The proposed method has excellent potential for practical application in deep rock engineering.

## KEYWORDS

rock burst proneness, post-peak dissipated energy index, strain rate, size effect, failure characteristics

## 1 Introduction

Rock burst is a potential disaster that poses a significant threat to deep rock excavation and mining operations (Cook, 1976; Wang and Park, 2001; Sousa et al., 2017; Keneti and Sainsbury, 2018; Wojtecki et al., 2021; Wang et al., 2022a; Yang et al., 2022a; Wang et al., 2022b; Yang et al., 2022b). This dangerous occurrence is characterized by the high-speed ejection of rock fragments accompanied by loud cracking sounds (Kaiser and Cai, 2012; Li et al., 2021a; Li et al., 2021b; Liu et al., 2022). As ground stress increases and environmental complexity intensifies, the likelihood and impact of rock bursts also rise (Li et al., 2012; Gale, 2018). To ensure mining efficiency and safety, it is necessary to study the prediction of rock burst (Singh, 1989; Cai et al., 2022; Liu et al., 2023). Typically, rock burst proneness is regarded as a prerequisite for determining the likelihood of rock burst (Feng et al., 2015; Liu S



**FIGURE 1**  
Partial group of rock samples.

M et al., 2020). Various criteria have been proposed to assess rock burst proneness, based on factors such as strength, deformation modulus, energy, acoustic emission, and failure characteristics (Kidybiński, 1981; Singh, 1988; Zhang et al., 2009; He et al., 2015; Khosravi and Simon, 2018; Malan and Napier, 2018; Dai et al., 2019; Gong et al., 2019; Yang et al., 2020a; Gong et al., 2020; Liu S M et al., 2020; Gong et al., 2021; Liu et al., 2022). However, the essence of rock burst is the rapid release of stored elastic strain energy (Kidybiński, 1981; Singh, 1988; Konicek and Waclawik, 2018; Dai et al., 2019), making criteria based on energy parameters particularly meaningful for determining rock burst proneness. Examples of such criteria include the stored energy index  $W_{et}$  (Kidybiński, 1981) and the modified bursting energy index  $K_E^P$  (Liu X L et al., 2020).  $W_{et}$  reflects the energy evolution process and is expressed as the ratio of elastic energy to dissipated energy (Kidybiński, 1981). In fact, rock burst phenomena can still occur during the post-peak stage until it enters the residual stage (Gong et al., 2018c). Although  $K_E^P$  considers the entire deformation process, this criterion typically underestimates the rock burst proneness of brittle rock (Liu X L et al., 2020; Zhou et al., 2022). To evaluate the risk of rock burst accurately, a new criterion for rock burst proneness is proposed based on the post-peak dissipated energy characteristic of rock deformation.

Considerable progress has been made in investigating the process and mechanism of rock burst from the perspective of stress path and unloading effect (He et al., 2023). However, the size of the rock has a significant impact on rock burst proneness, due to the mechanical properties and spatial structural characteristics of rock (Ai et al., 2016). The laboratory method considers the structural characteristics of a rock mass as the size of the rock sample, and the results of several experiments have shown that the size of the sample negatively affects rock strength due to the end effect (Wang and He, 2023a). However, the size effect of a rock sample on rock burst proneness has received little attention (Wang et al., 2023b). The size effect leads to stress concentration at the rock boundary and subsequently affects the stress adjustment rate of a rock mass (Kahraman, 2002). Thus, the dependence of rock burst proneness on stress adjustment rate is controlled by the size effect (Dai et al., 2022). Furthermore, the combined effect of high ground stress and external force disturbance is closely related to rock burst occurrence (Du et al., 2016). By enhancing the strain hardening effect, increasing the strain rate

leads to a strong brittleness deformation of rock, making it an essential factor in energy release-induced rock burst (Liu et al., 2023).

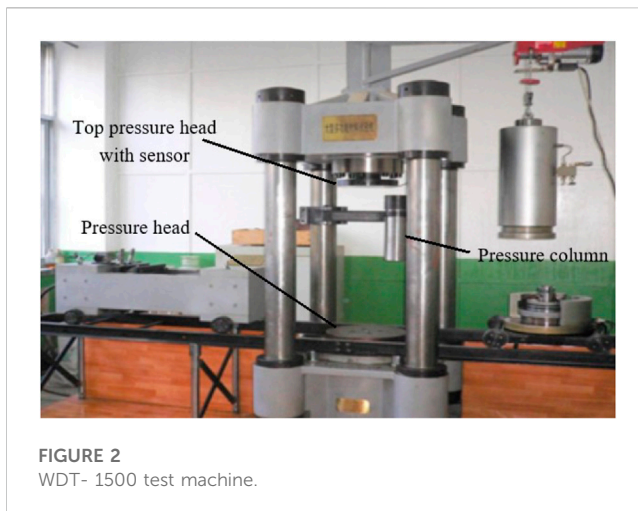
To effectively predict rock burst, it is crucial to establish a dependable criterion for rock burst proneness. For this study, conventional compression tests were conducted on samples of limestone and slate with various length-to-diameter (L/D) ratios, under four different strain rates, to investigate proneness to rock burst. A revised index, the post-peak dissipated energy index, was introduced to assess the rock burst proneness of a rock mass, taking into account the strain rate and size effects. Correspondingly, a new criterion has been developed, which can be used to calculate the ratio of elastic energy to total dissipated energy. The practical utility and accuracy of the new criterion were validated through testing.

## 2 Test method

The uniaxial compressive test is widely used to assess rock burst proneness (Singh, 1988). Strain rate and size effect both influence rock burst proneness (Masoumi et al., 2016; Rybacki et al., 2016; Tang et al., 2002; Tarasov and Potvin, 2013; Yumlu and Ozbay, 1995). According to the principle of thermodynamics, it is assumed that there is no heat exchange between the external environment and the sample during the loading process. Thus, input energy is converted into elastic energy and dissipated energy. The conventional compression test was carried out on two rock types to obtain the energy parameters.

### 2.1 Rock material

Two types of rock, limestone (sedimentary rock) and slate (metamorphic rock), were obtained from a tunnel construction site in Qinling Mountain, Shaanxi Province, China. During the sampling process, a strong rock burst and a series of residual rock bursts were observed in the field with a burial depth of 1 km. Due to the effects of mineral distribution and composition on the mechanical properties of rock, it was necessary to conduct SEM to investigate differences in mineral composition. The SEM results indicated that the majority of mineral particles in the limestone were lime mud (accounting for 68% of mineral content) and volcanic



chips (accounting for 24% of mineral content), with accompanying small amounts of pyrite (accounting for 6% of mineral content). These particles were crystallized in a manner that caused a small number of pores in the framework. The slate was composed of flake potash feldspar. In addition, the strong heterogeneity of slate was manifested in the distribution of layered structure. Since the typical layered structure has a strong effect on the mechanical properties of slate, the direction of each sample coring was perpendicular to the slate layer.

According to ISRM recommendations for compression tests (ISRM, 2007), the rock samples were processed into cylindrical shapes with different L/D ratios as follows. The rock specimens had a constant diameter of 50 mm and were of four different lengths (18, 42, 66, and 90 mm for limestone and 18, 24, 48, and 84 mm for slate), as shown in Figure 1.

## 2.2 Loading method

A series of unconfined compression tests were conducted on the WDT-1500 testing machine (shown in Figure 2). The maximum achieved load of 1800 kN can be applied by the bottom pressure head on the sample. The load and displacement sensors were installed in the top head, which detected a maximum axial displacement of 100 mm and lateral displacement of 5 mm. The error range of axial load and displacement was controlled within 0.1%. Moreover, the loading equipment was installed with three additional systems: a digital control system, a detection system, and a hydraulic loading system. The specific test steps satisfied the recommendations of the ISRM (2007). There was a pressure column upon the sample to concentrate the load on the center axis of the sample. In order to minimize the friction caused by the increased load, a spherical seat was located between the upper surface of the pressure column and the top pressure head. Similarly, two thermally hardened plates were placed on the upper and lower surfaces of the sample to eliminate friction. The conventional compression test was conducted at different loading rates to obtain the uniaxial compressive strength and elastic modulus of the rock. To ensure the consistency of the loading

effect on samples of different sizes (ISRM, 2007), the strain rate  $\epsilon_e$  was introduced as

$$\epsilon_e = \frac{d\epsilon}{dt} = \frac{(dl/dt)}{l} = \frac{u}{l}, \quad (1)$$

where  $\epsilon_e$  represents the strain rate,  $u$  is the loading rate, and  $l$  is the length of the rock sample.

To study the variation of rock burst proneness according to different strain rates, four strain rates (0.005, 0.01, 0.5, and 1.0 s<sup>-1</sup>) were considered based on the typical range of strain rate  $\epsilon_e$  associated with rock burst (Wasantha et al., 2015). The specific test plan is listed in Table 1. Moreover, to avoid the heterogeneity of the rock material (especially the layered structure of slate), the average mechanical parameter from more than three samples under the same conditions was used in subsequent investigation.

## 3 Revised criteria for rock burst proneness

Several criteria indicating rock burst proneness (Kidybiński, 1981; Singh, 1988; Zhang et al., 2009; He et al., 2015; Khosravi and Simon, 2018; Malan and Napier, 2018; Yang et al., 2018; Dai et al., 2019; Gong et al., 2019; Gong et al., 2020; Gong et al., 2021; Liu X L et al., 2020) have been reported. Although these criteria analyze the actual conditions of rock burst from different perspectives, the rapid release of stored energy is the essence of rock burst (Cook, 1976; Khosravi and Simon, 2018). During rock burst, the stored elastic energy is consumed by the ejection of rock fragments and dissipated through crack deformation of the rock mass. In particular, the ratio of elastic energy the dissipated energy, namely,  $W_{et}$ , is widely used to evaluate rock brittleness (Gong et al., 2019) and rock burst proneness (Kidybiński, 1981). The  $W_{et}$  index is determined when rock undergoes yield deformation until failure (the corresponding stress level progresses from 80% to 90%). According to Figure 3,  $W_{et}$  can be obtained by

$$U = \int_0^{\epsilon_l} \sigma d\epsilon, \quad (2)$$

$$U^e = \frac{\sigma_c^2}{2E}, \quad (3)$$

$$U^d = U - U^e = \int_0^{\epsilon_l} \sigma d\epsilon - \frac{\sigma_c^2}{2E}, \quad (4)$$

$$W_{et} = \frac{U^e}{U^d}, \quad (5)$$

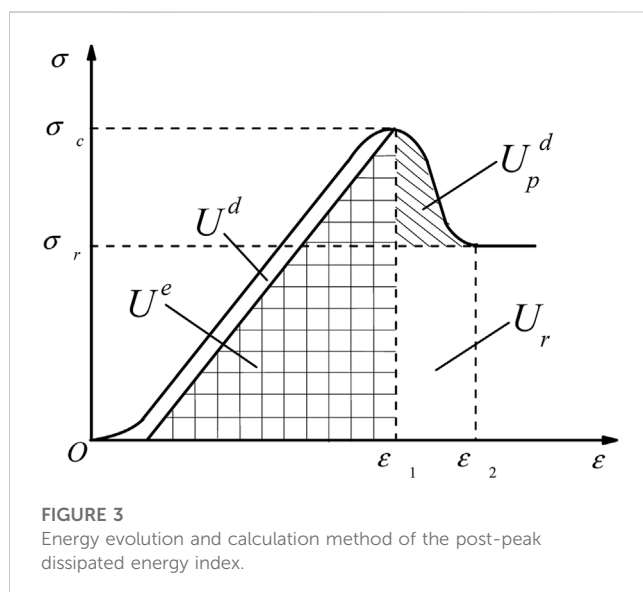
where  $\sigma_c$  and  $\epsilon_l$  are the UCS and corresponding failure strain, respectively,  $E$  is the elastic modulus, and  $W_{et}$  is the stored energy index. There are three categories of rock burst proneness quantified by  $W_{et}$  (Kidybiński, 1981):

$$\begin{cases} W_{et} \geq 5, & \text{high risk,} \\ 2 \leq W_{et} \leq 4.99, & \text{low risk,} \\ W_{et} < 2, & \text{no risk.} \end{cases} \quad (6)$$

The  $W_{et}$  index reveals the essence of rock burst occurrence from a theoretical perspective. Nevertheless, the determination of the  $W_{et}$  index is only dependent on the pre-peak energy storage characteristic corresponding to the most violent rock burst. During the excavation process, rock failure induced by stress

TABLE 1 Test method and sample serial number.

Rock type	No.	L/D ratio	Strain rate $\varepsilon_e$ (s <sup>-1</sup> )	Rock type	No.	L/D ratio	Strain rate $\varepsilon_e$ (s <sup>-1</sup> )
Limestone	L-1-1	0.3	0.005	Slate	S-1-1	0.3	0.005
	L-1-2		0.01		S-1-2		0.01
	L-1-3		0.5		S-1-3		0.5
	L-1-4		1		S-1-4		1
	L-2-1	0.4	0.005		S-2-1	0.7	0.005
	L-2-2		0.01		S-2-2		0.01
	L-2-3		0.5		S-2-3		0.5
	L-2-4		1		S-2-4		1
	L-3-1	0.8	0.005		S-3-1	1.1	0.005
	L-3-2		0.01		S-3-2		0.01
	L-3-3		0.5		S-3-3		0.5
	L-3-4		1		S-3-4		1
	L-4-1	1.4	0.005		S-4-1	1.5	0.005
	L-4-2		0.01		S-4-2		0.01
	L-4-3		0.5		S-4-3		0.5
	L-4-4		1		S-4-4		1



disturbance is manifested in two modes, spalling and rock burst (Diederichs et al., 2004). Spalling (the progressive failure of a rock mass) is identified as a precursor to rock burst (Martin and Maybee, 2000; Diederichs, 2007). As ground stress increases, spalling evolves into rock burst (Mazaira and Konicek, 2015). Owing to the instability of the stress adjustment during the excavation process, it is believed that spalling and rock burst occur at the same time until the stress state is stabilized (Gong et al., 2018a; b). This judgment of rock burst should involve the rock deformation before entering the residual stage. The dissipated energy consumed after peak is

considered the post-peak dissipated energy  $U_p^d$  and used to improve the criteria for rock burst proneness. According to Figure 3, the post-peak dissipated energy  $U_p^d$ , consumed from the post-peak stage to residual stage, can be calculated as

$$U_p = \int_{\varepsilon_1}^{\varepsilon_2} \sigma d\varepsilon, \quad (7)$$

$$U_p^d = U_p - U_r = \int_{\varepsilon_1}^{\varepsilon_2} \sigma d\varepsilon - \sigma_r (\varepsilon_2 - \varepsilon_1), \quad (8)$$

where  $\sigma_r$  is the residual strength and  $\varepsilon_2$  is the strain when first entering the residual stage. The post-peak dissipated energy index  $W_{et}^p$  is calculated as

$$W_{et}^p = \frac{U_p^d}{U^e + U_p^d}. \quad (9)$$

## 4 Analysis and results

### 4.1 Mechanical properties and energy storage characteristics

To obtain the energy characteristics during rock deformation to failure, the stress-strain curve under different strain rates and L/D ratios is shown in Figure 4. Several deformation stages can be identified in the stress-strain curve: the compaction stage, elastic stage, yield stage, and residual stage. For limestone, the curve of the initial compaction stage is longer than that for slate. This indicates that the mineral composition and structure of limestone are relatively loose. Limestone specimens have been shown to



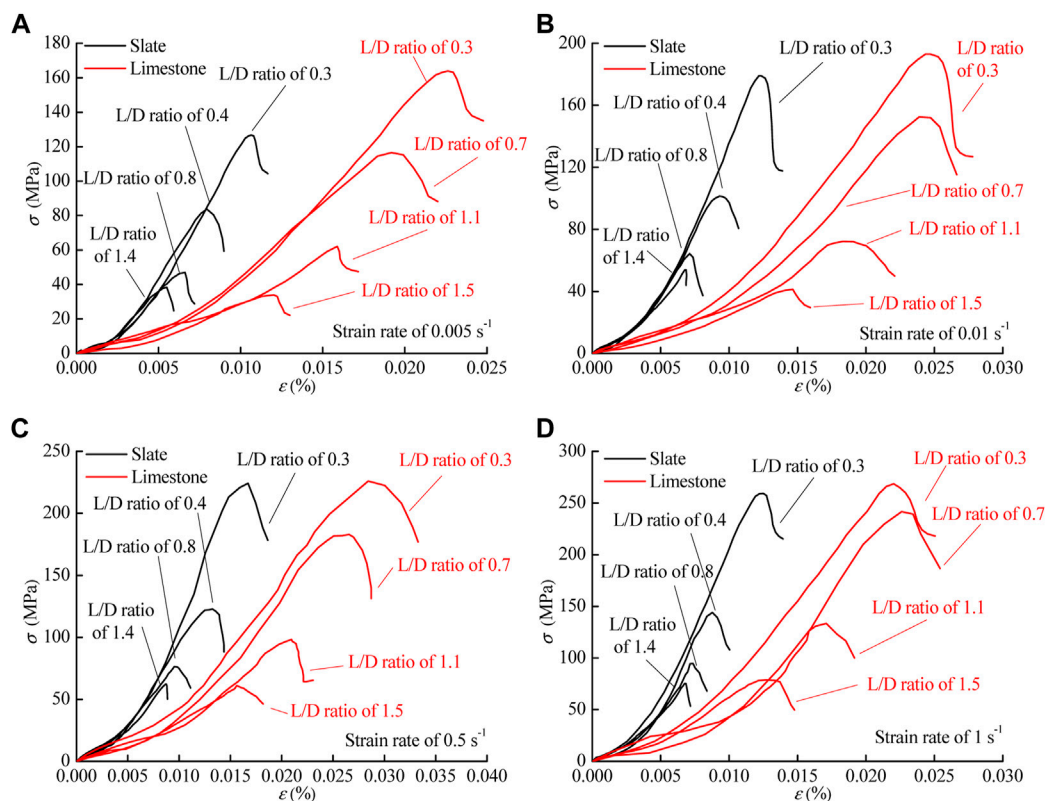


**FIGURE 4**  
Stress–strain curve of slate and limestone under different loading rates. (A)  $0.005 \text{ s}^{-1}$ , (B)  $0.01 \text{ s}^{-1}$ , (C)  $0.5 \text{ s}^{-1}$ , and (D)  $1 \text{ s}^{-1}$ .

undergo greater deformation until they are at maximum density (Konsztowicz, 2010). The elastic modulus of rock was calculated as the slope of the second stage of the curve in investigation of the influence of scale effect and strain rate. An obvious yield stage was observed in the stress–strain curve of limestone. This phenomenon indicated a strong plastic deformation in this stage. Due to strong brittleness, slate demonstrated a rapid stress drop after the elastic deformation stage. The energy parameters  $U$ ,  $U^e$ ,  $U^d$ , and  $U_p^d$  are calculated in Eqs. (2), (3), (4) and (8), as shown in Table 2. The expression of these energy parameters is in the form of energy density ( $\text{kJ/m}^3$ ) to eliminate the effect of rock column volume differences.

The relationship between the UCS and L/D ratio is shown in Figure 5. As the L/D ratio increased, the UCS showed a non-linear decreasing trend. The L/D ratio-dependent variation of UCS gradually stabilized when the L/D ratio reached 1.5. The elastic modulus presented a decreasing trend with increasing L/D, similar to that of UCS, as shown in Figure 6. This indicates that the L/D ratio has a negative effect on the mechanical performance of limestone and slate. It is worth noting that the elastic modulus of limestone decreased linearly. To explain this result, the typical failure characteristics of samples with different L/D ratios are presented in Table 3. For slate and limestone, the failure characteristic changed from complex to single with the increasing L/D ratio. Due to the relatively short stress path of the specimen with a low L/D ratio, the stress concentration phenomenon at the end of the specimen generated a large amount of friction between the pressure head

and the end face of the sample (Tekalur and Sen, 2011). This end friction effect reflects a heterogeneous stress distribution at the end face. In order to maintain the integrity of the rock under mechanical compression, the stress distribution is frequently adjusted. Therefore, there are various failure characteristics observed in rock samples (Walton et al., 2019). When the L/D ratio reaches 1.5, limestone and slate undergo split failure and shear failure, respectively. The typical failure characteristic can be explained in terms of mineral composition and structure. For slate, its typical clastic structure contains a lot of pores at the clastic junction. When the sample enters the critical state of elastoplastic deformation, the stress path passes the weak area of the clastic structure and forms a plastic deformation zone (Quinones et al., 2017). As the axial load increased constantly to exceed the yield limit of the rock, the stress path penetrated the specimen to form a shear sliding surface. The microstructural properties of the limestone skeleton suggested a muddy supporting texture. When a compressive load was applied, cracks expanded along the cemented boundary of lime mud particles. Therefore, the limestone exhibited splitting failure under compressive load.

The energy indices  $U$ ,  $U^e$ ,  $U^d$ , and  $U_p^d$  of limestone and slate were calculated using Eqs 2–4 to obtain the data distribution of energy storage, as shown in Table 3 and Figure 7. As the input energy  $U$  increased, both the elastic energy  $U^e$  and dissipated energy  $U^d$  showed a linear growth trend. This typical trend is based on the linear energy storage law (Gong et al., 2020). There is an intercept in the fitting formula with a value of approximately 5% of  $U^e$ . The

TABLE 2 Mechanical properties and two indices,  $W_{et}$  and  $W_{et}^p$  of rock burst proneness for limestone and slate.

Rock type	L/D ratio	$\varepsilon_e$	$E$	UCS	$U^e$	$U^d$	$U_{post-peak}$	$W_{et}$	$U^p$	$W_{et}^p$
		( $s^{-1}$ )	(GPa)	(MPa)	(kJ/m <sup>3</sup> )	(kJ/m <sup>3</sup> )	(kJ/m <sup>3</sup> )		(kJ/m <sup>3</sup> )	
Slate	0.3	0.005	8.70	126	687	266	389	2.58	25.5	2.36
		0.01	9.75	179	883	212	308	4.17	25.7	3.71
		0.5	17.8	233	1261	165	233	7.64	26.5	6.59
		1.0	21.5	259	1803	195	283	9.25	39.4	7.69
	0.4	0.005	8.08	82.8	353	137	196	2.58	56.5	1.82
		0.01	9.18	101	442	142	203	3.11	46.1	2.35
		0.5	14.3	122	838	158	227	5.30	32.9	4.39
		1.0	18.6	144	1092	169	243	6.46	24.5	5.64
	0.8	0.005	7.77	47.7	138	86.7	120	1.59	8.55	1.45
		0.01	8.45	63.7	251	105.9	148	2.37	26.2	1.90
		0.5	13.1	76.3	345	89.9	124	3.84	47.5	2.51
		1.0	15.5	95.2	439	94.2	131.3	4.66	39.8	3.28
	1.4	0.005	7.56	39.6	95.4	53.5	70.3	1.78	9.80	1.51
		0.01	8.25	54.0	111.6	65.6	88.4	1.70	10.3	1.47
		0.5	10.2	62.1	135.3	62.8	84.2	2.15	10.3	1.85
		1.0	12.4	75.5	172	56.7	75.1	3.03	13.4	2.45
Limestone	0.3	0.005	11.1	164	718	212	308	3.39	12.9	3.19
		0.01	19.5	193	1103	223	324	4.95	11.1	4.71
		0.5	21.2	226	1523	232	338	6.56	23.0	5.97
		1.0	29.2	268	1978	261	381	7.58	26.7	6.88
	0.7	0.005	8.39	116	530	229	333	2.31	9.11	2.23
		0.01	13.3	152	649	189	273	3.43	10.1	3.26
		0.5	16.8	183	685	173	249	3.96	8.95	3.76
		1.0	24.5	241	841	135	192	6.23	7.09	5.92
	1.1	0.005	4.4	62.1	301	151	216	1.99	11.8	1.85
		0.01	7.58	72.3	355	144	206	2.47	9.14	2.32
		0.5	13.0	98.2	400	138	197	2.90	13.7	2.64
		1.0	18.0	133	475	102	143	4.66	12.7	4.14
	1.5	0.005	3.90	34.3	153	97	135	1.58	10.8	1.42
		0.01	6.11	41.6	196	112	158	1.75	8.00	1.63
		0.5	13.5	61.7	227	112	158	2.03	6.07	1.92
		1.0	15.1	79.5	305	100	140	3.05	3.33	2.95

fitting coefficient  $R^2$  ranged from 0.94 to 0.99, indicating an accurate linear correlation between the energy storage and dissipation. For slate and limestone, the slope value of  $U^e$  versus  $U$  represents the storage ability of elastic energy. The figure demonstrates that the energy storage ability of slate was stronger than that of limestone (slope values were 0.93 and 0.71 for slate and limestone, respectively). The difference in slope value is related to the deformation characteristics of slate. The stress–strain curves in [Figure 4](#) indicate that slate samples usually underwent brittle failure, which hardly contained a yield stage. The typical failure characteristic indicated that the input energy transformed into elastic energy stored in the sample, instead of being dissipated by crack propagation ([Wang et al., 2021](#)). Moreover, a linear correlation between the post-peak dissipated energy  $U_p^d$  and pre-

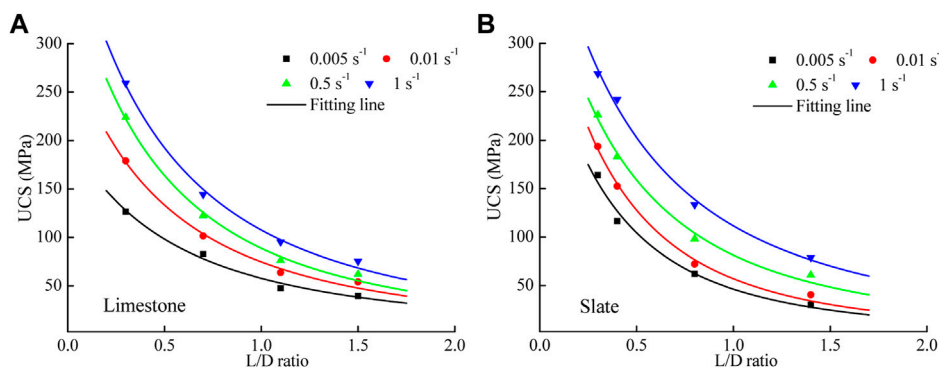


**FIGURE 5**  
Relationship between the UCS and the L/D ratio for (A) limestone and (B) slate.

peak dissipated energy  $U^d$  is presented in Figure 7B. The linear correlation between  $U_p^d$  and  $U^d$  can be explained by the failure process. The failure process of limestone and slate followed a similar principle in that the failure path extended along the weakest part. As for the post-peak stage, energy was dissipated through the friction of the pre-existing crack surfaces when the applied loading on the sample was increased.

To obtain the effects of L/D and strain rate on these linear energy characteristics, the correlation between the ratio of elastic energy to input energy and two influence factors are presented in Figure 8. Due to the large range of strain rates, the variation of strain rate is usually described as a semi-log equation. The error bar represents the range of the  $U^e/U$  values under the same condition to emphasize the influence of individual factors. The effects of L/D and strain rate on the linear energy characteristics were observed in limestone and slate. As the strain rate  $\epsilon_e$  increased,  $U^e/U$  increased in segments. When  $\epsilon_e$  had a range from 0.01 to 0.5  $s^{-1}$ , the increased value of  $U^e/U$  averaged 8% for slate and limestone. The elastic deformation capacity of rock can be characterized by  $U^e/U$ . With increasing  $\epsilon_e$ , the strain rate-hardening effect becomes more significant, resulting in a reinforcement of elastic deformation under compressive load. The size effect of rock on the linear energy characteristic is demonstrated as a linear trend. The difference in slope values between slate and limestone (33.3%) revealed the effect of slate brittleness on the failure characteristics induced by the size of the sample. There was an apparent stress concentration at end face caused by size effect. Stress concentrations not only created cracks but also caused friction to dissipate energy. The detrital distribution of slate was beneficial for crack propagation and energy dissipation. Therefore, the decreased  $U^e/U$  of slate was more obvious than that of limestone.

## 4.2 Proposed criteria for rock burst proneness

Failure of rock specimens is accompanied by the rapid propagation of cracks and ejection of rock chips (Małkowski and Niedbalski, 2020). The failure characteristics are affected by the energy storage property of a rock mass. Pre-stored energy







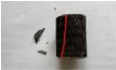






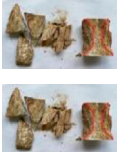


releases rapidly and transforms into the kinetic energy consumed by the ejection of rock chips (Feng et al., 2021). The rapid energy conversion is similar to the mechanism of rock burst in a mine (Cai et al., 2021). Nevertheless, it is difficult to capture rock fragments and calculate the total kinetic energy to determine rock burst proneness (Gong et al., 2021). In the actual rock burst, failure sound, observed size distribution of rock fragments, and failure characteristics are considered the standard. To establish criteria for rock burst proneness based on the  $W_{et}^p$  index, the actual failure situation of slate and limestone was recorded. Table 4 shows the typical failure modes of limestone and slate under the maximum and minimum strain rates. According to the failure characteristics under different conditions, the rock burst proneness was characterized into three categories (high risk, low risk, and no risk). The specific descriptions of the three categories for actual rock burst proneness are included as follows.

**No risk of rock burst:** At a low strain rate, the slate specimens with an L/D ratio of 1.5 and 1.8 had only one oblique shear crack, accompanied by a few scattered slate particles, as shown in Table 4. There was no obvious sound upon specimen failure. Moreover, the rock fragments slid down along the failure surface under the action of gravitational potential energy instead of being ejected.

**Low risk of rock burst:** For most slate and limestone specimens, large fragments could be observed to fall off, but the specimens retained their main shape. The limestone with low-risk rock burst proneness showed typical split failure. Only a small amount of rock particles had been observed to eject at low velocity. Taking the limestone specimen with an L/D ratio of 1.1 at low strain rate, a majority of limestone flakes were distributed on the pressure head, and only a few small pieces were ejected on the pressure platform.

**High risk of rock burst:** The failure modes of slate specimens and limestone specimens with the L/D ratio of 1.1 under high strain rate presented typical failure characteristics of rock burst. The specimens were broken into many rock chunks and particles that were no more than 3.0 cm in size, which were ejected on the platform at high velocity. Therefore, the failure characteristics of high risk of rock burst can be described as a large amount of rock debris and particles ejected at a high speed, accompanied by a

TABLE 3 Failure characteristics of slate and limestone with different L/D ratios under different strain rates.

Rock type	L/D ratio	Failure characteristics		
		Strain rate of 0.005 s <sup>-1</sup>	Strain rate of 1.0 s <sup>-1</sup>	Description
Slate	0.3			X-shape shear failure
	0.4			X-shape shear failure
	0.8			Oblique shear failure
	1.4			Oblique shear failure
Limestone	0.3			Oblique shear failure and split failure
	0.7			Split failure and X-shape shear failure
	1.1			Split failure and shear failure
	1.5			Split failure at a low rate and X-shape shear failure at a high rate

strong crackling sound and fall on the platform when the specimen disintegrated.

According to the actual rock burst proneness determined by the failure characteristics, the post-peak dissipated energy index  $W_{et}^p$  of limestone and slate were classified into three categories, no risk, low risk, and high risk, as shown in Figure 9A. The risk level of rock burst proneness improved with increasing  $W_{et}^p$  values. The  $W_{et}^p$  data points indicate a quantitative correlation between the  $W_{et}^p$  value and the actual rock burst proneness. In summary, the  $W_{et}^p$  index is a feasible method for evaluation of rock burst proneness, and the specific criterion for rock burst proneness is confirmed as

$$\begin{cases} W_{et}^p > 5.5, & \text{high risk,} \\ 2.5 \leq W_{et}^p \leq 5.5, & \text{low risk,} \\ W_{et}^p < 2.5, & \text{no risk.} \end{cases} \quad (10)$$

The occurrence of rock burst is closely associated with stored energy release. By considering post-peak energy dissipation, the rock burst proneness can be modified to adapt to the actual situation. Compared with the criterion for rock burst proneness using  $W_{et}$ , the

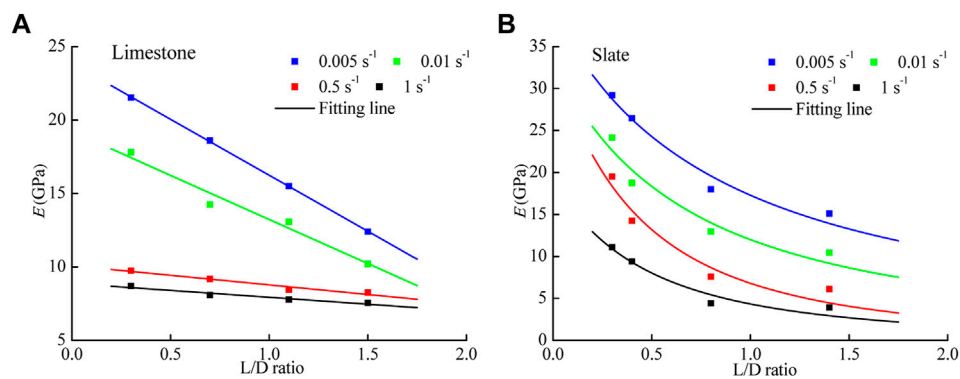


**FIGURE 6**  
Relationship between the elastic modulus and the L/D ratio under different strain rates. (A) Limestone and (B) Slate.

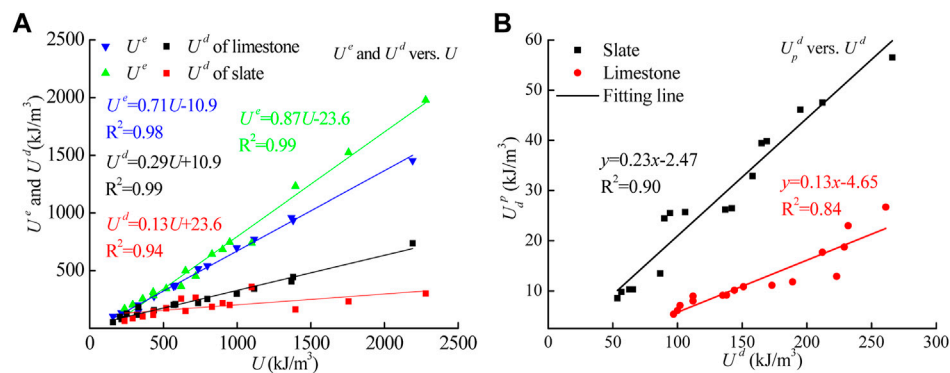


**FIGURE 7**  
Relationship between (A)  $U^e$  and  $U^d$  versus  $U$  and (B)  $U_p^d$  versus  $U^d$  for limestone and slate.

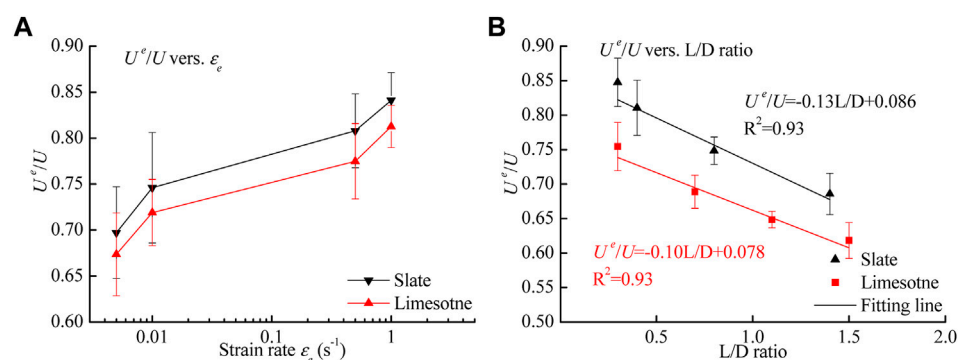


**FIGURE 8**  
Effect of the strain rate and L/D ratio on the linear energy characteristics. (A) strain rate and (B) L/D ratio.

three criterion categories of the revised rock burst proneness, determined using the  $W_{et}^p$  index, increased by 0.5. Comparison between the actual rock proneness and the rock burst criterion (Eq. 6) proposed by Kidybiński (1981) is shown in Figure 9B. Obviously, the data point distribution of  $W_{et}$  is more dispersed than that of  $W_{et}^p$ .

Taking slate as an example, when L/D ratio is 0.8 and strain rate is  $0.5 \text{ s}^{-1}$ , the  $W_{et}$  value is calculated as 5.30 and identified as at high risk of rock burst. The revised index  $W_{et}^p$  calculated under the same conditions identified the sample as low risk, with a value of 4.39. The failure characteristic presented only a small amount of debris falling



TABLE 4 Fitting formula of  $W_{et}^p$  versus L/D ratio.

Rock type	$\varepsilon_e$ ( $s^{-1}$ )	Fitting function	Rock type	$\varepsilon_e$ ( $s^{-1}$ )	Fitting function
Limestone	0.005	$W_{et}^p=4.26 (1+ L/D)^{-1.2}$ , $R^2=0.98$	Slate	0.005	$W_{et}^p=2.97 (1+ L/D)^{-1.2}$ , $R^2=0.86$
	0.01	$W_{et}^p=7.24 (1+ L/D)^{-1.6}$ , $R^2=0.99$		0.01	$W_{et}^p=4.89 (1+ L/D)^{-1.5}$ , $R^2=0.85$
	0.5	$W_{et}^p=9.39 (1+ L/D)^{-2.2}$ , $R^2=0.99$		0.5	$W_{et}^p=11.6 (1+ L/D)^{-2.2}$ , $R^2=0.90$
	1.0	$W_{et}^p=9.67 (1+ L/D)^{-1.7}$ , $R^2=0.88$		1.0	$W_{et}^p=12.7 (1+ L/D)^{-2.5}$ , $R^2=0.92$

TABLE 5 Summary of rock burst proneness based on three indices from Liu S M et al. (2020), Małkowski and Niedbalski (2020), and Bukowska (2005).

Rock type	L/D	$\varepsilon_e$	$M$	$W_{TG}$	$P_{ES}$	$K_E^P$	Rock type	L/D	$\varepsilon_e$ ( $s^{-1}$ )	$M$ (GPa)	$W_{TG}$	$P_{ES}$ (kJ)	$K_E^P$
		( $s^{-1}$ )	(GPa)		(kJ)								
Slate	0.3	0.005	13.8	0.63	36.9	1.77	Limestone	0.3	0.005	26.5	0.42	46.1	2.33
		0.01	21.0	0.47	90.0	2.87			0.01	17.0	1.15	87.9	3.40
		0.5	16.3	1.10	278	5.41			0.5	8.50	2.49	131	4.51
		1.0	13.5	1.59	385	6.37			1.0	12.8	2.28	324	5.19
	0.4	0.005	12.2	0.66	18.4	1.80		0.7	0.005	17.1	0.49	27.5	1.59
		0.01	20.9	0.44	35.7	2.18			0.01	26.8	0.50	68.8	2.38
		0.5	22.1	0.65	81.1	3.69			0.5	23.7	0.71	126	2.75
		1.0	18.4	1.01	12.8	4.49			1.0	24.1	1.02	346	4.38
	0.8	0.005	25.7	0.30	7.34	1.15		1.1	0.005	21.1	0.21	10.7	1.39
		0.01	22.0	0.38	15.5	1.70			0.01	22.0	0.34	20.1	1.72
		0.5	16.9	0.78	34.5	2.78			0.5	11.3	1.16	63.6	2.03
		1.0	13.4	1.16	58.3	3.34			1.0	13.6	1.33	201	3.32
	1.4	0.005	36.9	0.20	6.32	1.36		1.5	0.005	34.1	0.11	3.90	1.13
		0.01	21.8	0.38	14.3	1.26			0.01	24.5	0.25	6.41	1.24
		0.5	36.8	0.28	23.4	1.61			0.5	21.2	0.64	31.2	1.44
		1.0	28.3	0.44	37.7	2.29			1.0	39.6	0.38	81.0	2.18

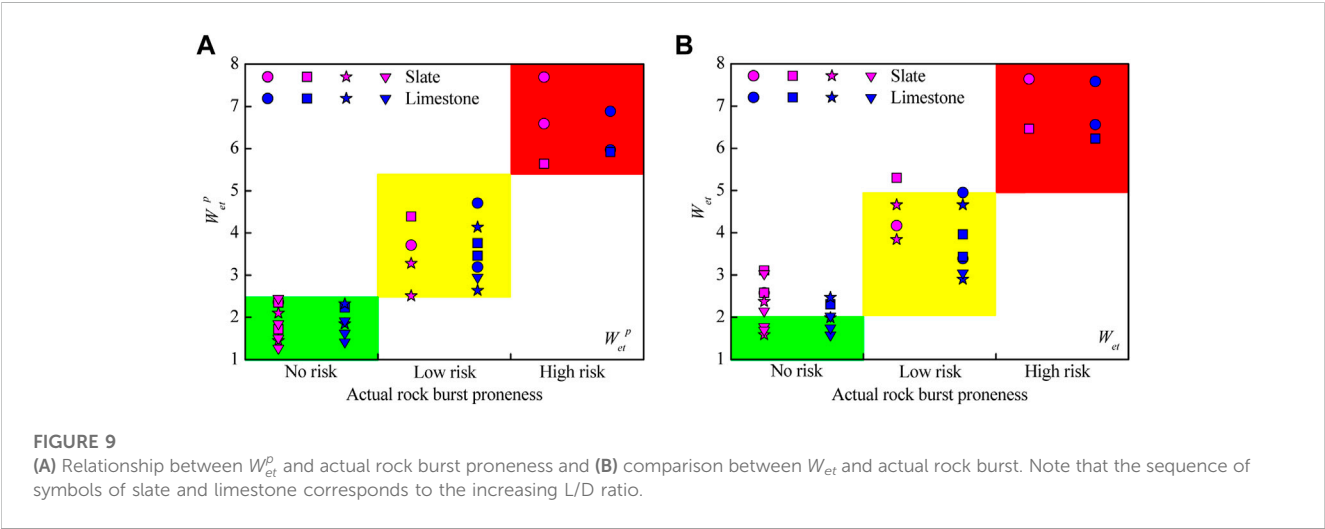
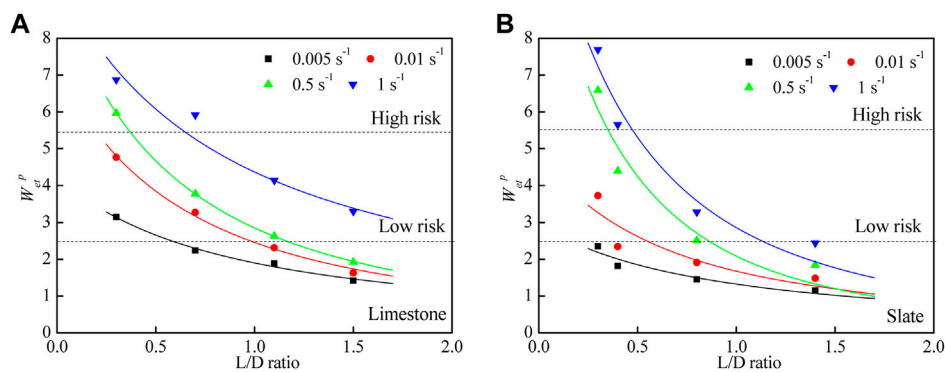
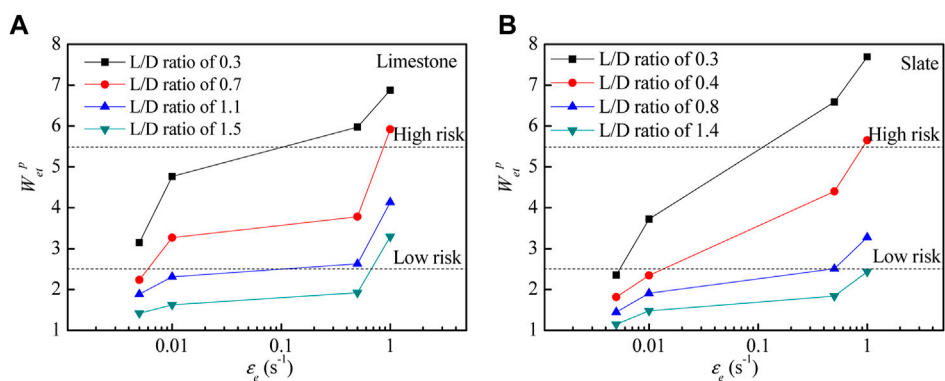


FIGURE 9 (A) Relationship between  $W_{et}^p$  and actual rock burst proneness and (B) comparison between  $W_{et}$  and actual rock burst. Note that the sequence of symbols of slate and limestone corresponds to the increasing L/D ratio.



**FIGURE 10**  
Correlation between  $W_{et}^p$  and the L/D ratio for (A) Limestone and (B) Slate.



**FIGURE 11**  
Correlation between  $W_{et}^p$  and  $\epsilon_e$  under various L/D ratio conditions using the semi-log equation for (A) Limestone and (B) Slate.

on the pressure head, accompanied by a small sound, which suggests that the revised index  $W_{et}^p$  provides a more accurate judgment of rock burst proneness.

### 4.3 Effect of the L/D ratio and strain rate on rock burst

Based on the relationship between the post-peak energy dissipation and failure characteristics, the criterion for rock burst proneness has three categories: no risk, low risk, and high risk. The  $W_{et}^p$  value corresponding to the same category of rock burst proneness had a significantly different distribution. This suggests a strong quantitative correlation between  $W_{et}^p$  index and rock burst proneness. Thus, the effect of L/D ratio and strain rate on the  $W_{et}^p$  index was investigated to clarify the correlation between the post-peak dissipated energy index and actual rock burst proneness, as shown in Figures 10, 11. The influence of L/D ratio on the  $W_{et}^p$  index was fitted as a function, as evident in Table 4 and shown in Figure 10. In addition, the dashed line was added in the figure to emphasize the risk categories of actual rock burst. The fitting coefficient  $R^2$  exceeded 0.85, but the  $R^2$  value of slate was relatively smaller than that of limestone. According to Table 3, the rock failure characteristic becomes more typical with the increasing L/D

ratio. This indicates that crack propagation is concentrated around the failure path. The concentration of crack behavior enhances the interaction among cracks (Konsztowicz, 2010). Thus, crack deformation behavior became more frequent to dissipate energy, resulting in a decline of  $W_{et}^p$ . Moreover, the reduction of  $W_{et}^p$  was affected by strain rate. Especially for slate, the function parameters of strain rate at 0.5 and 1.0  $s^{-1}$  were 200% of that of strain rate at 0.05 and 0.1  $s^{-1}$ . There was a phenomenon of strain hardening in the stage of yield deformation. The acceleration of the strain rate enhanced the strain hardening effect, which extended the yield deformation stage (Lundborg, 1967). As the stored energy increased, the risk of rock burst increased correspondingly. Moreover, the fitting trend was similar to that of UCS, suggesting that the occurrence of rock burst was related to the compressive performance of rock.

For most conditions of limestone and slate, the increase in  $W_{et}^p$  with increasing  $\epsilon_e$  can be characterized as having three stages, as shown in Figure 11. There was a steady platform stage for  $W_{et}^p$ , with an increase of no more than 20% within a strain rate range from 0.01 to 0.5  $s^{-1}$ . As the L/D ratio increased, the plateau stage became more obvious. This suggests that the rate-dependent growth in  $W_{et}^p$  has a critical value with variation of L/D ratio. For slate samples with L/D ratios of 0.3 and 0.4,  $W_{et}^p$  had a nearly linear increasing trend, and the most violent rock bursts were also observed in these samples. Evolution of energy

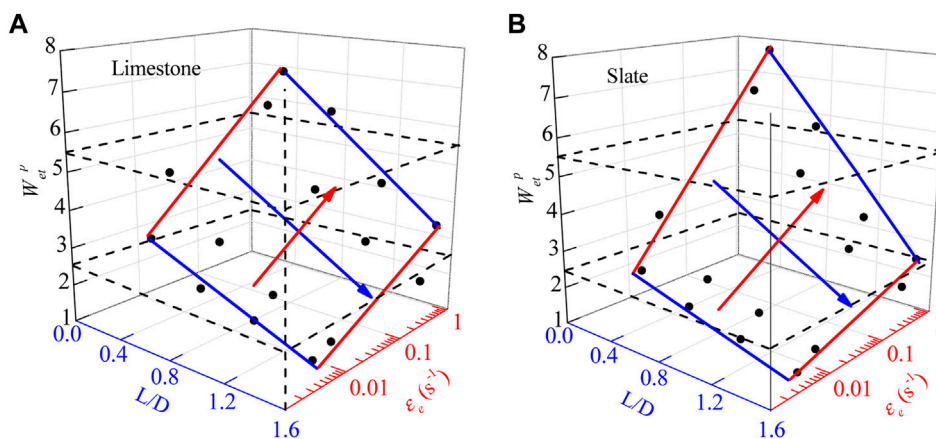


**FIGURE 12**  
Variation of  $W_{et}^p$  with different L/D ratios and strain rates for (A) Limestone and (B) Slate.

dissipation and release was closely related to the process of rock deformation until failure (Wang et al., 2019). The variation of the failure characteristics was dependent on the inertial effect of rock material under the condition of high-rate compression load. It has been shown that, when the strain rate reaches  $0.5 \text{ s}^{-1}$  (Luo et al., 2014), the period from crack initiation to rupture of a rock sample becomes shorter (Li et al., 2014). Similar results were obtained from the difference of failure characteristics, as listed in Table 3.

Comparing the curves in Figures 10, 11, it can be observed that the effects of strain rate and scale effect on  $W_{et}^p$  are opposite. There is a non-linear relationship between the L/D ratio and  $W_{et}^p$  index. This correlation is similar to the effect of L/D ratio on the UCS. This different trend induced different failure characteristics. Following the least energy consumption law, the failure of rock tends to be typical with variation of L/D ratio. However, the strain hardening effect (Wei et al., 2021) was enhanced by the increasing strain rate and generated the platform stage for the rate-dependent variation of  $W_{et}^p$ . Taking into account variation of  $W_{et}^p$  based on the combined effects of scale effect and strain rate,  $W_{et}^p$  can be obtained as follows:

$$W_{et}^p = c + a \cdot \epsilon_e - b \cdot (L/D), \quad (11)$$

where  $a$ ,  $b$ , and  $c$  are the fitting parameters with values of 3.05, 3.67, and 2.62 for limestone and 3.12, 4.27, and 2.21 for slate, respectively. The fitting result is shown in Figure 12, which is marked with a dashed line representing the risk grades of rock burst. The fitting coefficients  $R^2$  of the two rocks were 0.91 and 0.93, indicating an accurate determination of  $W_{et}^p$ . It should be noted that, for the test, the boundary of the fitting equation was set as an L/D ratio in the range of 0.3–1.5 and  $\epsilon_e$  in the range of  $0.005\text{--}1 \text{ s}^{-1}$ .

## 5 Discussion

### 5.1 Effect of strain rate and L/D ratio on linear energy characteristics

The process of rock failure is closely related to energy dissipation and storage during energy evolution. Previous studies have indicated that the characteristics of energy dissipation and storage are essential

in determining rock burst proneness (Kidybiński, 1981; Li et al., 2014; Wasantha et al., 2015; Gale, 2018; Liu X L, et al., 2020; Gong et al., 2021). To investigate the critical state of rock burst occurrence, this study proposed the post-peak dissipated energy index  $W_{et}^p$  to evaluate rock burst proneness and considers the effect of strain rate and size. Linear energy characteristics were obtained, which were influenced by variations in the L/D ratio and strain rate  $\epsilon_e$ , as demonstrated by segmented growth of  $U^e/U$  for slate and limestone in Figure 8. This finding is similar to that reported by Li et al. (2014), who noted that the strain rate has a threshold value of  $1 \times 10^{-2} \text{ s}^{-1}$  for the sudden release of elastic energy to induce splitting and even rock burst. The rate-dependent effect on rock energy characteristics was also investigated by Wasantha et al. (2015), from the perspective of mineral grain size distribution. The results revealed that the linear energy characteristic presents an increasing trend, resulting in  $U^e/U$  not maintaining a constant increasing trend with strain rate. Furthermore, the effect of strain rate on rock burst can be demonstrated through its stress adjustment response (Li et al., 2012). The size effect on rock burst is different from that of strain rate. Su (2004) analyzed size-dependent rock burst tendency from the perspective of changing brittleness and concluded that, at the same diameter, elastic energy is proportional to the L/D ratio. This result is also evident in Figure 8B. As a result, the weakening process of the sample is intensified, leading to increased brittleness (Darbor et al., 2019). From a failure perspective, stress concentration becomes more obvious at the end face of the sample as the L/D ratio decreases (Lundborg N, 1967), and the energy storage process is accelerated, leading to the ejection of rock fragments at a faster speed. These two results illustrate the significant influence of rock size on the energy storage process (Li et al., 2023). To provide a reliable reference for predicting rock burst, these findings emphasize the importance of considering the strain rate and size effects when evaluating rock burst proneness.

To examine the validity of the linear energy principle, data from various types of rocks and rock-like materials (such as coal and concrete) from other literature sources have been introduced. The materials considered in this analysis include gas coal (Gong et al., 2020), TJH coal (Liu S M et al., 2020), ordinary concrete, EPS

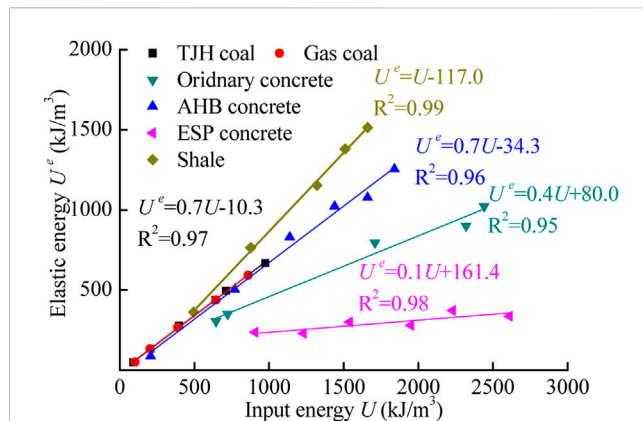


FIGURE 13

Relationship between  $U^e$  and  $U$ . Sources: shale, Iman et al. (2018); TJH coal, Liu S M et al. (2020); gas coal, Gong et al. (2020); and ordinary, ESP, and AHB concrete, Lu et al. (2017).

concrete, and AHB concrete (Lu et al., 2017), as well as shale (Iman et al., 2018), as shown in Figure 13. The results indicate a strong linear correlation between  $U^e$  and  $U$ , with a fitting coefficient  $R^2$  over 0.95. The difference in the slope values for different materials reflects their unique energy storage characteristics.

Although gas coal and TJH coal are obtained from different regions (Shaanxi and Shandong provinces, respectively), their energy storage trends are fitted to the same function (marked in black). This suggests that the energy distribution of coal is relatively stable compared to shale and concrete. However, due to the different properties of additive materials in concrete, the energy storage characteristics differ significantly. Under compressive load, the addition of AHB material causes the concrete to undergo crushed failure earlier, thus dissipating a portion of the input energy instead of storing it in the sample. Furthermore, the addition of AHB matrix generates pores at the contact surface, leading to further crack deformation and energy dissipation (Luo et al., 2014). Conversely, the addition of EPS material in concrete plays a key role in buffering the compressive loading to enhance elastic deformation, thereby improving the energy storage ability of the concrete sample (Kirane et al., 2015). The comparative analysis indicates that shale has a stronger ability to store energy than coal or concrete. This is related to the strong brittleness of shale and its elastic energy storage performance.

## 5.2 Comparative analysis of $W_{et}^P$ on rock burst proneness

Rock burst is characterized by the sudden release of stored elastic strain energy, which results in the high-speed ejection of rock fragments. The intensity of a rock burst depends on the rate of release of elastic energy. After stress adjustment in the rock mass, the stress concentration occurs at the rock mass to generate a rock burst (Feng et al., 2015). To better estimate rock burst proneness, we propose the post-peak dissipated energy index, which is based on the linear energy storage characteristics of rocks. This index accounts for the strain energy dissipation after

failure, resulting in improved accuracy in estimating rock burst proneness.

To assess the effectiveness of the proposed  $W_{et}^P$  index in predicting rock burst susceptibility, this study compared it to other indices for analyzing limestone and slate, such as the modified bursting energy index  $K_E^P$  (Liu S M et al., 2020), the potential elastic energy index  $P_{ES}$  (Małkowski and Niedbalski, 2020), and the rock burst index for rock mass  $W_{TG}$  (Bukowska M, 2005). The modified bursting energy index  $K_E^P$ , proposed by Liu X L et al. (2020), evaluates the energy release capability of rock by considering its post-failure energy behavior.

$$K_E^P = \frac{U^e}{U_{post-peak}}, \quad (12)$$

where  $K_E^P < 2$  indicates no proneness to rock burst,  $K_E^P = 2-5$  indicates low proneness to rock burst, and  $K_E^P > 5$  indicates strong proneness to rock burst.

Małkowski and Niedbalski (2020) found that the tendency for rock burst under pressure load can be evaluated by the storage of potential elastic energy. On this basis, the potential elastic energy index  $P_{ES}$  was derived using the UCS and elastic modulus as

$$P_{ES} = 500 \frac{\sigma_c^2}{E}, \quad (13)$$

where  $P_{ES}$  (kJ) classifies the rock burst tendency into four grades:  $P_{ES} < 40$  indicates no proneness,  $40 < P_{ES} < 100$  indicates weak proneness,  $100 < P_{ES} < 200$  indicates high proneness, and  $P_{ES} > 200$  indicates extreme proneness.

The characteristics of the geo-mechanical system (coal seam-surrounding rock) were analyzed to develop the criterion for rock burst tendency. In accordance with the stress-strain curves of rock mass, post-failure deformation modulus  $M$  and Young's modulus  $E$  were introduced to assess the rock burst tendency (Bukowska M, 2005):

$$W_{TG} = \frac{M}{E}, \quad (14)$$

where  $W_{TG} < 1$  indicates no proneness to rock burst,  $1 < W_{TG} < 2$  indicates little proneness to rock burst, and  $W_{TG} > 2$  indicates strong proneness to rock burst.

The modified bursting energy index  $K_E^P$  (Liu S M et al., 2020), the potential elastic energy index  $P_{ES}$  (Małkowski and Niedbalski, 2020), and the rock burst index for rock mass  $W_{TG}$  (Bukowska M, 2005) were compared to estimate the burst proneness of limestone and slate, as shown in Figure 14 and Table 5.  $P_{ES}$  exhibited a relatively accurate prediction of rock burst compared to  $K_E^P$  and  $W_{TG}$ . However, one limestone sample with an L/D ratio of 0.7 and a strain rate of  $0.5 \text{ s}^{-1}$  was overestimated as having high risk of actual rock burst.  $W_{TG}$  misjudged numerous cases, particularly those with little and strong risk of rock burst. As rock burst proneness increased, the presented brittleness in rock failure became more apparent. This indicated that an obvious stress drop occurred after the peak, leading to a large value of failure modulus  $M$ . However, the brittleness-dependent strain hardening effect led to an enhancement of the elastic deformation capacity of rock, which manifested in an increase in the elastic modulus  $E$ .  $W_{TG}$  is expressed as the ratio of  $E$  to  $M$ ; therefore, the variation of  $W_{TG}$  does not reflect the difference between  $E$  and  $M$  values in

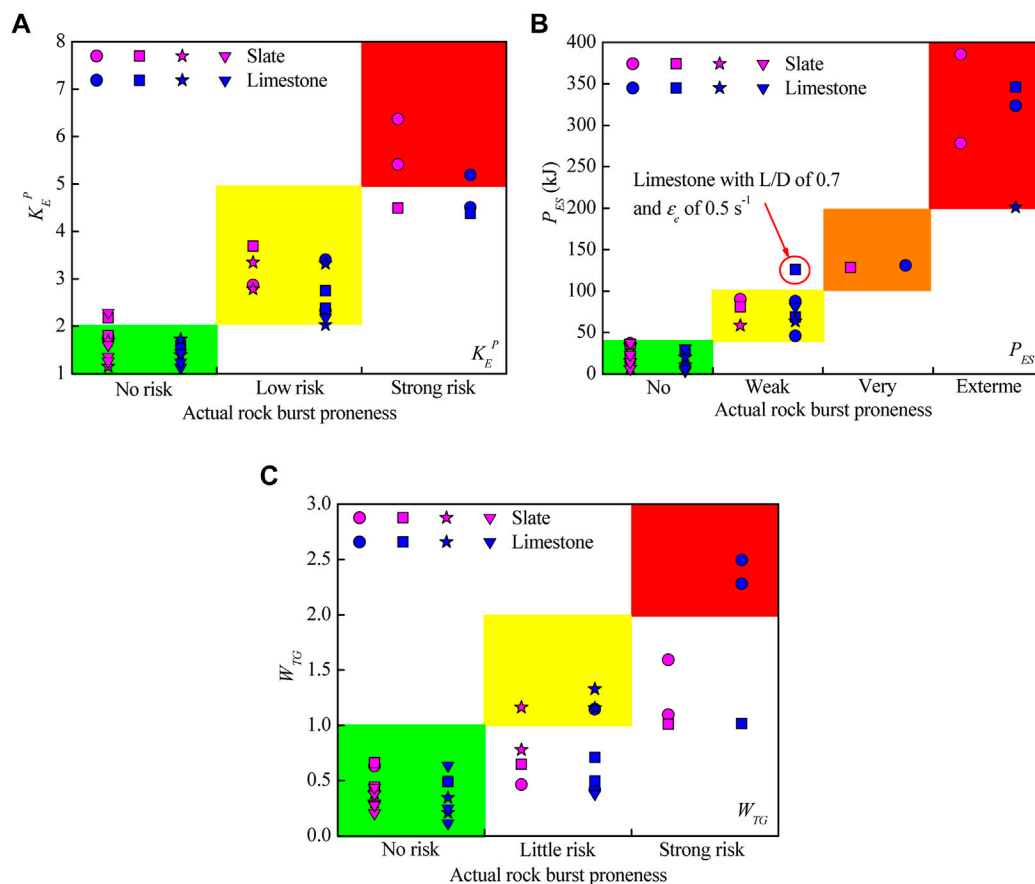


**FIGURE 14**  
Relationship between the three indices, (A)  $K_E^P$ , (B)  $P_{ES}$ , and (C)  $W_{TG}$ , and actual rock burst proneness.

representation of rock burst proneness. Moreover, a small number of  $K_E^P$  data points were distributed outside the corresponding category area of rock burst proneness. The  $K_E^P$  values of limestone and slate underestimated the low risk of actual rock burst, whereas the proposed index  $W_{et}^P$  accurately predicted rock burst proneness. The difference between the  $U^e$  and  $U_{post-peak}$  used in  $K_E^P$  did not reflect the essence of rock burst, which is the release of stored elastic strain energy.

## 6 Conclusion

Conventional compression tests were carried out on limestone and slate samples under different conditions (including variations in strain rate and sample size). By considering the energy dissipated in the post-peak stage, the  $W_{et}^P$  index was proposed to evaluate rock burst proneness. The effects of sample size and strain rate on the  $W_{et}^P$  index were investigated. Our conclusions are as follows.

(1) Under different L/D ratios and strain rates, the typical failure characteristics of limestone and slate were obtained to analyze the effect of L/D ratios and strain rates on rock mechanical parameters. As the L/D ratio increases, UCS and elastic

modulus show a non-linear decreasing trend, which is caused by the end effect of the rock sample. Variation of the strain rate changed the failure path, leading to the complexity of the rock failure type.

- (2) A linear correlation between  $U^e$  and  $U$ , namely, the linear energy storage law, was found, along with a relationship between  $U^d$  and  $U^p$ . The linear energy characteristic has different correlations with strain rate and L/D as it is positively correlated with strain rate and negatively correlated with L/D. The  $W_{et}$  index was modified to the  $W_{et}^P$  index to allow assessment of rock burst proneness by considering energy dissipation in the post-peak stage of rock deformation. Combined with the failure characteristics of rock samples associated with the different conditions, the actual rock burst proneness can be classified into three grades: no risk ( $W_{et}^P$  below 2.5), low risk ( $W_{et}^P$  between 2.5 and 5.5), and high risk ( $W_{et}^P$  exceeding 5.5) to establish the criterion for rock burst.
- (3) L/D ratio-dependent variation of the  $W_{et}^P$  index is similar to that of UCS. There is a platform stage in the relationship between  $W_{et}^P$  and strain rate, indicating that the rate-dependent growth in  $W_{et}^P$  has a critical value ( $0.1$  to  $1 \text{ s}^{-1}$ ). The accuracy of rock burst proneness based on the  $W_{et}^P$  index was verified through comparison with existing criteria. The results suggest that  $W_{et}^P$  provides an effective description of rock burst proneness.



## Data availability statement

The original contributions presented in the study are included in the article/Supplementary Material; further inquiries can be directed to the corresponding author.

## Author contributions

XL: methodology and writing—original draft. YZ: software and formal analysis. HX: investigation and resources. LL: investigation and resources. HW: conceptualization, methodology, supervision, and writing—review and editing.

## Acknowledgments

The authors acknowledge the financial support provided by the Key R&D and Transformation Plan of Qinghai Province (Grant No. 2021-SF-167).

## References

- Ai, C., Zhang, J., Li, Y. W., Zeng, J., Yang, X. L., and Wang, J. G. (2016). Estimation criteria for rock brittleness based on energy analysis during the rupturing process. *Rock Mech. Rock Eng.* 49 (12), 4681–4698. doi:10.1007/s00603-016-1078-x
- Bukowska, M. (2005). Indicative methods for assessment of liability of rocks and rock mass to rock-bumps. *Res. Rep. Min. Environ.* 2, 95–107.
- Cai, W., Dou, L. M., Si, G. Y., and Hu, Y. W. (2021). Fault-induced coal burst mechanism under mining-induced static and dynamic stresses. *Engineering-Proc.* 7 (5), 687–700. doi:10.1016/j.eng.2020.03.017
- Cai, W. Q., Zhu, H. H., and Liang, W. H. (2022). Three-Dimensional tunnel face extrusion and reinforcement effects of underground excavations in deep rock masses. *Int. J. Rock Mech. Min. Sci.* 150, 104999. doi:10.1016/j.ijrmms.2021.104999
- Cook, N. G. W. (1976). Seismicity associated with mining. *Eng. Geol.* 10, 99–122. doi:10.1016/0013-7952(76)90015-6
- Dai, L. P., Pan, Y. S., Zhang, C. G., Wang, A. W., Canbulat, I., Shi, T. W., et al. (2022). New criterion of critical mining stress index for risk evaluation of roadway rockburst. *Rock Mech. Rock Eng.* 55 (8), 4783–4799. doi:10.1007/s00603-022-02888-7
- Dai, S., Wang, X., Pan, Y., and Liu, L. (2019). Experimental study on the evaluation of coal burst tendency utilizing modulus index. *J. China Coal Soc.* 44 (6), 1726–1731.
- Darbor, M., Faramarzi, L., and Sharifzadeh, M. (2019). Size-dependent compressive strength properties of hard rocks and rock-like cementitious brittle materials. *Geosystem Eng.* 22 (4), 179–192. doi:10.1080/12269328.2018.1431961
- Diederichs, M. S. (2007). The 2003 Canadian geotechnical colloquium: Mechanistic interpretation and practical application of damage and spalling prediction criteria for deep tunnelling. *Can. Geotech. J.* 44 (9), 1082–1116. doi:10.1139/t07-033
- Diederichs, M. S., Kaiser, P. K., and Eberhardt, E. (2004). Damage initiation and propagation in hard rock during tunnelling and the influence of near-face stress rotation. *Int. J. Rock Mech. Min. Sci.* 41 (5), 785–812. doi:10.1016/j.ijrmms.2004.02.003
- Du, K., Tao, M., Li, X. B., and Zhou, J. (2016). Experimental study of slabbing and rockburst induced by true-triaxial unloading and local dynamic disturbance. *Rock Mech. Rock Eng.* 49 (9), 3437–3453. doi:10.1007/s00603-016-0990-4
- Feng, G. L., Chen, B. R., Jiang, Q., Xiao, Y. X., Niu, W. J., and Li, P. X. (2021). Excavation-induced microseismicity and rockburst occurrence: Similarities and differences between deep parallel tunnels with alternating soft-hard strata. *J. Cent. South. Univ.* 28, 582–594. doi:10.1007/s11771-021-4623-z
- Feng, G. L., Feng, X. T., Chen, B. R., Xiao, Y. X., and Yu, Y. (2015). A microseismic method for dynamic warning of rockburst development processes in tunnels. *Rock Mech. Rock Eng.* 48 (5), 2061–2076. doi:10.1007/s00603-014-0689-3
- Gale, W. J. (2018). A review of energy associated with coal bursts. *Int. J. Min. Sci. Technol.* 28 (5), 755–761. doi:10.1016/j.ijmst.2018.08.004
- Gong, F. Q., Luo, S., and Yan, J. Y. (2018c). Energy storage and dissipation evolution process and characteristics of marble in three tension-type failure tests. *Rock Mech. Rock Eng.* 51 (11), 3613–3624. doi:10.1007/s00603-018-1564-4
- Gong, F. Q., Luo, Y., Li, X. B., Si, X. F., and Tao, M. (2018a). Experimental simulation investigation on rockburst induced by spalling failure in deep circular tunnels. *Tunn. Undergr. Space. Technol.* 81, 413–427. doi:10.1016/j.tust.2018.07.035
- Gong, F. Q., Si, X. F., Li, X. B., and Wang, S. Y. (2018b). Experimental investigation of strain rockburst in circular caverns under deep three-dimensional high-stress conditions. *Rock Mech. Rock Eng.* 52, 1459–1474. doi:10.1007/s00603-018-1660-5
- Gong, F. Q., Wang, Y. L., and Luo, S. (2020). Rockburst proneness criteria for rock materials: Review and new insights. *J. Cent. South Univ.* 27 (10), 2793–2821. doi:10.1007/s11771-020-4511-y
- Gong, F. Q., Wang, Y. L., Wang, Z. G., Pan, J. F., and Luo, S. (2021). A new criterion of coal burst proneness based on the residual elastic energy index. *Int. J. Min. Sci. Tec.* 31, 553–563. doi:10.1016/j.ijmst.2021.04.001
- Gong, F. Q., Yan, J. Y., Li, X., and Luo, S. (2019). A peak-strength strain energy storage index for rock burst proneness of rock materials. *Int. J. Rock Mech. Min. Sci.* 117, 76–89. doi:10.1016/j.ijrmms.2019.03.020
- He, M. C., Sousa, L. R. E., Miranda, T., and Zhu, G. L. (2015). Rockburst laboratory tests database-application of data mining techniques. *Eng. Geol.* 185, 116–130. doi:10.1016/j.enggeo.2014.12.008
- He, M. M., Wang, J., Yuan, Z. Y., Wang, H. T., Ma, X. D., and Luo, B. (2023). Evaluating the anisotropy of drilling mechanical characteristics of rock in the process of digital drilling. *Acta geophys.*, doi:10.1007/s00603-023-03242-1
- Iman, R., Kivi, I. R., Ameri, M., and Molladavoodi, H. (2018). Shale brittleness evaluation based on energy balance analysis of stress-strain curves. *J. Pet. Sci. Eng.* 167, 1–19. doi:10.1016/j.petrol.2018.03.061
- Kahraman, S. (2002). Correlation of TBM and drilling machine performances with rock brittleness. *Eng. Geol.* 65 (4), 269–283. doi:10.1016/s0013-7952(01)00137-5
- Kaiser, P. K., and Cai, M. F. (2012). Design of rock support system under rockburst condition. *J. Rock Mech. Geotech. Eng.* 4, 215–227. doi:10.3724/sp.j.1235.2012.00215
- Keneti, A., and Sainsbury, B. A. (2018). Review of published rockburst events and their contributing factors. *Eng. Geol.* 246, 361–373. doi:10.1016/j.enggeo.2018.10.005
- Khosravi, A., and Simon, R. (2018). Verification of the CSDS model in estimating the postpeak behavior of hard rocks. *Int. J. Geomech.* 18 (3), 04017166. doi:10.1061/(asce)gm.1943-5622.0001090
- Kidybiński, A. (1981). Bursting liability indices of coal. *Int. J. Rock Mech. Min. Sci.* 18, 295–304. doi:10.1016/0148-9062(81)91194-3
- Kirane, K., Su, Y., and Bazóant, Z. P. (2015). Strain-rate-dependent micro plane model for high rate comminution of concrete under impact based on kinetic energy release theory. *Proc. R. Soc. A Math. Phys. Eng. Sci.* 471, 20150535. doi:10.1098/rspa.2015.0535
- Konicek, P., and Waclawik, P. (2018). Stress changes and seismicity monitoring of hard coal longwall mining in high rockburst risk areas. *Tunn. Undergr. Space Technol.* 81, 237–251. doi:10.1016/j.tust.2018.07.019

## Conflict of interest

Author XL was employed by Qinghai Traffic Construction Management Co., Ltd., and authors XL, HX, and LL were employed by Qinghai Xihu Expressway Management Co., Ltd.

The remaining authors declare that the research was conducted in the absence of any commercial or financial relationships that could be construed as a potential conflict of interest.

## Publisher's note

All claims expressed in this article are solely those of the authors and do not necessarily represent those of their affiliated organizations, or those of the publisher, the editors, and the reviewers. Any product that may be evaluated in this article, or claim that may be made by its manufacturer, is not guaranteed or endorsed by the publisher.

- Konsztowicz, K. J. (2010). Crack growth and acoustic emission in ceramics during thermal shock. *J. Am. Ceram. Soc.* 73 (3), 502–508. doi:10.1111/j.1151-2916.1990.tb06545.x
- Li, S. J., Feng, X. T., Li, Z. H., Chen, B. R., Zhang, C. Q., and Zhou, H. (2012). *In situ* monitoring of rockburst nucleation and evolution in the deeply buried tunnels of Jinping II hydropower station. *Eng. Geol.* 137 (7), 85–96. doi:10.1016/j.enggeo.2012.03.010
- Li, X. L., Chen, S. J., Liu, S. M., and Li, Z. H. (2021a). AE waveform characteristics of rock mass under uniaxial loading based on Hilbert-Huang transform. *J. Cent. South Univ.* 28 (6), 1843–1856. doi:10.1007/s11771-021-4734-6
- Li, X. L., Chen, S. J., and Wang, S. (2021b). Study on *in situ* stress distribution law of the deep mine taking Linyi Mining area as an example. *Adv. Mater. Sci. Eng.* 9 (4), 5594181.
- Li, X. L., Zhang, X. Y., Shen, W. L., Zeng, Q., Chen, P., Qin, Q., et al. (2023). Research on the mechanism and control technology of coal wall sloughing in the ultra-large mining height working face. *Int. J. Env. Res. Pub. He* 20 (2), 868. doi:10.3390/ijerph20010868
- Li, Y., Huang, D., and Li, X. A. (2014). Strain rate dependency of coarse crystal marble under uniaxial compression: Strength, deformation and strain energy. *Rock Mech. Rock Eng.* 47 (4), 1153–1164. doi:10.1007/s00603-013-0472-x
- Liu, H. Y., Zhang, B. Y., Li, X. L., Liu, C., Wang, C., Wang, F., et al. (2022). Research on roof damage mechanism and control technology of gob-side entry retaining under close distance gob. *Eng. Fail. Anal.* 138 (5), 106331. doi:10.1016/j.engfailanal.2022.106331
- Liu, S. M., Li, X. L., and Wang, D. K. (2020). Investigations on the mechanism of the microstructural evolution of different coal ranks under liquid nitrogen cold soaking. *Energy Sources, Part A Recovery, Util. Environ. Eff.* 17, 1. doi:10.1080/15567036.2020.1841856
- Liu, X. L., X. L., Liu, Q., Liu, B., and Kang, Y. (2020). A modified bursting energy index for evaluating coal burst proneness and its application in ordos coalfield, China. *China. Energies* 13 (7), 1729. doi:10.3390/en13071729
- Liu, X. Q., Wang, G., Song, L. B., Han, G. S., Chen, W. Z., and Chen, H. (2023). A new rockburst criterion of stress-strength ratio considering stress distribution of surrounding rock. *B Eng. Geol. Environ.* 82 (1), 29. doi:10.1007/s10064-022-03042-x
- Lu, S., Xu, J. Y., Bai, E. L., and Luo, X. (2017). Effect of particles with different mechanical properties on the energy dissipation properties of concrete. *Constr. Build. Mat.* 144, 502–515. doi:10.1016/j.conbuildmat.2017.02.161
- Lundborg, N. (1967). The strength-size relation of granite. *Int. J. Rock Mech. Min. Sci. Geomech. Abstr.* 4 (3), 269–272. doi:10.1016/0148-9062(67)90011-3
- Luo, X., Xu, J. Y., Bai, E. L., and Li, W. (2014). Study on the effect of basalt fiber on the energy absorption characteristics of porous material. *Constr. Build. Mat.* 68 (6), 384–390. doi:10.1016/j.conbuildmat.2014.06.072
- Malan, D. F., and Napier, J. A. L. (2018). Rockburst support in shallow-dipping tabular stope at great depth. *Int. J. Rock Mech. Min. Sci.* 112, 302–312. doi:10.1016/j.ijrmms.2018.10.026
- Małkowski, P., and Niedbalski, Z. (2020). A comprehensive geomechanical method for the assessment of rockburst hazards in underground mining. *Int. J. Min. Sci. Tech.* 30 (3), 345–355. doi:10.1016/j.ijmst.2020.04.009
- Martin, C. D., and Maybee, W. G. (2000). The strength of hard-rock pillars. *Int. J. Rock Mech. Min. Sci.* 37 (8), 1239–1246. doi:10.1016/s1365-1609(00)00032-0
- Masoumi, H., Saydam, S., and Hagan, P. C. (2016). Unified size-effect law for intact rock. *Int. J. Geomech.* 16 (2), 04015059. doi:10.1061/(asce)gm.1943-5622.0000543
- Mazaira, A., and Konicek, P. (2015). Intense rockburst impacts in deep underground construction and their prevention. *Can. Geotech. J.* 52 (10), 1426–1439. doi:10.1139/cgj-2014-0359
- Quñones, J., Arzúa, J., Alejano, L., García-Bastante, F., Ivars, D. M., and Walton, G. (2017). Analysis of size effects on the geomechanical parameters of intact granite samples under unconfined conditions. *Acta. Geotech.* 12 (6), 1229–1242. doi:10.1007/s11440-017-0531-7
- Rybacki, E., Meier, T., and Dresen, G. (2016). What controls the mechanical properties of shale rocks? – Part II: Brittleness. *J. Pet. Sci. Eng.* 144, 39–58. doi:10.1016/j.petrol.2016.02.022
- Singh, S. P. (1989). Classification of mine workings according to their rockburst proneness. *Min. Sci. Technol.* 8, 253–262. doi:10.1016/s0167-9031(89)90404-0
- Singh, S. P. (1988). Burst energy release index. *Rock Mech. Rock Eng.* 21 (2), 149–155. doi:10.1007/bf01043119
- Sousa, L. R. E., Miranda, T., Sousa, R. L. E., and Tinoco, J. (2017). The use of data mining techniques in rockburst risk assessment. *Engineering-Proc* 3 (4), 552–558. doi:10.1016/j.eng.2017.04.002
- Su, C. D. (2004). Testing study on the effect of crystal size and specimen length on the rockburst tendency. *China. J. Rock Mech. Eng.* 23 (22), 3750–3753.
- Tang, L. Z., Pan, C. L., and Wang, W. X. (2002). Surplus energy index for analyzing rock burst proneness. *J. Cent. South Univ. Technol.* 33, 129–132.
- Tarasov, B., and Potvin, Y. (2013). Universal criteria for rock brittleness estimation under triaxial compression. *Int. J. Rock Mech. Min.* 59, 57–69. doi:10.1016/j.ijrmms.2012.12.011
- Tekalur, S. A., and Sen, O. (2011). Effect of specimen size in the Kolsky bar. *Procedia Eng.* 10, 2663–2671. doi:10.1016/j.proeng.2011.04.444
- ISRM (2007). “The complete ISRM suggested methods for rock characterization, testing and monitoring: 1974–2006,” in *Prepared by the commission on testing methods*. Editors R. Ulusay and J. A. Hudson (Ankara: ISRM).
- Walton, G., Labrie, D., and Alejano, L. R. (2019). On the residual strength of rocks and rock masses. *Rock Mech. Rock Eng.* 52, 4821–4833. doi:10.1007/s00603-019-01879-5
- Wang, H. T., He, M. M., Pang, F., Chen, Y., and Zhang, Z. (2021). Energy dissipation-based method for brittleness evolution and yield strength determination of rock. *J. Pet. Sci. Eng.* 200, 108376. doi:10.1016/j.petrol.2021.108376
- Wang, H. T., He, M. M., Zhang, Z. Q., and Zhu, J. (2022a). Determination of the constant  $m$  in the Hoek-Brown criterion of rock based on drilling parameters. *Int. J. Min. Sci. Technol.* 32 (4), 747–759. doi:10.1016/j.ijmst.2022.06.002
- Wang, H. T., He, M. M., Zhu, J. W., Guo, S., and Chen, Y. (2022b). Experimental investigation of linear damping characteristics on granite and red sandstone under dynamic cyclic loading. *Eur. J. Environ. Civ. En.* 26 (11), 5259–5278. doi:10.1080/19648189.2021.1890230
- Wang, H. T., and He, M. M. (2023a). Determining method of tensile strength of rock based on friction characteristics in the drilling process. *Rock Mech. Rock Eng.* doi:10.1007/s00603-023-03276-5
- Wang, J., He, M. M., Yuan, Z. Y., Luo, B., and Ma, Y. D. (2023b). Ductile-brittle failure transition of rocks in process of drilling with high confining pressure: Model and experiment. *J. Pet. Sci. Eng.* 2023, 211505. doi:10.1016/j.jgeo.2023.211505
- Wang, J. A., and Park, H. D. (2001). Comprehensive prediction of rockburst based on analysis of strain energy in rocks. *Tunn. Undergr. Space Technol.* 16, 49–57. doi:10.1016/s0886-7798(01)00030-x
- Wang, S. F., Li, X. B., Yao, J. R., Gong, F. Q., Li, X., Du, K., et al. (2019). Experimental investigation of rock breakage by a conical pick and its application to non-explosive mechanized mining in deep hard rock. *Int. J. Rock Mech. Min.* 122, 104063. doi:10.1016/j.ijrmms.2019.104063
- Wasantha, P. L. P., Ranjith, P. G., Zhao, J., Shao, S. S., and Permata, G. (2015). Strain rate effect on the mechanical behaviour of sandstones with different grain sizes. *Rock Mech. Rock Eng.* 48 (5), 1883–1895. doi:10.1007/s00603-014-0688-4
- Wei, M. D., Dai, F., Liu, Y., Li, A., and Yan, Z. L. (2021). Influences of loading method and notch type on rock fracture toughness measurements: From the perspectives of T-stress and fracture process zone. *Rock Mech. Rock Eng.* 54 (9), 4965–4986. doi:10.1007/s00603-021-02541-9
- Wojtecki, L., Iwaszenko, S., Apel, D. B., and Cichy, T. (2021). An attempt to use machine learning algorithms to estimate the rockburst hazard in underground excavations of hard coal mine. *Energies* 14 (21), 6928. doi:10.3390/en14216928
- Yang, B. B., He, M. M., Zhang, Z. Q., Zhu, J. W., and Chen, Y. S. (2022a). A new criterion of strain rockburst in consideration of the plastic zone of tunnel surrounding rock. *Rock Mech. Rock Eng.* 55 (3), 1777–1789. doi:10.1007/s00603-021-02725-3
- Yang, F. J., Hui, Z., Xiao, H. B., Azhar, M. U., Yong, Z., and Chi, F. D. (2022b). Numerical simulation method for the process of rockburst. *Eng. Geol.* 306, 106760. doi:10.1016/j.enggeo.2022.106760
- Yang, X., Ren, T., Tan, L., Remennikov, A., and He, X. (2018). Developing coal burst propensity index method for Australian coal mines. *Int. J. Min. Sci. Technol.* 28 (5), 783–790. doi:10.1016/j.ijmst.2018.08.008
- Yumlu, M., and Ozbay, M. U. (1995). A study of the behaviour of brittle rocks under plane strain and triaxial loading conditions. *Int. J. Rock Mech. Min. Sci.* 32 (7), 725–733. doi:10.1016/0148-9062(95)00025-c
- Zhang, X., Feng, G., Kang, L., and Yang, S. (2009). Method to determine burst tendency of coal rock by residual energy emission speed. *J. China Coal. Soc.* 34 (9), 1165–1168.
- Zhou, X. M., Wang, S., Li, X. L., Meng, J., Li, Z., Zhang, L., et al. (2022). Research on theory and technology of floor heave control in semicool rock roadway: Taking longhu coal mine in Qitaihe mining area as an Example. *Lithosphere-US* 11, 3810988. doi:10.2113/2022/3810988



## OPEN ACCESS

## EDITED BY

Xuelong Li,  
Shandong University of Science and  
Technology, China

## REVIEWED BY

Rulong Bn,  
Guilin University of Technology, China  
Junlong Sun,  
Kunming University of Science and  
Technology, China

## \*CORRESPONDENCE

Liu Menghua,  
✉ lmhczzx@163.com

## SPECIALTY SECTION

This article was submitted to  
Environmental Informatics  
and Remote Sensing,  
a section of the journal  
Frontiers in Earth Science

RECEIVED 01 March 2023

ACCEPTED 31 March 2023

PUBLISHED 09 May 2023

## CITATION

Jianbo M, Zhongqi W, En Y and  
Menghua L (2023), Research on  
evaluation model of rock failure integrity  
under complex geological conditions in  
karst area.

*Front. Earth Sci.* 11:1177459.

doi: 10.3389/feart.2023.1177459

## COPYRIGHT

© 2023 Jianbo, Zhongqi, En and  
Menghua. This is an open-access article  
distributed under the terms of the  
[Creative Commons Attribution License  
\(CC BY\)](https://creativecommons.org/licenses/by/4.0/). The use, distribution or  
reproduction in other forums is  
permitted, provided the original author(s)  
and the copyright owner(s) are credited  
and that the original publication in this  
journal is cited, in accordance with  
accepted academic practice. No use,  
distribution or reproduction is permitted  
which does not comply with these terms.

# Research on evaluation model of rock failure integrity under complex geological conditions in karst area

Ma Jianbo, Wang Zhongqi, Yang En and Liu Menghua\*

State Key Laboratory of Explosion Science and Technology, School of Mechatronics Engineering, Beijing  
Institute of Technology, Beijing, China

Blasting lumpiness prediction is one of the most important research contents in engineering blasting. Although the traditional KUZ-RAM model is widely used, it often overestimates the size of blasting. Therefore, the KUZ-RAM model was updated or corrected in this paper by simplifying the difficult problem of statistical burst fragmentation in LS-DYNA. Based on the theory of area measurement method, the fitting mechanism of machine learning is used to study the lumpiness of simulation results. The updated KUZ-RAM model adds a coefficient of 0.623 to the original equation of average lumpiness  $x_m$ . The linear coefficient  $R^2$  between the predicted results and the field blasting results increases from  $-1.99$  to  $0.97$ , which significantly improves the prediction of blasting lumpiness.

## KEYWORDS

step blasting, average lumpiness, KUZ-RAM model, area measurement method, numerical simulation calculation

## 1 Introduction

The karst area in the world accounts for 7%–12% of the total land area. As a drinking water source, karst water supplies 20%–25% of the world's population. China is the country with the widest karst distribution area in the world, accounting for about 1/3 of the land area. With the development of engineering construction in China, a large number of projects need to pass through karst areas. Due to the complex geological conditions, large differences in water-rich characteristics and strong heterogeneity of karst areas, various disasters and accidents are very likely to occur during the construction process.

The fragmentation of rocks is an important factor that affects the efficiency and economy of mining (Shim et al., 2009). Blasting is one of the most commonly used methods for mining, and the size of rock fragmentation and the blasting distribution function after blasting are often used as a basis for scientific judgment and description to evaluate the mining benefits of blasting. Blast fragmentation is a complex issue that has been studied by many scholars in the past few decades. Based on theories such as energy theory and stress wave theory, many models have been established and widely recognized and applied, such as the Hanukayev model (Favreau, 1983), the Harries model (Harries, 1977), the Lilly blasting capability index model (Lilly, 1986), the BLASPA blasting mathematical model (Favreau et al., 1983), the NAG-FRAG model (McHugh, 1983), and the KUZ-RAM block distribution calculation formula (Cunningham, 1987) proposed by Cunningham (1987) base on the Kuznetsov equation (Kuznetsov, 1973) and R-R formula (Just, 1974). However, the prediction results are still less accurate and have great application limitations due to

rock classification problems. In recent years, many scholars are still paying attention to the stability of the mining site and the influence of the collapse mechanism on block size Li et al. (2021a), and trying to revise and optimize existing models in a more scientific way, such as Gheibie et al. (2009) has corrected KUZ-RAM; Lawal (2021) also used image processing technology to optimize the KUZ-RAM model; Liu et al. (2020) established its relationship with pore parameters based on the comprehensive study of fractal dimension by Turcotte (1986) and Harries (1973); L.G.Margolin, etc. Margolin et al. (1985) proposed the BCM layered crack model, etc., also some important empirical formulas summarized from field experience da Gama (1971). However, there are still problems of narrow application scope and poor practical use effect.

The fragmentation of rocks is an important factor that affects the efficiency and economy of mining (Shim et al., 2009). Blasting is one of the most commonly used methods for mining, and the size of rock fragmentation and the blasting distribution function after blasting are often used as a basis for scientific judgment and description to evaluate the mining benefits of blasting.

Blast fragmentation is a complex issue that has been studied by many scholars in the past few decades. Based on theories such as energy theory and stress wave theory, many models have been established and widely recognized and applied, such as the Hanukayev model (Favreau, 1983), the Harries model (Harries, 1977), the Lilly blasting capability index model (Lilly, 1986), the BLASPA blasting mathematical model FavreauR. (1983), the NAG-FRAG model (McHugh, 1983), and the KUZ-RAM block distribution calculation formula (Cunningham, 1987) proposed by Cunningham (1987) base on the Kuznetsov equation (Kuznetsov, 1973) and R-R formula (Just, 1974). However, the prediction results are still less accurate and have great application limitations due to rock classification problems. In recent years, many scholars are still paying attention to the stability of the mining site and the influence of the collapse mechanism on block size Li et al. (2021a), and trying to revise and optimize existing models in a more scientific way, such as Gheibie et al. (2009) has corrected KUZ-RAM; Lawal (2021) also used image processing technology to optimize the KUZ-RAM model; Liu et al. (2020) established its relationship with pore parameters based on the comprehensive study of fractal dimension by Turcotte (1986) and Harries (1973); L.G.Margolin, etc. (Margolin et al., 1985) proposed the BCM layered crack model, etc., also some important empirical formulas summarized from field experience da Gama (1971). However, there are still problems of narrow application scope and poor practical use effect.

In recent years, computer science and image processing methods have gradually been applied to the field of blast fragmentation research. Trivedi (TRIVEDI and GUPTAN, 2015) was the first to apply neural networks (ANN) and adaptive neural networks (ANFIS) to open pit blasting research. Shim et al. (2009) combined the KUZ-RAM block prediction model and SIS three-dimensional data prediction technology to optimize blast parameters in their research. A. Bahrami et al. (2010) established a BP neural network using 220 data to optimize blasting. Asl PF (Asl et al., 2018) used the firefly algorithm to predict flying rocks and fragmentation; and Mehrdaneh A (Mehrdaneh et al., 2018) introduced robotic technology into the evaluation of rock fracture. Xie et al. (2021) found the stability and applicability of the FFA-GBM algorithm after comparing various machine learning algorithms. Zhou et al. (2022) studied the stability of floor through numerical simulation. These

studies provide the basis for computer study of blasting block size, but there is still a lack of detailed determination of blasting block size.

In addition, image processing methods were introduced to study the impact of blasting on mine stability and block size as early as 1960 by the line segment measurement method proposed by Bapon (Sanchidrián et al., 2006). In recent years, there have been new developments in the image method, with the use of photography technology to determine the actual size of the blast block having taken off (Ozkahraman, 2006; Kabwe, 2018). Kruttschnitt et al. (Sanchidrián et al., 2009) have achieved the extraction of ore particle size information from multiple parallel belt conveyors using laser sensors; Lange and Crida (Cao et al., 2015) have respectively developed an ore particle size detection system and ore separation software. The commercial software such as Wipfrag, FragScan, SplitDesktop, and WIEP, which are used to analyze rock fragment size distributions, also indicate the continuous improvement and maturity of image processing.

In conclusion, a variety of methods have been applied in the research of blasting, but there are still some defects in the determination of blasting block size. Considering the KUZ-RAM prediction model overestimates the size of the blasting block, this paper, combining computer science and image processing technology, optimizes the empirical prediction formula for  $x_m$  in the original model based on the results of actual blasting and simulated calculation. Taking the results of area measurement as the standard and adding the necessary correction factors, the accuracy of the modified model in the actual mine application is further verified. This is of great significance for improving the evaluation of the blasting effect of open-air step blasting.

## 2 Computational theory and method

### 2.1 R-R distribution and KUZ-RAM model

In this paper, R-R distribution model is used to describe the block size distribution. The R-R distribution model can be expressed as:

$$Y = 1 - \exp \left[ - \left( \frac{x}{x_0} \right)^n \right] \quad (1)$$

where,  $Y$  is the accumulation rate (%) under the screen if the particle size is less than  $x$ ;  $x$  is the rock block size or screen size (mm);  $x_0$  is the characteristic size of the rock block, that is, the block size (mm) when the accumulation rate under the screen is  $(1-1/e)\%$ ,  $x_0 = \frac{x_m}{n \sqrt{0.693}}$ ,  $x_m$  is the average block size (mm);  $n$  is the rock block particle size distribution parameter (SpathisAlex, 2004).

The relationship between explosive consumption per unit and blasting average block size  $x_m$  in open-pit mines is as follows, according to the relationship between average block size  $x_m$  and blasting parameters established by Kuznetsov (1973) and Thomas Busuyi (2009):

$$x_m = Ak^{-0.8} e^{1/6} \left( \frac{115}{S_{anfo}} \right)^{-\frac{19}{30}} \quad (2)$$

Where,  $x_m$  is the average diameter of block size (mm);  $A$  is the rock coefficient;  $k$  is the single consumption of explosive;  $e$  is the single



TABLE 1 Parameter values in various rock mass conditions.

Symbol	Quantity	Rating
A	Rock factor	
RMD	Rock Mass Description	
	-powdery/friable	10
	-vertically jointed	JF
	-massive	50
JF	JPS + JPA	
JPS	Vertical Joint Spacing	
	- < 0.1m	10
	-0.1 to MS	20
	-MS to DP	50
MS	Oversize(m)	
DP	Drilling pattern size(m) assuming	
	DP > MS	
JPA	Joint plane angle	
	-dip out of face	20
	-strike perpendicular to face	30
	-dip into face	40
RDI	Density influence	25 × RD – 50
RD	Density (t/m <sup>3</sup> )	
HF	Hardness factor	
	-If Y < 50 GPa	HF=Y/3
	-If Y > 50 GPa	HF=UCS/5
Y	Youngs modulus (GPa)	
UCS	Unconfined compressive strength (MPa)	

hole charge (kg);  $S_{anfo}$  is the weight power of explosive relative to ANFO explosive (115-TNT).

Rock coefficient (A) can be calculated from Eq. 4 according to the related studies of Cunningham (1987) and Lilly (1986). Specific parameters are shown in Table 1.

$$A = 0.06(RMD + JF + RDI + HF) \quad (3)$$

## 2.2 Area measurement method

Rock screening can be regarded as the process of standard ellipsoid passing through the sieve, and its size can be calculated according to the best matching ellipsoid and area measurement method (Zhao, 2015):

$$a = \frac{\frac{p}{\pi} + \sqrt{\frac{p^2}{\pi^2} - \frac{4s}{\pi}}}{2}, b = \frac{\frac{p}{\pi} - \sqrt{\frac{p^2}{\pi^2} - \frac{4s}{\pi}}}{2} \quad (4)$$

where,  $a$  is the maximum radius of the best matching ellipsoid (mm); and  $b$  is the minimum radius of the best matching ellipsoid (mm);  $p$  is the perimeter of the exposed part of the rock (mm),  $s$  is the area of the exposed part of the rock (mm<sup>2</sup>).

There is a functional relationship between the sifting diameter ( $d$ ) of rock blocks and the maximum and minimum radius of the best matching ellipse of rock blocks:

$$d = 1.16b\sqrt{\frac{1.35a}{b}} \quad (5)$$

Thus, the sieving size of the rock block can be calculated by areal measurement. The measurement accuracy of area measurement method can reach 50 mm, and too small rock has no reference value.

In order to verify the accuracy of the area measurement method, this paper compares the image processing results with the field measurement results, as shown in Table 2.

As can be seen from the comparison in the table, the error between the image processing result and the measured result is about 5%. Considering the possible errors in the application, it can be considered that the image processing result is consistent with the real value.

A scientific extended application of the area measurement was adopted in this paper. Specifically, assuming that the density ( $\rho$ ) of the rock block is same, the mass ( $m$ ) of the rock block was replaced by the volume ( $V$ ). Then, the volume accumulation rate of the best matching ellipsoid is used to approximate the mass accumulation rate of the rock block under the sieve. The sieving diameter ( $d$ ) of the rock and the volume ( $V'$ ) of the corresponding best matching ellipsoid are taken as a set of data, and arranged by the size  $d$ . According to the superposition principle, if the volume corresponding to a certain screen size  $d'$  is  $V'_j$ , then the ratio of the sum of all volumes ( $\sum_{n \leq j}^j V'_n$ ) corresponding to  $\sum V'$  under the screen size to the sum of the total volume is the accumulation rate under the screen  $Y$ . Then,  $x_m$ ,  $x_0$ , and the accumulation rate of each screen size can be obtained. Finally, the R-R distribution model can be obtained.

## 2.3 Comparison between traditional KUZ-RAM model and area measurement method

The actual engineering data of Shenghua Quarry in Hebei Province and Yuanjiacun Iron Mine in Shanxi Province (in China) were used to verify the accuracy of the proposed model. In order to ensure the scientificity and accuracy of the field measured data, 15 groups of blasting measurement data under different blasting conditions at the two sites are selected for analysis and comparison. It is worth mentioning that stratified sampling is used to collect the size of the burst pile rock after rock blasting. The average diameter  $x_m$  and characteristic diameter  $x_0$  of rock block obtained by area measurement method and traditional KUZ-RAM model are shown in Table 3.

The comparison of the calculation results of the two blasting rocks is shown in Figure 1. The results predicted by the traditional KUZ-RAM model are all larger than those obtained by the area measurement method. It can be seen that it is necessary for KUZ-RAM to add a correction coefficient term to the prediction model of  $x_m$  to correct the above errors.



TABLE 2 Comparison between image analysis results and measured results.

Conditions	Actual perimeter $L_1$ (mm)	Calculated perimeter $L_2$ (mm)	Error ( $\frac{ L_1-L_2 }{L_1}$ )
1	342	336	1.8%
2	106	102	3.8%
3	191	187	2.1%
4	168	175	4.2%
5	109	102	6.4%

TABLE 3 Rock size characteristics predicted by acreage measurement and initial model.

Data source	Area measurement method ( $x_m$ /mm)	Traditional KUZ-RAM model ( $x_m$ /mm)
Shenghua Quarry	314.7	512.4
	266.4	423.5
	269.9	438.1
	377.4	625.7
	387.6	652.4
Yuanjiacun Iron Mine	364.7	588.3
	277.2	435.2
	410.2	643.6
	422.9	668.2
	358.2	593.6
	261.1	406.6
	397.4	627.4
	383.1	624.2
	413.3	637.7
	382.8	628.9

### 3 Simulation calculation

#### 3.1 Model construction

The three-hole model is constructed by simplifying the blasting situation in the field mining to simulate the field experiment. Its geometric structure and size are shown in [Figures 2, 3](#). In the figures,  $H$  is the step height (9 m);  $T$  is the plugging length (2 m);  $L$  is the charge length (8 m);  $B$  is the minimum resistance line (2 m, roughly equal to the row spacing);  $S$  is the hole distance (3 m);  $D$  is the hole distance (150 mm).

The whole model is modeled by Euler element, and the side, bottom and back of the model are set as non-reflective boundary surface. The top surface and the front face of the model are modeled in the way of free surface. The initiation point is located in the center of the top surface and the bottom surface of the charge cylinder, and is set for simultaneous initiation at both ends of the explosive column, delay detonation between different column ([Qi et al., 2022](#)) (see [Figure 4](#)).

Riedel-Hiermaier-Thoma material model was adopted for rocks ([Riedel et al., 1999](#)), and the damage level was determined by [Eq. 7](#).

$$D = \sum \frac{\Delta \epsilon^p}{\epsilon^f} \tag{6}$$

where,  $\Delta \epsilon^p$  is the cumulative plastic deformation of the model;  $\epsilon^f$  is the failure strain.

As a brittle material, rock mass has the characteristics of pressure correlation of compressive strength, strain hardening, damage softening and different strain rate effects of tension and pressure, etc. RHT constitutive model can be simplified according to the above basic assumptions of rock mass, and the rock mass blasting crushing model is used to study. The RHT material parameters used in the model have been calibrated by tests ([Schill, 2012](#)). The material used for the in-cavity blockage in the model was soil and foam (MAT\_SOIL\_AND\_FOAM, generally used when the soil is not confined to a structure or when geometric boundaries do not exist) considering the RHT material does not support the Euler algorithm. The RHT material parameters are shown in [Table 4](#).

The air in the model is assumed to be an ideal gas, and its equation of state is [Rogers and Mayhew \(1995\)](#):

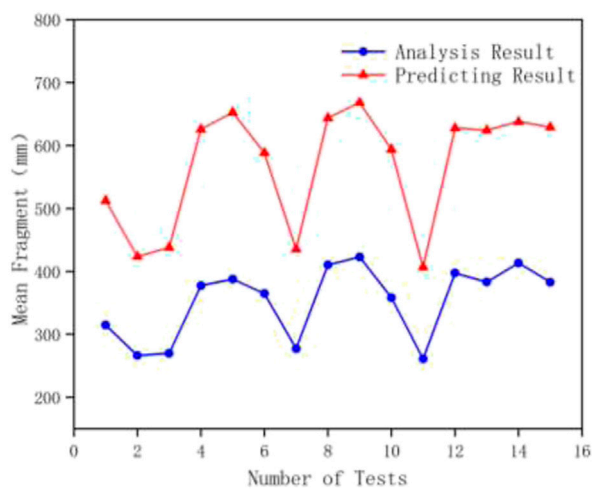


FIGURE 1

The results of  $x_m$  calculation by the traditional KUZ-RAM model and the area measurement method.

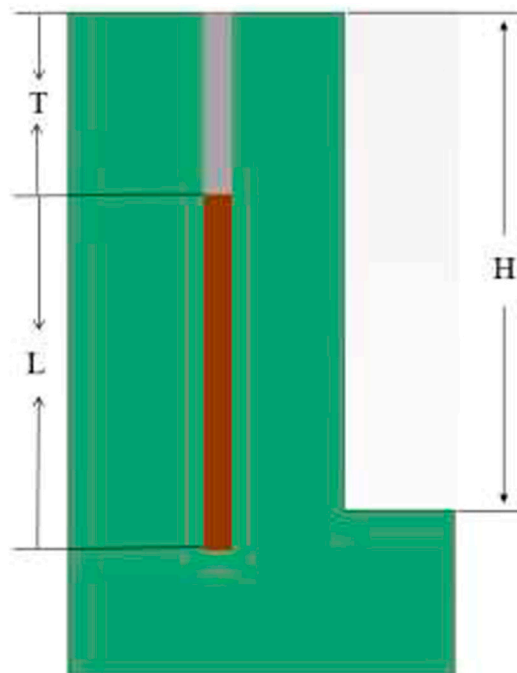


FIGURE 2

Front view of the model.

$$P = (\gamma - 1) \frac{\rho}{\rho_0} e_0 \quad (7)$$

where,  $P$  is gas pressure;  $\rho$  is the air density,  $1.225 \text{ kg/m}^3$ ;  $e_0$  is the initial internal energy density of air,  $254.3 \text{ kJ/m}^3$ ;  $\gamma$  is the adiabatic index, 1.4; the specific heat capacity of air is  $717.6 \text{ J/kg}\cdot\text{K}$ ; and the reference temperature is  $288.2 \text{ K}$ .

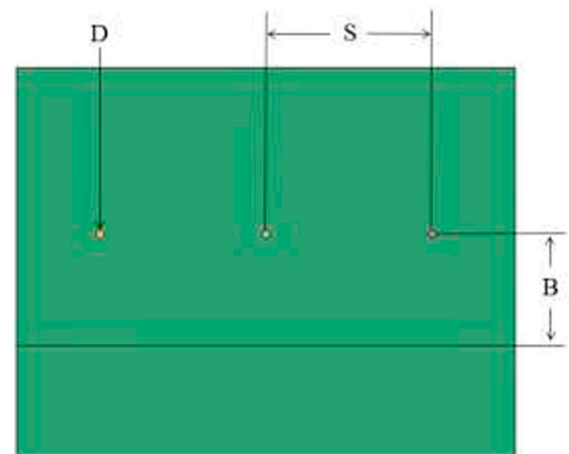


FIGURE 3

Top view of the model.

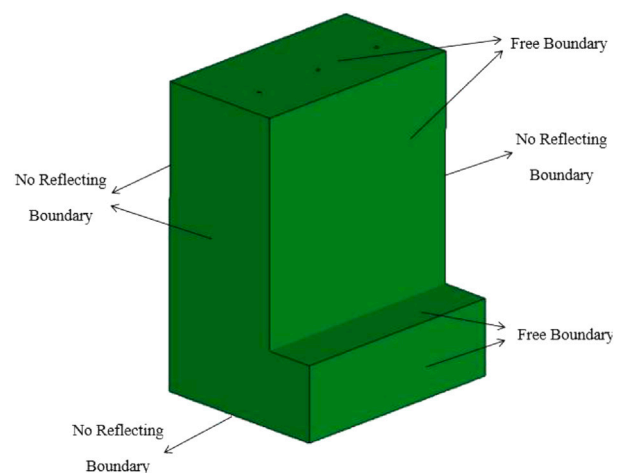


FIGURE 4

Boundary case of the model.

The explosive is TNT, and its explosion equation can be described by standard JWL equation of state (Lee et al., 1973):

$$p = A_1 \left( 1 - \frac{\mu}{R_1 v} \right) e^{-R_1 v} + A_2 \left( 1 - \frac{\mu}{R_2 v} \right) e^{-R_2 v} + \frac{\mu e}{v} \quad (8)$$

where,  $p$  is detonation pressure;  $v$  is the relative volume of detonation products;  $e$  is the initial specific internal energy;  $A_1$ ,  $A_2$ ,  $R_1$ ,  $R_2$ , and  $\mu$  are equation of state parameter constants (Qi et al., 2023). Related parameters are shown in Table 5.

### 3.2 Working condition design

According to the field test conditions, simulation conditions are designed in the simulation calculation (Table 6). The parameters of

TABLE 4 RHT model parameters for rock mass in Lagrangian elements.

Density	2627 kg/m <sup>3</sup>	Ref. compressive strain rate	3.0e8
Shear Modulus	18.6 Gpa	Ref. tensile strain rate	3.0e9
Pore crush B0	1.22	Failure tensile strain rate	3.0e22
Pore crush B1	1.22	Failure compressive strain rate	3.0e22
Bulk Modulus T1	40 Gpa	Compressive strain rate dependence exponent	0.032
Bulk Modulus T2	0	Tensile strain rate dependence exponent	0.036
Bulk Modulus A1	40 Gpa	Volumetric plastic strain	0.001
Bulk Modulus A2	0	Compressive yield strength	200 Mpa
Bulk Modulus A3	0	Tensile yield strength	7 Mpa
Failure surface A	2.618	Damage parameter D1	0.04
Failure surface N	0.7985	Damage parameter D2	1.0
Shear strength	36 Mpa	Minimum damaged residual strain	0.01
Uniaxial tensile strength	10 Mpa	Residual surface parameter AF	0.873
Lode Angle Q0	0.567	Residual surface parameter AN	0.559
Lode Angle B	0.0105	Grunnisen Gamma	0
Compaction pressure	6 Gpa	Crush pressure	133 Mpa
Initial porosity	1.0	Porosity exponent	3

TABLE 5 Explosive parameters of TNT.

$\rho \text{ (g} \cdot \text{cm}^{-3}\text{)}$	$A_1 \text{ (GP}_a\text{)}$	$A_2 \text{ (GP}_a\text{)}$	$R_1$	$R_2$	$e \text{ (J} \cdot \text{m}^{-3}\text{)}$	$\mu$
1.63	373.7	3.747	4.15	0.9	$6.0 \times 10^9$	0.35

the first five groups of conditions correspond to the mine field production conditions, and the remaining conditions are used to study the relationship between blasting design parameters and blasting average block size.

### 3.3 Blasting assessment of rock

The rock mass will have the maximum damage at the instantaneous energy peak (Li et al., 2021b). Taking the first group of working conditions in Table 3 as an example, the overall pressure distribution is shown in Figure 5. After removing elements with damage degree greater than 0.1, cracks will be formed in the rock mass, and detailed structural characteristics related to damage at different loading stages will be obtained (Li et al., 2023). The damage situation is shown in Figure 6.

Similar to the area measurement method, 3D was converted into 2D pictures by slicing considering the difficulty of estimating the size of debris directly on a 3D model. The multiple incisions were selected for fragment evaluation, as shown in Figure 7. Slices were sliced between each hole to obtain the fragmentation conditions between different cross sections.

The circumference and area of the rock fragments are calculated by operations in LS-DYNA and then combined with the area measurement method to determine the sifting size of the rock

blocks. Section conditions of the first group of working conditions in Table 3 are shown in Figures 8, 9.

### 3.4 Comparison of simulation results with field tests

In order to verify the accuracy of model calculation, the calculation results of the first five groups of working conditions are compared with the field mining data, as shown in Table 7.

It can be seen from Table 5 that under the same working conditions as mine field production, the error of numerical calculation is within 10%. Considering the deviation of actual sampling accuracy, it is reasonable to think that the model can simulate the blasting mining process. After obtaining a large number of data, the original average block size prediction model is optimized.

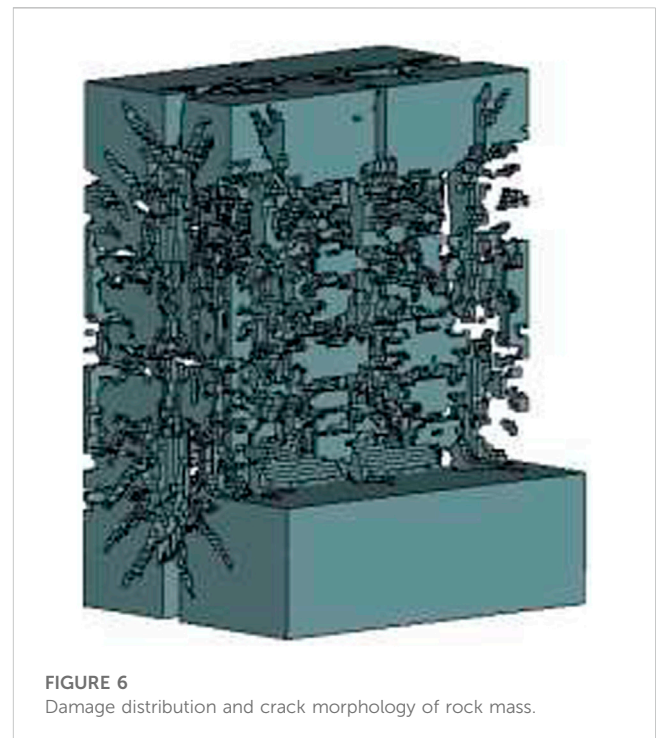
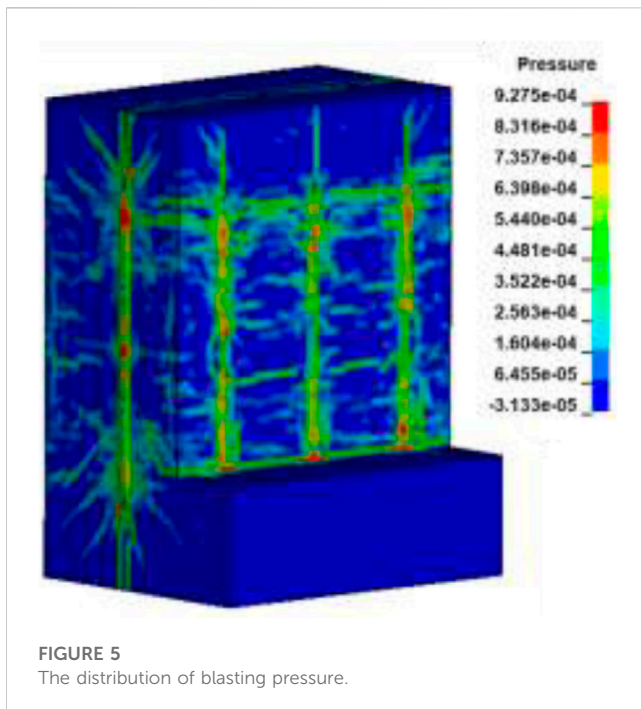
## 4 Updating and discussion of the model

### 4.1 Model updating

The original KUZ-RAM formula is optimized and improved because the original formula overestimates the average block size  $x_m$ .

TABLE 6 Model simulation conditions.

Conditions	Rock coefficient	Specific explosive consumption $k$ (kg/m <sup>3</sup> )	Single-hole charge $e$ (kg)	Conditions	Rock coefficient	Specific explosive consumption $k$ (kg/m <sup>3</sup> )	Single-hole charge $e$ (kg)
1	14.0	0.82	699.4	21	10.8	0.66	477.6
2	14.0	0.70	746.8	22	10.8	0.60	376.1
3	14.0	0.65	699.4	23	11.4	0.60	406.9
4	10.2	0.72	447.6	24	11.4	0.76	477.6
5	10.2	0.57	406.9	25	11.4	0.75	406.9
6	8.1	0.63	282.6	26	11.7	0.66	477.6
7	8.1	0.57	310.9	27	11.7	0.76	477.6
8	8.1	0.69	310.9	28	11.7	0.75	406.9
9	8.7	0.69	310.9	29	12	0.74	533.9
10	8.7	0.63	341.9	30	12	0.75	406.9
11	8.7	0.54	341.9	31	12	0.66	477.6
12	9	0.54	341.9	32	12.6	0.66	477.6
13	9	0.60	406.9	33	12.6	0.73	525.4
14	9	0.75	406.9	34	12.6	0.74	533.9
15	9.6	0.75	406.9	35	13.2	0.81	587.3
16	9.6	0.76	477.6	36	13.2	0.89	533.9
17	9.6	0.66	477.6	37	13.2	0.76	553.9
18	10.2	0.66	477.6	38	13.5	0.89	533.9
19	10.2	0.67	366.2	39	13.5	0.88	635.9
20	10.8	0.75	406.9	40	13.5	0.87	635.9



The prediction formula for the average block size shown in Eq. 3 is divided into two parts, which are the part representing the characteristics of rock mass (rock coefficient) and the parameter of blasting design. That is:

$$x_m = A \cdot R \quad (9)$$

$$R = k^{-0.8} e^{1/6} \left( \frac{115}{S_{anfo}} \right)^{-\frac{19}{30}} \quad (10)$$

Lawal (2021) believes that coefficient 0.06 in Eq. 4 is the root cause of error when revising the KUZ-RAM model. However, this redefinition of rock coefficient not only reduces the application range of the original rock coefficient, but also fails to consider the influence of blasting design parameters on the prediction results. Therefore, the paper maintains the original rock coefficient in the optimization process of the model, and focuses on the optimization of blasting design parameters. The revised model is:

$$x'_m = A \cdot K \cdot R \quad (11)$$

where,  $x'_m$  is the corrected average blasting block size.

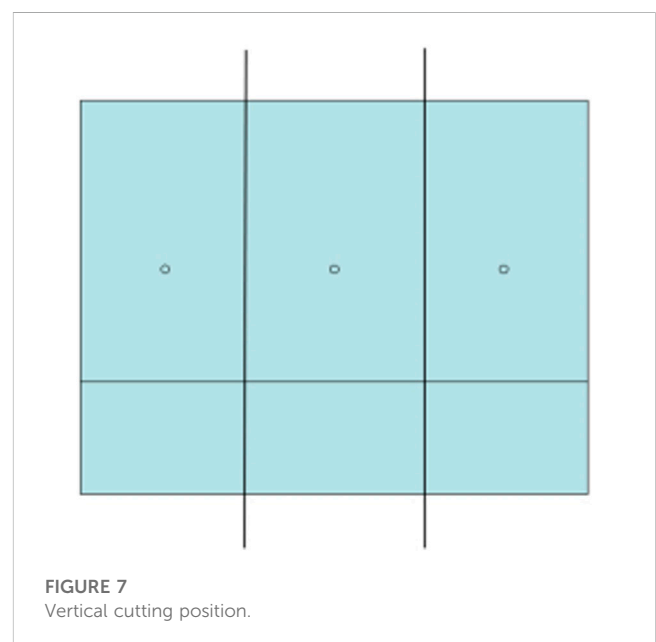
Equation 12 can also be rewritten as:

$$x'_m = K A k^{-0.8} e^{1/6} \left( \frac{115}{S_{anfo}} \right)^{-\frac{19}{30}} \quad (12)$$

50 groups of blasting results and simulation data from two mines are selected, and Levenberg-Marquardt algorithm (L-M algorithm) is applied to fit the coefficient K of Eq. 13. The result of this coefficient is 0.623, which is more reasonable.

Therefore, Eq. 12 can be updated as:

$$x'_m = 0.623 A k^{-\frac{4}{5}} Q^{1/6} \left( \frac{115}{S_{ANFO}} \right)^{19/30} \quad (13)$$



The symbol in the formula has the same meaning as in the previous text.

## 4.2 Comparison between the updated and original model

Data sampling is conducted on the blasting results of another 15 groups under different working conditions in field blasting, and after sorting,  $x_m$  and  $x_o$  are compared between the prediction



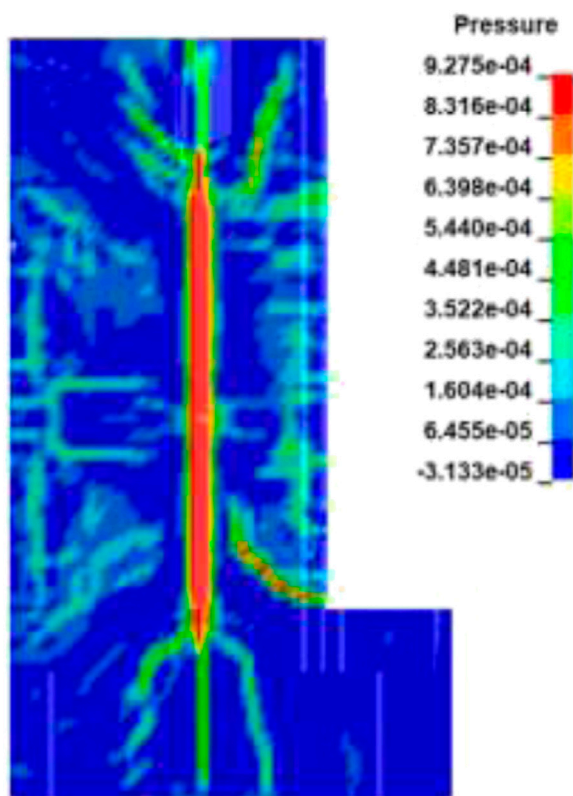


FIGURE 8  
The blasting pressure distribution.

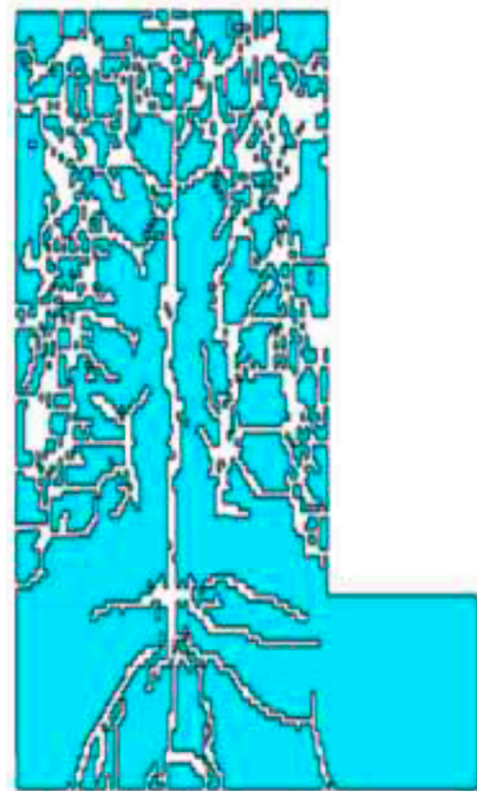


FIGURE 9  
Crack distribution on one of cross sections.

results of the original, updated KUZ-RAM model, and obtained by the area measurement method (field measurement). The comparison results are shown in Table 8. From the comparison results of the three, it can be seen that the prediction results of the updated KUZ-RAM model are very close to that of the area measurement method. The prediction errors of  $x_m$  were all below 6%, and the linear correlation coefficient  $R^2$  reached 0.97. This is significantly higher than the prediction accuracy of the original KUZ-RAM model with an average error of more than 60% ( $R^2 = -1.99$ ). In addition, the prediction error of the original model in  $x_0$  is further amplified due to the inaccuracy of the  $x_m$  prediction results. The prediction error of  $x_0$  in the original model is more than 50% ( $R^2 = -2.61$ ), but the updated model is less than 8% ( $R^2 = 0.96$ ). It can be seen that the prediction accuracy of the updated thickness model in both  $x_m$  and  $x_0$  has been greatly improved, which is very close to the actual measured results.

The comparison results of Figures 10, 11 show that the optimized model in this paper can predict the size of blasting block size more accurately, and has a good effect on the prediction and description of the blasting distribution model. Moreover, the combination of image processing, area measurement and numerical simulation is easier to realize and cheaper than traditional statistical methods.

### 4.3 Evaluation of the updated model

The regularity of calculation block size and field explosion and error before and after model updating is also further studied. The calculation results of the updated KUZ-RAM model were compared with those of the original KUZ-RAM model through the field blasting results. All the data are from the field test results under different blasting conditions, including large and small blasting conditions. The blasting results under different lithology and blasting parameters are analyzed and compared.

As discussed above, the prediction result of the original KUZ-RAM model for  $x_m$  is generally larger than that of the updated model. As shown in Figure 12, the horizontal axis is the image analysis result of  $x_m$  (measured I); vertical axis is the original KUZ-RAM model prediction error ( $|x_m - I|$ ), linear fitting results for both:  $|x_m - I| = 0.53I + 24.12$ , linear coefficient  $R^2 = 0.86$ . It can be considered that the error has a linear relationship with the actual average block size, which also proves the feasibility of using a single correction coefficient to correct the model. Another obvious phenomenon is that the error is further amplified with the increase of  $x_m$ . In open-pit mines, large-scale blasting is the main mining method, and its average block size is usually greater than 500 mm, which indicates that the original KUZ-RAM model has great limitations in application.

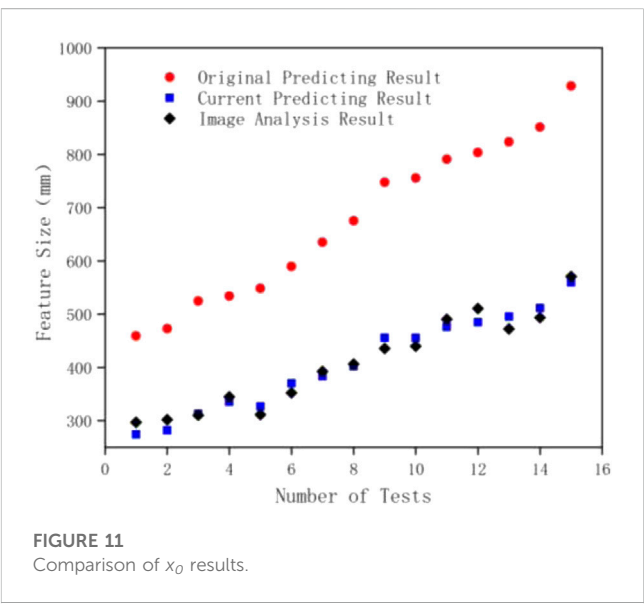
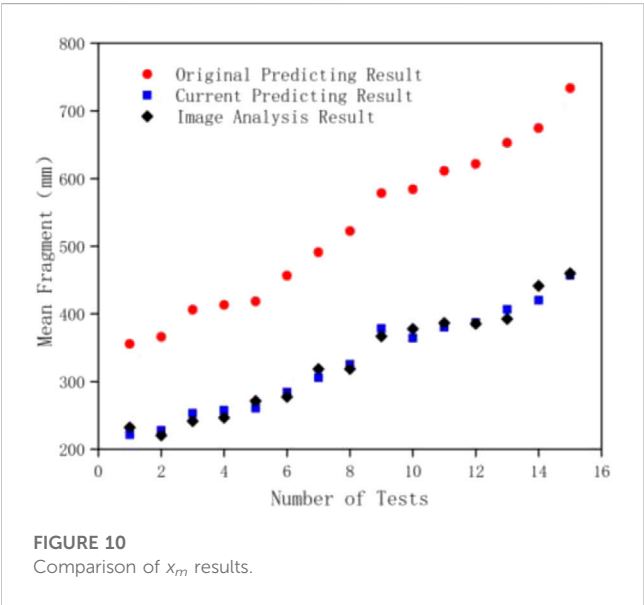
TABLE 7 Comparison between model calculation and field test.

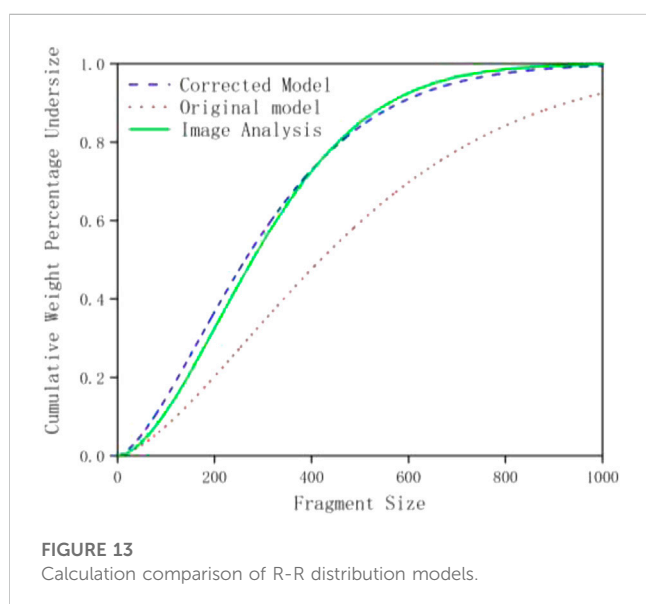
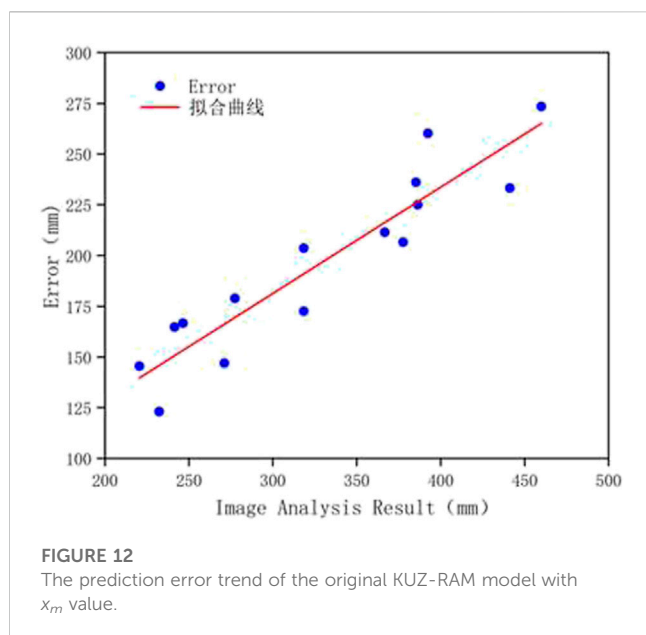
Conditions	A	$k$ (kg/m <sup>3</sup> )	$e$ (kg)	R (mm)	I (mm)	$\sigma$ (%)
1	14	0.82	699.4	332.8	358.2	7.1
2	14	0.70	746.8	381.8	382.8	0.3
3	14	0.65	699.4	400.7	410.2	2.3
4	10	0.72	447.6	244.8	266.4	8.1
5	10	0.57	406.9	290.5	314.7	7.7

Note: A is rock coefficient;  $k$  is the single cost of explosive;  $e$  is single-hole charge; R is the result of numerical calculation; I is field test results;  $\sigma$  is relative error sigma,  $\sigma = \frac{I-R}{I} \times 100\%$ .

TABLE 8 Comparison of original KUZ-RAM model, updated model and field measured results.

Data groups	Original model $x_m$ (mm)	Updated model $x'_m$ (mm)	Field measurement $I_m$ (mm)	Original model $x_0$ (mm)	Updated model $x'_0$ (mm)	Field measurement $I_0$ (mm)
1	355.4	221.4	232.3	459.1	274.4	296.9
2	366.1	228.1	220.6	472.9	281.8	302.1
3	406.2	253.1	241.5	524.7	312.9	310.5
4	413.3	257.5	246.6	533.8	335.5	344.6
5	418.2	260.5	271.2	548.2	326.8	311.6
6	456.4	284.3	277.5	589.5	370.3	352.2
7	491.1	305.8	318.5	635.1	383.5	392.4
8	522.1	325.3	318.5	675.1	402.1	406.3
9	578.2	378.4	366.8	747.6	455.7	435.6
10	584.2	364.1	377.7	755.4	455.7	439.9
11	611.4	380.1	386.4	790.6	475.9	490.5
12	621.4	387.2	385.3	803.5	485.1	510.4
13	652.6	406.6	392.4	823.5	495.4	472.2
14	674.5	420.2	441.3	851.1	511.7	493.8
15	733.4	456.9	460.0	928.4	559.6	570.7





In order to further verify the accuracy of the updated model, image analysis and updated model prediction are used to calculate and optimize different blasting results. The calculation comparison of R-R distribution models is shown in Figure 13. The linear relationship between the updated model and the results of image analysis ( $R^2 = 0.99$ ) is higher than that of the original model ( $R^2 = 0.72$ ). It can be seen that the R-R distribution model obtained by KUZ-RAM model is basically consistent with the results of image analysis, which can provide a more accurate description of the block distribution of field mines.

## 5 Conclusion

In this paper, we use the fitting method in image processing and machine learning to propose a correction to the prediction formula of the average block size  $x_m$  by using the original formula and combining the field blasting images and data, adding a coefficient of 0.623 to the empirical formula, increasing the  $R^2$  between the original model prediction results and the real blasting results from  $-2.0176$  to  $0.9912$ , and improving the accuracy of the prediction for large-scale blasting results without changing the accuracy of the fine grain prediction. The accuracy of the prediction of large-scale blasting results is improved without changing the accuracy of the prediction of fine grains, and a higher prediction accuracy is achieved. In addition, the related ideas and theories of slice sampling calculation for the simulated rock mass model simplify the difficult problem of statistical blasting fragmentation in the three-dimensional LS-DYNA model. A more simple and convenient method is used to obtain the internal block size of rock mass.

At the same time, for karst areas with complex geological conditions, modified blasting block parameters are realized according to the comparison results of different rock damage integrity, which can better evaluate the rock integrity after project crushing, which is of great significance for practical engineering applications.

## Data availability statement

The original contributions presented in the study are included in the article/Supplementary Material, further inquiries can be directed to the corresponding author.

## Author contributions

MJ: Responsible for experiment, data processing and manuscript writing. WZ: Data collection and analysis. YE: Data collection, Experimental work. LM: Responsible for experiment, data processing and Proofreading of data.

## Funding

This work was supported by National Natural Science Foundation of China (No: 51678050).

## Conflict of interest

The authors declare that the research was conducted in the absence of any commercial or financial relationships that could be construed as a potential conflict of interest.

# Publisher's note

All claims expressed in this article are solely those of the authors and do not necessarily represent those of their affiliated

# References

- Asl, P. F., Monjezi, M., Hamidi, J. K., and Armaghani, D. J. (2018). Optimization of fly rock and rock fragmentation in the Tajareh limestone mine using metaheuristics method of firefly algorithm. *Eng. Comput.* 34, 241–251. doi:10.1007/s00366-017-0535-9
- Bahrami, A., Monjezi, M., Goshtasbi, K., and Ghazvinian, A. (2010). Prediction of rock fragmentation due to blasting using artificial neural network. *Eng. Comput.*, 27(2), 1–5. doi:10.1007/s00366-010-0187-5
- Cao, L., Tan, H., and Peng, H. (May 2015). Mixed dynamic task allocation for multiple UAV. *J. Nanjing Univ. Sci. Technol.* 39 (2), 206–214.
- Cunningham, C. V. B. (1987). Fragmentation estimations and the kuz—ram model, Proceedings of the second international symposium on rock fragmentation by blasting. Keystone: Colorado, 475–487.
- da Gama, C. D. (1971). Size distribution general law of fragments resulting from rock blasting. *Trans. Soc. Min. Eng. AIME* 250 (4), 314–316. doi:10.1016/j.jrmms.2014.08.007
- Favreau, R. F. 1983. "Rock displacement velocity of bench blasting[J]," in Proceedings of the first International Conference on Blasting and Rock Fragmentation, 47:408–418.
- Favreau, R. F. 1983. "Displacement velocity of rock by step blasting," in Proceedings of the First International Conference on Rock Blasting.
- Gheibie, S., Aghababaei, H., Hoseinie, S. H., and Pourrahimian, Y. (2009). Modified kuz—ram fragmentation model and its use at the sungun copper mine. *J. Rock Mech. Min. Sci.* 46 (6), 967–973. doi:10.1016/j.jrmms.2009.05.003
- Harries, A. (1973). *Mathematical model of cratering and blasting national symp.* Adelaide: Australia: Rock Frag.
- Harries, G. (1977). "The Calculation of the Fragmentation of rock from cratering," in *15th Aplom symposium Apcom '77*. (Brisbar, Australia).
- Just, G. D. (1974). The application of size distribution equations to rock breakage by explosives. *J. Rock Mech. Min. Sci. Geomech. Abstr.* 11 (1), 22. doi:10.1007/BF01238045
- Kabwe, E. (2018). Velocity of detonation measurement and fragmentation analysis to evaluate blasting efficacy. *J. Rock Mech. Geotech. Eng.* 10, 523–533. doi:10.1016/j.jrmge.2017.12.003
- Kuznetsov, V. M. (1973). The mean diameter of the fragments formed by blasting rock. *Sov. Min. Sci.* 9, 144–148. doi:10.1007/bf02506177
- Lawal, A. I. (2021). A new modification to the Kuz-Ram model using the fragment size predicted by image analysis. *J. Rock Mech. Min. Sci.* 138, 104595. doi:10.1016/j.jrmms.2020.104595
- Lee, E., Finger, M., and Collins, W. . *JWL equation of state coefficients for high explosives*. Lawrence Livermore National Laboratory Report, 1973. Livermore, CA, USA.
- Li, X. L., Chen, S. J., Liu, S. M., and Li, Z. H. (2021). AE waveform characteristics of rock mass under uniaxial loading based on Hilbert-Huang transform. *J. Central South Univ.* 28 (6), 1843–1856. doi:10.1007/s11771-021-4734-6
- Li, X. L., Chen, S. J., Wang, S., Zhao, M., and Liu, H. (2021). Study on *in situ* stress distribution law of the deep mine taking Linyi Mining area as an example. *Adv. Mater. Sci. Eng.* 9 (4), 5594181–5594211. doi:10.1155/2021/5594181
- Li, X. L., Zhang, X. Y., Shen, W. L., Zeng, Q., Chen, P., Qin, Q., et al. (2023). Research on the mechanism and control technology of coal wall sloughing in the ultra-large mining height working face. *Int. J. Environ. Res. Public Health* 20 (2), 868. doi:10.3390/ijerph20010868
- Lilly, P. A. (1986). An empirical method of assessing rock mass blastability, Proceedings of the large open pit planning conference. Parkville, Victoria: Australian IMM, 89–92.
- Liu, S. M., Li, X. L., Wang, D. K., and Zhang, D. (2020). Investigations on the mechanism of the microstructural evolution of different coal ranks under liquid nitrogen cold soaking. *Energy Sources, Part A Recovery, Util. Environ. Eff.*, 28, 1–17. doi:10.1080/15567036.2020.1841856
- Margolin, G., Numerical simulation of failure . Changsha, China: Proceedings of the First International Conference on Blasting Rock Breaking, 1985:203–210.
- McHugh, S. Numerical simulation of dynamic induced failure and breakage. Proceedings of the first International Conference on Blasting and Rock Fragmentation. Bristol, UK, 1983; 234–243.
- Mehrdanesh, A., Monjezi, M., and Sayadi, A. R. (2018). Evaluation of effect of rock mass properties on fragmentation using robust techniques. *Eng. Comput.* 34, 253–260. doi:10.1007/s00366-017-0537-7
- Ozkahraman, H. T. (2006). Fragmentation assessment and design of blast pattern at Goltas Limestone Quarry, Turkey. *Int. J. Rock Mech. Min. Sci.* 43 (4), 628–633. doi:10.1016/j.jrmms.2005.09.004
- Qi, J., Wang, D., Liu, Q., Liu, C., Wang, Z., He, Z., et al. (2022). Deflagration evolution characteristic and chemical reaction kinetic mechanism of JP-10/DEE mixed fuel in a large-scale tube. *Fuel* 322, 124238. doi:10.1016/j.fuel.2022.124238
- Qi, J., Wang, D., and Shi, C. (2023). Effects of aluminum powder additives on deflagration and detonation performance of JP-10/DEE mixed fuel under weak and strong ignition conditions. *Appl. Energy* 331, 120477. doi:10.1016/j.apenergy.2022.120477
- Riedel, W., Thoma, K., Hiermaier, S., and Schmolsinske, E. (1999). Penetration of reinforced concrete by BETA-B-500, numerical analysis using a new macroscopic concrete model for hydrocodes, Proceedings of the 9th International Symposium on Interaction of the Effects of Munitions with Structures. Berlin, Germany, 315–322.
- Rogers, G. F. C., and Mayhew, Y. R. *Thermodynamic and transport properties of fluids*. John Wiley & Sons, 1995. Hoboken, NJ, USA.
- Sanchidrián, J. A., Segarra, P., and López, L. M. (2006). A practical procedure for the measurement of fragmentation by blasting by image analysis. *Rock Mech. Rock Eng.* 39 (4), 359–382. doi:10.1007/s00603-005-0073-4
- Sanchidrián, J. A., Segarra, P., Ouchterlony, F., and Lopez, L. M. (2009). On the accuracy of fragment size measurement by image analysis in combination with some distribution functions. *Rock Mech. Rock Eng.* 42 (1), 95–116. doi:10.1007/s00603-007-0161-8
- Schill, M. *Finite Element Simulations Of Blasting And The Effects Of Precise Initiation On Fragmentation*. Swedrec: Norrbotten, Sweden; 2012.
- Shim, H.-J., Ryu, D.-W., Chung, S.-K., Synn, J.-H., and Song, J.-J. (2009). Optimized blasting design for large-scale quarrying based on a 3-D spatial distribution of rock factor. *J. Rock Mech. Min. Sci.* 46 (2), 326–332. doi:10.1016/j.jrmms.2008.07.006
- Spathis and Alex, T. (2004). A correction relating to the analysis of the original kuz-ram model. *Fragblast* 8 (4), 201–205. doi:10.1080/13855140500041697
- Thomas Busuyi, J. (2009). Optimization of drilling and blasting operations in an open pit mine—The SOMAIR experience. *Min. Sci. Technol.* 19 (3), 736–739. doi:10.1016/s1674-5264(09)60134-4
- Trivedir, S. I. N. G. H. T. N., and Gupta (2015). Prediction of blast-induced flyrock in opencast mines using ANN and ANFIS. *Geotechnical Geol. Eng.* 33 (4), 875–891. doi:10.1007/s10706-015-9869-5
- Turcotte, D. L. (1986). Fractals and fragmentation. *J. Geophys. Res.* 91 (132), 1921–1926. doi:10.1029/jb091ib02p01921
- Xie, C., Nguyen, H., Bui, X.-N., Choi, Y., Zhou, J., and Nguyen-Trang, T. (2021). Predicting rock size distribution in mine blasting using various novel soft computing models based on meta-heuristics and machine learning algorithms. *Geosci. Front.* 12 (3), 101108. doi:10.1016/j.gsf.2020.11.005
- Zhao, M. (2015). *Study on lumpiness distribution of rock burst based on fractal theory*. Inner Mongolia University of Science and Technology. Inner Mongolia, China.
- Zhou, X. M., Wang, S., Li, X. L., Meng, J., Li, Z., Zhang, L., et al. (2022). Research on theory and technology of floor heave control in semicircular rock roadway: Taking longhu coal mine in Qitaihe mining area as an Example. *Lithosphere* 2022 (11), 3810988. doi:10.2113/2022/3810988

# Frontiers in Earth Science

Investigates the processes operating within the major spheres of our planet

Advances our understanding across the earth sciences, providing a theoretical background for better use of our planet's resources and equipping us to face major environmental challenges.

## Discover the latest Research Topics

[See more →](#)

### Frontiers

Avenue du Tribunal-Fédéral 34  
1005 Lausanne, Switzerland  
[frontiersin.org](https://frontiersin.org)

### Contact us

+41 (0)21 510 17 00  
[frontiersin.org/about/contact](https://frontiersin.org/about/contact)

